

**ANA MARÍA MOLINA ARCILA**

**High resolution Fabry-Pérot interferometer – dynamic system modeling  
and nan positioning control system design.**

Dissertation presented to the Escola Politécnica  
of the Universidade de São Paulo to obtain the  
Master of Science.

São Paulo  
2014

**ANA MARÍA MOLINA ARCILA**

**High resolution Fabry-Pérot interferometer – dynamic system modeling  
and nan positioning control system design.**

Dissertation presented to the Escola Politécnica  
of the Universidade de São Paulo to obtain the  
Master of Science.

Major Area of Specialization:  
Systems Engineering

Advisor  
Prof. Dr. Fábio de Oliveira Fialho

São Paulo  
2014

Este exemplar foi revisado e alterado em relação à versão original, sob responsabilidade única do autor e com a anuência de seu orientador.

São Paulo, 18 de Março de 2014

Assinatura do autor

Assinatura do orientador

## FICHA CATALOGRÁFICA

**Molina Arcila, Ana Maria**  
**High resolution Fabry-Pérot interferometer: dynamic system modeling and nanopositioning control system design / A.M. Molina Arcila. -- ed. corr. -- São Paulo, 2014.**  
**206 p.**

**Dissertação (Mestrado) - Escola Politécnica da Universidade de São Paulo. Departamento de Engenharia de Telecomunicações e Controle.**

**1.Engenharia de sistemas de computação 2.Identificação de sistemas I. Universidade de São Paulo. Escola Politécnica. Departamento de Engenharia de Telecomunicações e Controle II.t.**

A Juan David, mis papás Alberto, Olga, y mi hermana Natalia.

## ACKNOWLEDGEMENTS

I would like to thank the Fundação de Amparo a Pesquisa do Estado de São Paulo, FAPESP, process number 2011/11877-5 for financial support.

I am also grateful to my advisor Professor Dr. Fábio Fialho, for his academic guidance and advice and Professor Dr. Cláudia Mendes de Oliveira for giving me the opportunity to be part of the BTFI team and for her continuous support. Sincere thanks are extended to the members of the examining committee of the qualification and defense: Prof. Dr. Jose Jaime da Cruz, Prof. Fuad Kassab Júnior and Prof. Dr. Pedro Paglione, for their time and expertise. Their various insights are much appreciated.

Special thanks to Claudia Marcelino, for her always efficient help and to the Laboratório de Microeletrônica of the Escola Politécnica for welcoming us in their laboratory and providing the needed resources for the development of this project.

Many thanks to my team mates in this project: Victor, Rafael, Tiago, Fernando and Leonardo, for giving me the pleasure of being part of an amazing and extremely talented engineering team. I am also grateful to Jair and Mauricio for being always ready to give me their technical support but especially for their friendship. My university life was filled with great memories thanks to the amazing friends I made along the way: Robert, Mary, Gustavo, Roberto, Filipe, Juan and Andres. And special thanks to my Colombian friends during my experience in Brazil: Jairo, Natalia, Arturo, Miguel and Santiago. During this stage of our lives when we were all away from home, we were like a family. I am grateful for the great moments and the innumerable things they did for me.

More importantly I would never have been able to do my dissertation and master program without the support of my family. I thank my mom, dad and sister because despite being physically separated from them I could always count with their love and unconditional support. And I am especially grateful to my husband, Juan David, who was always ready to listen to my greatest frustrations, celebrate my greatest accomplishments and giving me the strength and support I needed along the way. It was an incredible journey during our time in Brazil and there are no words to express how grateful I am for his unconditional love, support, his faith in me and for taking my dreams as his.

## SUMMARY

This work represents the research project to obtain the degree of Master of Sciences in Electrical Engineering, specializing in Systems Engineering, at the Escola Politécnica of the Universidade de São Paulo, in São Paulo, Brazil.

The main objective of the project is to design the mirror nan positioning controller of the state-of-the-art Fabry-Pérot interferometer to be installed in the Brazilian Tunable Filter Imager (BTFI) on the Southern Astrophysical Research (SOAR) telescope in Chile.

A three-input-three-output multivariable prototype of the Fabry-Pérot system is comprised of three high-range Amplified Piezoelectric Actuators (APA) of 360  $\mu\text{m}$  stroke and three 400  $\mu\text{m}$  range capacitive measurement systems.

A characterization of the instrumentation of the system, which consists of capacitive sensors and capacitance-to-voltage converters, piezoelectric actuators, power drivers of the piezoelectric actuators and data acquisition system was done as part of the identification and study of the system.

With the characterization of the system, a sixth-order complete system model was built on top of a second-order piezoelectric actuator parametric model, required for the design of the controllers.

Subsequently, the scientific specifications were translated to a control problem and the design of a robust controller was made following the Linear Quadratic Gaussian/Loop Transfer Recovery (LQG/LTR) method. Also a Proportional-Integral controller tuned using a genetic algorithm was designed to be used as benchmark.

Finally the built controllers were validated in the real system. Results show that both controllers achieve the performance requirements of following reference signals and having null steady-state error. However, the robust controller is by far the best suited for the Fabry-Pérot instrument in terms of performance and stability because of its higher bandwidth and robustness to modeling errors.

Key-words: Nanopositioning. Fabry-Pérot interferometer. Control systems. Robust controller. Dynamic modeling.

## RESUMO

Este trabalho apresenta o projeto de pesquisa para obtenção do título de Mestre em Engenharia Elétrica, área de concentração de engenharia de sistemas, da Escola Politécnica da Universidade de São Paulo.

O objetivo principal deste projeto foi desenvolver um controlador de nanoposicionamento para o interferômetro de Fabry-Pérot que será instalado no instrumento BTFI (Brazilian Tunable Filter Imager), no telescópio SOAR (Southern Astrophysical Research Telescope), no Chile.

O interferômetro de Fabry-Pérot é um sistema multivariável de três entradas e três saídas composto por três atuadores piezoelétricos de  $370 \mu\text{m}$  de deslocamento, e três sistemas capacitivos de medida de distância de  $400 \mu\text{m}$  de faixa de medição.

A caracterização da instrumentação do sistema, que consiste em sensores capacitivos, conversores de capacitância para tensão, atuadores piezoelétricos, drivers de potência para os atuadores piezoelétricos e sistemas de aquisição de dados, fez parte do estudo e da identificação do sistema.

Após a caracterização da instrumentação, foi desenvolvido um modelo físico de sexta ordem para o sistema completo, partindo do modelo de segunda ordem dos atuadores piezoelétricos. Este modelo é necessário para o projeto dos controladores.

Subsequentemente, as especificações científicas foram traduzidas em um problema de controle e o projeto do controlador robusto foi feito seguindo a técnica LQG/LTR (Linear Quadratic Gaussian/Loop Transfer Recovery). Um controlador Proporcional-Integral (PI) também foi desenvolvido e sintonizado usando um algoritmo genético, para funcionar como ponto de comparação.

Finalmente, os controladores desenvolvidos foram validados no sistema real. Com os resultados concluiu-se que ambos controladores atingiram as especificações de desempenho no que diz respeito a seguir sinais de referência com erro nulo no estado estacionário. Pôde-se concluir ainda que o controlador robusto mostrou-se mais adaptado ao instrumento Fabry-Pérot em termos de desempenho e estabilidade, pois, comparado ao PI, é um controlador com maior largura de banda e robustez aos erros de modelamento.

## TABLE OF CONTENTS

TABLE OF CONTENTS .....	VIII
LIST OF FIGURES.....	X
LIST OF TABLES.....	XII
LIST OF ABBREVIATIONS AND ACRONYMS .....	XIII
LIST OF SYMBOLS .....	XV
<b>1 INTRODUCTION .....</b>	<b>18</b>
1.1 MOTIVATION AND WORK OBJECTIVES .....	18
1.2 DISSERTATION STRUCTURE .....	20
1.3 DEVELOPMENT METHODOLOGY .....	21
<b>2 BRAZILIAN TUNABLE FILTER INTERFEROMETER.....</b>	<b>23</b>
2.1 IMAGING BRAGG TUNABLE FILTER.....	24
2.2 FABRY-PÉROT .....	25
2.2.1 <i>The Classical Fabry-Pérot Mode</i> .....	26
2.2.2 <i>Tunable Filter Mode</i> .....	27
2.2.3 <i>Low and High Resolution Fabry-Pérot in series</i> .....	27
2.3 DETECTORS.....	27
2.4 THE SOAR TELESCOPE.....	28
<b>3 THE FABRY-PÉROT INTERFEROMETER .....</b>	<b>29</b>
3.1 PHYSICAL STRUCTURE AND MIRRORS .....	32
3.2 ACTUATOR SYSTEM .....	32
3.2.1 <i>Piezoelectric Actuators</i> .....	33
3.2.2 <i>Actuators Power Drivers</i> .....	34
3.3 POSITION MEASUREMENT SYSTEM .....	36
3.3.1 <i>Capacitive Sensors</i> .....	37
3.3.2 <i>Capacitance-Voltage Converter Modules</i> .....	38
3.4 DIGITAL CONTROL SYSTEM .....	39
3.4.1 <i>BTFI Fabry-Pérot Controller Board</i> .....	41
3.4.2 <i>Data Acquisition System</i> .....	42
3.4.3 <i>Digital Control System Signal Flow</i> .....	43
<b>4 CHARACTERISTICS OF THE DISTANCE MEASUREMENT SYSTEM .....</b>	<b>44</b>
4.1 MEASUREMENT RANGE.....	44
4.2 SENSITIVITY .....	45
4.3 LINEARITY AND STABILITY.....	46
4.4 REPEATABILITY .....	46
4.5 MEASUREMENT ERROR DUE TO NON-PARALLELISM OF MEASURING SURFACES .....	47
4.6 ENVIRONMENTAL CHARACTERISTICS .....	48
4.6.1 <i>Target Surface</i> .....	48
4.6.2 <i>Environmental Influences</i> .....	48
4.7 RESOLUTION AND MEASUREMENT NOISE.....	49
4.7.1 <i>Noise Statistical Analysis for the FOGALE system</i> .....	53
4.7.2 <i>LION Measurement System</i> .....	64
<b>5 CHARACTERISTICS OF THE ACTUATOR SYSTEM.....</b>	<b>66</b>
5.1 ELECTRICAL AND MECHANICAL LIMITS.....	66
5.2 THERMAL LIMITS .....	67
5.3 WORKING CONDITIONS AND APPLICATIONS OF THE APA400MML .....	67
5.4 CHARACTERISTICS OF THE APA400MML PIEZOACTUATORS .....	69
5.5 SHIFT VERSUS VOLTAGE .....	70
5.6 PRE-STRESSED CERAMICS .....	72
5.7 RESONANCE IN PIEZOACTUATORS .....	72

<b>6</b>	<b>DYNAMIC MODELING OF THE FABRY-PÉROT INTERFEROMETER .....</b>	<b>74</b>
6.1	MODEL OF THE POSITION MEASUREMENT SYSTEM.....	74
6.1.1	<i>Static Model of the Capacitive Sensors .....</i>	<i>74</i>
6.1.2	<i>Static Model of the Capacitance to Voltage Converters .....</i>	<i>75</i>
6.1.3	<i>Model of the Complete Measurement System .....</i>	<i>76</i>
6.2	MODEL OF THE ACTUATOR SYSTEM .....	77
6.2.1	<i>Model of the Drivers by Voltage .....</i>	<i>78</i>
6.2.2	<i>Model of the Drivers by Charge .....</i>	<i>80</i>
6.2.3	<i>Model of the Piezoelectric Actuators .....</i>	<i>82</i>
6.3	MODEL OF THE COMPLETE SYSTEM.....	90
6.3.1	<i>Theoretical Development.....</i>	<i>90</i>
6.3.2	<i>Gray Box System Identification .....</i>	<i>96</i>
6.3.3	<i>Simulation and Validation Results of the Fabry-Pérot System Model.....</i>	<i>97</i>
6.3.4	<i>Singular Values of the Fabry-Pérot System.....</i>	<i>99</i>
6.3.5	<i>Modeling Error of the Fabry-Pérot Model.....</i>	<i>101</i>
<b>7</b>	<b>CONTROL PROBLEM OF THE FABRY-PÉROT INTERFEROMETER .....</b>	<b>103</b>
7.1	OPERATION MODES .....	103
7.2	CHARACTERIZATION OF THE CONTROL PROBLEM .....	104
<b>8</b>	<b>CHARACTERISTICS OF THE DIGITAL SYSTEM .....</b>	<b>105</b>
8.1	ANALOG-TO-DIGITAL CONVERTER RESOLUTION .....	105
8.1.1	<i>Fabry-Pérot ADC and DAC Minimum Resolution .....</i>	<i>106</i>
8.1.2	<i>NI-DAQ ADC and DAC Resolution.....</i>	<i>107</i>
8.2	CONTROL FREQUENCY .....	108
8.3	SAMPLING FREQUENCY.....	109
8.3.1	<i>Digital Redesign of the Continuous Time Controller.....</i>	<i>109</i>
8.3.2	<i>Fabry-Pérot Digital to Analog Sampling Frequency .....</i>	<i>111</i>
8.3.3	<i>Fabry-Pérot Analog to Digital Sampling Frequency .....</i>	<i>111</i>
8.3.4	<i>NI-DAQ Sampling Frequency.....</i>	<i>111</i>
8.4	SUMMARY OF THE CHARACTERISTICS OF THE DIGITAL SYSTEM .....	112
<b>9</b>	<b>DESIGN OF THE CONTROLLERS, SIMULATIONS AND EXPERIMENTAL VALIDATION. ....</b>	<b>113</b>
9.1	GENERAL RESTRICTIONS OF THE SYSTEM .....	113
9.1.1	<i>Definition of the Performance Specifications for the Fabry-Pérot Prototype .....</i>	<i>114</i>
9.2	PROPORTIONAL-INTEGRAL COMPENSATOR.....	114
9.2.1	<i>Stability Analysis of the Fabry-Pérot system .....</i>	<i>115</i>
9.2.2	<i>Tuning of the PI Compensator using a Genetic Algorithm.....</i>	<i>115</i>
9.2.3	<i>Simulation Results of the Proportional-Integral Compensator .....</i>	<i>118</i>
9.2.4	<i>Experimental Validation of the Proportional-Integral Compensator.....</i>	<i>123</i>
9.3	MIMO ROBUST COMPENSATOR .....	129
9.3.1	<i>Prerequisites of the Parametric Model of the System.....</i>	<i>129</i>
9.3.2	<i>Theory of the Robust Compensator .....</i>	<i>131</i>
9.3.3	<i>Design of the Robust Compensator .....</i>	<i>135</i>
9.3.4	<i>Simulation Results of the Robust Compensator .....</i>	<i>137</i>
9.3.5	<i>Experimental Validation of the Robust Compensator.....</i>	<i>142</i>
<b>10</b>	<b>DISCUSSION AND CONCLUSIONS .....</b>	<b>148</b>
<b>11</b>	<b>FUTURE WORK .....</b>	<b>154</b>
	<b>REFERENCES .....</b>	<b>156</b>
	<b>APPENDIX A - PUBLISHED PAPERS.....</b>	<b>159</b>

## LIST OF FIGURES

FIGURE 1 - FLOW DIAGRAM OF THE CONTROL DESIGN PROCESS .....	22
FIGURE 2 - SIMPLIFIED REPRESENTATION OF THE BTFI INSTRUMENT .....	23
FIGURE 3 - IBTF FILTER CONFIGURATION AND RESULTS .....	25
FIGURE 4 - TUNABLE FILTER AND FABRY-PÉROT INTERFEROMETERS IN ASTRONOMY .....	26
FIGURE 5 - PICTURE OF THE SOAR TELESCOPE .....	28
FIGURE 6 - LIGHT PATH IN A FABRY-PÉROT INTERFEROMETER .....	29
FIGURE 7 - RING PATTERN OF THE FABRY-PÉROT INTERFEROMETER .....	29
FIGURE 8 - GRAPHICAL REPRESENTATION OF THE MOVING MIRROR AND THE THREE PIEZOACTUATORS ON THE FABRY-PÉROT .....	31
FIGURE 9 - PICTURE OF THE FRONT AND BACK OF THE FABRY-PÉROT INSTRUMENTATION.....	31
FIGURE 10 - CEDRAT APA400MML PIEZOACTUATOR PICTURE .....	33
FIGURE 11 - DRIVER BY VOLTAGE SCHEMATIC.....	34
FIGURE 12 - DRIVER BY CHARGE SCHEMATIC.....	36
FIGURE 13 - FLOW OF CHARGE INSIDE A CAPACITIVE SENSOR .....	37
FIGURE 14 - MCCHS10 SENSORS DESIGN .....	38
FIGURE 15 - MC900 CONVERTERS MODULES PICTURE .....	39
FIGURE 16 - DIGITAL CONTROL SYSTEM PRINCIPAL COMPONENTS .....	40
FIGURE 17 - FABRY-PÉROT FORMER CONTROLLER BOARD SCHEMATIC.....	41
FIGURE 18 - COMPONENTS OF A TYPICAL DAQ SYSTEM .....	42
FIGURE 19 - SIGNAL FLOW OF THE FABRY-PÉROT DIGITAL CONTROL SYSTEM .....	43
FIGURE 20 - ZOOM EFFECT OF MC900 MODULES .....	45
FIGURE 21 - NOISE (NM RMS) OF THE FOGALE SYSTEM IN DIFFERENT BANDWIDTHS .....	50
FIGURE 22 - NOISE MEASURE FOR MC900 MODULES.....	52
FIGURE 23 - FOGALE MEASUREMENT SYSTEM TOTAL NOISE (NM) .....	52
FIGURE 24 - SNR OF DATA ACQUIRED WITH AGILENT 34410A .....	60
FIGURE 25 - SINGLE SIDED SPECTRUM OF MC900 SIGNAL ACQUIRED WITH NI-DSA 4552 .....	61
FIGURE 26 - SINGLE SIDED SPECTRUM OF MC900 SIGNAL ACQUIRED WITH NI-DAQ 6221 .....	62
FIGURE 27 - BLOCK DIAGRAM OF THE ANALOG FILTER TEST ASSEMBLY .....	62
FIGURE 28 - SINGLE SIDED SPECTRUM OF WAVE GENERATOR SIGNAL ACQUIRED WITH NI-DAQ .....	63
FIGURE 29 - AMPLITUDE SPECTRUM OF A FILTERED 8 KHZ SIGNAL SAMPLED BY THE NI-DAQ 6221 .....	64
FIGURE 30 - FOGALE AND LION MEASUREMENT SYSTEMS NOISE (NM RMS).....	65
FIGURE 31 - HYSTERESIS BEHAVIOR OF PIEZOACTUATORS .....	71
FIGURE 32 - HYSTERESIS CURVE OF APA400MML PIEZOACTUATORS A) WHEN DRIVEN BY THE DRIVERS BY VOLTAGE B) WHEN DRIVEN BY THE DRIVERS BY CHARGE .....	71
FIGURE 33 - THEORETICAL STATIC MODEL OF CAPACITIVE SENSORS.....	75
FIGURE 34 - STATIC MODEL OF MC900 MODULES .....	76
FIGURE 35 - SENSITIVITY OF THE MEASUREMENT SYSTEM .....	77
FIGURE 36 - LINEAR AMPLIFIERS FIRST-ORDER MODEL .....	78
FIGURE 37 - DRIVER BY VOLTAGE CUTOFF FREQUENCY .....	79
FIGURE 38 - AMPLITUDE VS. FREQUENCY OPERATION LIMITS OF THE DRIVERS BY CHARGE.....	80
FIGURE 39 - DYNAMIC RESPONSE OF THE DRIVER BY CHARGE .....	81
FIGURE 40 - PIEZOACTUATOR FREQUENCY RESPONSE TEST MOUNT .....	82
FIGURE 41 - APA400MML PIEZOACTUATOR STRUCTURE .....	82
FIGURE 42 - APA400MML FREQUENCY RESPONSE BODE PLOT. ....	83
FIGURE 43 - MASS SPRING DAMPER ACTUATOR MODEL.....	84
FIGURE 44 - APA400MML STEP RESPONSE .....	85
FIGURE 45 - GRAY BOX IDENTIFICATION GRAPHICAL USER INTERFACE.....	86
FIGURE 46 - PIEZOACTUATOR PARAMETRIC MODEL FREQUENCY RESPONSE VALIDATION .....	88
FIGURE 47 - PIEZOACTUATOR IDENTIFIED MODEL FREQUENCY RESPONSE VALIDATION .....	89
FIGURE 48 - PHYSICAL DISTRIBUTION OF THE COMPONENTS OF THE FP AND RELATED FORCES .....	90
FIGURE 49 - MODEL OF THE FABRY-PERÓT COMPLETE SYSTEM .....	91
FIGURE 50 - FABRY-PÉROT INPUT-OUTPUT COMBINATION AMPLITUDE BODE PLOT .....	96
FIGURE 51 - FREQUENCY RESPONSE OF THE REAL FABRY-PÉROT SYSTEM AND MODELS. A.SYSTEM OUTPUT WHEN INPUT DIRECTION IS IN PIEZOACTUATOR 1. B. SYSTEM OUTPUT WHEN INPUT DIRECTION IS IN PIEZOACTUATOR 2. C.SYSTEM OUTPUT WHEN INPUT DIRECTION IS IN PIEZOACTUATOR 3.....	98
FIGURE 52 - FABRY-PÉROT SYSTEM REAL RESPONSE AND PARAMETRIC MODEL SINGULAR VALUES .....	100
FIGURE 53 - INVERSE OF THE MODELING ERROR OF THE PARAMETRIC AND IDENTIFIED MODELS OF THE FABRY- PÉROT SYSTEM .....	102

FIGURE 54 - SCANNING MODE GRAPHICAL REPRESENTATION AND PARAMETERS .....	104
FIGURE 55 - VIBRATIONAL STUDY OF THE ENVIRONMENT OF THE FABRY-PÉROT INSTRUMENT LOCATION .....	109
FIGURE 56 - SUMMARY OF FREQUENCIES OF THE FABRY-PÉROT DIGITAL SYSTEM. A) BLOCK DIAGRAM OF THE DIGITAL SYSTEM WITH THE CORRESPONDING FREQUENCIES OF EACH SUBSYSTEM. B) SPECTRUM OF THE DEFINED FREQUENCIES, INCLUDING THE ANALOG AND THE DIGITAL. ....	112
FIGURE 57 - ILLUSTRATIVE STEP RESPONSES TO DIFFERENT PI CONTROLLERS .....	117
FIGURE 58 - SIMULATION BLOCK DIAGRAM OF THE FABRY-PÉROT MODEL WITH PI CONTROLLER .....	119
FIGURE 59 - RESPONSE OF THE FABRY-PÉROT SYSTEM MODEL USING A PI CONTROLLER TO DIFFERENT SET-POINT SIGNALS. A) RAMP RESPONSE, B) STEP RESPONSE, C) FREQUENCY RESPONSE TO A SINUSOIDAL SIGNAL OF 10 HZ. ....	121
FIGURE 60 - REAL TIME PI CONTROLLER FOR THE FABRY-PÉROT PROTOTYPE .....	123
FIGURE 61 - RESPONSE TO DIFFERENT SET-POINT SIGNALS OF THE FABRY-PÉROT PROTOTYPE USING A PI CONTROLLER. A) RAMP RESPONSE, B) STEP RESPONSE, C) FREQUENCY RESPONSE TO A SINUSOIDAL SIGNAL OF 10 HZ. ....	124
FIGURE 62 - SPECTRAL ANALYSIS OF THE OPEN-LOOP MC900 ACQUIRED SIGNAL .....	127
FIGURE 63 - SPECTRAL ANALYSIS OF THE RAMP (A) AND STEP (B) CLOSED-LOOP RESPONSE, IN BLUE, FOR THE PI CONTROLLER. THE OPEN-LOOP SPECTRUM IS ALSO PLOTTED IN BLACK FOR VISUAL COMPARISON. THE RED POINTS ARE NOT CONSIDERED ON THE STATISTICAL ANALYSIS. ....	127
FIGURE 64 - LQG/LTR CONTROLLER GRAPHICAL USER INTERFACE .....	134
FIGURE 65 - SINGULAR VALUES OF THE CLOSED-LOOP OF THE ROBUST CONTROLLER A IN RED, AND B IN BLUE..	136
FIGURE 66 - BLOCK DIAGRAM OF THE MIMO ROBUST CONTROLLER SIMULATION .....	137
FIGURE 67 - RESPONSE OF THE FABRY-PÉROT SYSTEM MODEL USING THE ROBUST CONTROLLER A.....	138
FIGURE 68 - RESPONSE OF THE FABRY-PÉROT SYSTEM MODEL USING THE ROBUST CONTROLLER B.....	140
FIGURE 69 - REAL TIME ROBUST CONTROLLER FOR THE FABRY-PÉROT PROTOTYPE .....	142
FIGURE 70 - RESPONSE TO DIFFERENT SET-POINT SIGNALS OF THE REAL FABRY-PÉROT SYSTEM USING A ROBUST CONTROLLER. ....	143
FIGURE 71 - SPECTRUM OF THE ACQUIRED SIGNAL IN OPEN-LOOP.....	146
FIGURE 72 - SPECTRAL ANALYSIS OF THE RAMP (A) AND STEP (B) CLOSED-LOOP RESPONSE, IN BLUE, FOR THE ROBUST CONTROLLER. THE OPEN-LOOP SPECTRUM IS ALSO PLOTTED IN BLACK FOR VISUAL COMPARISON. THE RED POINTS ARE NOT CONSIDERED ON THE STATISTICAL ANALYSIS. ....	146

## LIST OF TABLES

TABLE 1 DRIVER BY VOLTAGE CHARACTERISTICS .....	35
TABLE 2 FOGALE SYSTEM NOISE (NM RMS) AT DIFFERENT OPERATION BANDWIDTHS .....	51
TABLE 3 NOISE OF THE MC900 MODULES IN TERMS OF THE BANDWIDTH OF OPERATION .....	51
TABLE 4 TOTAL THEORETICAL NOISE OF THE FOGALE DISTANCE MEASUREMENT SYSTEM .....	52
TABLE 5 MC900 NOISE DEPENDENCE ON HARDWARE .....	55
TABLE 6 NATIONAL INSTRUMENTS DATA ACQUISITION BOARD 6221 RESOLUTION. ....	57
TABLE 7 NOISE OF FOGALE SYSTEM MEASURED WITH DIFFERENT DAQ INPUT RESOLUTIONS.....	57
TABLE 8 AGILENT 34410A VOLTAGE RESOLUTION AND MC900 DISTANCE RESOLUTION .....	58
TABLE 9 NOISE OF THE FOGALE SYSTEM MEASURED WITH DIFFERENT DAQ INPUT RESOLUTIONS .....	58
TABLE 10 SNR OF THE FOGALE SYSTEM FOR DIFFERENT SIGNAL MEANS .....	59
TABLE 11 WORKING CONDITIONS AND APPLICATIONS OF THE PIEZOACTUATORS.....	68
TABLE 12 CHARACTERISTICS OF THE CEDRAT APAMML PIEZOACTUATORS .....	69
TABLE 13 FABRY-PERÓT PIEZOACTUATORS PARAMETER VALUES .....	85
TABLE 14 INSTRUMENTATION OF THE FABRY-PÉROT PROTOTYPE .....	113
TABLE 15 SUMMARY OF THE RESPONSE OF THE FP SYSTEM MODEL WHEN CONTROLLED WITH A PI COMPENSATOR .....	122
TABLE 16 SUMMARY OF THE RESPONSE OF THE FP SYSTEM WHEN CONTROLLED WITH A PI COMPENSATOR .....	126
TABLE 17 SUMMARY OF THE RESPONSE CHARACTERISTICS OF THE FP SYSTEM MODEL WHEN CONTROLLED WITH A ROBUST COMPENSATOR A.....	138
TABLE 18 SUMMARY OF THE RESPONSE CHARACTERISTICS OF THE FP SYSTEM MODEL WHEN CONTROLLED WITH THE ROBUST COMPENSATOR B.....	139
TABLE 19 SUMMARY OF THE RESPONSE CHARACTERISTICS OF THE FP SYSTEM WHEN CONTROLLED WITH ROBUST COMPENSATOR B .....	145

## LIST OF ABBREVIATIONS AND ACRONYMS

ADC	- Analog to Digital Converter
APA	- Amplified Piezoelectric Actuator
BTFI	- Brazilian Tunable Filter Imager
CCD	- Charge Coupled Device
CG	- Collimator Group
CVC	- Capacitance to Voltage Converter
DAC	- Digital to Analog Converter
DAQ	- Data Acquisition Board
DC	- Direct Current
DPM	- Design Plant Model
DSA	- Dynamic Signal Analyzer
DSO	- Digital Storage Oscilloscope
EMCCD	- Electron Multiplying Charge Coupled Device
FM	- Fold mirror
FP	- Fabry-Pérot
FP1	- Low resolution Fabry-Pérot
FP2	- High resolution Fabry-Pérot
FPGA	- Field Programmable Gate Array
FSR	- Free Spectral Range
GA	- Genetic Algorithm
GS	- Grating Support
GUI	- Graphical User Interface
IAG	- Instituto de Astronomia, Geofísica e Ciências Atmosféricas
I/O	- Input/Output
iBTF	- Imaging Bragg Tunable Filter
LAM	- Laboratoire d'Astrophysique de Marseille
LQG	- Linear Quadratic Gaussian
LTR	- Loop Transfer Recovery
MIMO	- Multiple Inputs Multiple Outputs
MLA	- Multi-layer Amplifiers
MR	- Measurement Range
NI	- National Instruments

NOAO	- National Optical Astronomy Observatory
NTT	- New Technology Telescope
PC	- Personal Computer
PCI	- Peripheral Component Interconnect
PI	- Proportional Integral
R	- Spectral Resolution
RMS	- Root Mean Square
RH	- Relative Humidity
SAM	- SOAR Adaptive Module
SESO	- Société Européenne de Systèmes Optiques
SISO	- Single Input Single Output
SNR	- Signal to Noise Ratio
SOAR	- Southern Astrophysical Research Observatory
SPS	- Samples per Second
SPI	- Serial Peripheral Interface Bus
TFL	- Target Feedback Loop
VPH	- Volume Phase Holographic

## LIST OF SYMBOLS

$A$	- Area of the sensors
$\mathbf{A}$	- State matrix of the space-state system representation
$\lambda$	- Wavelength
$\mathbf{B}$	- Input matrix of the space-state system representation
$\mathbf{C}$	- Output matrix of the space-state system representation
$C_{ref}$	- Reference capacitance
$c$	- Damping coefficient
$\epsilon_0$	- Dielectric constant
$\epsilon_r$	- Relative static permittivity
$e$	- Distance between the etalon plates
$F$	- Generated force
$F_{control}$	- Control frequency of the control system
$F_r$	- Resonance frequency
$F_s$	- Sampling frequency
$F_{S_{ADC}}$	- Sampling frequency of the Analog-to-Digital converter
$F_{S_{DAC}}$	- Sampling frequency of the Digital-to-Analog converter
$F_{S_{DR}}$	- Sampling frequency of the Digital Redesign process
$G_{MC900}$	- Gain of the MC900 modules
$G_{driver}$	- Transfer function of the driver
$i$	- Angle of incidence of light to the interferometer
$k$	- Stiffness of the piezoactuators
$K_{cut-off}$	- Cut-off frequency of the continuous-time controller
$m$	- Effective mass of the piezoactuators
$m_{mirror}$	- Mass of the mirror of the Fabry-Pérot
$M_{FP1}$	- Number of bits of the FP1 ADC and DAC converters

$M_{FP2}$	- Number of bits of the FP2 ADC and DAC converters
$\mu$	- Statistical mean
$\mu_{\text{signal}}$	- Mean of the signal
$\mu\text{m}$	- Micrometers
N	- Force of the actuator
nm	- Nanometers
n	- Refractive index
p	- Interference order
P1	- Piezoactuator 1
P2	- Piezoactuator 2
P3	- Piezoactuator 3
$P_{\text{signal}}$	- Power of the signal
$P_{\text{noise}}$	- Power of the noise
$Q_m$	- Quality factor
S12	- Output of the FP system on sensor between P1 and P2
S23	- Output of the FP system on sensor between P2 and P3
S13	- Output of the FP system on sensor between P1 and P3
$s_{ij}$	- Output $j$ related to the input $i$ of the Fabry-Pérot system
$\sigma_M$	- Maximum singular value
$\sigma$	- Statistical standard deviation
$\sigma_{\text{FOGALE}}$	- FOGALE system standard deviation
$\sigma_{\text{Sensor}}$	- Sensors standard deviation
$\sigma_{\text{MC900}}$	- MC900 standard deviation
$\sigma_{\text{Signal}}$	- Distance signal standard deviation
$\sigma_{\text{Total}}$	- Total standard deviation
$U_{\text{min}}$	- Minimum input of the piezoactuator

$U_{\max}$	- Maximum input of the piezoactuator
$u$	- Input matrix of the space-state system representation
$\mu_{LQG/LTR}$	- Free design parameter for the design of a LQG/LTR robust controller.
$V$	- Applied voltage to the piezoactuator
$V_{pp}$	- Peak to peak voltage
$\omega_n$	- Natural frequency
$x$	- State matrix of the space-state system representation
$y$	- Output matrix of the space-state system representation

# 1 INTRODUCTION

## 1.1 MOTIVATION AND WORK OBJECTIVES

The Brazilian Tunable Filter Interferometer, BTFI, is an astronomical instrument developed by the Instituto de Astronomia, Geofísica e Ciências Atmosféricas, of the Universidade de São Paulo, in collaboration with the Escola Politécnica, from the same university in São Paulo, SP, Instituto Nacional de Pesquisas Espaciais, Laboratório Nacional de Astrofísica, in São Jose dos Campos, SP, and Universidade Federal do Rio Grande do Sul, Universidade Estadual De Santa Cruz, Ilhéus, BA, all of them in Brazil, and international collaborations with the Laboratoire d'Astrophysique de Marseille, in Marseille, France, and the University of Montreal in Quebec, Canada, and the Universidad Católica in Santiago de Chile, Chile.

The BTFI will be a visitor instrument of the SOAR (Southern Astrophysical Research Observatory) telescope, located in the Atacama Desert, in Chile, and it is at the current time in commissioning phase. It will operate using the SAM (SOAR Adaptive Module) Ground-Layer Adaptive Optics facility and the telescope Nasmyth focus for spectroscopy science over a wide range of spectral resolving powers.

The BTFI is comprised mainly by two Fabry-Pérot interferometers, two Volume Phase Holographic gratings, one collimator group, two cameras and two detectors Electron Multiplying Charge Coupled Devices that will be properly presented in this work.

Of special interest to the Brazilian community is the study of the centers of nearby active galaxies, the study of kinematics and metallicities of cluster and group galaxies at redshifts 0.1-0.3 and of stellar mass loss phenomena in the surrounding interstellar medium.

There are a great number of galactic and extra-galactic studies which can benefit from the unique tunable filter imaging properties of the BTFI. The planned studies in the extra-galactic include:

- The centers of normal and active galaxies.
- Nearby galaxies in clusters and groups.
- Mass distribution of galaxies and their building blocks.

- 2D kinematics of fine structure for galaxy modeling.
- Noncircular motions in the disks of galaxies.
- Barred galaxies.
- Kinematics of galaxies at intermediate redshift.
- Galaxy interactions and merging.
- Blue compact dwarfs, HII galaxies and tidal dwarf galaxies.

While for Galactic work and study of the interstellar medium the following topics of interest include:

- Galactic HII regions.
- Studies of Herbig-Haro objects and associated jets.
- Kinematics of Proplyds.
- Mass loss in stellar systems.
- Structure, metallicities and kinematics of planetary nebulae.

The BTFI will be also highly complementary to the SOAR Integral Field Spectrograph, which will also work with the SAM module.

There is currently no Fabry-Pérot Tunable Filter instrument on any telescope working with adaptive optics, so it is therefore clearly recognized within the Brazilian community that the BTFI offers new capabilities that are worth exploring (Oliveira et al, 2013).

A scanning process is required to provide two dimension (2D) images within a given spectral band using a Fabry-Pérot interferometer. Such process is implemented by changing the distance between its two highly reflective parallel mirrors, better known as the interferometer etalon. Current Fabry-Pérot interferometers are designed to work in a fixed spectral resolution and allow for an initial adjustment of the distance between the mirrors in a range of 10  $\mu\text{m}$  with a scan range of 2  $\mu\text{m}$ . Since the proposed Fabry-Pérot interferometer is designed to work in a larger range of spectral resolutions, it requires a mirror distance of at least 200  $\mu\text{m}$ .

To meet such specific requirement, high-excursion piezoelectric actuators are used to position the etalon, and high-sensitivity capacitive sensors are used to give a feedback signal to a nanopositioning controller.

The BTFI Fabry-Pérot project started at the Escola Politécnica of the Universidade de São Paulo in 2008 by a master student with guidance of the Laboratoire d'Astrophysique de Marseille, LAM. A control program was designed and validated on the system, and the resulting work was compiled in the master dissertation of Cavalcanti, 2011.

However, upon making performance tests in the system, it was concluded that the system, as it was, could not achieve the scientific requirements and that a deeper study had to be conducted on the instrumentation in order to design a proper controller for the system.

The main objective of this master dissertation was then set to design the nanopositioning controller for the mirrors of the BTFI Fabry-Pérot over its whole range of operation. For this purpose, a study of the instrument functioning principles, definition and understanding of the technical performance requirements, study of the actual instrumentation characteristics, dynamical modeling of the components and controller design, are all part of the author's master degree research and this document is a compilation of the work done on each of these steps.

## 1.2 DISSERTATION STRUCTURE

This dissertation is organized in the following way:

- *Chapter 1:* Describes the motivations and objectives of this dissertation and the structure of the content of the following chapters.
- *Chapter 2:* Presents a general description of the BTFI instrument and its components.
- *Chapter 3:* Presents a description of the functioning principles and characteristics of the components of the BTFI Fabry-Pérot interferometer.
- *Chapter 4:* Presents the technical characteristics of the distance measurement system and presents the results of the noise study of the system.
- *Chapter 5:* Presents the characteristics of the actuator system.

- *Chapter 6:* Presents the dynamical modeling of the main subsystems of the Fabry-Pérot interferometer.
- *Chapter 7:* Presents the control problem and performance specifications.
- *Chapter 8:* Presents the definition of the parameters of the digital system of the Fabry-Pérot and presents the characteristics of the actual digital system used in the laboratory.
- *Chapter 9:* Presents the design of the control system compensators. It also shows the simulations and results of the experimental validation of the control systems on the instrument prototype.
- *Chapter 10:* Presents an analysis of the obtained results.
- *Chapter 11:* Presents the proposed future work.

### 1.3 DEVELOPMENT METHODOLOGY

Based on what was presented on item 1.1, the objectives of this work are summarized in the following way:

- To understand the operation of the Fabry-Pérot instrument and performance requirements.
- To study the characteristics of the electronic components of the Fabry-Pérot.
- To model the electronic components of the BTFI Fabry-Pérot.
- To analyze the suitability of the current Fabry-Pérot components.
- To design a controller for the nanopositioning system.

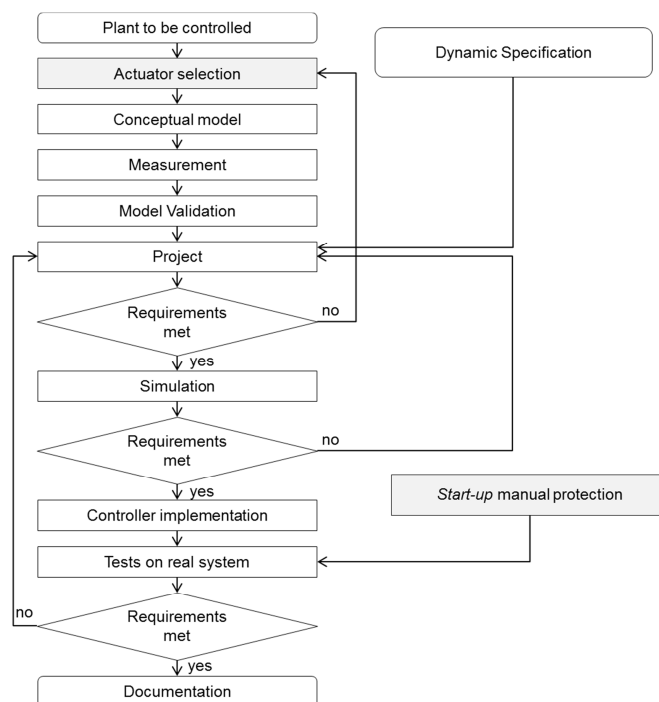
In order to accomplish these objectives the following activities are needed:

- Study the functioning principles of the BTFI and Fabry-Pérot instrument and get to know the state of the art.
- Characterize the distance measurement system which comprises the capacitive sensors and capacitance to voltage converters.
- Study the characteristics of the actuator system, which consists of the piezoelectric actuators and its drivers.
- Build the model of the distance measurement system.
- Build the dynamical model of the piezoelectric actuators and its drivers.

- Build the dynamical model of the Fabry-Pérot instrument.
- Define the characteristics of the digital system.
- Define the control problem for the Fabry-Pérot system.
- Design a Proportional-Integral controller to be used as benchmark.
- Design a multivariable robust controller following the LQG/LTR technique.
- Perform tests on the real system and analyze the results.

Figure 1 shows the flow diagram of the methodology for the implementation of a controller for a given plant or system. This methodology was the adopted scheme for the development of this master project and summarizes the stages of the mentioned activities. The gray boxes highlight the activities that are not included in this work: The actuator selection and the Start-up manual protection. The actuator and the complete instrumentation of the Fabry-Pérot was already defined and purchased at the beginning of the project, and the secure-operation protections are out of the scope of this project.

Figure 1 - Flow diagram of the control design process



Source: Castrucci P.D.L, et al. 2011. P. 11

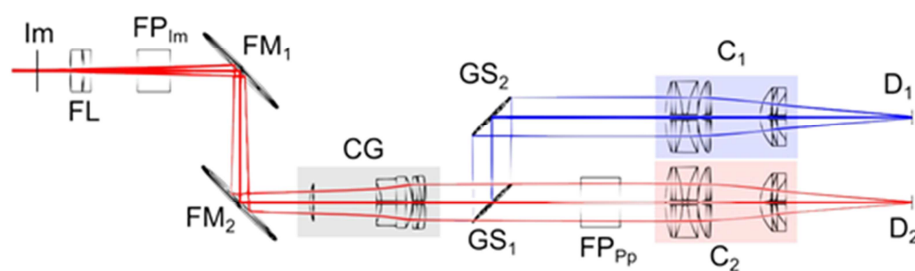
## 2 BRAZILIAN TUNABLE FILTER INTERFEROMETER

The Brazilian Tunable Filter Interferometer takes advantage of three new technologies. As a tunable filter, the imaging Bragg Tunable Filter (iBTF) concept utilizes Volume Phase Holographic Gratings in a double-pass configuration, while a new Fabry-Pérot (FP) concept involves the use of commercially available technologies which allow a single FP etalon to act over a very large range of interference orders and hence spectral resolutions. Both these filter technologies will be used in the same instrument and the combination allows for highly versatile capabilities in spectroscopy.

The BTFI instrumentation is composed mainly by one low resolution Fabry-Pérot interferometer ( $FP_{lm}$ ), one high resolution Fabry-Pérot interferometer ( $FP_{pp}$ ), two fold mirrors ( $FM_1, FM_2$ ), two Volume Phase Holographic (VPH) gratings that can be located in the grating supports ( $GS_1, GS_2$ ), one collimator group (CG), two cameras ( $C_1, C_2$ ) and two detectors EMCCD ( $D_1, D_2$ ).

An optical layout of the mentioned BTFI instrumentation is shown in Figure 2.

Figure 2 - Simplified representation of the BTFI instrument



Source: Oliveira et al. (2013)

The light path of the instrument is as follows:

The incident light from the telescope enters the instrument and is focused at the input image plane ( $I_m$ ). The diverging beam propagates through the Field Lenses (FL) which is optionally followed by the first Fabry-Pérot ( $FP_{Im}$ ) according to the operational mode of the instrument. Afterwards, the light beam is reflected by two fold mirrors ( $FM_1$  and  $FM_2$ ) that are needed to accommodate space constraints.

The light then passes through the collimator group (CG) and, in the collimated space, it hits the first iBTF support ( $GS_1$ ) that can hold a grating, a mirror or be empty. In the case where a grating lies in  $GS_1$ , the 0th diffraction order goes straight to where the second Fabry-Pérot ( $FP_{Pp}$ ) may be. Then, it goes to the  $C_2$  camera and reaches the detector  $D_2$ .

The 1st diffraction order that leaves the grating at  $GS_1$  goes to the second grating support  $GS_2$  where the dispersion is canceled by the second twin grating. The resultant “undispersed” light is finally imaged by the  $C_1$  camera at the  $D_1$  detector. (Oliveira et al., 2013)

A brief description of the functioning principles and applications of the mentioned instrumentation is summarized in the following items.

## 2.1 IMAGING BRAGG TUNABLE FILTER

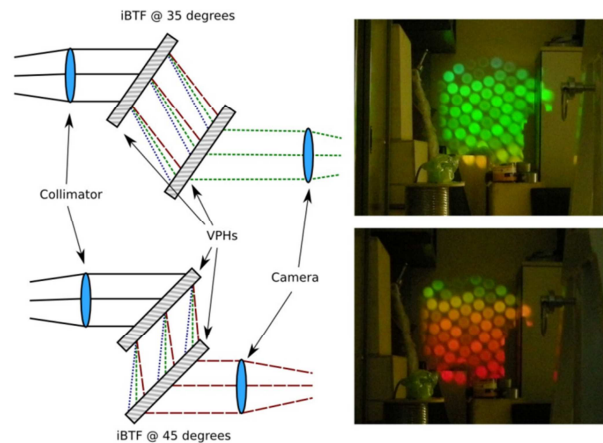
The iBTF brings an interferometer filter concept that is based on a dual VPH grating using both in transmission and reflection modes. With this configuration, the BTFI will be the first instrument of this kind in astronomy.

The operating principle is as follows: A first grating disperses collimated light that satisfies the Bragg condition. Then a second grating recombines the beam which is then re-imaged onto a detector.

Figure 3 shows an example of the filtration of a light beam coming from tungsten light and an optical fiber bundle as source, with a 2300 lines/mm transmission grating. At the top of the figure, on the left, it is shown the configuration of the iBTF with a grating angle of  $30^\circ$  and passband centered on 500 nm for a 2300 lines/mm VPH. At the top right is shown the filtered light projected in the laboratory wall.

In the bottom left is shown the configuration of the iBTFI with a grating angle of  $45^\circ$  and passband centered on 618 nm for the same VPHs and bottom right shows again the projection of the filtered light for this new angle configuration.

Figure 3 - iBTfI filter configuration and results



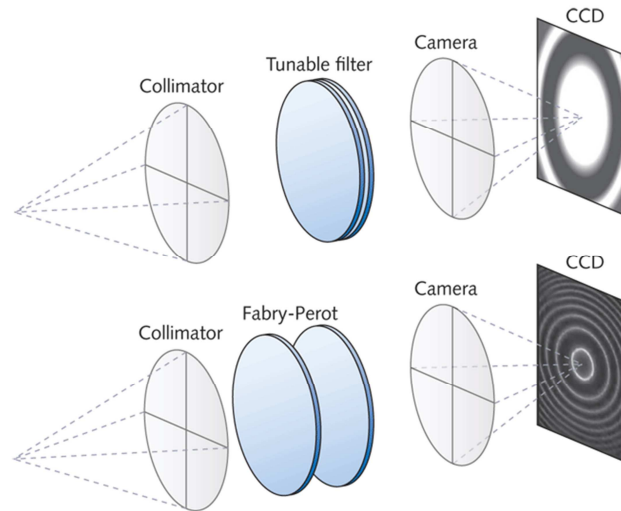
Source: Oliveira et al. (2013)

## 2.2 FABRY-PÉROT

In astronomy, Fabry-Pérot interferometers are most commonly used at wide plate spacings that generate a high-order ring pattern at the detector. When they are used with low-order spacings they are called tunable filters that are able to generate a large monochromatic field. Figure 4 shows a representation of both configurations.

The BTfI instrument is composed of two Fabry-Pérot interferometers, one for high-order of interference that gives high spectral resolution (classical Fabry-Pérot mode), and the other for low-order of interference that gives low spectral resolution (Tunable Filter mode). Also, the two Fabry-Pérots can be in series, where the low-order interferometer is used as a tunable order blocker, or spectral band selector, for the high resolution etalon.

Figure 4 - Tunable Filter and Fabry-Pérot interferometers in astronomy



Source: Bland-Hawthorn, Joss; Allington-Smith, Jeremy 3D spectrophotometric imaging opens a new window into the cosmos.

The following items give a deeper definition of the three operation modes of the BTFI Fabry-Pérots.

### 2.2.1 The Classical Fabry-Pérot Mode

With the classical Fabry-Pérot mode the instrument obtains series of images at different wavelengths, which are filtered and processed to give the spectral decomposition of the studied object.

This mode of operation uses the high-order interferometer because it comprises high spectral resolution.

The two main sciences applications of this mode are:

- To obtain precise line profiles, with resolving power  $R$ , greater than 25000, in order to derive the physical parameters of emission-line regions.
- To obtain the complete 2D kinematics of an emission-line source.

### **2.2.2 Tunable Filter Mode**

The low resolution etalon, deployed in the diverging beam just above the input focus, is used for the tunable filter mode. The etalon of this Fabry-Pérot has the capability of spanning FP gaps of  $\sim 250 \mu\text{m}$ , which would, in principle allow a spectral resolution range between  $500 < R < 30,000$ . However, the higher end of this range is curtailed by the divergent beam, allowing resolutions of  $500 < R < 2000$ , for this instrumental mode.

### **2.2.3 Low and High Resolution Fabry-Pérot in series**

When the Fabry-Pérot of the divergent beam near the input focus is put in series with the other in the collimated beam (for higher spectral resolutions) the first operates as an order sorter for the second. In this manner great flexibility is achieved in the ability to select a particular order for the higher resolution etalon.

## **2.3 DETECTORS**

The BTFI uses Electron Multiplying Charge Coupled Devices, EMCCD, detectors with a format of  $1600 \times 1600$  pixels, matched to the required pixel-scale ( $0.12''/\text{pixel}$ ), and the SOAR telescope field of view (3 by 3 arcmin).

The use of EMCCDs instead of traditional CCD detectors allows rapid and cyclically wavelength scanning while mitigating the damaging effect of atmospheric variability through the acquisition of the data cube.

The BTFI EMCCD cameras were designed and assembled by the BTFI team in order to be able to achieve the instrument requirements, such as deep-cooling (lower than  $-100 \text{ }^\circ\text{C}$ ) and arbitrary clocking. They were built in collaboration with Universidad Católica in Santiago de Chile, Chile and with read-out electronics provided by the University of Montreal in Quebec, Canada.

## 2.4 THE SOAR TELESCOPE

The Southern Astrophysical Research Telescope is a 4.1 meter aperture telescope funded by a partnership between the Ministério da Ciência, Tecnologia e Inovação of Brazil, the National Optical Astronomy Observatory, NOAO, the University of North Carolina at Chapel Hill, NC, and Michigan State University, MI, of United States.

The telescope was designed to work from the atmospheric cut-off in the blue (320 nm) to the near infrared. Its principal characteristics are excellent image quality, with image size equal to 0.22 arcseconds/pixel, fast slewing and capability to have up to nine instruments mounted ready for use.

The SOAR telescope, shown in Figure 5, is situated on Cerro Pachón, Chile, at an altitude of 2,700 meters above sea level.

Figure 5 - Picture of the SOAR telescope



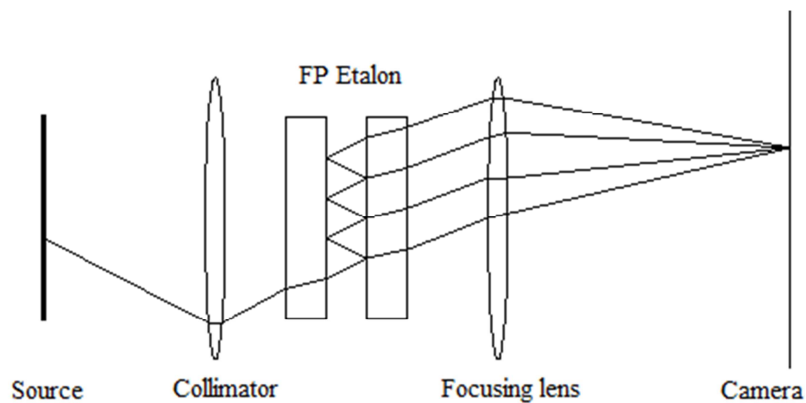
Source: Courtesy of SOAR telescope.

### 3 THE FABRY-PÉROT INTERFEROMETER

The Fabry-Pérot interferometer is concisely described as a pair of reflective glass plates, spaced micrometers apart, with the reflective surfaces facing each other.

The light of the object of study enters at the focal plane of a collimating lens and all the light is focused to a single point in the image plane of the instrument. When the light passes through the reflective surfaces of the etalon, it is reflected multiple times, as shown in Figure 6, to produce multiple transmitted rays which are collected by the focusing lens and directed to the detector. The complete interference pattern takes the appearance of a set of concentric rings as shown in Figure 7.

Figure 6 - Light path in a Fabry-Pérot interferometer



Source: <http://www.cmp.ucl.ac.uk/~ahh/teaching/1B24n/lect29/node3.html>

Figure 7 - Ring pattern of the Fabry-Pérot interferometer



Source: [http://cord.org/cm/leot/course10\\_Mod05/Module10-5.htm](http://cord.org/cm/leot/course10_Mod05/Module10-5.htm)

The Fabry-Pérot interference formula as explained in Oliveira et al. 2011, is presented in eq.(1):

$$2ne \cos(i) = p\lambda \quad (1)$$

where:

- $n$  is the refractive index;
- $e$  is the distance between the two parallel plates;
- $i$  is the angle of incidence of the light;
- $\lambda$  is the wavelength;
- $p$  is the interference order.

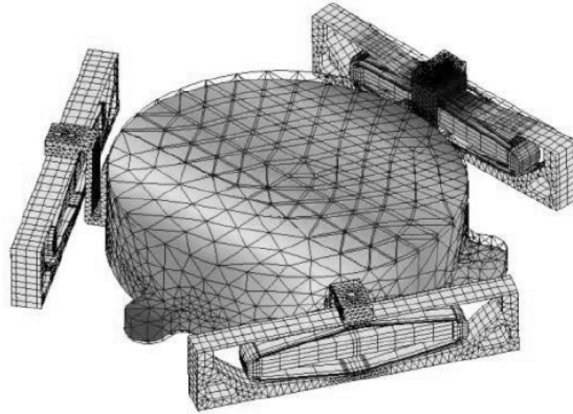
The scan can be achieved by changing  $i$ , which depends on the selection of the angle on the sky,  $n$ , that is the index of the layer between the plates, or  $e$ , by moving the distance between the two plates. Modern interferometers have generally chosen to scan by changing the reflective plates distance, and it is also the case for the BTFI Fabry-Pérots.

Both Fabry-Pérots on the BTFI instrument have the same components: One physical structure, one pair of reflective mirrors (the etalon), three piezoelectric actuators, three piezoactuator drivers, three capacitive sensors and three capacitance to voltage converters.

The instrument configuration is as follows: one mirror is mounted firmly in the physical structure that comprises the body of the Fabry-Pérot interferometer. The three piezoelectric actuators are fixed on one side to the physical structure and in the other side they support the other mirror of the interferometer, as shown in Figure 8, which is the only moving part of the interferometer while scanning. The three capacitive sensors that measure the distance between the two plates of the interferometer for feedback are also fixed to the physical structure, and the measurement target is on the moving mirror.

All of the instrumentation used in the laboratory, except for the mirrors of the interferometer and the digital system hardware, are planned to be part of the final system, supposing they meet the scientific specifications.

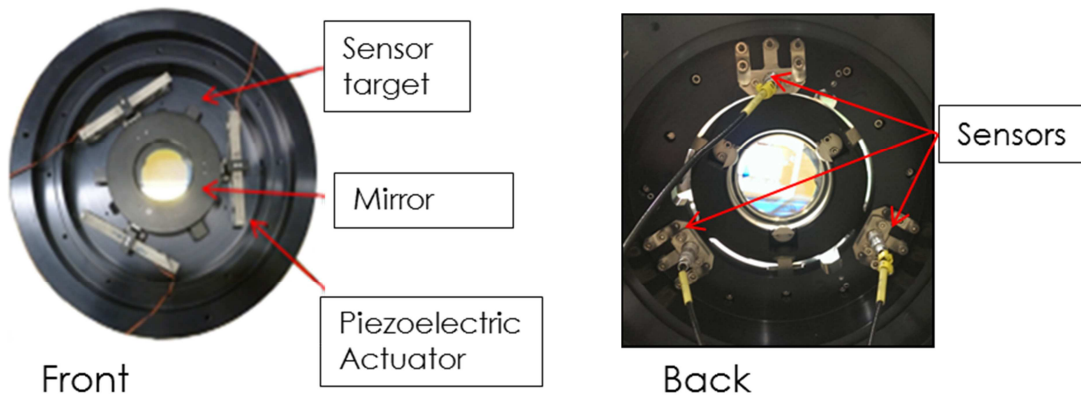
Figure 8 - Graphical representation of the moving mirror and the three piezoactuators on the Fabry-Pérot



Source: Image credit to CEDRAT Nanotechnologies

Figure 9 shows a picture of the Fabry-Pérot physical structure and instrumentation.

Figure 9 - Picture of the front and back of the Fabry-Pérot instrumentation.



Source: Author

The following sections present a description of the subsystems of the BTFI Fabry-Pérot interferometer.

### 3.1 PHYSICAL STRUCTURE AND MIRRORS

The physical structure of the Fabry-Pérot consists in a metallic structure designed and manufactured by the Société Européenne de Systèmes Optiques, SESO, Aix-en-Provence, France.

The mirrors of the etalon of both Fabry-Pérot are currently being manufactured also by SESO to allow a far greater range of spectral resolutions than available using the more traditional designs. The mirrors used at the current time in the laboratory are borrowed from a former Fabry-Pérot.

### 3.2 ACTUATOR SYSTEM

Piezoelectric actuators, or piezoactuators, are the most common devices used for positioning in applications when a component must be moved with sub-micron accuracy from one position to another. The main advantages of these systems are:

- Unlimited resolution, i.e. the infinitely high relative positioning sensitivity of the piezoceramic converts an infinitely small voltage variation into an infinitely small motion. This has been proven explicitly down to the picometer range (Piezomechanik, 2010).
- Low power consumption.
- High force-mass ratio, allowing them to have fast response time.

The main disadvantage is that they have limited displacement ranges, which restrict the spectral range that can be covered in spectroscopy application.

Older style Fabry-Pérots can only cover a few free spectral ranges due to their low displacement range  $\sim 10 \mu\text{m}$ , but the technology developed in the piezoactuators for the new BTFI Fabry-Pérots, enlarge the scan range of the piezoelectric transducer from just above zero up to  $\sim 350 \mu\text{m}$ , allowing the BTFI Fabry-Pérot to cover hundreds of orders.

The actuator system for each Fabry-Pérot of the BTFI instrument consists of three piezoactuators, provided by the French company CEDRAT Technologies, and three power drivers that provide the necessary voltage to take the piezoactuators up to their maximum displacement.

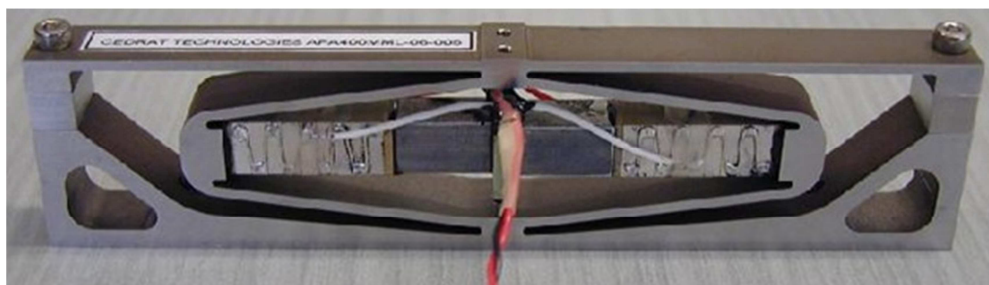
### 3.2.1 Piezoelectric Actuators

The BTFI Fabry-Pérots use the CEDRAT APA400MML amplified piezoactuators, designed exclusively for this project. These are pre-stressed solid-state long-stroke actuators based on the expansion of the active material and on an elastic mechanical amplifier that maximizes the displacement, allowing a maximum displacement of  $\sim 250 \mu\text{m}$  for the low-resolution Tunable Filter FP, and a maximum displacement of  $\sim 350 \mu\text{m}$  for the high-resolution FP.

The advantages of the APA piezoactuators are their relatively large displacements combined with their high forces and compact size along the active axis (CEDRAT Catalogue, 2013).

Figure 10 shows a picture of one of the APA400MML piezoactuators of the BTFI instrument.

Figure 10 - CEDRAT APA400MML piezoactuator picture



Source: Courtesy CEDRAT.

### 3.2.2 Actuators Power Drivers

The principal characteristic of piezoactuators is that they convert electrical signal into an equivalent shift in position. Consequently, any undesired electrical signal variation, like noise, is transformed into an equivalent undesired displacement as well. That is, the resolution of the device is limited by the noise of the driving electronics.

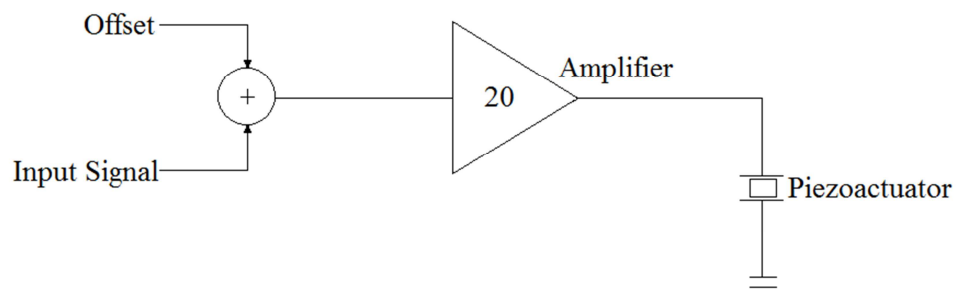
The displacement of the APA400MML piezoactuators is proportional to the applied voltage within a 170 V range. To achieve the maximum stroke of the piezoactuators a power driver supplying from -20 V to 150 V is necessary and because of the capacitive electrical nature of the piezoactuators the driver electronics need to have a significant charge transfer rate in order to achieve a fast response.

Two solutions, based on linear amplifiers, have been implemented for the Fabry-Pérots piezoactuators drivers. The initial concept was based on a voltage amplifier driver, and later, in order to compensate the non-linear dynamics of the actuators, a driver by charge was proposed by Marchiori et al. (2013).

The voltage driver was initially chosen because of its high signal-to-noise ratio and easiness of control and implementation. In this solution, the input signal of the amplifier is directly proportional to the voltage applied to the actuator, which is also directly proportional to the displacement of the piezoactuators.

A simple schematic of the voltage driver is shown in Figure 11.

Figure 11 - Driver by voltage schematic.



Source: CEDRAT Technologies Catalogue 2013

The piezoactuator manufacturer, CEDRAT, also manufactures piezoactuators drivers, but the BTFI Fabry-Pérot voltage drivers were designed by former team members in order to benefit from a personalized design and low cost of implementation (Cavalcanti, 2011). The technical specifications of the implemented voltage driver are shown in Table 1.

Table 1 Driver by voltage characteristics

<b>Parameter</b>	<b>Value</b>	<b>Units</b>
Voltage Gain	20	V
Bandwidth	50	Hz
Max. Output Current	100	mA

Because the gain of the driver is set to 20, the input signal of the driver varies from -1 to 7.5 V to achieve the needed -20 V to 150 V range.

Despite of the linear amplifier drivers' good performance supplying the 170 Volts for the piezoactuators, after studying and characterizing this initial solution, as will be presented in the dynamic modeling section 6.2.1, it was concluded that these drivers were limiting the performance of the Fabry-Pérot system in terms of bandwidth and rising time.

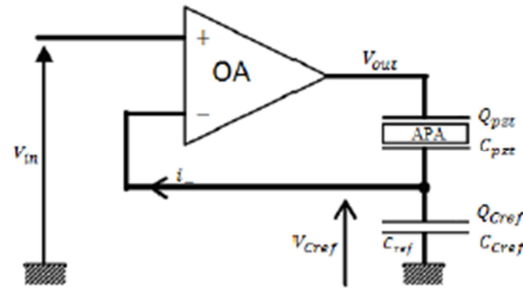
The need for another driver arose, and different solutions for the piezoactuators drivers were studied by other team members.

One of the possible solutions was to implement a charge control technique based on the principle that the displacement of a piezoelectric material is linearly proportional to the applied charge on it, as presented in Perez, R. (2001).

The main advantage of this solution is that the driver by charge minimizes the hysteresis behavior, which is the main non-linearity of the actuator, while supplying the power necessary to operate the piezoactuators at its full capacity.

Figure 12 shows the electronic schematic of the driver by charge.

Figure 12 - Driver by charge schematic



Source: Comstock R.H.(1981)

The operating principle of this implementation is based on the fact that voltage  $V_{Cref}$  across the reference capacitor,  $C_{ref}$ , is practically equal to the voltage  $V_{in}$  at the positive input of the operational amplifier. It also implies that the charge  $Q_{pzt}$  across the APA is practically equal to charge  $Q_{Cref}$  across the reference capacitor and therefore, the charge  $Q_{pzt}$  across the APA is proportional to the input voltage signal  $V_{in}$ .

Since the piezoactuator displacement is linearly proportional to the applied charge  $Q_{pzt}$ , it implies that its displacement will be linearly proportional to the input voltage signal  $V_{in}$  as well, making the Fabry-Pérot actuator system a linear system.

These drivers are currently under development by Marchiori et al. (2013).

### 3.3 POSITION MEASUREMENT SYSTEM

Capacitive displacement sensors are the chosen solution to measure the distance between the plates of the Fabry-Pérot etalon because they measure nanometric distances with highest reliability and accuracy.

The measurement system was manufactured by FOGALE Nanotech, from Nimes, France, and consists of three capacitive sensors and three capacitance-to-voltage converters for each Fabry-Pérot.

### 3.3.1 Capacitive Sensors

The FOGALE MCC10HS capacitive sensors are metal-resin sensors with triaxial technology with measurement range up to 1 mm.

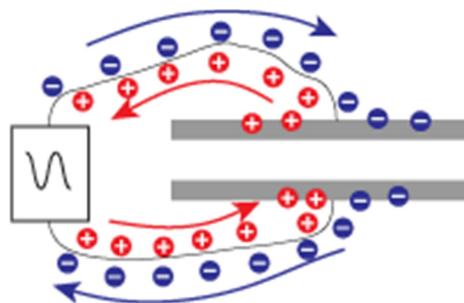
In the capacitive sensor system, the quantity measured is the change of capacitance between the sensor surface and the target surface using a homogenous electric field.

The sensing surface of the capacitive sensor is formed by two concentrically shaped metal electrodes, of an unwound capacitor. The sensor measures changes in capacitance, which is in other words the description of how two separate conductive objects respond to a voltage difference applied to them. When a voltage is applied to the conductors, an electric field is created between causing positive and negative charges to collect on each object. If the polarity of the voltage is reversed, the charges will also reverse.

Capacitive sensors use an alternating voltage which causes the charges to continually reverse their positions. The movement of the charges creates an alternating electric current that is detected by the sensor, as seen in Figure 13. The current flow is determined by the capacitance, and the capacitance is determined by the area and proximity of the conductive objects. Larger and closer objects cause greater current than smaller and more distant objects.

The capacitance is also affected by the nonconductive material in the measurement gap.

Figure 13 - Flow of charge inside a capacitive sensor

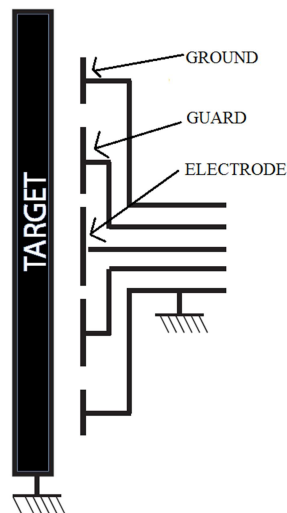


Source: <http://www.lionprecision.com/tech-library/technotes/cap-0020-sensor-theory.html>

A technique called guarding, shown in Figure 14, is used to prevent spreading of the sensors electrical field to other areas on the target or closed conductor items, which could lead to measure a fake change position on target.

To create a guarded probe, the back and sides of the sensing area are surrounded by another conductor that is kept at the same voltage as the sensing area itself. When the excitation voltage is applied to the sensing area, a separate circuit applies the exact same voltage to the guard. Because there is no difference in voltage between the sensing area and the guard, there is no electric field between them to cause current flow. Any conductors beside or behind the probe form an electric field with the guard instead of the sensing area. Only the unguarded front of the sensing area is allowed to form an electric field to the target.

Figure 14 - MCCHS10 sensors design



Source: FOGALE Technical Note, 2008

### 3.3.2 Capacitance-Voltage Converter Modules

Each of the six MCC10HS capacitive sensors is connected directly to one of the MC900 modules. These modules convert the capacitance of the sensors measure into a voltage value that is proportional to the measured distance.

Since the measurement range of the two Fabry-Pérots are different, three of the MC900 modules are calibrated so that 10 V correspond to a measured distance of 200  $\mu\text{m}$ , and the other three calibrated so that 10 V correspond to a measured distance of 400  $\mu\text{m}$ .

A picture of the six MC900 modules of the two Fabry-Pérot is shown in Figure 15.

Figure 15 - MC900 converters modules picture



Source: Author

### 3.4 DIGITAL CONTROL SYSTEM

Although the piezoactuators driver by charge minimizes significantly the nonlinearities of the piezoactuators, it is still not enough for open-loop nanopositioning. Also, when accuracy or speed is required, additional controllers are implemented in specific control loop to improve the performances of the piezoelectric mechanisms.

Before the late 1970's, the idea of implementing piezoelectric actuators built into optical etalon assemblies had been attempted without success. By incorporating capacitance sensors and a highly stable feedback control system, Queensgate Instruments<sup>1</sup>, Torquay, Devon, United Kingdom, was able to start the development of a Fabry-Pérot interferometer that eliminated the hysteresis and creep effects and maintained both the parallelism and separation of the plates.

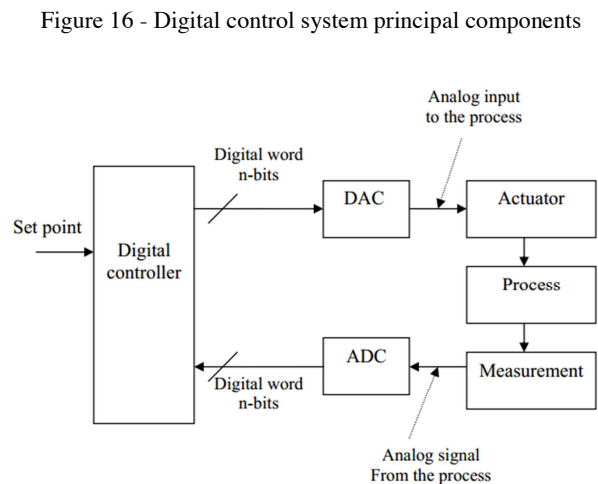
<sup>1</sup> Now named IC Optical Systems Ltd. (ICOS)

The Queensgate Fabry-Pérot Control system is named “CS100 Controller and ET Series II Servo-stabilized Interferometer System” and was the first control system to use capacitance micrometers as the distance sensors in a feedback loop, affording great precision in the measurement of changes in separation.

It is beyond the scope of this work to emphasize in the functioning principles of the former Queensgate CS100 controller, but it is to say, briefly, that it is a completely analog controller, with 12 bits resolution for a  $6 \mu\text{m}$  stroke range, that could control the etalon spacing and parallelism to better than 0.01% of a free spectral range (FSR).

When it came to decide the type of controller to be used for the BTFI Fabry-Pérot instrument a digital solution was chosen because of its flexibility in terms of control algorithm reconfiguration, versatility, long durability of its components, higher rejection to noise and low cost of implementation.

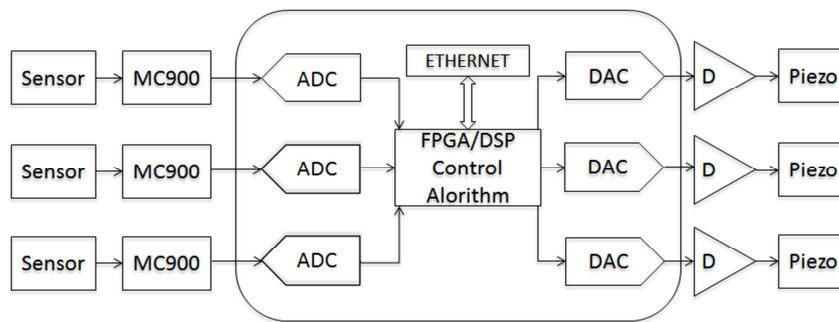
Figure 16 shows the block diagram of a general digital control system and its main constituents.



### 3.4.1 BTFI Fabry-Pérot Controller Board

In the initial stage of the BTFI work a controller board, designed and assembled by the Laboratoire d'Astrophysique de Marseille, LAM, was used for experiments on the Fabry-Pérot etalon. Figure 17 shows a schematic of this controller board and its main constituents.

Figure 17 - Fabry-Pérot former controller board schematic



Source: Cavalcanti, 2011.

This board communicated via Ethernet with a graphical user interface developed in LabVIEW<sup>®</sup> where the user could set a reference point. The output voltage of the MC900 modules was then read by the analog-to-digital converter, ADC, and sent via Serial Peripheral Interface Bus, SPI, to the Field-Programmable Gate Array, FPGA.

The control action was done calculating, with a programmed control algorithm, the input value of voltage for the piezoactuators and converting this digital value to an analog signal to enter the piezoactuators drivers, using a digital-to-analog, DAC, converter. The analog control signal was then amplified by the drivers that actuate the piezoactuators.

In the initial stage of the project this controller board was studied and characterized by a member of the BTFI Fabry-Pérot team and lead to the conclusion that the electronic components, especially the microprocessor of the FPGA was not enough to host a control algorithm of the desired bandwidth in real time. For this reason this controller board was

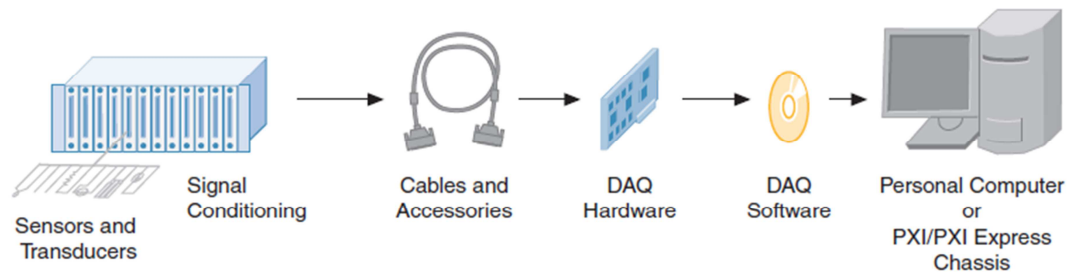
considered obsolete and the design of a new board was planned for the final stage of the project.

### 3.4.2 Data Acquisition System

In order to characterize, model and test the Fabry-Pérot system, a data acquisition board (DAQ) system was implemented in the laboratory instead of using the already obsolete controller board.

The DAQ system, as Figure 18 shows, is composed by the sensors, and signal conditioning devices, cabling and accessories, a data acquisition board with the analog-to-digital converters, software installed in a computer and a personal computer with the software for processing the data.

Figure 18 - Components of a typical DAQ system



Source: NI-DAQ M series User Manual, page 26

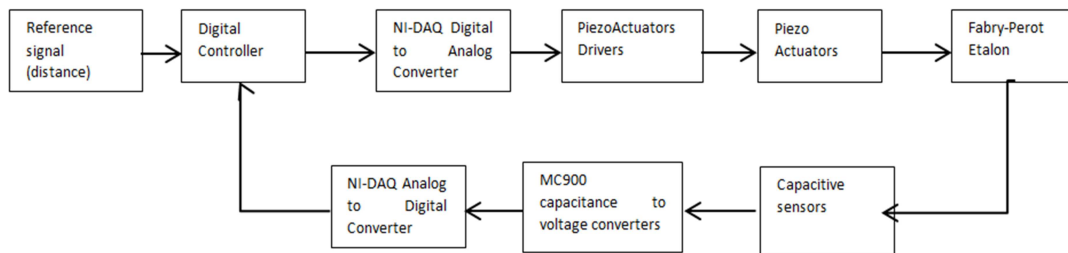
Two DAQs are necessary to operate the prototype of the instrument because the Fabry-Pérot is a 3 channel input system and each of the NI-DAQ 6221 has only two analog outputs.

The control program is written in MATLAB scripts and then they are run using real-time Simulink simulations that communicate with the NI-DAQs.

### 3.4.3 Digital Control System Signal Flow

The signal flow of the control system of the Fabry-Pérot system is represented by the block diagram of Figure 19.

Figure 19 - Signal flow of the Fabry-Pérot digital control system



Source: Author

First, the user enters a reference signal in a graphical user interface that the computer control script translates into an input for the piezoactuators. The digital signal is then converted to an analog signal using a DAC. This analog signal is amplified with the piezoactuators' drivers and then inputs the piezoactuators. Because of the piezoelectric effect, the piezoactuators change the distance in the Fabry-Pérot etalon.

The capacitive sensors measure the displacement in distance in the etalon and the capacitive signal goes to the MC900 capacitance-to-voltage converter, CVC. The output of this converter is a voltage proportional to the distance of the etalon. This analog voltage is converted to a digital value using the NI-DAQ ADC converter and enters the control script as a feedback signal that is afterwards compared to the reference. The control script calculates the error and compensates it with a new control signal.

This process is repeated continuously.

## 4 CHARACTERISTICS OF THE DISTANCE MEASUREMENT SYSTEM

For the study and characterization of the measurement system the following hardware and software was used in the laboratory:

Hardware:

- FOGALE MC900 Capacitance to Voltage Converters (6 units).
- FOGALE MCC10HS Capacitive Sensor (6 units).
- National Instruments Data Acquisition Board NI-DAQ 6221 (2 units).
- National Instruments Dynamic Signal Analyzer board, NI-DSA 4552.
- Hewlett Packard 34401A Multimeter.
- Agilent Technologies DSO3062A Digital Storage Oscilloscope.
- Personal Computer (2 units): PC 1, PC 2.
- Hewlett Packard 35665A Dynamic Signal Analyzer.

Software:

- Mathworks MATLAB<sup>®</sup> and Simulink<sup>®</sup>.
- National Instruments LabVIEW<sup>®</sup> and DSA soft front panel.

### 4.1 MEASUREMENT RANGE

The measurement range represents the values that a measuring instrument can display and in the case of the capacitive sensors, it depends on the size of the active sensor area as well as on the electronics used.

The measurement range of the six FOGALE MCC10HS sensors is 1 mm. This is enough to measure the distance displacement of both Fabry-Pérots, which are 200  $\mu\text{m}$  and 400  $\mu\text{m}$ .

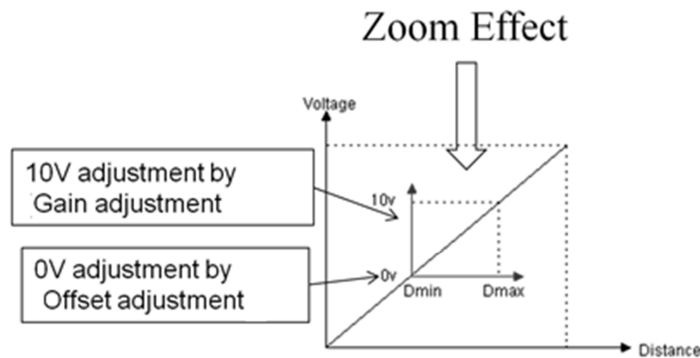
## 4.2 SENSITIVITY

Sensitivity in the distance measurement system (MCC10HS sensors + MC900 converter modules) indicates how much the output voltage changes as a result of a change in the gap between the target and the capacitive sensor. When the output voltage is plotted against the gap size, the slope of the line is the sensitivity (Physik Instrumente 1, 2007).

The electronics of the MC900 modules are calibrated to generate specific voltage changes for corresponding changes in capacitance. In other words, the sensitivity of the modules can be changed according to the application needs.

Figure 20 shows the zoom effect option in the FOGALE system.

Figure 20 - Zoom effect of MC900 modules



Source: FOGALE Technical Note, 2008.

For the MC900 modules the sensitivity is as defined in eq.(2).

$$MC900 \text{ Sensitivity} = \frac{10V}{MR} \quad (2)$$

For the converter modules 1, 2 and 3, the measurement range (MR) is of 200  $\mu\text{m}$ , so the output changes 1 V with a change in distance of 20  $\mu\text{m}$ . For the other three MC900 converter modules (4, 5, 6), the sensitivity is 0.025V/ $\mu\text{m}$ .

### 4.3 LINEARITY AND STABILITY

The linearity of a measurement in the capacitive sensor denotes the consistency in the proportional relation between change in probe-target distance and the output signal. It is highly influenced by homogeneity of the electric field and thus by any non-parallelism of the probe and target in application.

It is usually referred to as the linearity error, calculated as a percentage of the full measurement range, and has no influence whatsoever upon resolution and repeatability of a measurement (Physik Instrumente 1, 2007).

According to FOGALE, the MC900 system has an error of linearity of  $\pm 0.1\%$  measure extent, in standard sensor and standard distance (FOGALE, 2008), as shown in eq.(3).

$$\text{Linearity}_{error} \leq \pm 0.01MR \quad (3)$$

### 4.4 REPEATABILITY

Repeatability is a statistical term associated with accuracy. On capacitive sensors, it is the ability of the sensor to measure precisely the same capacitance when there is the same distance between the sensor and the target, and under the same conditions.

According to FOGALE technical note (FOGALE, 2008), MC900 modules have a repeatability of 0.001% measure extent in statistics.

That is, for the three MC900 of 200  $\mu m$  measurement range:

$$\text{Repeatability}_{MC900\ 1,2,3} = \frac{0.001 * 200 \mu m}{100} = 0.002 \mu m = 2 \text{ nm} \quad (4)$$

For the three MC900 modules of 400  $\mu m$  of measurement range:

$$Repeatability_{MC900\ 1,2,3} = \frac{0.001 * 400\ \mu m}{100} = 0.004\ \mu m = 4\ nm \quad (5)$$

#### 4.5 MEASUREMENT ERROR DUE TO NON-PARALLELISM OF MEASURING SURFACES

Target and probe plates must remain parallel to each other during measurement to avoid errors in linearity and gain. For small measurement distances and small active areas, any divergence has a strong influence on the measurement results although it does not affect resolution or repeatability.

Systems are calibrated with the probe perpendicular to the target surface. As the angle changes, the output will show a direct current, DC, shift (offset) relative to the actual gap from the probe's center axis to the target.

Equation 6 shows the distance measurement error due to the non-parallelism of the measurement surfaces as presented in LION, 2004. This distance error is proportional to the size of the probe sensor and the probe-target angle.

$$d_{error} = \left( \frac{1 - \sqrt{1 - \left(\frac{r \cdot \theta}{d}\right)^2}}{2} \right) \cdot d \cdot k \quad (6)$$

where:

- $r$  is the radius of probe sensor area;
- $d$  is the probe/target gap, directly under the probe center axis;
- $\theta$  is the probe/target angle;
- $k$  is the experimentally determined constant to account for field fringing errors.

Typical  $k$  values are around 5 and the radius of the sensor probe area is 0.0027 m.

It is important to point that even though the error introduced by non-parallelism of the probe can be very high, it only affects the absolute measure. A relative measure eliminates the error (Physik Instrumente 2, 2007).

## 4.6 ENVIRONMENTAL CHARACTERISTICS

### 4.6.1 Target Surface

Target surface characteristics can significantly influence the results. A curved or rough surface will affect the resolution because the results refer to an average gap.

Surface shape also influences the homogeneity of the electric field and thereby the measurement linearity (Physik Instrumente 1, 2007). If the target area is too small, the electric field will begin to wrap around the sides of the target meaning the electric field extends farther than it did in calibration and will measure the target as farther away. Because this distance differs from the original calibration, error will be introduced (FOGALE, 2008).

The FOGALE Nanotech technical manual does not specify the targets size at the time of the MC900 modules calibration. Based on (Physik Instrumente 2, 2007), unless otherwise specified, factory calibrations are done with a flat conductive target that is considerably larger than the sensing area. A sensor calibrated in this way will give accurate results when measuring a flat target more than 30% larger than the sensing area.

The MCC10HS sensors have a sensing area of 5.5 mm, so the size of the target should be at least of 7.2 mm. The target at the Fabry-Pérot upper mirror mount has a size of 10 mm which is enough for the MCC10HS sensors.

### 4.6.2 Environmental Influences

Precision measurement with nanometer accuracy requires minimizing environmental influences like temperature and humidity changes. Temperature changes cause all material in the system to expand or contract, thus changing the actual measured gap. And since the dielectric constant of air is affected by humidity, the sensitivity curve changes and repeatability is affected.

In general more temperature related errors are due to expansion and contraction of the measurement mounting than probe or electronics drift. International standards specify that

measurements shall be done at 20°C or corrected to “true length” at 20°C (Physik Instrumente 2, 2007).

According to the technical manual, the maximum temperature of operation of the MCC10HS sensors is 200 °C and thermal drift for the MC900 converter modules is 0.002%, measure extent by °C.

The thermal drift error relation, for the 200  $\mu\text{m}$  MC900 modules is as in eq.(7):

$$Thermal_{DriftError} = \frac{0.002}{100} * \frac{200 \mu\text{m}}{1^\circ\text{C}} * \Delta^\circ\text{C} \quad (7)$$

And the thermal drift error relation, for the 400  $\mu\text{m}$  MC900 modules is as in eq.(8):

$$Thermal_{DriftError} = \frac{0.002}{100} * \frac{400 \mu\text{m}}{1^\circ\text{C}} * \Delta^\circ\text{C} \quad (8)$$

Considering the temperature range of the telescope environment is -10 °C to 25 °C the thermal drift error can be as high as 24 nm.

#### 4.7 RESOLUTION AND MEASUREMENT NOISE

Resolution in nanopositioning relates to the smallest change in displacement that can still be detected by the measuring devices. For a capacitive sensor, resolution is in principle unlimited, but in practice it is limited by electronic noise. Limiting the bandwidth reduces noise and there-by improves resolution. The working distance also influences the resolution: the smaller the working distance of the system, the lower the absolute value of the electronic noise (Physik Instrumente 1, 2007).

Electrical noise appears in the output voltage of the MC900 modules, causing small instantaneous errors in the output. Even when the probe/target gap is perfectly constant, the output voltage of the capacitance converter modules have some small but measurable amount of noise that would seem to indicate that the gap is changing.

This noise is inherent to electronic components and can be minimized, but never eliminated (Physik Instrumente 2, 2007).

According to FOGALE technical manual the measurement noise of the MCCHS10 sensors in terms of the frequency of operation of the MC900 modules is given by:

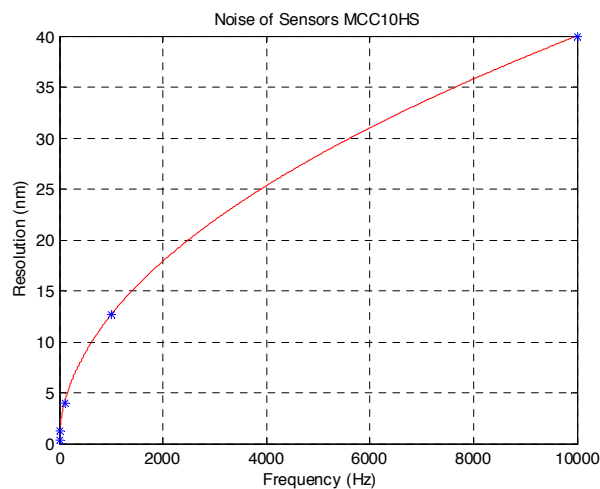
$$\text{Sensor}_{\text{Noise}} = 0.4 \left[ \frac{\text{nm} * \text{RMS}}{\sqrt{\text{Hz}}} \right] * \sqrt{F_{\text{MC900}}} \quad (9)$$

where:

$F_{\text{MC900}}$  is the frequency at which the MC900 converter modules are working.

A plot of eq.(9) evaluated from 0 to 10000 Hz is shown in Figure 21.

Figure 21 - Noise (nm RMS) of the FOGALE system in different bandwidths



Source: Author

The MC900 modules have a bandwidth selector, so it can measure static values at 1 Hz or measure dynamically at 10000 Hz. For the Fabry-Pérot instrument, the bandwidth was factory-fixed to 10000 Hz but the measurement noise was calculated for the other bandwidth options as reference.

The blue asterisks in Figure 21 represent the noise in those bandwidth options and Table 2 summarizes these values.

Table 2 FOGALE system noise (nm RMS) at different operation bandwidths

<b>Bandwidth (Hz)</b>	<b>Noise (nm RMS)</b>
1	0.4
10	1.3
100	4
1000	12.6
10000	40

As shown in Table 2, the lower the bandwidth, the lower the electronic noise and better resolution; but at the same time, measuring the distance at a lower frequency limits the velocity of response of the control system to which the sensors are given feedback, making it unable to respond and compensate high frequency perturbations.

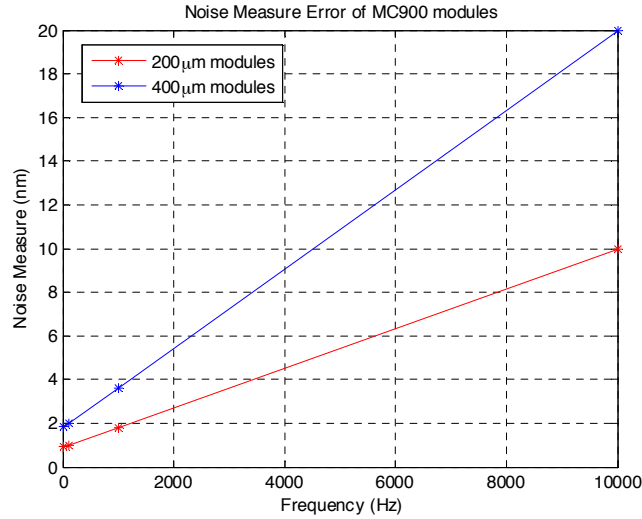
The FOGALE technical note also specifies the noise measure of the MC900 modules separately as maximum 0.005% RMS measure extent at 10 kHz and 0.0005% RMS measure extent at 100 Hz.

It was assumed that the noise measure error is linear, and so it was interpolated for the whole range of operation, as plotted in Figure 22. The values for the bandwidth options are also summarized in Table 3.

Table 3 Noise of the MC900 modules in terms of the bandwidth of operation

<b>Bandwidth (Hz)</b>	<b>Noise Measure 200 <math>\mu\text{m}</math> MC 900 modules (nm RMS)</b>	<b>Noise Measure 400 <math>\mu\text{m}</math> MC 900 modules (nm RMS)</b>
1	0.91	1.82
10	0.92	1.84
100	1	2
1000	1.82	3.64
10000	10	20

Figure 22 - Noise Measure for MC900 modules



Source: Author

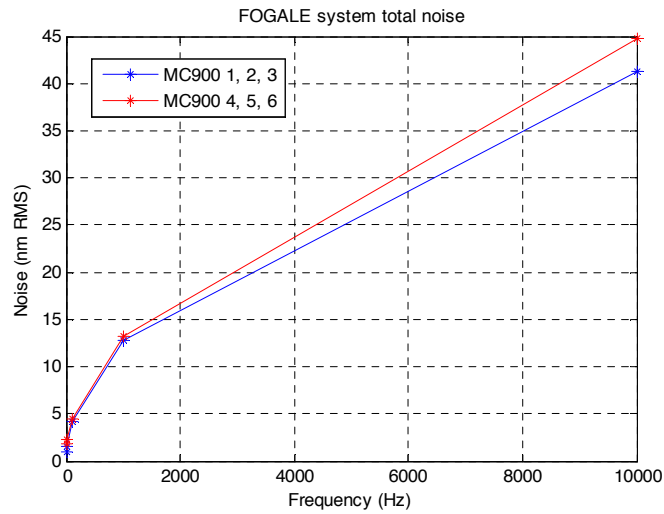
The total noise of the distance measurement system,  $\sigma_{FOGALE}$  can be calculated, as presented in eq.(10), as the square root of the sum of the square of the noise of the sensors,  $\sigma_{sensor}$ , and the square of the noise measure of the MC900 modules,  $\sigma_{MC900}$ , at the different MC900 bandwidth options. The total theoretical system noise in terms of the bandwidth of the system is plotted in Figure 23 and summarized in Table 4.

$$\sigma_{FOGALE} = \sqrt{\sigma_{sensor}^2 + \sigma_{MC900}^2} \quad (10)$$

Table 4 Total theoretical noise of the FOGALE distance measurement system

Bandwidth (Hz)	Distance measurement system of 200 μm noise (nm)	Distance measurement system of 400 μm noise (nm)
1	0.99	1.86
10	1.56	2.23
100	4.12	4.47
1000	12.78	13.16
10000	41.23	44.72

Figure 23 - FOGALE measurement system total noise (nm)



Source: Author

Looking at the calculated values of the theoretical measurement noise shown in Table 4, it can be inferred that the FOGALE measurement system, with a fixed bandwidth of 10000 Hz, cannot achieve the resolution of the instrument scientific specification of 3 nm.

However, it is to be said that this theoretical specification is provided as a general specification by the manufacturer, which is usually valid for the worst-case scenario.

A characterization of the system's real noise in the laboratory was then proposed in order to decide if the system was suitable or not, especially because the FOGALE equipment was already purchased for the BTFI project.

#### 4.7.1 Noise Statistical Analysis for the FOGALE system

As stated before, the measurement noise plotted in Figure 22, in terms of the bandwidth of operation of the MC900 system, represents only the theoretical measurement noise of the FOGALE technical manual, which is usually the worst-case scenario value.

One of the objectives of this project was to characterize the real noise of the system so that a proper solution could be found to help the system achieve the scientific resolution required for operation, or to finally conclude that the system has to be replaced.

Taking the MC900 modules output in volts, a statistical analysis is performed to determine the noise of the signal, calculating its standard deviation. The standard deviation of the sampled signal,  $\sigma$ , expresses the fluctuation of a signal around its average value, and corresponds to the noise (RMS), and other interference, in volts.

To convert the noise in volts to nanometers, the standard deviation of the signal is multiplied by the gain of the MC900 modules and by a conversion of microns to nanometers as in eq.(11).

$$\sigma_{signal}(nm) = \sigma_{signal}(V) * G_{MC900} * \frac{1000 \text{ nm}}{1\mu m} \quad (11)$$

Where the gain depends on the measurement range of the modules:

$$G_{MC900}1,2,3 = \frac{200 \mu m}{10 V} \quad (12)$$

$$G_{MC900}4,5,6 = \frac{400 \mu m}{10 V} \quad (13)$$

The cases of study performed in the laboratory were the following:

Case of study 1: Find the standard deviation of an output signal of the MC900 modules, for different hardware setups including changing the used NI-DAQ, the input/output cables, the PCI slot on the computer and the personal computers where the NI-DAQs are installed.

Case of study 2: Find the standard deviation of the output signal of the MC900 modules changing the input resolution of the NI-DAQ.

Case of study 3: Find the standard deviation of the output signal of the MC900 modules, for different distance measures, *i.e.* different signal means, using a multimeter.

Case of study 4: Take the one-sided amplitude spectrum of the MC900 output using the NI-DAQ and a Dynamic Signal Analyzer.

#### 4.7.1.1 Case of study 1: Noise Dependence on Hardware

To study the noise dependency on hardware, different acquisition systems setups, interchanging the different available hardware components, were tested in the laboratory to analyze the noise of a single signal.

A signal from the output of the MC900, with mean  $\mu = 9.5$  V was acquired switching the two NI-DAQ boards for acquisition, the two input/output I/O cables of the two NI-DAQ boards, installing the NI-DAQ boards to different peripheral component interconnect (PCI) slots and using two different computers. Only one computer had two different PCI slots, which is why there are no tests setups with Personal Computer 2 and PCI slot 2..

Table 5 summarizes the tests configurations and the standard deviation of the same signal, acquired at the same sample frequency of 25600 Hz.

Table 5 MC900 noise dependence on hardware

Test setup	NI-DAQ Board	Personal Computer	PCI slot on computer	I/O Cable for the NI-DAQ board	Noise standard deviation $\sigma$ (nm)
1	1	1	1	1	188,12
2	1	1	1	2	187,55
3	1	1	2	1	189,67
4	1	1	2	2	170,07
5	1	2	1	1	23,08
6	1	2	1	2	22,90
7	2	1	1	1	351,82
8	2	1	1	2	338,10
9	2	1	2	1	347,54
10	2	1	2	2	318,49
11	2	2	1	1	51,08
12	2	2	1	2	49,53

The difference of noise in the signals acquired with different configurations of PCs and boards is very significant. The best case is the test setup number 6, using the NI-DAQ unit 1 on the PC 2, where the acquired signal has a standard deviation of ~23 nm.

The worst case is the test setup number 7, using the NI-DAQ unit 2 on the PC 1 with an error of ~350 nm. The input-output (I/O) cable for the NI-DAQ board also has an impact on the noise, but not as significant as the PC.

On the cases where only one NI-DAQ is needed, for example to take the dynamic response of the piezoactuators or their drivers, the configuration with less noise is the one that will be used, that is test setup 6 (NI-DAQ1 on PC 2).

However, for tests in the complete Fabry-Pérot system, the worst scenario (test setup 7, 8, 9 and 10) has to be used because of the need for three analog outputs, which are provided by the two NI-DAQs, configured on PC 1.

#### 4.7.1.2 Case of study 2: Resolution of the Acquisition Instrument

The National Instruments Data Acquisition board NI-DAQ 6221 has an ADC of 16 bits, configurable measurement range, and a configurable sample frequency that can be as high as 250000 samples per second, SPS.

The resolution of the ADC depends on the measurement range of the input signal, so the 16 bits of the DAQ can be distributed in different voltage ranges, increasing the resolution for low input values.

Table 6 summarizes the different resolution setups of the NI-DAQ system in volts and its corresponding value in nanometers, when the acquired signal is the output of the FOGALE system.

For the MC900 modules output signal, the measurement range setup for the NI-DAQ has to be set in [-10 to 10] V. However, depending on the mean value of the output signal of the MC900 the signal can be acquired with different resolutions.

Table 6 National Instruments Data Acquisition Board 6221 resolution.

<b>NI-DAQ Measurement Range (V)</b>	<b>NI-DAQ ADC Resolution (V)</b>	<b>Resolution (nm) MC900 1, 2, 3</b>	<b>Resolution (nm) MC900 4, 5, 6</b>
[-10 to 10]	3.0517e-4	6.1	12.2
[-5 to 5]	1.5259e-4	3	6
[-1 to 1]	3.0517e-5	0.6	1.2

Even though the noise of the signal depends also on the mean of the signal, as the next case of study will show, it is interesting to check the noise dependence on the acquisition system resolution.

Table 7 Noise of FOGALE system measured with different DAQ input resolutions.

<b>NI-DAQ Measurement Range (V)</b>	<b>Short-circuit input. <math>\sigma</math> (mV)</b>	<b>MC900 1, 2, 3 <math>\sigma</math> (nm RMS)</b>	<b>MC900 4,5,6 <math>\sigma</math> (nm RMS)</b>
[-10 to 10]	0.2726	28.8195	56.2961
[-5 to 5]	0.1476	20.9581	39.0346
[-1 to 1]	0.0642	12.7082	25.4164

Comparing the NI-DAQ resolution values of Table 6 with the standard deviation of a short-circuit signal in Table 7, it is inferred that the Data Acquisition System comprised of the NI-DAQ and the computer, introduces electronic noise in the measurement.

The results also show that the noise of the acquired signal depends on the resolution of the NI-DAQ.

The same test was repeated using a 6½ digit multimeter, Agilent 34410A.

The resolution specification of the multimeter also depends on the configurable measurement range, MR, and it is calculated taking into account the mean of the measured signal, as in eq.(14) (Agilent, 2006).

$$Res_{Agilent-34410A} = \pm(0.0015\% \mu + 0.0004\% MR + 0.0003\% MR) \quad (14)$$

The different measurement ranges and resolutions of the Agilent 34410A multimeter, and the respective MC900 distance resolution values, are summarized in Table 8.

Table 8 Agilent 34410A voltage resolution and MC900 distance resolution

<b>AGILENT 34410A Measurement Range (V)</b>	<b>AGILENT 34410a Resolution (V)</b>	<b>MC900 1, 2, 3 Resolution (nm)</b>	<b>MC900 4,5,6 Resolution (nm)</b>
10	2.2e-4	4.4	8.8
1	2.2e-5	0.44	0.88
0.1	2.2e-6	0.044	0.088

For an output signal of the MC900 modules with a mean of 0.1 V, the measured standard deviation, in the different resolutions setups of the Agilent 34410A are summarized in Table 9.

Table 9 Noise of the FOGALE system measured with different DAQ input resolutions

<b>AGILENT 34410A Measurement Range (V)</b>	<b>AGILENT 34410a Resolution (V)</b>	<b>MC900 1, 2, 3 <math>\sigma</math> (nm RMS)</b>	<b>MC900 4,5,6 <math>\sigma</math> (nm RMS)</b>
10	2.2e-4	6,234	12,454
1	2.2e-5	5,154	10,345
0.1	2.2e-6	3.645	7.245

The dependence of the noise on the data acquisition system resolution is noticeable, and that is why it is important to define a proper acquisition system for the Fabry-Pérot instrument, as will be presented in section 8.

#### 4.7.1.3 Case of study 3: Signal to Noise Ratio.

The intention of this case of study is to find the signal-to-noise ratio (SNR) of the output of the distance measurement system, in its whole range of operation.

The SNR is defined as the ratio of signal power,  $P_{signal}$ , to the noise power,  $P_{noise}$ , and is a measure of the signal strength relative to background noise. It can be also calculated as the relation between the mean and the standard deviation of a signal, as eq.(15) shows.

$$SNR = \frac{P_{signal}}{P_{noise}} = \frac{\mu_{signal}}{\sigma_{signal}} \quad (15)$$

A SNR value higher than 1 indicates more signal than noise.

To accomplish the test objective it was calculated the mean and the standard deviation of different output signals of the MC900 modules, in its whole range of operation (0 - 10 V).

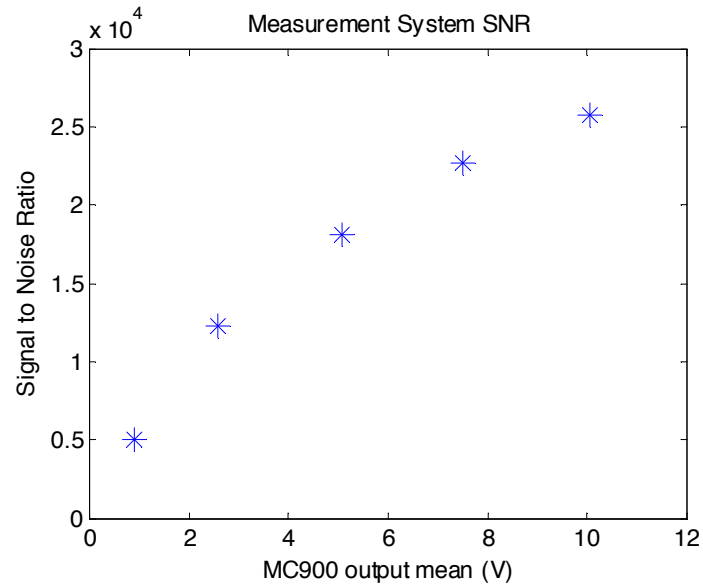
The acquisition of the signal was done using the Agilent 34410A multimeter, with a measurement range of 10 V. Table 10 presents the mean, noise and SNR of all the performed tests.

Table 10 SNR of the FOGALE system for different signal means

<b>MC900 Signal Mean (V)</b>	<b>Signal <math>\sigma</math> (V RMS)</b>	<b>Signal to Noise Ratio</b>
0.8977	0.18e-3	4987.22
2.5762	0.21e-3	12267.62
5.0652	0.28e-3	18090.00
7.4949	0.33e-3	22711.82
10.0603	0.39e-3	25795.64

The signal-to-noise ratio of the NI-DAQ measurements is shown in Figure 24.

Figure 24 - SNR of data acquired with Agilent 34410A



Source: Author

It is evident that for signals with higher mean, the quality of the signal compared with signals with lower mean, is better.

#### 4.7.1.4 Case of study 4: Spectral Analysis of Noise

The objective of this test is to take the single-sided amplitude spectrum of the MC900 signal in order to see frequency decomposition of the distance signal.

Since the output signal of the MC900 is set and fixed on 10000 Hz, the spectral distribution is expected to be a smooth spectrum, decaying around 10000 Hz, and with a noise distribution similar to a Gaussian noise distribution.

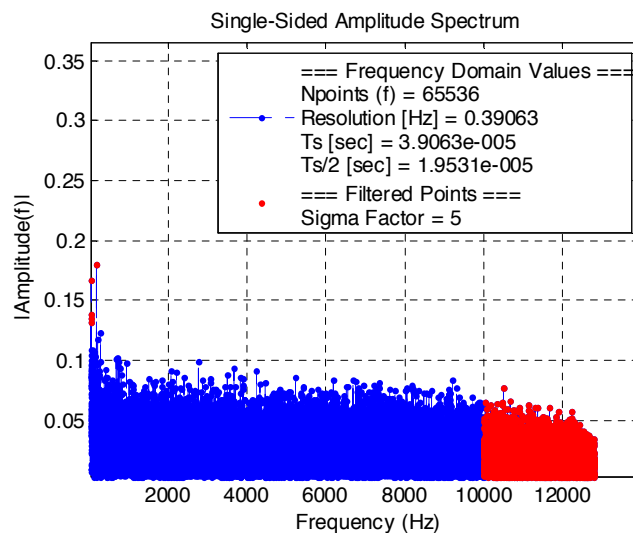
Two tests setups were used for this case of study:

1. Acquiring the MC900 signal, using the dynamic signal analyzer, NI-DSA 4552.
2. Acquiring the MC900 signal, using the NI-DAQ 6221 unit 1 on PC 2.

Figure 25 shows the one-sided amplitude spectrum of the MC900 signal on the test setup 1, with sampling frequency,  $F_s$ , equal to 25600 Hz. This frequency was chosen among the different options of the dynamic signal analyzer because it has at least two times the frequency of the acquired signal, which is necessary to reconstruct the wave, as the Nyquist sampling theorem states.

It can be seen in the figure that after 10000 Hz the frequencies are attenuated and that there are no dominant frequencies in the spectrum, showing a noise behavior similar to a Gaussian distribution, as expected.

Figure 25 - Single sided spectrum of MC900 signal acquired with NI-DSA 4552

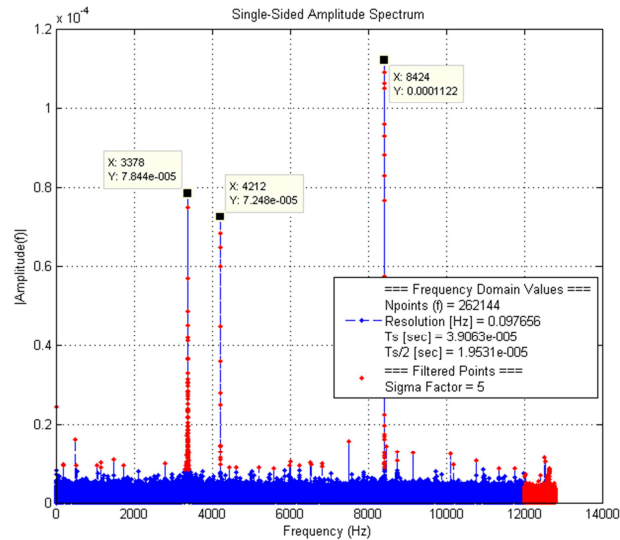


Source: Author

On the other hand, Figure 26 shows the one-sided amplitude spectrum of the MC900 output signal, on test setup 2, with  $F_s$  equal to 25600 Hz.

Different to the spectrum of the acquired signal with the NI-DSA, this last spectrum shows some dominant frequencies (3378 Hz, 4212 Hz and 8424 Hz) that are not expected to be in the MC900 signal.

Figure 26 - Single sided spectrum of MC900 signal acquired with NI-DAQ 6221



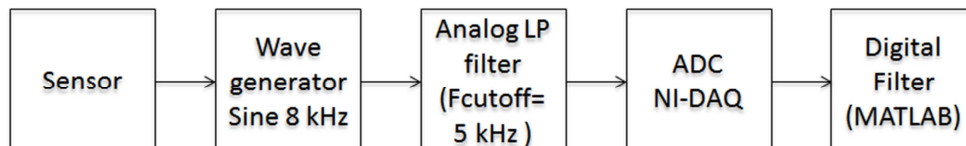
Source: Author

The first hypothesis was that those frequencies were aliased frequencies, appearing in the spectrum because the analog antialiasing filter of the NI-DAQ 6221 does not auto-adjust the sample frequency as the NI-DSA board does.

To test this hypothesis, a Bessel analog filter was designed, implemented and introduced in the signal chain. The signal used for this test was not the MC900 output signal but a sine wave of 8000 Hz generated by a wave generator Agilent 33120A.

The test setup is as in the block diagram of Figure 27.

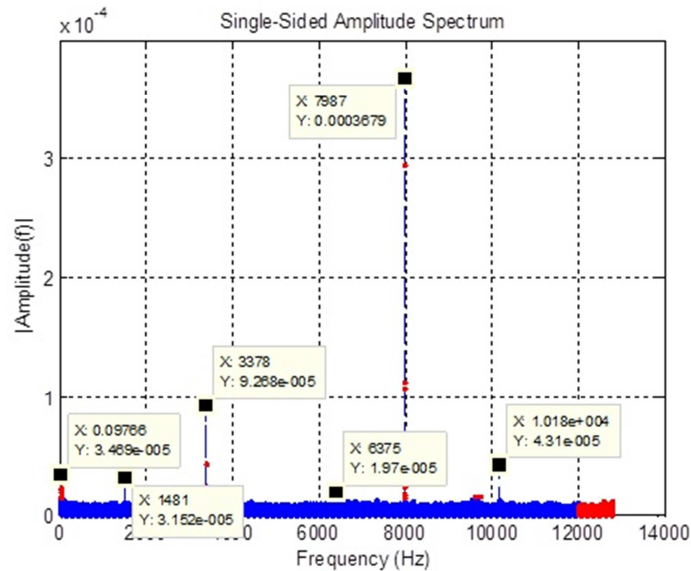
Figure 27 - Block diagram of the analog filter test assembly



Source: Author

Figure 28 shows the single sided amplitude spectrum of the signal without the antialiasing filter.

Figure 28 - Single sided spectrum of wave generator signal acquired with NI-DAQ



Source: Author

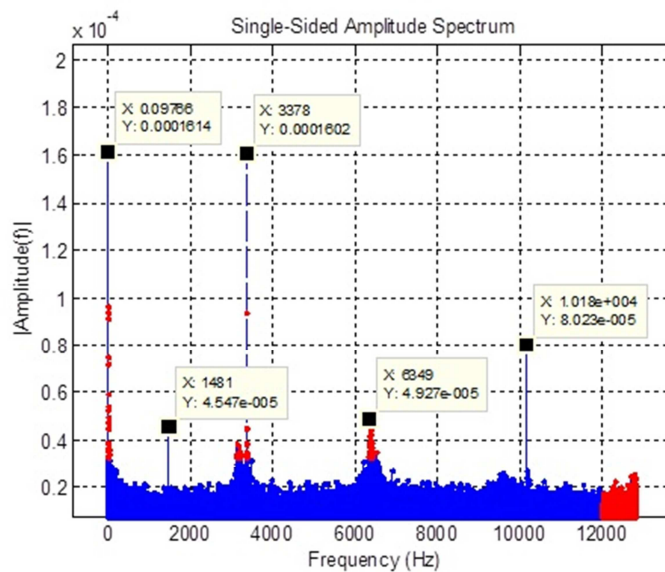
As expected, the 8000 Hz frequency is the dominant frequency in the signal, and the supposedly aliased frequencies (1481 Hz, 3378 Hz, 6375 Hz and 10180 Hz) are present as well.

If the hypothesis of the aliasing effect on the spectrum was correct, the spectrum of the filtered signal on 5000 Hz should be similar to the spectrum of the NI-DSA on Figure 25, that is, a spectrum without dominant frequency in 8000 Hz, without aliased frequencies and starting to attenuate the amplitude of the signal in 5000 Hz.

Figure 29 shows the single sided amplitude spectrum of the filtered signal. The 8000 Hz signal was indeed completely attenuated by the filter, as expected, but what were supposed to be aliased frequencies were not attenuated.

This led to the conclusion that these frequencies are definitely not aliased frequencies related to the aliasing effect of the sampling theorem as initially thought, but they are noise frequencies introduced by the NI-DAQ board hardware. The nature of these frequencies is still open for discussion.

Figure 29 - Amplitude Spectrum of a filtered 8 kHz signal sampled by the NI-DAQ 6221



Source: Author

#### 4.7.2 LION Measurement System

Even though it was not possible to characterize properly the measurement noise of the FOGALE system because of the higher noise of the data acquisition system, just by the factory specification of Table 2, it was concluded that the Fabry-Pérot system was restricted to operate in a bandwidth smaller than 100 Hz.

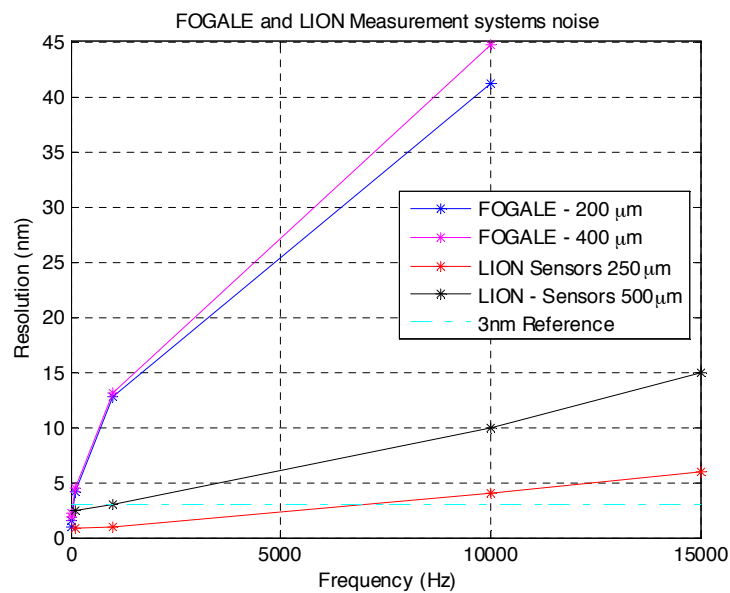
A bandwidth of 100 Hz limits the ability of compensation of external disturbances such as vibrations in the location of the instrument, and a higher value for the control frequency is desired for the robustness of the control system.

Because of the importance of low noise in the measurement, and the benefits of operating the system at a higher frequency, the need for measurement systems based on capacitive sensors that could accomplish the required resolution arose.

LION PRECISION manufactures capacitive sensors in a wide variety of ranges and resolutions, and the sensors that fit the most the BTFI Fabry-Pérot specifications are the Elite Series of 2 mm sensing area with measurement range of 250  $\mu\text{m}$  and 500  $\mu\text{m}$  (LION Precision, 2011).

The 250  $\mu\text{m}$  sensors have a resolution of 1 nm, and the extended calibration sensors have a resolution of 3 nm, both operating with a bandwidth of 1000 Hz. A comparison plot of the FOGALE system and the LION systems with both sensors is shown on the following figure.

Figure 30 - FOGALE and LION Measurement Systems noise (nm RMS)



Source: Author

## 5 CHARACTERISTICS OF THE ACTUATOR SYSTEM

In a complex piezomechanical positioning system, influences outside the actuator result in a potential limitation of accuracy, so it is important to study and understand the characteristics and effects of the system to design a proper compensator for it.

The following sections present a brief summary of the electrical, mechanical and environmental characteristics of the BTFI actuator system.

### 5.1 ELECTRICAL AND MECHANICAL LIMITS

Piezoelectric materials are crystalline solids whose asymmetric structures create an electric dipole moment in the crystal lattice, which is sensitive to both the elastic strain and applied electrical field. That is, when the piezoelectric material is exposed to a voltage it will have a mechanical physical deformation, and when it experiences a mechanical deformation it will generate an electrical discharge.

When piezoelectricity was studied for positioning purposes, it was concluded that to obtain the deformation level required for this type of applications, it was necessary to use high input voltages. For instance, 0.5 mm thick piezoactuators rings required an excitation voltage of approximately one thousand volts (CEDRAT, 2013, p 13)

Because the need for high input voltage was not practical, multilayer actuators (MLAs) were introduced in 1988. MLAs are easy to operate and they have been increasingly used in positioning applications, since modern electronics can easily supply the required excitation voltage of 150 volts.

At 150 V, the APA400MML actuator produces free displacements up to 400  $\mu\text{m}$  and blocked forces up to 38 N along its 14.3 mm short axis, which corresponds to a deformation of 2.8% along the active axis.

The applied voltage cannot decrease under -20 V because the polarization would be reversed and since multilayer piezoceramics are laminated materials they cannot bear any tensile forces.

The lifetime of a piezoactuator depends on the conditions of use but usually up to  $10^{10}$  full stroke cycles can be achieved. Humidity and thermal conditions also have high influence and should be controlled in the telescope environment.

## 5.2 THERMAL LIMITS

Thermo-mechanics and thermal effects are an important issue to be taken into account in the case of fine positioning applications.

Due to the dielectric and mechanical losses, the piezoactuator warms up under continue operation. To avoid a depoling effect of the ceramic, the temperature of the piezoactuator must be monitored and controlled to guarantee that it stays below the ceramic's Curie temperature and avoid electrical polarization.

On the other hand, the relative dielectric constant of piezoceramics varies noticeably with temperature and the capacitance can increase significantly with temperature, reducing the stroke of the actuator.

## 5.3 WORKING CONDITIONS AND APPLICATIONS OF THE APA400MML

The function category of the Fabry-Pérots piezoactuators is nanopositioning. The instrument, as will be presented in section 8, does not have any scientific specification for the bandwidth of the system, and in theory, could work at any frequency.

Table 11 summarizes the working conditions and different applications of the APA400MML piezoactuators according to the frequency region of operation. The working conditions that suit the BTFI Fabry-Pérot applications are highlighted in this table.

Table 11 Working conditions and applications of the piezoactuators<sup>2</sup>

Working conditions	Frequency region	Inertial forces	Electric Power	Functions	Applications
Static	From 0 to $F_r/3$	negligible	negligible	Micropositioner	Micro and nano positioning
				Slow actuator	flow control
				Force Generator	Material stress testing
Dynamic Strain non resonant	Between $F_r/3$ and resonance region	not negligible	Can be very high	Wide bandwidth vibration generation	High frequency shaker
				Vibration damper	Food vibration assistance
				Fast actuator	Active damping isolation
					Fast positioning
Dynamic Strain at resonance	Resonance region	high	Not negligible	High amplitude vibration generator	Resonance Vibration Assistance to process
				Sonic transducer	Ultrasonic welding, micro injection moulding
				Ultrasonic transducers	Fluid degassing cleaning
Dynamic Force	Frequency above resonance region	high	High	Proof-mass vibration/force generator	SHM structure excitors
				Proof-mass vibration damper	Hammer
Impulse Strain (Dynamic)	Whole frequency range	can be high	Can be very high	On-off fast actuators	Shutter
				Long-stroke actuation	Circuit breaker
					Fast positioning
					Long-stroke positioning
Dynamic sensing		can be high	Negligible	Electric generator	Energy harvesting
				Force sensor	Igniters

<sup>2</sup> CEDRAT Catalogue 2013.

According to this information of the manufacturer, the APA400MML piezoactuators can work in Static and Dynamic Strain for nanopositioning applications although the operation at higher frequency is not prohibited.

#### 5.4 CHARACTERISTICS OF THE APA400MML PIEZOACTUATORS

The amplified piezoelectric actuators, APA, are based on the expansion of the active material and on a mechanism to amplify the displacement.

The advantages of the CEDRAT APA actuators are their relatively large displacements, high forces, compact size along the axis, wide range of operating frequency, including resonance, and deformations of 1% (10  $\mu\text{m}/\text{mm}$ ) of the actuator size, or more. (CEDRAT, 2013)

Table 12 shows the electrical and mechanical characteristics of the APA400MML piezoactuators, provided by the manufacturer.

Table 12 Characteristics of the CEDRAT APAMML piezoactuators

<b>References</b>	<b>Unit</b>	<b>APA400MML</b>
Displacement	$\mu\text{m}$	344
Blocked force	N	188
Stiffness	$\text{N}/\mu\text{m}$	0,5
Resonance frequency (free-free)	Hz	2378
Response time (free-free)	ms	0,18
Resonance frequency (blocked-free)	Hz	834
Response time (blocked-free)	ms	0,79
Force limit (0-pk)	N	95
Max. Displacement at resonance (pk-pk)	$\mu\text{m}$	310
Voltage range	V	-20,15
Capacitance	$\mu\text{F}$	10
Resolution	nm	1
Thermo-mechanical behavior	$\mu\text{m}/\text{K}$	1,51
Height H (in actuation direction)	mm	58
Length	mm	78
Width	mm	11,5
Mass	g	50

The free-free configuration refers to the piezoactuator mount setting that permits the actuators mechanical interfaces to move freely. On the other hand the block-free configuration is the mount setting where one side of the actuator is fixed to a rigid base and the other end can move freely.

The piezoactuators in the Fabry-Pérot instrument are in a block-free configuration, fixed on one side to the physical structure of the etalon, and on the other side to the mirror they intend to position.

The aforementioned electrical and mechanical parameter values are the ones used for the piezoactuators second-order model in section 6.

## 5.5 SHIFT VERSUS VOLTAGE

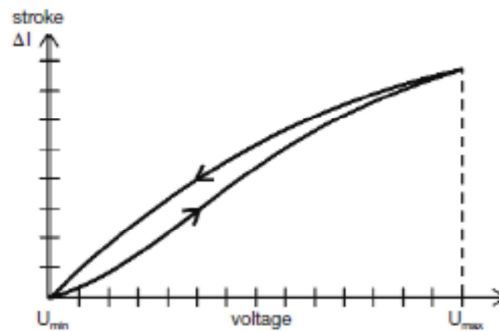
Piezoactuators, when driven in open-loop, exhibit hysteresis effects, based on crystalline polarization and molecular friction. Correlation of piezostack's open-loop cycle over a voltage range going from the minimum input value to the maximum input value and going the way back,  $U_{min}-U_{max}-U_{min}$ , leads to the hysteresis diagram of Figure 31.

An acceptable reproducibility of the hysteresis diagram is achieved only after reaching an equilibrium attained by cycling the system many times while all other operation parameters like temperature, force and load are held constant. If the cycling conditions are changed, the system will adjust towards a new equilibrium after the application of a sufficient number of cycles.

The final position of the stack upon application of a distinct voltage level depends on the "history" of stack's operation (memory-effect for open-loop) and to model this behavior is beyond the scope of this work. That is why a driver to minimize this effect, and a control loop to fully compensate it, was the chosen solution to deal with this non-linearity.

Marchiori et al. (2013) describes the design and the realization of an analog charge control solution to attenuate the hysteresis nonlinear phenomenon of the Fabry-Pérot interferometer's Amplified Piezoelectric Actuators (APA).

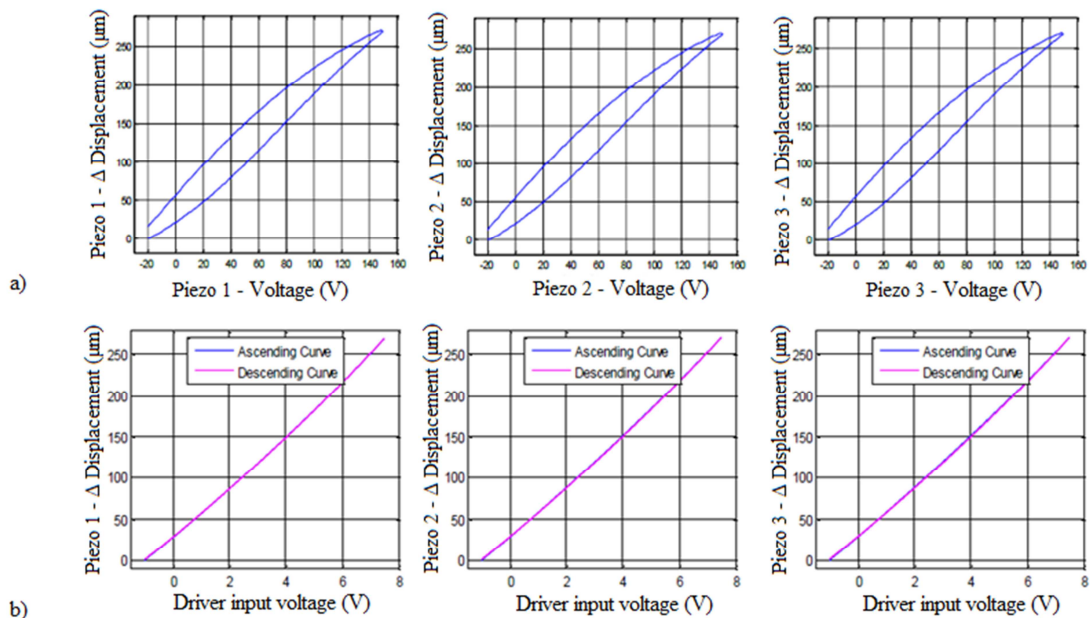
Figure 31 - Hysteresis behavior of piezoactuators



Source: Piezomechanik katalog 2010, p.19

Figure 32.a shows the hysteresis diagram of the three CEDRAT APA400MML used in the laboratory when using a driver by voltage. Figure 32.b shows the main results of Marchiori's work using the driver by charge. It shows that the hysteresis magnitude is almost eliminated (up to 98,2% reduction) compared to the classic voltage control solution.

Figure 32 - Hysteresis curve of APA400MML piezoactuators a) when driven by the drivers by voltage b) when driven by the drivers by charge



Source: Marchiori et al. 2013

## 5.6 PRE-STRESSED CERAMICS

The pre-stressed piezoactuators use an external deformable frame to pre-stress the ceramics inside the actuator. This pre-stressed configuration helps to maintain the compression on the material, avoiding tensile forces during dynamic operations which can lead to mechanical breakdown (Piezomechanik katalog, 2010).

## 5.7 RESONANCE IN PIEZOACTUATORS

When the actuator is operated in quasistatic bandwidth, which is until about one third of the resonance frequency of the piezoactuator, its displacement depends both on the applied voltage and the generated force, and follows the input excitation with the relation of eq.(16) (CEDRAT,2013):

$$\Delta U = \frac{NV - F}{K} \quad (16)$$

where:

- $\Delta U$  is the displacement;
- $N$  is the force factor of the actuator;
- $V$  is the applied voltage;
- $F$  is the generated force;
- $K$  is the stiffness.

Operating at resonance frequency, considering a constant voltage amplitude input, the displacement of the piezoactuator is magnified by the mechanical quality factor  $Q_m$ , as shown in eq.(17) (CEDRAT,2013):

$$\Delta U = \frac{Q_m NV}{K} \quad (17)$$

Due to this amplification and to mechanical limits, the maximum voltage input that can be applied to the piezoactuator in resonance frequency is much lower than in static frequencies.

In addition to this, the resonance is also responsible for overshoot and oscillations on the dynamic response of the actuators.

Under dynamic conditions, the piezoactuator requires a careful design and driving because of the mechanical breaking risks, and it is the responsibility of the control system to take into account this high-risk dynamics.

## 6 DYNAMIC MODELING OF THE FABRY-PÉROT INTERFEROMETER

As presented in the previous sections, the BTFI has two Fabry-Pérots, one of low resolution and one of high resolution. Both Fabry-Pérots incorporate the same elements: three piezoelectric actuators and three distance measurement systems, with three capacitive sensors and three MC900 capacitance to voltage converting modules.

The dynamic modeling of all of these components of the Fabry-Pérot system is a requirement to understand the behavior and nature of the electronic components and to be able to design a proper compensator that leads to achieve the scientific performance requirements.

The Fabry-Pérot prototype used in the laboratory for simulation and tests is composed of the three piezoactuators of 350  $\mu\text{m}$  stroke and the three 400  $\mu\text{m}$  measurement range units.

The knowledge and work summarized in the following items will be the theoretical and practical background for the dynamical modeling of the ultimate Fabry-Pérots interferometers, which will also have the final digital control system board.

### 6.1 MODEL OF THE POSITION MEASUREMENT SYSTEM

The position measurement system, as presented in section 3.2.3 and section 4, is comprised of six capacitive sensors and six capacitance-to-voltage converters. The following items present the static model of these components.

#### 6.1.1 Static Model of the Capacitive Sensors

The capacitive position sensors MCC10HS from FOGALE nanotech follow the law of capacitance for parallel plates of eq.(18) which is based on the geometry of the conductors of area  $A$ , and the dielectric properties of the insulators.

$$C = \frac{(\varepsilon_0 \cdot \varepsilon_r \cdot A)}{d} \quad (18)$$

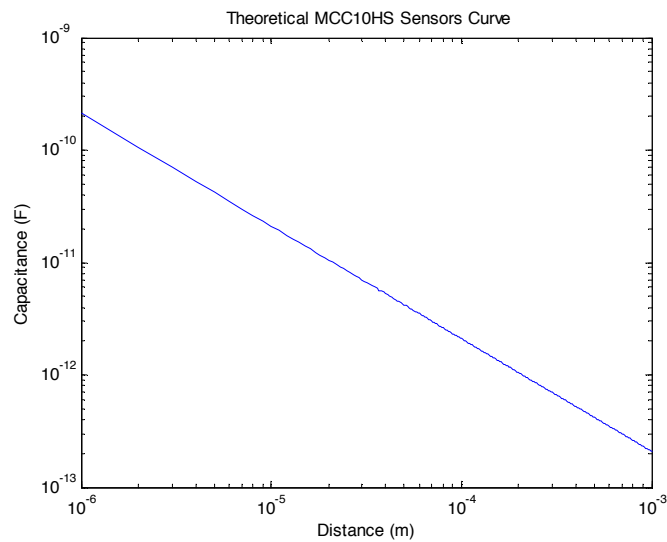
where:

$C$  is the capacitance;

$A$  is the surface area of the sensors;  
 $d$  is the sensed distance;  
 $\epsilon_r$  is the relative static permittivity, or dielectric constant of the material between the plates, which in the case of the Fabry-Pérot interferometer is air;  
 $\epsilon_0$  is the electric constant.

Figure 33 shows the theoretical model of the MCC10HS sensors.

Figure 33 - Theoretical static model of capacitive sensors.



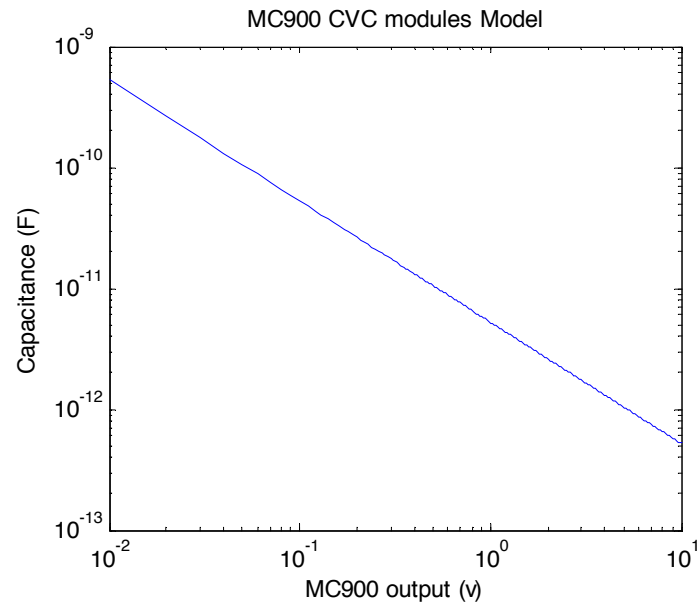
Source: Author

### 6.1.2 Static Model of the Capacitance to Voltage Converters

The output signal of the capacitive sensors, in Farads, enters the MC900 modules that convert the capacitance into a voltage value.

Figure 34 shows the relationship between the capacitance that inputs the modules and the output in volts. The red line represents the model of the MC900 units 1, 2 and 3, which are calibrated for a 200  $\mu\text{m}$  measurement range, and the blue line represents the model of the MC900 units 4, 5 and 6, which are calibrated for a 400  $\mu\text{m}$  measurement range.

Figure 34 - Static model of MC900 modules



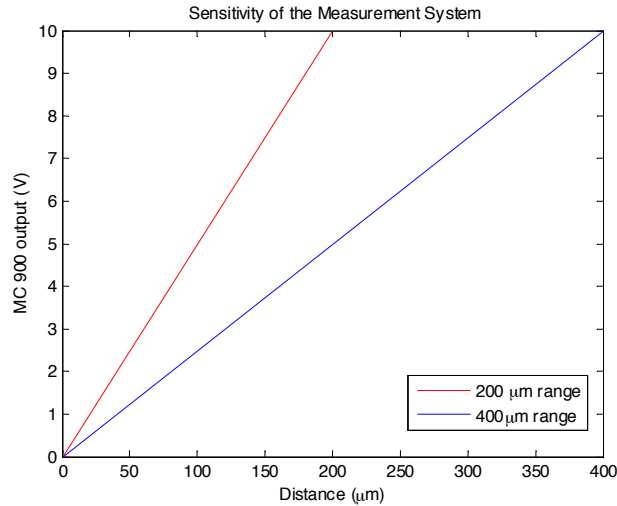
Source: Author

### 6.1.3 Model of the Complete Measurement System

Looking at the system as a whole, the distance between the sensor and the measurement target is directly proportional to the output voltage value of the MC900 modules.

The model of the BTFI Fabry-Pérot position measurement system is presented in Figure 35. The red line represents the input-output relation for the measurement system of 200  $\mu\text{m}$  distance range, and the blue line the model of the 400  $\mu\text{m}$  measurement system.

Figure 35 - Sensitivity of the Measurement System



Source: Author

## 6.2 MODEL OF THE ACTUATOR SYSTEM

The actuator system is the principal component of the Fabry-Pérot instrument, and it is also the more complex device of the system because of its high dynamics, resonant behavior and non-linear response.

It is of extreme importance to have the model of the actuator system in order to be able to understand the nature of the system and as a first step to build the model of the complete system of the Fabry-Pérot instrument.

The actuator system is composed of the actuators drivers and the piezoactuators.

As mentioned in section 3.2 two types of power drivers for the piezoactuators have been studied and developed for the BTFI Fabry-Pérots. The first one is a linear voltage driver acting like a gain of 20 in the system, developed by Cavalcanti, (2011). The second one is a driver by charge that minimizes the non-linearities of the piezoactuators, currently being developed by Marchiori et al. (2013).

The model of these three subsystems are presented in the following items.

### 6.2.1 Model of the Drivers by Voltage

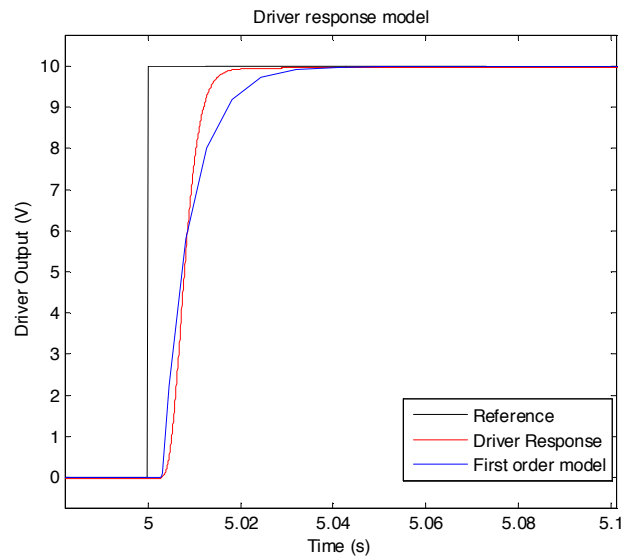
The drivers by voltage were designed by Cavalcanti (2011), and the performance specifications were to have a voltage gain of 20, a cutoff frequency of 50 Hz, and a maximum output current of 100 mA.

The step response of the driver was taken and a first order model of the form of eq.(19) was made.

$$G_{driver}(s) = \frac{20}{0.006s + 1} e^{-0.003s} \quad (19)$$

Figure 36 shows the real (red) and the model (blue) step response. The input signal of 0.5 V multiplied by the ideal gain of the system (black) is plotted for reference.

Figure 36 - Linear amplifiers first-order model



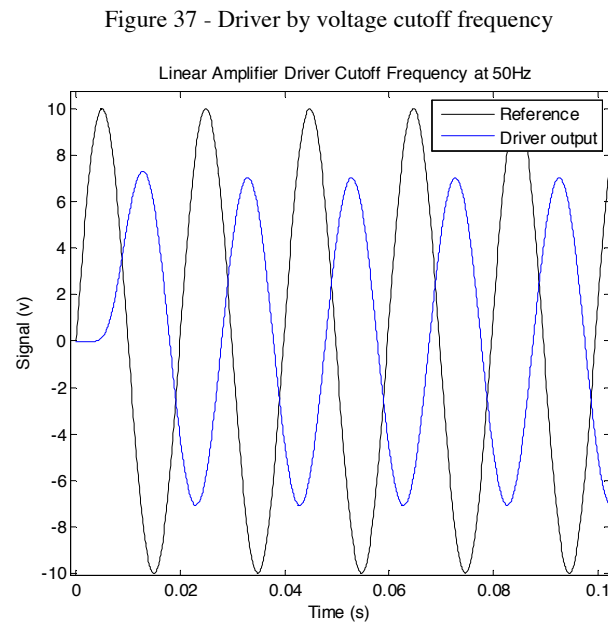
Source: Author

As can be seen in the figure, the first order model fits correctly the response time delay, the time constant (which is the time required for the output to reach 63.2% of the steady state value of the system) and the steady state value, but does not fit correctly the settling time, which in the real response is much faster than the model.

To fit the settling time parameter of the real system, the model of the driver should be of a higher order.

The cutoff frequency of a system is the frequency at which the amplitude gain decays 0.3dB of the gain in 0 Hz.

To test the cutoff frequency of the driver, a sine wave with a frequency of 50 Hz and 0.5 V of amplitude was used as input. Figure 37 shows the output of the voltage driver (blue line) and the input signal multiplied by the drivers' gain, to use as reference (in black).



Source: Author

The amplitude of the output of the driver, which was expected to be 10 V for frequencies below the cutoff frequency, was of 7.03 V, which is 70.3% of the expected amplitude at 0 Hz.

This experiment results indicate that the cut-off frequency of the driver is indeed ~50 Hz, as designed in Cavalcanti, (2011).

### 6.2.2 Model of the Drivers by Charge

A current controlling amplifier primarily modulates an actuator's velocity and not the position, handling quantitatively the charge flow between the amplifier and the actuator.

The dynamic response of the driver by charge depends directly on a relation between the amplitude of the driver input and its frequency of operation, as shown in eq.(20) (Marchiori, 2013) :

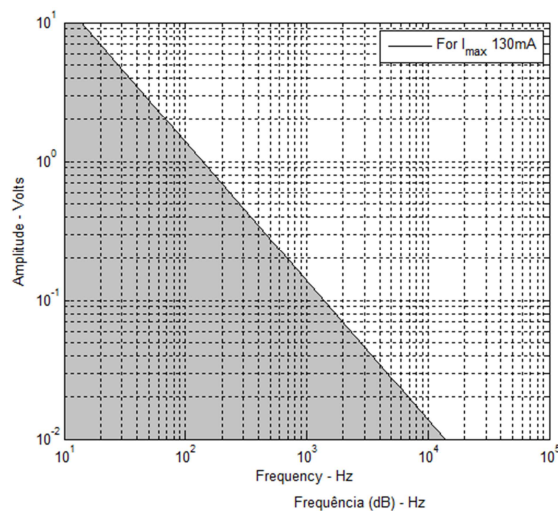
$$F = \frac{i}{2\pi C_{ref} A} \quad (20)$$

where:

- $F$  is the frequency of operation;
- $C_{ref}$  is the reference capacitor;
- $i$  is the maximum output current of the operational amplifier;
- $A$  is the input amplitude of the driver.

Figure 38 is the logarithmic representation of eq.(20) for a  $C_{ref}$  of  $150 \mu\text{F}$  and a maximum output current,  $i$ , of  $130 \text{ mA}$ .

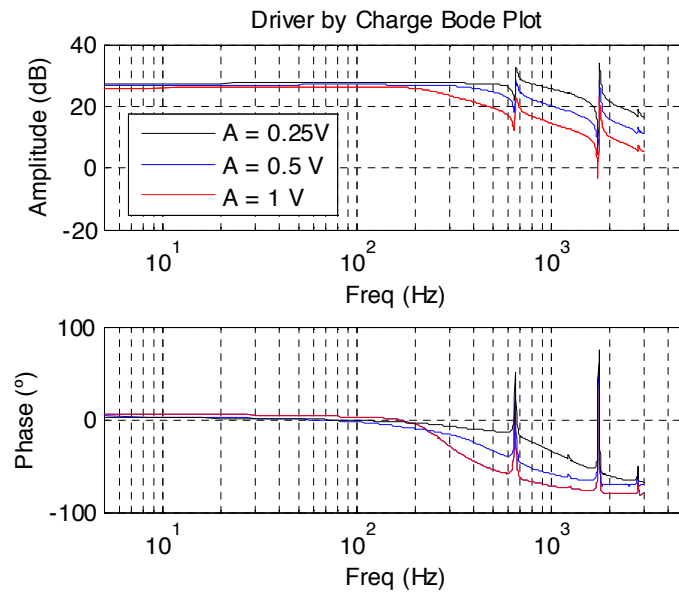
Figure 38 - Amplitude vs. Frequency operation limits of the Drivers by Charge



Source: Courtesy of Victor A. Marchiori

For the purpose of noticing this relation, the frequency response of the driver was taken for input signals of 0.25 V, 0.5 V and 1 V of amplitude using the HP 35665A DSA over a frequency range of 1 Hz to 3 kHz. The Bode Plot of these three frequency responses is shown in Figure 39.

Figure 39 - Dynamic response of the Driver by Charge



Source: Author

It can be seen that the lower the amplitude the higher the cutoff frequency of the driver. Operating the driver at higher frequencies, the output amplitude has to be very small to guarantee the linear behavior of the piezoactuator.

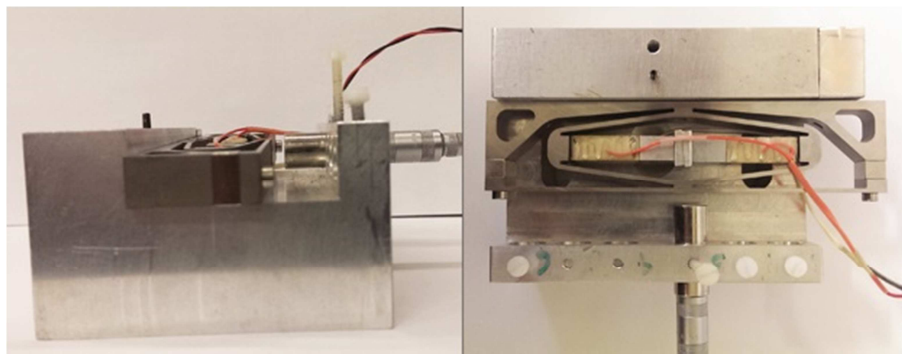
As long as the amplitude and frequency relation is respected, i.e. as long as the operation is within the colored area of Figure 36, the model of the driver by charge is just a linear gain as shown in eq.(21).

$$G_{Driver-charge}(s) = 20 \quad (21)$$

### 6.2.3 Model of the Piezoelectric Actuators

For the model of the piezoactuators, the test fixture shown in Figure 40 was set up in the laboratory. In this fixture, the piezoactuator was fixed on one side to an aluminum base, and the capacitive sensor was fixed to measure the displacement of the piezoactuator on the opposite side.

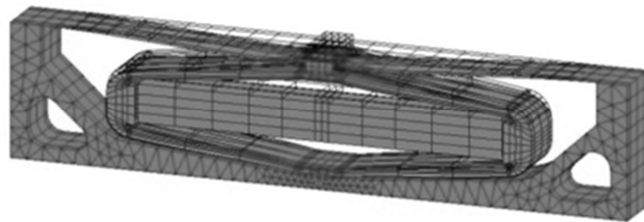
Figure 40 - Piezoactuator frequency response test mount



Source: Author

The APA400MML piezoactuators have an internal piezoelectric stack and an external mechanical amplifier structure, as shown in Figure 41.

Figure 41 - APA400MML piezoactuator structure



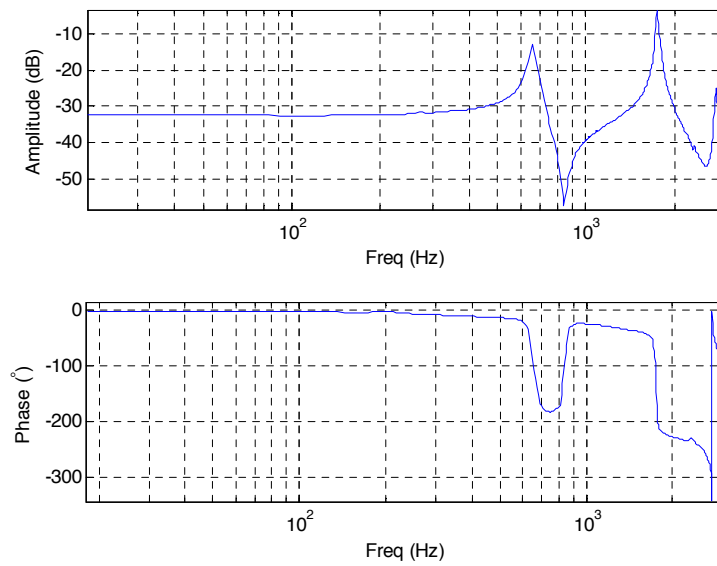
Source: Courtesy of CEDRAT Technologies

#### 6.2.3.1 Theoretical Physical Modeling

The first step to understand the nature of the system was to take the frequency response of the piezoactuator. For this purpose a dynamic signal analyzer, DSA, HP35665A was used to

make a sweep in frequency over a relatively high frequency range (1 Hz to 3000 Hz) using a sine wave signal of 1 V<sub>pp</sub> of amplitude. The Bode plot of this frequency response test is shown in Figure 42.

Figure 42 - APA400MML frequency response Bode Plot.



Source: Author

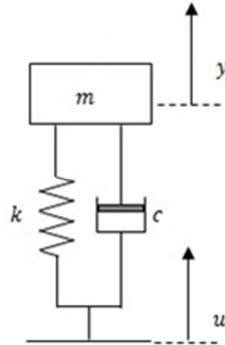
According to Adriaens et al. (2000) because of the resonant nature of the piezoactuator, it can be modeled as a mass-spring-damper system (Figure 43), and the model equation is the well-known general differential equation for the linear time invariant second order system of eq.(22).

$$m\ddot{y} + c\dot{y} + ky = c\dot{u} + ku \quad (22)$$

where:

- u*** is the piezoactuator's initial dislocation;
- y*** is the output in displacement of the FP mirror;
- m*** is the effective mass, defined in eq. (23);
- c*** is the damping coefficient, defined in eq.(24).

Figure 43 - Mass spring damper actuator model



Source: Author

The mass,  $m$ , is defined as:

$$m = \frac{k}{Wn^2} \quad (23)$$

where:

$Wn$  is the natural frequency;

$k$  is the stiffness of the piezoactuator, which is specified in the piezoactuator datasheet (CEDRAT Technologies, 2013).

The damping coefficient  $c$ , is calculated as shown in eq.(24):

$$c = 2 m \zeta Wn \quad (24)$$

where:

$\zeta$  is the damping ratio, calculated as a function of the gain ( $P$ ) of the natural frequency  $Wn$  as shown in eq.(25). Both  $P$  and  $Wn$  are inferred from the piezoactuator frequency response.

$$\zeta = \sqrt{\frac{1}{4(P^2 - 1)}} \quad (25)$$

These equations are applied to the three piezoactuators of the system; therefore  $m_1$ ,  $c_1$  and  $k_1$ , refer to these variables in piezoactuator 1;  $m_2$ ,  $c_2$  and  $k_2$  refer to the variables in piezoactuator 2; and  $m_3$ ,  $c_3$  and  $k_3$  for piezoactuator 3.

Table 13 shows the parameter values for the APA400MML piezoactuators.

Table 13 Fabry-Perót piezoactuators parameter values

	<b>APA400MML</b>
<b><i>m</i></b>	0.0262 kg
<b><i>k</i></b>	520000 N/m
<b><i>c</i></b>	47.342 N/m/s
<b><i>W<sub>n</sub></i></b>	660 Hz
<b><i>P</i></b>	-13 dB

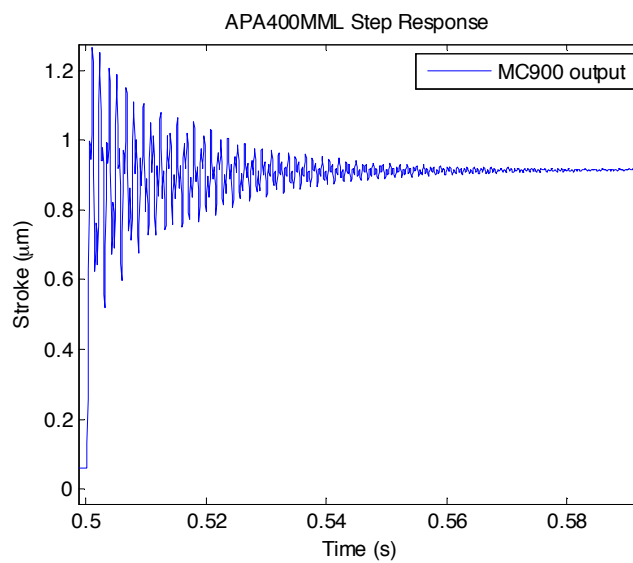
Figure 44 shows the step response of the APA400MML piezoactuator, after filtering the electronic noise. This process was done taking the mean of 10000 step responses.

A small time delay  $\tau$  was introduced to the model to fit better the phase curve and the step response of the real response of the piezoactuator of Figure 42 and 44.

After Laplace transformation of eq.(22) the transfer function of the model of the piezoactuator, with the identified time delay,  $\tau$ , can be written as eq.(26).

$$G_{piezo}(s) = \frac{cs + k}{ms^2 + cs + k} e^{-\tau s} \quad (26)$$

Figure 44 - APA400MML step response



Source: Author

### 6.2.3.2 Gray Box Identification

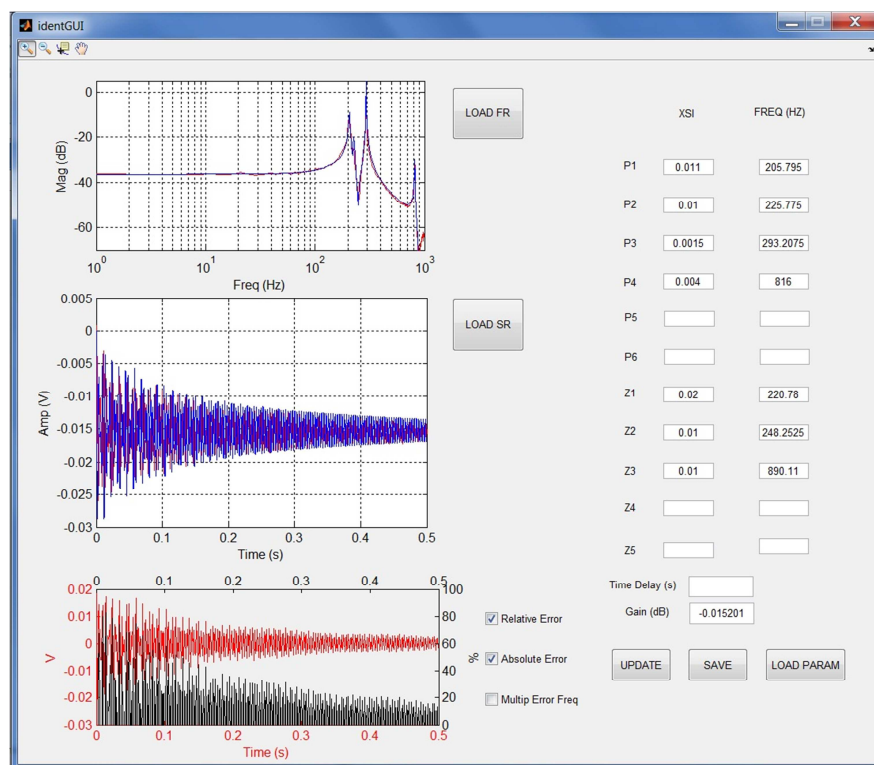
Besides making a parametric physical model, another approach for the model of the piezoactuator system was done using a gray box identification method.

System identification consists in taking a real response of the plant to a known input and creating a transfer function that delivers the same output, even though the structure of the transfer function does not provide full understanding of the physical process.

There are several methods to identify a system, and taking advantage of a known resonant behavior of the system, a grey box model was constructed for the piezoactuators, using a graphical user interface developed for this project.

The Graphical User Interface, shown in Figure 45, was built using the GUIDE tool of MATLAB.

Figure 45 - Gray box identification graphical user interface



Source: Author

With this interface, the amplitude Bode plot of the frequency response of the piezoactuator is loaded and plotted in the upper figure. Below the Bode Plot, in the middle of the interface, the step response of the piezoactuator is plotted.

The transfer function of the identified model is the product of uncoupled second-order transfer functions, whose natural frequencies and damping ratios,  $Wn$  and  $\zeta$  are the parameters that the user inputs in the boxes on the right side of the interface.

The form of the model depends on if it is a model for a resonant peak or a valley in the frequency response.

To fit the resonant peak behavior, the transfer function is of the form of eq.(27):

$$P_i(s) = \frac{Wn_i^2}{s^2 + 2\zeta_i Wn_i s + Wn_i^2} \quad (27)$$

where:

- $P_i$  is the name of the transfer function, whose parameters are defined in the corresponding row in the right side of the interface;
- $Wn$  is the frequency of the peak;
- $\zeta$  is the damping ratio of the peak.

On the other hand, to fit a resonant valley behavior, the transfer function is of the form of eq.(28):

$$Z_k = \frac{(s^2 + 2\zeta_k Wn_k s + Wn_k^2)}{Wn_k^2} \quad (28)$$

where:

- $Z_k$  is the name of the transfer function, whose parameters are defined in the corresponding row in the right side of the interface.

The user has also the possibility to adjust the time delay  $\tau$  and the gain  $Gain$  of the transfer function, in the last input boxes on the interface.

The transfer function of the identified model of the piezoactuators is the multiplication of the mentioned components and it takes the form of eq.(29):

$$G_{piezo}(s) = Gain \left( \prod_i P_i(s) \prod_k Z_k(s) \right) e^{-\tau s} \quad (29)$$

The number of zeros, or  $k$ , is limited to maximum  $i$  minus 1, to guarantee that the final transfer function of the piezoactuator model is strictly proper, *i.e.*, that the degree of the numerator is lower than the degree of the denominator.

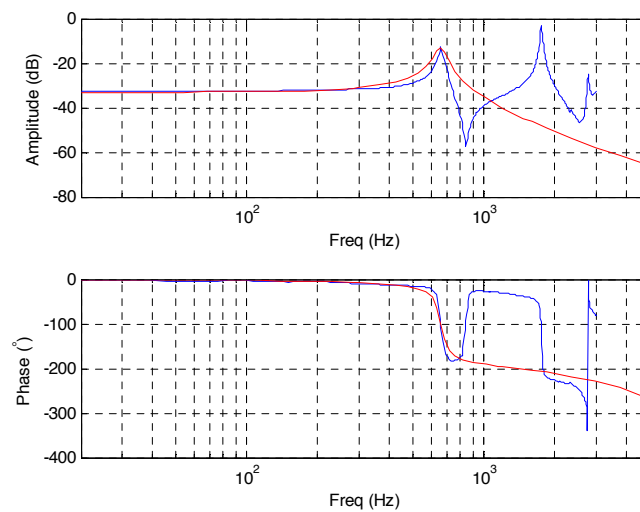
The amplitude Bode plot and the step response of the  $G_{Actuator}(s)$  model is plotted on the same axis of the real response of the piezoactuator, and analyzing the fit of the model to the real system, the user can vary the parameters until the error is reasonable small.

The last plot of the interface, in the bottom left, is an error analysis. The user can choose to see the absolute or relative error between the real system and model step response, and it has also the choice to plot the multiplicative modeling error in terms of the frequency.

### 6.2.3.3 Simulation Results of the Piezoelectric Actuators Model

The experimental validation of the Piezoelectric Actuators Model was done taking the frequency response of the system, presented in Figure 42 and comparing it to the model frequency response. Figure 46 shows the frequency response of one of the piezoactuators (in blue) and of the second-order parametric model (in red).

Figure 46 - Piezoactuator parametric model frequency response validation



Source: Author

The transfer function of the second order parametric model of the piezoactuator is presented in eq.(30).

$$G_{piezo}(s) = \frac{12.49 s + 4.257e5}{s^2 + 557.9 s + 1.901e7} \quad (30)$$

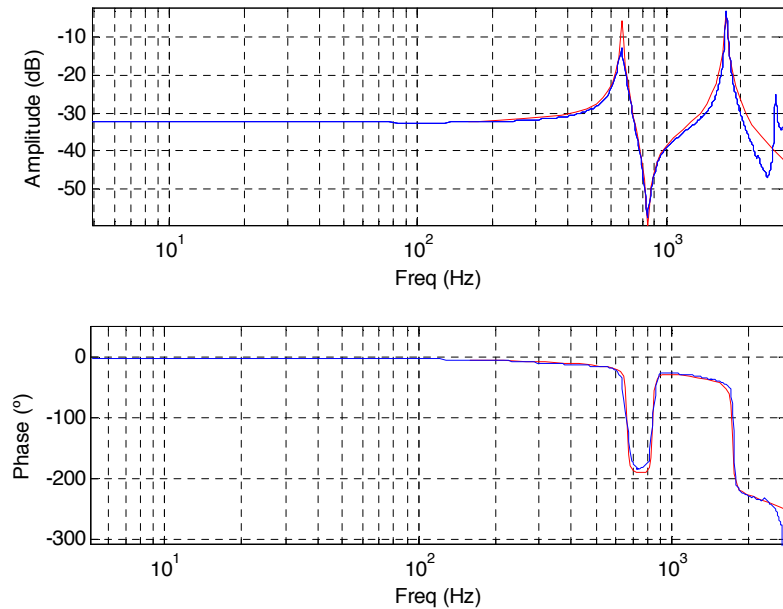
The second-order model approach only fits the first resonant peak, while experimental results (solid blue line) indicate that there are more peaks and valleys in between every two peaks.

On the other hand, Figure 47 shows the frequency response of the identified model, which is a fourth-order model whose transfer function is as eq.(31).

$$G_{piezo}(s) = \frac{1.798e6 s^2 + 1.898e8 s + 5.008e13}{s^4 + 302.2 s^3 + 1.37e8 s^2 + 1.381e10 s + 2.087e15} e^{-7e-5s} \quad (31)$$

The fourth-order identified model fits the first two resonant peaks and the first valley.

Figure 47 - Piezoactuator identified model frequency response validation



Source: Author

### 6.3 MODEL OF THE COMPLETE SYSTEM

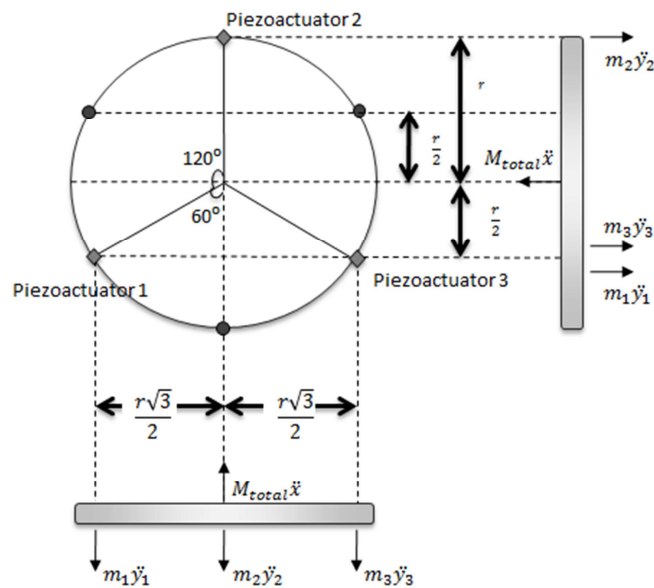
A sixth-order parametric model for the Fabry-Pérot system, which is composed of three piezoactuators coupled with the mirror mass, was built on top of the previously presented second-order parametric model for the piezoactuator.

The input of the multiple input multiple output, MIMO, system are the dislocations of the base of the three piezoactuators,  $u_1$ ,  $u_2$  and  $u_3$ , and the outputs are the measurement of the capacitive sensors,  $s_{12}$ ,  $s_{23}$ ,  $s_{13}$ , all of them in Volts.

#### 6.3.1 Theoretical Development

The model, developed by one of the team members, Dr. Fernando Orsatti, considers the system as a rigid disk of mass,  $m_{mirror}$ , and radius,  $r$ , upon which several forces actuate. The forces come from the three piezoactuators which are located in different points on the disk, as Figure 48 shows. As the output of the system is measured on the sensors and not in the center of the disk, the geometrical position of the sensors, whose measurement targets are placed at 60 degrees from each of the piezoactuators, must also be considered.

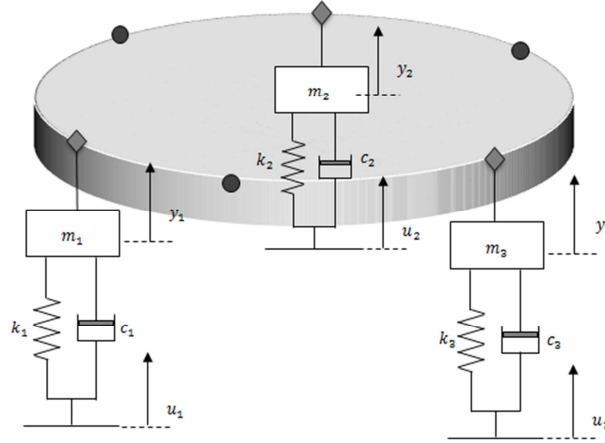
Figure 48 - Physical distribution of the components of the FP and related forces



Source: Courtesy of Dr. Fernando Orsatti

The graphical representation of the system is shown in Figure 49.

Figure 49 - Model of the Fabry-Perót complete system



Source: Author

The total mass of the system is the sum of the masses of the mirror plate and the effective masses of the piezoactuators second order model, as stated in eq.(32).

$$M_{total} = m_{mirror} + m_1 + m_2 + m_3 \quad (32)$$

where:

$m_{mirror}$  is the mass of the moving mirror of the Fabry-Pérot;  
 $m_1$ ,  $m_2$  and  $m_3$  are the masses of the model of each piezoactuator, defined as in eq.(23).

Taking  $x$  as the total displacement of the center of the mirror plate, the force-balance equation of eq.(22) results in eq.(33) when considering the forces of the three piezoactuators.

$$M_{total}\ddot{x} = -k_1y_1 - k_2y_2 - k_3y_3 - c_1\dot{y}_1 - c_2\dot{y}_2 - c_3\dot{y}_3 + k_1u_1 + k_2u_2 + k_3u_3 + c_1\dot{u}_1 + c_2\dot{u}_2 + c_3\dot{u}_3 \quad (33)$$

where:

$k_1$ ,  $k_2$  and  $k_3$  are the corresponding stiffness of each of the three piezoactuators;  
 $c_1$ ,  $c_2$  and  $c_3$  are the corresponding damping coefficients of each of the three piezoactuators as defined in eq.(24).

The values of the parameters of the piezoactuators are found on Table 19. All the piezoactuators present similar dynamic response and have the same physical characteristics.

The moment of force for the plate in the  $y$  axis  $I_y \ddot{\theta}_y$  is:

$$I_y \ddot{\theta}_y = -[k_1(y_1 - u_1) + c_1(\dot{y}_1 - \dot{u}_1)] \frac{r\sqrt{3}}{2} + [k_3(y_3 - u_3) + c_3(\dot{y}_3 - \dot{u}_3)] \frac{r\sqrt{3}}{2} \quad (34)$$

where:

$r$  is the radius of the mirror plate, which is 0.06 m.

Similarly, the moment of force for the plate in the  $z$  axis  $I_z \ddot{\theta}_z$  is:

$$I_z \ddot{\theta}_z = -[k_1(y_1 - u_1) + c_1(\dot{y}_1 - \dot{u}_1)] \frac{r}{2} + [k_2(y_2 - u_2) + c_2(\dot{y}_2 - \dot{u}_2)] r - [k_3(y_3 - u_3) + c_3(\dot{y}_3 - \dot{u}_3)] \frac{r}{2} \quad (35)$$

The distance output in the location of the capacitive sensors measurement targets:

$$s_{12} = x + \theta_y \frac{r\sqrt{3}}{2} - \theta_z \frac{r}{2} \quad (36)$$

$$s_{23} = x - \theta_y \frac{r\sqrt{3}}{2} - \theta_z \frac{r}{2} \quad (37)$$

$$s_{13} = x + \theta_z r \quad (38)$$

Finally, the space state representation is given by eq.(39) and eq.(40). The result is a linear and time-invariant (LTI) model with 3 controls or inputs, 3 outputs and 6 state variables.

$$\dot{\mathbf{x}}(t) = \mathbf{A}\mathbf{x}(t) + \mathbf{B}\mathbf{u}(t) \quad (39)$$

$$\mathbf{y}(t) = \mathbf{C}\mathbf{x}(t) \quad (40)$$

where:

$\mathbf{x}$  is called the "state vector",  $\mathbf{x}(t) \in \mathbb{R}^6$  defined by:

$$\begin{aligned} x_1 &= x \\ x_2 &= \dot{x} - \frac{c_1}{M_{total}} * u_1 - \frac{c_2}{M_{total}} * u_2 - \frac{c_3}{M_{total}} * u_3 \\ x_3 &= \theta_y \\ x_4 &= \dot{\theta}_y - c_1 * r * \frac{\sqrt{3}}{2Iy} * u_1 + c_3 * r * \frac{\sqrt{3}}{2Iy} * u_3 \\ x_5 &= \theta_z \\ x_6 &= \dot{\theta}_z - c_1 * \frac{r}{2Iz} * u_1 + c_2 * \frac{r}{Iz} * u_2 - c_3 * \frac{r}{2Iz} * u_3 \end{aligned}$$

$\mathbf{y}$  is called the "output vector",  $\mathbf{y}(t) \in \mathbb{R}^3$  and is defined by:

- $y_1$ : Dislocation on the base of piezoactuator 1.
- $y_2$ : Dislocation on the base of piezoactuator 2.
- $y_3$ : Dislocation on the base of piezoactuator 3.

$\mathbf{u}$  is called the "input vector",  $\mathbf{u}(t) \in \mathbb{R}^3$  and is defined by:

- $u_1$ : Dislocation on the base of piezoactuator 1.
- $u_2$ : Dislocation on the base of piezoactuator 2.
- $u_3$ : Dislocation on the base of piezoactuator 3.

$\mathbf{A}$ ,  $\mathbf{B}$  and  $\mathbf{C}$  are the space state matrices, defined in the following equations. The computed values using the parameter values of Table 19 are shown for reference.

$$A = \begin{bmatrix} 0 & 1 & 0 & 0 & 0 & 0 & 0 \\ -\frac{k_1+k_2+k_3}{M} & -\frac{c_1+c_2+c_3}{M} & \frac{k_1-k_3\sqrt{3}}{M} & \frac{k_1-k_2+\frac{k_3}{2}}{M} & \frac{k_1-k_2+\frac{k_3}{2}}{M} & \frac{c_1-c_2+\frac{c_3}{2}}{M} & 0 \\ 0 & 0 & 0 & 0 & 0 & 0 & 0 \\ -\frac{k_1-k_3}{Iy} & -\frac{c_1-c_3}{Iy} & \frac{c_1+c_3\sqrt{3}}{Iy} & \frac{k_1+k_3}{Iy} & \frac{k_1-k_3\sqrt{3}}{Iy} & \frac{c_1-c_3}{Iy} & \frac{c_1-c_3\sqrt{3}}{Iy} \\ 0 & 0 & 0 & 0 & 0 & 0 & 0 \\ -\left(\frac{k_1-k_2+k_3}{2}\right) & -\left(\frac{c_1-c_2+c_3}{2}\right) & -\frac{k_1-k_3}{Iz} & -\frac{k_1-k_3}{Iz} & -\frac{k_1-k_3}{Iz} & -\frac{c_1-c_3}{Iz} & -\frac{c_1-c_3}{Iz} \end{bmatrix} \quad (41)$$

$$A = \begin{bmatrix} 0 & 1 & 0 & 0 & 0 & 0 & 0 \\ -1.7294e6 & -55.3284 & 0 & 0.2495 & 0 & -0.1570 & 0 \\ 0 & 0 & 0 & 1 & 0 & 0 & 0 \\ 0 & 298.0885 & -3.7198e6 & -124.6354 & 0 & 8.9427 & 0 \\ 0 & 0 & 0 & 0 & 0 & 0 & 1 \\ 0 & -187.6080 & 0 & 8.9427 & -3.7198e6 & -113.3789 & 0 \end{bmatrix}$$

$$B = \begin{bmatrix} -\frac{c_1+c_2+c_3}{M} & \frac{c_1}{M} & \frac{\sqrt{3}}{Iy} & \frac{c_1-c_2+c_3}{M} & \frac{c_1-c_2+c_3}{M} & \frac{c_1-c_2+c_3}{M} & \frac{c_3}{M} \\ c\alpha r \frac{\sqrt{3}}{Iy} & 0 & 0 & 0 & 0 & 0 & 0 \\ \frac{c_1-c_3}{Iy} & -\frac{c_1+c_3}{Iy} & \frac{c_1+c_3\sqrt{3}}{Iy} & \frac{c_1-c_3}{Iy} & \frac{c_1-c_3}{Iy} & \frac{c_1-c_3}{Iy} & \frac{c_1-c_3}{Iy} \\ -\frac{c_1-c_2+c_3}{Iz} & \frac{c_1}{Iz} & \frac{\sqrt{3}}{Iy} & \frac{c_1+c_2+c_3}{Iz} & \frac{c_1+c_2+c_3}{Iz} & \frac{c_1+c_2+c_3}{Iz} & \frac{c_3}{Iz} \end{bmatrix} \quad (42)$$

$$B = \begin{bmatrix} -1.5147e-5 & -1.4953e-5 & -1.9446e-5 \\ -0.5155 & -0.5156 & -0.5153 \\ -9.4050e-4 & 0 & -0.0012 \\ -31.9453 & 0.0051 & 32.0282 \\ -5.4300e-4 & 0.0011 & -6.9711e-4 \\ -18.4499 & 36.8930 & -18.4340 \end{bmatrix}$$

$$C = \begin{bmatrix} 1 & 0 & \frac{\sqrt{3}}{2} & 0 & -\frac{r}{2} & 0 \\ 1 & 0 & -\frac{\sqrt{3}}{2} & 0 & -\frac{r}{2} & 0 \\ 1 & 0 & 0 & 0 & r & 0 \end{bmatrix}$$

(43)

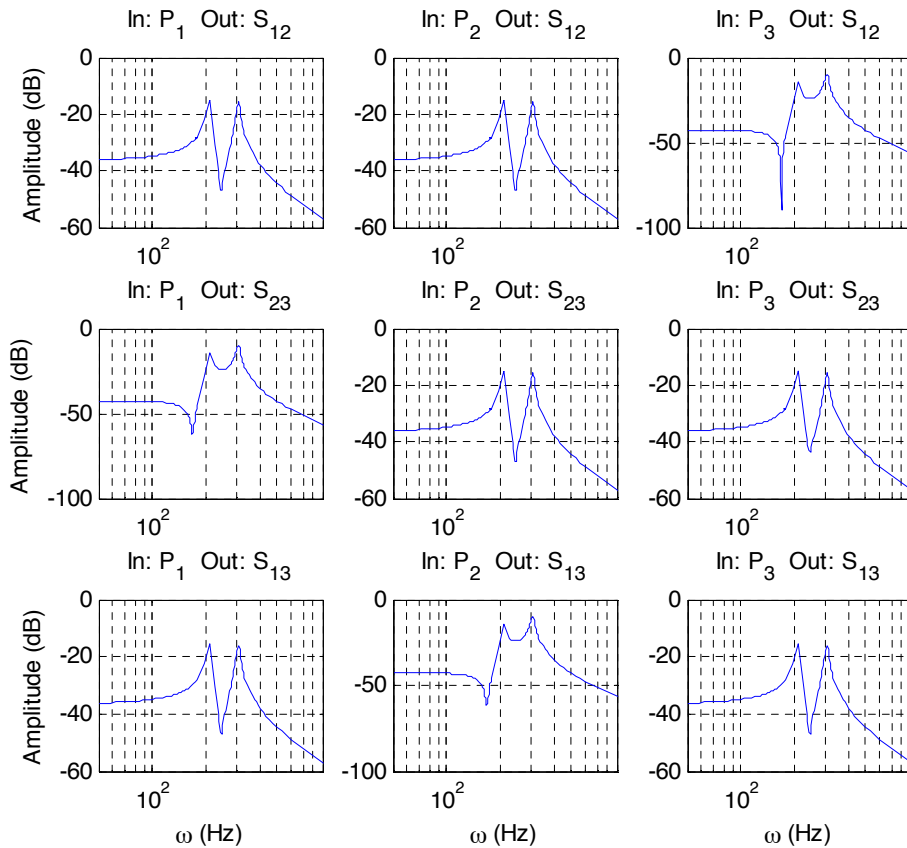
$$C = \begin{bmatrix} 2.5e4 & 0 & 1.299e3 & 0 & -750 & 0 \\ 2.5e4 & 0 & -1.299e3 & 0 & -750 & 0 \\ 2.5e5 & 0 & 0 & 0 & 1.5e3 & 0 \end{bmatrix}$$

### 6.3.2 Gray Box System Identification

As with the modeling of the piezoactuators, the GUI for Gray Box Identification was used to identify the model the complete system of the Fabry-Pérot system.

The frequency response for each input and output combination was taken using the DSA HP35665A over the frequency range of interest (1 Hz-1000 Hz) that resulted in a total of nine frequency response data sets. Figure 50 shows the nine amplitude Bode plots of all the possible input directions.  $P_1$ ,  $P_2$ ,  $P_3$  represent the input entering only on piezoactuator 1, piezoactuator 2 and piezoactuator 3, respectively. And  $S_{12}$ ,  $S_{23}$  and  $S_{31}$  represent the output in the sensors located between  $P_1$  and  $P_2$ ,  $P_2$  and  $P_3$  and  $P_1$  and  $P_3$ , respectively.

Figure 50 - Fabry-Pérot input-output combination amplitude Bode plot



Source: Author

With this frequency response data, the IdentGUI interface of Figure 45 was used to identify the transfer function of all of the nine responses, ending up with a 3x3 matrix of transfer functions that make up the identified model of the Fabry-Pérot system as shown in eq.(44)

$$G(s) = \begin{bmatrix} G_{11} & G_{12} & G_{13} \\ G_{21} & G_{22} & G_{23} \\ G_{31} & G_{32} & G_{33} \end{bmatrix} \quad (44)$$

where:

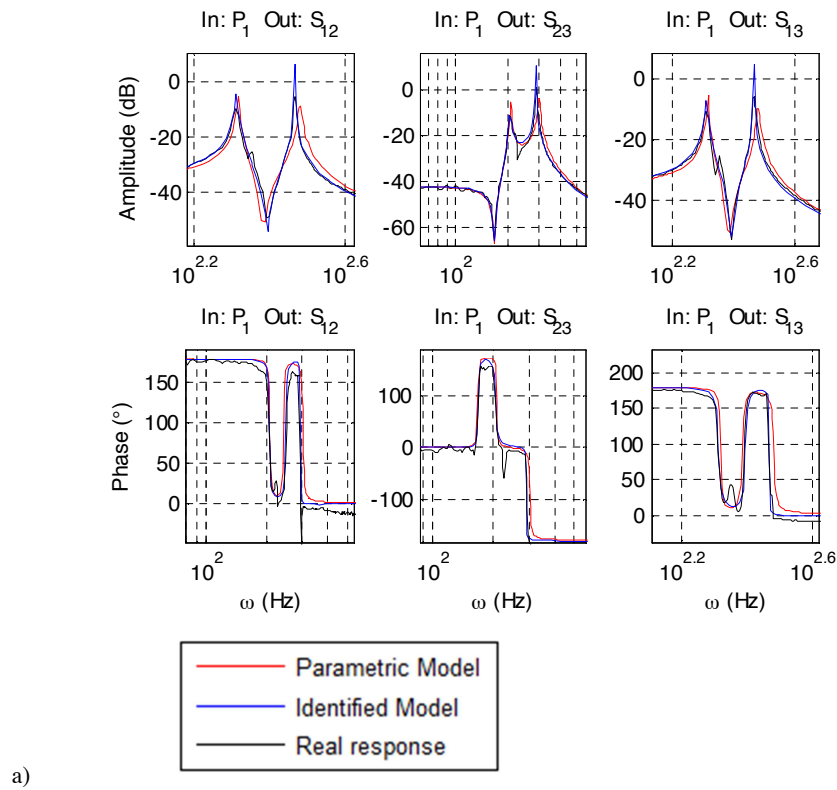
$G$  represents the nominal model of the Fabry-Pérot system;  
 $G_{11}, G_{12}, G_{13}, G_{21}, G_{22}, G_{23}, G_{31}, G_{32}, G_{33}$  represent the transfer function from every input/output combination on the three channel system, where the first index represents the output and the second index the input

### 6.3.3 Simulation and Validation Results of the Fabry-Pérot System Model

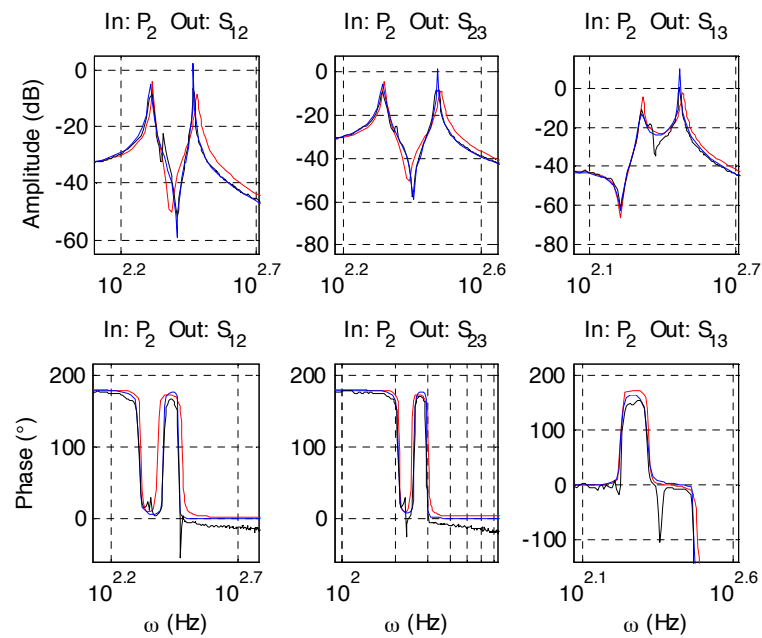
The experimental validation of the Fabry-Pérot system model was done by taking the frequency response of the system, for every input and output combination, and then comparing it to the model frequency response.

Both model approaches, parametric and identified models, are compared against the real frequency response of every channel of the system. Figure 50 shows the resulting nine Bode plots for the Fabry-Pérot system. The real response is plotted in black, the parametric model is plotted in red and the identified model is plotted in blue. The title of each Bode Plots indicate the piezoactuator where the input was ( $P_1, P_2, P_3$ ) and the name of the sensor that measured the output ( $S_{12}, S_{23}, S_{13}$ )

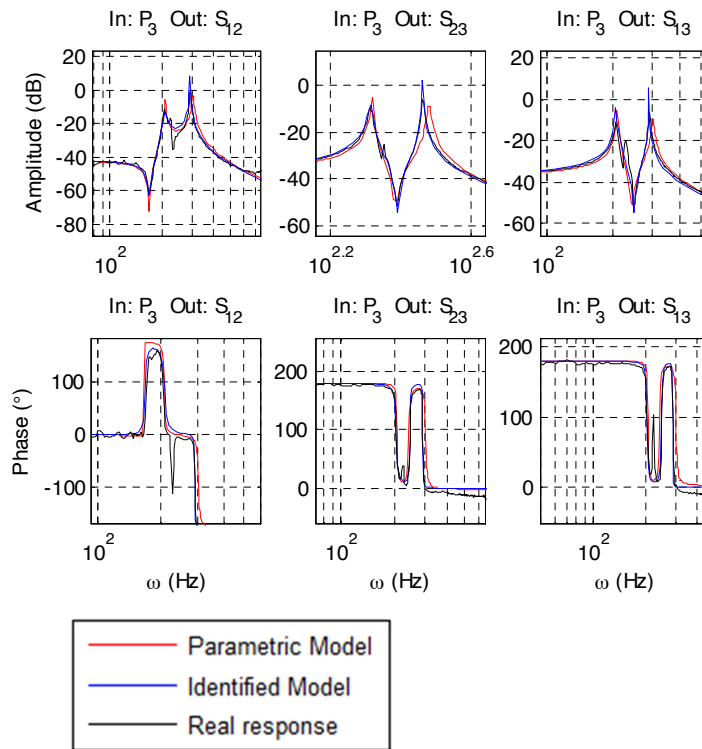
Figure 51 - Frequency Response of the real Fabry-Pérot system and models. A. System output when input direction is in piezoactuator 1. B. System output when input direction is in piezoactuator 2. C. System output when input direction is in piezoactuator 3



a)



b)



c)

Source: Author

Similar to the results on the simulations of the piezoactuator model, the identified model is a better fitting to the real response of the system.

The main disadvantage of using high-order models is that they are more expensive to compute and is directly related to the order of the controller to be designed. Besides it is more interesting for the project to have a parametric model developed using an equivalent physical model that enriches the understanding of the system than to have an identified transfer function that says little about the physical properties of the system.

### 6.3.4 Singular Values of the Fabry-Pérot System

The singular values of the frequency response extend the Bode magnitude response for MIMO systems and are useful in robustness analysis. They are defined as in eq.(45) (Cruz, 1996):

$$\sigma_i(G) = \sqrt{\lambda_i(G^H G)} \quad i = 1, 2, \dots, m \quad (45)$$

where:

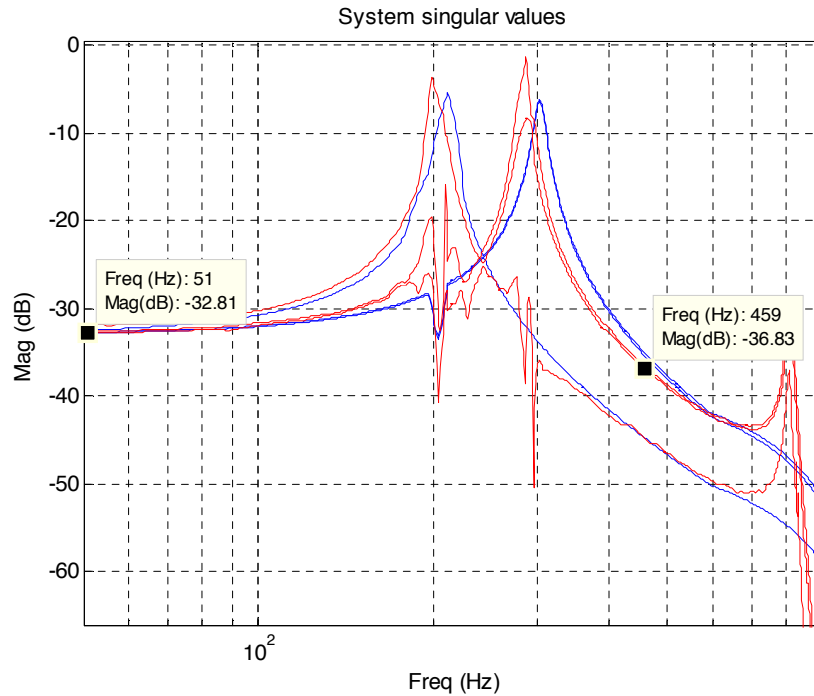
$G$  is the nominal model of the system;  
 $\lambda_i$  is the group of eigenvalues of the system.

The maximum singular value  $\sigma_M(G)$  is known as the spectral norm and is equal to the norm of the matrix  $G$ , as shown in eq.(46).

$$\sigma_M(G) = \|G\| \quad (46)$$

Figure 52 shows the singular values of the Fabry-Pérot system. The red line represents the singular values calculated from the acquired data of the real system. The blue line represents the singular values of the parametric model of the Fabry-Pérot.

Figure 52 - Fabry-Pérot system real response and parametric model singular values



Source: Author

The singular values of a MIMO system is the extended representation of the SISO Magnitude Bode Plot. The cut-off frequency of the MIMO system can be inferred from this diagram.

Taking the frequency at which the gain of the system in 0 Hz decays -3dB, the datatips on the singular values plot show the cutoff frequency of the system at 450 Hz. This is the frequency at which the physical gain of the complete systems starts to decay and should be the maximum frequency of the control system if a total control against all kinds of perturbations is desired.

### 6.3.5 Modeling Error of the Fabry-Pérot Model

Comparing the acquired frequency response data of the real system with the frequency response of the built model, for every input and output combination of the Fabry-Pérot system, it is possible to calculate the modeling error  $EM$ , using the following multiplicative error formula:

$$EM(s) = [G_R(s) - G_N(s)]G_N(s)^{-1} \quad (47)$$

$$e_M(w) = \|EM(s)\|$$

where:

$G_R$  is the transfer function of the real plant;

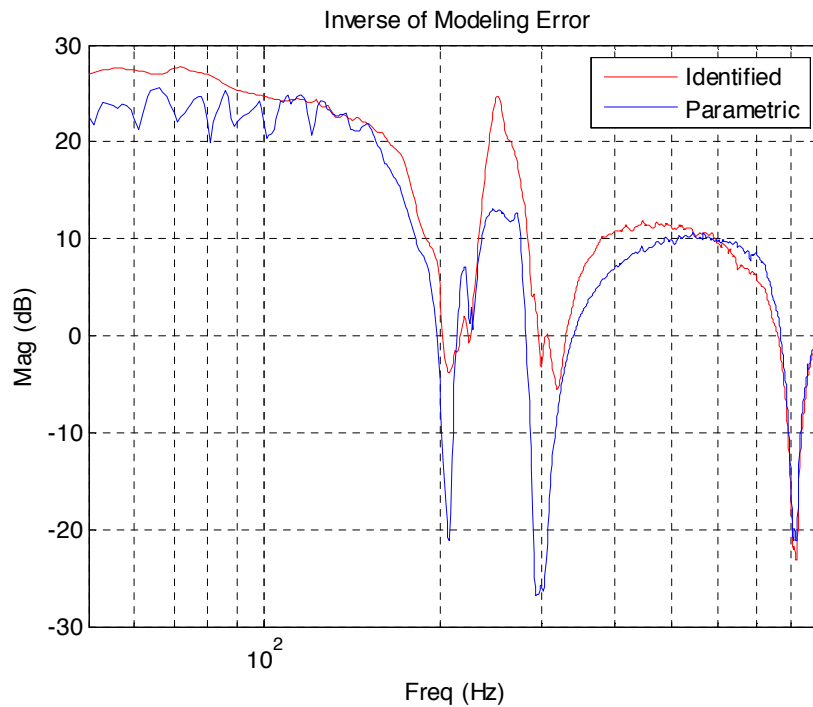
$G_N$  is the nominal model of the system;

$w$  represent all the frequency points acquired with the digital signal analyzer.

This representation for the error was adopted because it describes the modeling error of the plant transfer function, as well as the error in the loop transfer function, reflected in the output of the plant. (Cruz, 1996).

Figure 53 shows the inverse of this modeling error for the parametric and identified model of the complete system. This representation helps infer how well the model represents the system as a function of the frequency and is also needed for the LQG/LTR design method, which will be presented in section 9.

Figure 53 - Inverse of the modeling error of the parametric and identified models of the Fabry-Pérot system



Source: Author

It is interesting to note in the figure, that the higher modeling errors values correspond to the resonant frequencies of the complete system, located at the  $\sim 200$  Hz and  $\sim 300$  Hz.

The modeling error limits the bandwidth of the control system and therefore limits the performance of the compensator.

## 7 CONTROL PROBLEM OF THE FABRY-PÉROT INTERFEROMETER

### 7.1 OPERATION MODES

The objective of the Fabry-Pérot instrument is to acquire the light of the studied object in different wavelengths to analyze the emission and absorption lines of the object in a frequency range of the spectrum. For this purpose a sweep of this determined region of the spectrum must be done. First the Fabry-Pérot etalon distance must be *positioned* to a predefined wavelength and then, starting from this point the instrument *scans* the range of wavelengths.

Therefore, two operation modes are defined for the Fabry-Pérot interferometer: Positioning and Spectral Scanning.

Both operation modes can be interpreted as going from one distance point to another, but the main difference is that when positioning it can be done through a single step and in spectral scanning it is done in several small steps.

The positioning mode has the following performance restrictions. The transient response cannot present overshoot, to maximize the working distance of the interferometer and as a security measure when working in the distance limits of the actuator, because if the two mirrors of the interferometer touch each other they will glue. Also, once it has achieved the positioning distance, it must have a maximum steady-state error noise of 3 nm RMS.

On the other hand, the spectrum scan consists in going between one position to another, and going the way back, in a sequence of ladders as Figure 54 shows. The scanning parameters are defined by the astronomers according to the scientific applications.

$d_0$  is the initial positioning distance of the FP etalon.

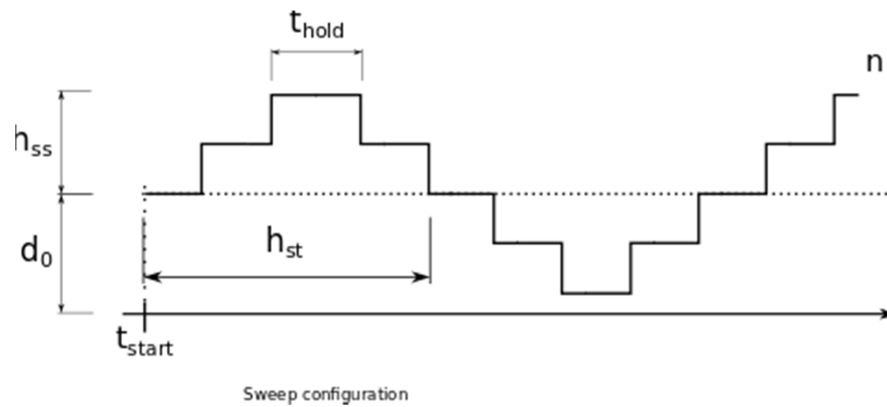
$h_{ss}$  is the half of the total gap that it is intended to be scanned.

$t_{hold}$  is the time each step must acquire steady-state data.

$h_{st}$  is the time it takes to scan half the total gap.

$n$  is the total steps in the sweep.

Figure 54 - Scanning mode graphical representation and parameters



Source: Author

The performance specifications for the spectral sweep are mainly that it has to be done fast enough to do several gap sweeps, but always guaranteeing the minimum steady-state resolution of 3 nm. This resolution specification implies driving the piezoactuators at high frequency and low current.

## 7.2 CHARACTERIZATION OF THE CONTROL PROBLEM

According to the specifications given by the scientific team of the BTFI instrument the technical characteristics of the Fabry-Pérot instrument are:

- Minimum gap of the Fabry-Pérot etalon  $200 \mu\text{m}$ .
- Minimum gap of the high resolution Fabry-Pérot etalon  $400 \mu\text{m}$ .

The performance specifications for the feedback control system in both operation modes are:

1. Follow the reference, small steps or ramp signals.
2. Null steady-state average error.
3. Steady state maximum standard deviation of 3 nm rms.
4. Reject disturbances on the telescope environment.
5. No overshoots on the transient response.

## 8 CHARACTERISTICS OF THE DIGITAL SYSTEM

The digital system that hosts the controller algorithm works with digital signals which are translated into analog signals to the system instrumentation using analogue-to-digital converters (ADC) and digital-to-analogue converters (DAC), in a dual process called digitalization.

In the Fabry-Pérot system, the resolution of the acquisition system determines the minimum resolution of the positioning system, which is the performance specification with highest impact in the instrument. Therefore it is of extreme importance to define the minimum resolution of the digital control system.

It is the aim of this chapter to present the definition of the minimum number of bits of the analog to digital converters, the minimum frequency at which the control system must operate and the sampling frequencies of the subsystems of the Fabry-Pérot.

The limitations of the current digital system comprised by the NI-DAQ 6221 data acquisition boards are also presented.

### 8.1 ANALOG-TO-DIGITAL CONVERTER RESOLUTION

The ADCs are specified in terms of their measurement range (MR), and number of bits (M). The number of discrete levels (N) is as defined in eq.(48) (National Instruments, 2006). The resolution of the converter refers to the minimum step between levels, and is equal to the measurement range divided by the number of discrete levels.

$$N = 2^M \tag{48}$$

where:

- $N$  is the number of discrete levels;
- $M$  is the number of bits of the converter.

Equation 49 shows the ADC voltage resolution, which is a relation between the ADC measurement range,  $ADC_{MR}$ , and its discrete levels.

$$ADC_{res} = \frac{ADC_{MR}}{2^M} \quad (49)$$

### 8.1.1 Fabry-Pérot ADC and DAC Minimum Resolution

The scientific specification for the instrument resolution of the complete Fabry-Pérot system is 3 nm as stated in eq.(50).

$$\sigma_{Total} = 3nm \quad (50)$$

The total noise of the system is the sum of the resolution of the analog-to-digital converters, the noise of the drivers of the piezoactuators and the resolution of the FOGALE measurement system, as presented in section 4.7. Since the main source of the measurement noise comes from the measurement system, one can separate the sources of the noise into two groups, the FOGALE system noise contribution and the contribution from the rest subsystems of the instrument, as presented in eq.(51)

$$\sigma_{Total} = \sqrt{\sigma_{FOGALE}^2 + \sigma_{others}^2} \quad (51)$$

And because the FOGALE measurement system noise is the main source, it has to be guaranteed that the other noise sources will not have a significant contribution to the total noise of the system, respecting the relation of eq.(52).

$$\sigma_{others}^2 \ll \sigma_{FOGALE}^2 \quad (52)$$

To guarantee the low contribution of noise from such other subsystems (drivers and analog-to-digital converters) the square of the noise these other systems is limited to two orders of magnitude smaller than the FOGALE maximum noise, as defined in eq.(53).

$$\sigma_{others}^2 = 0.01 \sigma_{FOGALE}^2 \quad (53)$$

$$\sigma_{others} = 0.1 \sigma_{FOGALE}$$

The analog-to-digital converter must then be specified to have a resolution 10 times smaller than the complete system noise, as specified in eq.(54).

$$ADC_{res} = 0.3 \text{ nm} \quad (54)$$

The distance measurement range of the ADC for both Fabry-Pérots is as defined on eq.(55):

$$FP1 \text{ } ADC_{MR} = 400e3 \text{ nm} \quad (55)$$

$$FP2 \text{ } ADC_{MR} = 200e3 \text{ nm}$$

Finally, eq.(56) shows the minimum number of bits (M) that the digital system of FP1 and FP2 should have. This value was found using eq.(50) and the respective converter resolution and measurement range defined on eq.(54) and eq.(55).

$$FP1 \text{ } ADC_M = 19.4 \text{ bits} \quad (56)$$

$$FP2 \text{ } ADC_M = 20.4 \text{ bits}$$

Considering that the DAC has an output voltage range that will cause the same stroke on the piezoactuators that the ADC will measure, and it must have the same distance resolution, one can define the resolution and measurement range of the DAC equal to the ADC. The number of bits for the DAC is then the same number of bits than the ADC, as defined in eq.(57).

$$FP1 \text{ } DAC_M = 19.4 \text{ bits} \quad (57)$$

$$FP2 \text{ } DAC_M = 20.4 \text{ bits}$$

### 8.1.2 NI-DAQ ADC and DAC Resolution

The National Instruments Data Acquisition board NI-DAQ 6221 has an ADC and DAC of 16 bits and a configurable resolution according to the measurement range configuration.

Because the output of the MC900 is within the range [0 to 10] V, the resolution of the DAQ is configured for an input range of -10 V to 10 V.

As presented in section 4.7.1.2 the voltage and the value in nanometers of each code of NI-DAQ ADC, when using the MC900<sub>4,5,6</sub> is:

$$NIDAQ_{res} = \frac{10V - (-10V)}{2^{16}} = 305 \mu V = 12 nm \quad (58)$$

This error value is without considering the electronic noise, studied in section 4.7.

## 8.2 CONTROL FREQUENCY

The control frequency of the system must be defined in terms of the maximum frequency at which the instrument has to be able to respond. The science of the instrument does not impose a minimum operating frequency but environmental disturbances have to be rejected to guarantee satisfactory performance.

A vibration analysis of the future location of the Fabry-Pérot instrument was conducted by Dr. Fábio de Oliveira Fialho, with provided vibrational data acquired with two accelerometers at a sampling frequency of 500 Hz.

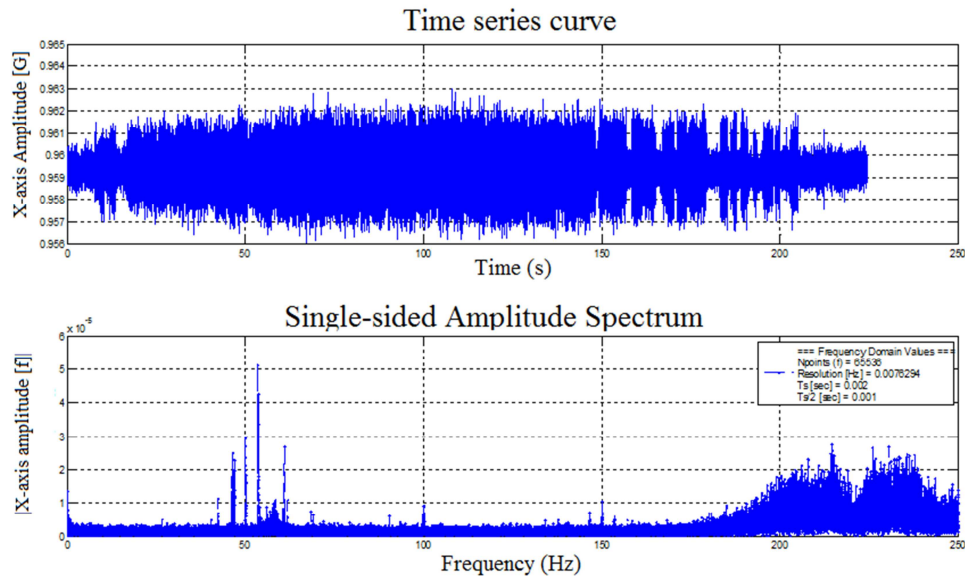
Figure 55 shows the acquired signal over time and its single sided amplitude spectrum. The spectrum reveals several frequencies of high amplitude around 50 Hz and 220 Hz.

Because the cut-off frequency of the complete system, presented in section 6.3.4, is around 450 Hz, any perturbation below the cut-off frequency of the Fabry-Pérot acts as perturbation on the system. Therefore the safest criteria for the bandwidth of the system would be to control in the whole range of operation as stated in eq.(59).

$$F_{control} = FP_{cut-off} = 450 Hz \quad (59)$$

More vibrational studies are presently being conducted at the SOAR telescope to determine if there are more high frequency perturbations and if they can be compensated mechanically so the controller could have a lower bandwidth.

Figure 55 - Vibrational study of the environment of the Fabry-Pérot instrument location



Source: Courtesy of Dr. Fábio de Oliveira Fialho.

### 8.3 SAMPLING FREQUENCY

Different sampling frequency criteria must be taken into account to define the adequate sampling frequency for each of the subsystems of the Fabry-Pérot system.

This section presents the used criteria to define the sampling frequency for the digital redesign of the continuous time controller, the sampling frequency for the digital-to-analog converter and the analog-to-digital converter and the maximum sampling frequency of the actual data acquisition system.

#### 8.3.1 Digital Redesign of the Continuous Time Controller.

Since the chosen techniques for the design of the Fabry-Pérot controllers, Proportional-Integral controller and robust controller following the LQG/LTR technique, are implemented in the continuous time domain, a discretization of the controller must be done to validate the controller in the real system.

The process of converting a continuous-time (or analog) controller into an equivalent discrete-time (or digital) controller is called *digital redesign*.

The continuous Fabry-Pérot controller will use the bilinear transformation for the redesign process. This transformation technique is also called Tustin's rule or the trapezoidal rule, which is based on the trapezoidal approximation of integrals. This technique was chosen because it has good matching in the frequency domain between the continuous and discrete time models and it is used when the model has important dynamics at some particular frequency, which is the case of the Fabry-Pérot system given the resonant behavior of the piezoactuators.

The discretization of the controller needs to preserve frequency-domain characteristics that are essential to the performance and stability requirements. As stated in Dorato, P. (1971), when the discrete system is the mathematical model of a sampled-data process, then two additional questions are of interest: the sensitivity of the optimal regulator to changes in the sampling rate and the possible loss of controllability due to sampling. The sampling time at which the controller is digitalized is constrained by the bandwidth of the control system and often by the system in which the controller is going to be implemented.

For the definition of the sample frequency for the digital redesign process,  $F_{SDR}$ , the chosen criterion was to use a sampling frequency at least 10 times higher than the cut-off frequency of the controller as stated in eq.(60).

$$F_{SDR} > 10 K_{cut-off} \quad (60)$$

where:

$K_{cut-off}$  is the crossover frequency of the controller continuous design.

However the actual digital system of the laboratory, presented in section 3.4.2 presents limitations in terms of the frequency at which the system can operate in real time. These limitations, presented in section 8.3.4 are the ones that define if the validation of the developed controllers on the real system can be done, using the actual laboratory resources.

### 8.3.2 Fabry-Pérot Digital-to-Analog Sampling Frequency

Given that the DAC sampling frequency is defined as the frequency at which the digital controller operates, the DAC sampling frequency depends directly on the sampling frequency at which the continuous controller was digitalized, as stated in eq.(61).

$$F_{S_{DAC}} = F_{S_{DR}} \quad (61)$$

### 8.3.3 Fabry-Pérot Analog-to-Digital Sampling Frequency

The Nyquist theorem states that a signal must be sampled at a rate larger than twice the highest frequency component of the signal to accurately reconstruct the waveform.

However, to avoid aliasing of the high frequency content in a frequency inside the spectrum of interest, a 10x oversampling criteria is used in practice to represent accurately the time domain signal in terms of frequency, amplitude, and shape.

If ideally the Fabry-Pérot system should be able to control up to the cut-off frequency of the complete system, as defined in eq.(59), the minimum sampling frequency of the ADC system is as stated in eq.(62), that is 4500 Hz.

$$F_{S_{ADC}} \geq 10 F_{P_{cut-off}}. \quad (62)$$

### 8.3.4 NI-DAQ Sampling Frequency

The NI-DAQ 6221 is specified to have a sample frequency that can be as high as 250 kSPS. However, experimental tests in the laboratory running real-time simulations have shown that it is only possible to operate the system without any computational limitations up to 10 kHz.

This limitation defines the maximum sampling frequencies of the ADC and DAC frequency as in eq.(63).

$$F_{S_{real-time}} \leq 10000 \text{ Hz} \quad (63)$$

This constraints does not affect the sampling frequency specification of the ADC, however, because the sampling frequency of the DAC is equal to the sampling frequency of the digital

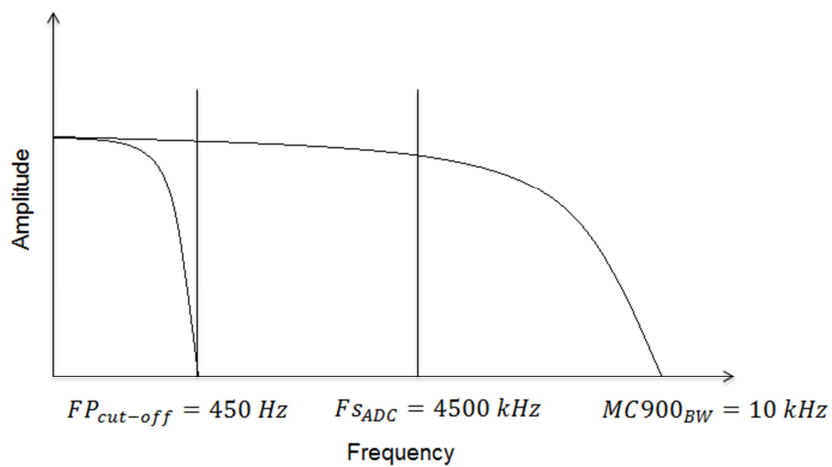
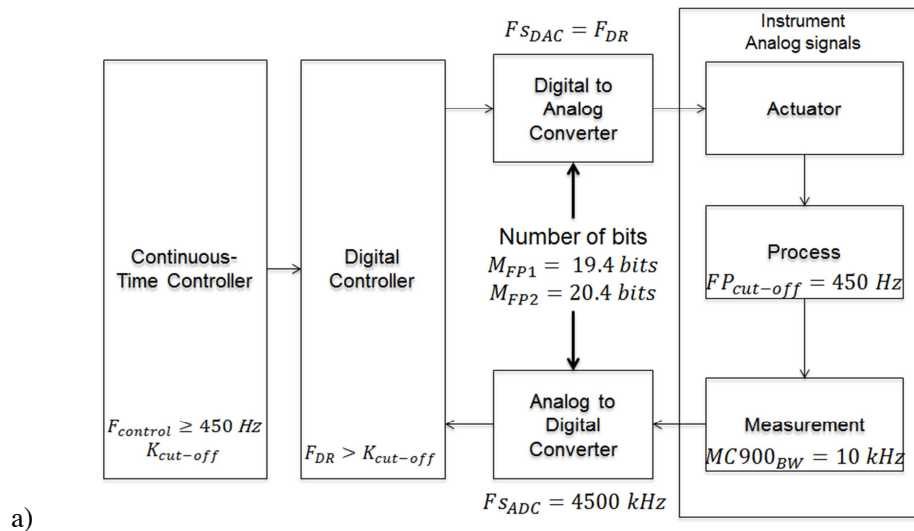
redesign process, which at the same time depends on the bandwidth of the controller, the real time sampling frequency limits the maximum bandwidth of the controller that can be tested on the laboratory as will be shown in section 9.3.3.

### 8.4 SUMMARY OF THE CHARACTERISTICS OF THE DIGITAL SYSTEM

Figure 56 shows for reference the frequencies of all the components of the digital system

Figure 56 - Summary of frequencies of the Fabry-Pérot digital system.

a) Block diagram of the digital system with the corresponding frequencies of each subsystem. b) Spectrum of the defined frequencies, including the analog and the digital.



b)

Source: Author

## 9 DESIGN OF THE CONTROLLERS, SIMULATIONS AND EXPERIMENTAL VALIDATION

### 9.1 GENERAL RESTRICTIONS OF THE SYSTEM

The prototype of the Fabry-Pérot system used in the laboratory for the modeling and simulation experiments is summarized in Table 14.

Table 14 Instrumentation of the Fabry-Pérot prototype

Fabry-Pérot component	Type
3 Piezoelectric actuators	APA400MML of 350 $\mu\text{m}$ of stroke
3 Capacitive sensors	MCC10HS of 1 mm of measurement range
3 CVC modules	MC900 <sub>4,5,6</sub> of 400 $\mu\text{m}$ of measurement range
2 Data acquisition boards	NI-DAQ 6221

As presented on section 4.7, the actual digital system, comprised by the NI-DAQs and the personal computer PC<sub>2</sub> introduces a measurement noise to the control loop. The source of this noise is not from external perturbations or the Fabry-Pérot instrumentation, but is from the temporary data acquisition boards, therefore, to impose a resolution specification of 3nm is not reasonable.

Also, as stated in section 8.3.4, the maximum sampling frequency of the control system for real time simulations without computational difficulties is limited to 10000 Hz, which also limits the bandwidth of the controller that can be validated on the laboratory.

On the other hand, the drivers by charge are currently under development so they cannot be implemented on the system for experiments. The voltage input of the Fabry-Pérot will be limited to -10 to 10 volts, which is the maximum analog output range of the NI-DAQ. This limits the achievable spacing of the Fabry-Pérot etalon.

And lastly, the modeling error imposes a limitation to the bandwidth of the system. Since the cross-over frequency of the modeling error is actually around the first resonance frequency of the FP dynamic response, the frequency performance barriers have to be defined below this value.

### 9.1.1 Definition of the Performance Specifications for the Fabry-Pérot Prototype

Taking into account the mentioned limitations imposed by the available laboratory instrumentation and the modeling error, the performance specifications for the controller of the instrument, previously defined in section 7.2, were redefined for the Fabry-Pérot prototype.

The new performance specifications are:

1. To follow a ramp and step reference signal.
2. To present null steady state average error.
3. Steady state standard deviation equal to the electronic noise of the data acquisition system.
4. To reject disturbances up to 60 Hz.
5. Minimize overshoot in the transient response.

Although they are simplified specifications, the applied theory to design the controllers does not change and constitute the theoretical and methodical process to design the ultimate controllers for the BTFI Fabry-Pérot.

## 9.2 PROPORTIONAL-INTEGRAL COMPENSATOR

As a benchmark, and due to its simplicity of implementation and satisfactory performance on following step references with zero steady-state error, a simple Proportional Integral (PI) controller of the form of eq. (64) has been implemented.

$$K_{PI} = kp + ki \frac{1}{s} \quad (64)$$

where:

- $kp$  is the proportional constant;
- $ki$  is the integral constant;
- $s$  is the Laplace complex angular frequency.

The derivative control mode of the traditional PID controller is not implemented due to the high measurement noise of the system.

The PI compensator for the Fabry-Pérot is assumed to be an ensemble of three SISO (single input single output) decoupled control loops.

The nominal model of the MIMO system can be expressed as a matrix of transfer functions as shown in eq.(44) of section 6.3.2. When considering a decentralized Proportional-Integral controller, coupling transfer functions of the system defined by  $G_{12}$ ,  $G_{23}$ ,  $G_{13}$  of the mentioned matrix are neglected, meaning that the model only considers the mass of glass over the actuators, not the coupling force provoked by the circular mirror over the three piezoactuators.

The same compensator,  $K_{PI}$ , was used for the three channels and a genetic algorithm was used in order to find the values of the proportional and integral parameters of the compensator.

### 9.2.1 Stability Analysis of the Fabry-Pérot system

To analyze the stability of the system, the roots of the characteristic equation of the three transfer functions of interest,  $G_{11}$ ,  $G_{22}$ ,  $G_{33}$  of equation (44) are calculated. For the parametric model of the Fabry-Pérot these three transfer functions are equivalent, which is also the reason why the three SISO PI controllers are the same for the three control loops of the system.

In open-loop configuration, the eigenvalues of the transfer function are all located in the open left-half plane, which guarantees the stability of the system.

### 9.2.2 Tuning of the PI Compensator using a Genetic Algorithm

As an initial approach to obtain the P and I parameter values for the PI compensator a trial and error technique was used in the laboratory. Then the need for a more robust method was identified and a genetic algorithm was proposed as a methodological solution.

A genetic algorithm, GA, is a heuristic search inspired by natural evolution, using techniques such as inheritance, mutation, selection, and crossover. In a genetic algorithm, a population of candidate solutions to an optimization problem is evolved toward better solutions.

The evolution starts from a population of randomly generated individuals. It is an iterative process, and the population of every iteration is called a generation. In each generation, the fitness of every individual in the population is evaluated using an objective function. The

individuals with better fit are selected from the current population, and new individuals are created by crossing the current solutions to form a new generation. The algorithm terminates when a maximum number of generations has been produced.

A genetic algorithm requires:

- A representation of the possible solutions as individuals.
- A population of different individuals.
- A fitness function to evaluate how good each individual solution is.
- A method to combine solutions to form new individuals.
- A mutation operator to avoid losing diversity in the solutions.

Once the genetic representation and the fitness function are defined, a GA proceeds to initialize a population of solutions and then to improve it through repetitive application of the mutation, crossover, inversion and selection operators.

#### Basic Genetic Algorithm

Generate initial population of random individuals

**repeat**

Evaluate each individual performance with the fitness function

**repeat**

Select two individuals with probability proportional to their fitness

Cross the two individuals and generate two new individuals

**until** New population is complete

Apply random mutation to new population

Replace old generation with the new population

Increase generation counter

**until** Maximum number of generations reached

---

In the case of the Fabry-Pérot system, each individual consists of a set with two values, P and I, representing a PI controller. These individuals are qualified according to a fitness function based on the behavior of the controlled system step response.

The fitness function takes into account three characteristics from the response: (a) The total difference between the output and the input, (b) the time it takes for it to reach stability in the expected steady-state value and (c) the amount of overshoot or values way over the expected ones.

Equation (65) shows the objective function with three terms, for (a), (b) and (c) as explained above.

$$Fitness = \sum |input_t - output_t| w_1 + \sum (output_t > input_t p_1) w_2 + \max_t (output_t > input_t p_2) w_3 \quad (65)$$

where:

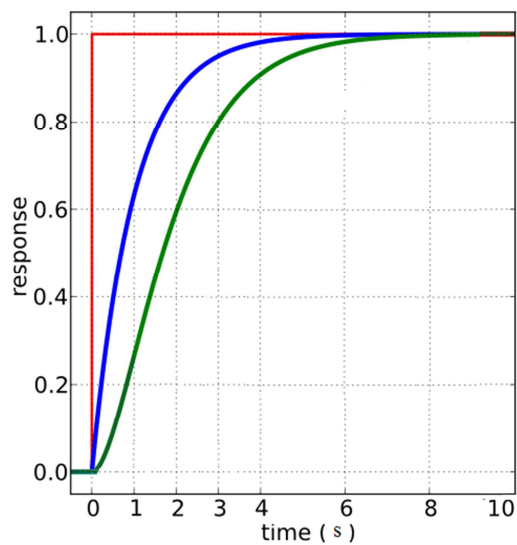
$w_1$ ,  $w_2$  and  $w_3$  are weighting factors for normalizing the three values and giving more or less importance to each of them.

$p_1$  and  $p_2$  are percentages to account for the acceptance intervals of overshoot or stability.

The main objective is to follow the step function with minimal error, i.e. to achieve the steady-state value with minimum rise and settling time, while having minimal overshoot on the response of the system.

Figure 57 is an illustrative figure to show the step response for different PI values and their corresponding error plots. Minimizing the error is equivalent to minimize the area between the step function and the response of the system. The closer the responses are, the smaller the area between them is and smaller error in time is.

Figure 57 - Illustrative step responses to different PI controllers



Source: Author

Each individual is evaluated using a simulation of the control system with the parametric model of the Fabry-Pérot system. The fittest individuals, the ones with the smaller error, survive to the next generation. The less fit solutions are discarded and the population is then completed by crossing individuals to generate new individuals. This process is called *mating*.

In the case of the GA for the Fabry-Pérot system, four individuals are randomly chosen, confronting them in two pairs and then the winner of each pair, i.e. the best fit, are then crossed to generate two children, using the P of one parent and the I of its pair, and vice versa.

After mating, a mutation operation takes place. Every gene (every P and I) of every individual has a probability  $P_m$  for mutation. The mutation consists on adding or subtracting a previously determined percentage from the chosen gene. This is done in order to explore new solutions and avoid loss of diversity.

The new generation is again evaluated and the algorithm runs for a new iteration, until the desired number of generations is achieved. The best fit individual in the last generation is used as the best solution for the PI controller.

### 9.2.3 Simulation Results of the Proportional-Integral Compensator

Figure 58 shows the block diagram of the three SISO PI control loop. Since the reference signal is a distance signal, and the output of the compensator is a voltage signal that actionate the piezoactuators, it is possible to define two types of PI control systems: one that receives a distance value as input, and one that accepts a voltage value equivalent to a distance value. Both PI control systems have a voltage signal as output. The first is a negative feedback loop and the other is a positive feedback loop.

Figure 58a shows the block diagram of the decentralized PI control system with the input of the control loop as a distance signal. This control loop is a negative feedback loop and the parameters values of the compensator of eq.(64) found by the genetic algorithm are:

$$k_p = 0.0628$$

$$k_i = 37.643$$

On the other hand, Fig.58b shows the block diagram of the decentralized PI control system with the input of the control loop as a voltage signal equivalent to the desired distance value.

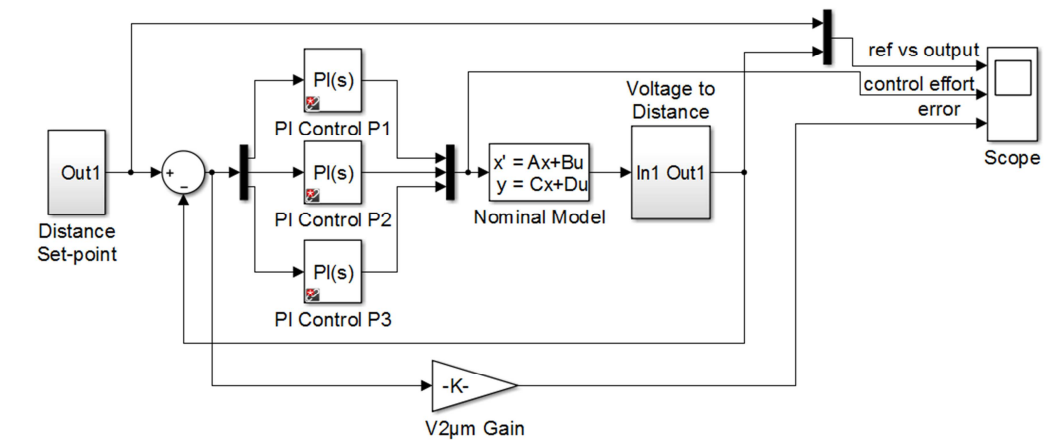
This control loop is a positive feedback loop, however it can be represented as a negative feedback loop with a PI compensator with negative values for the parameters defined on eq.(64). The values found by the genetic algorithm for this controller are:

$$k_p = -0.00445$$

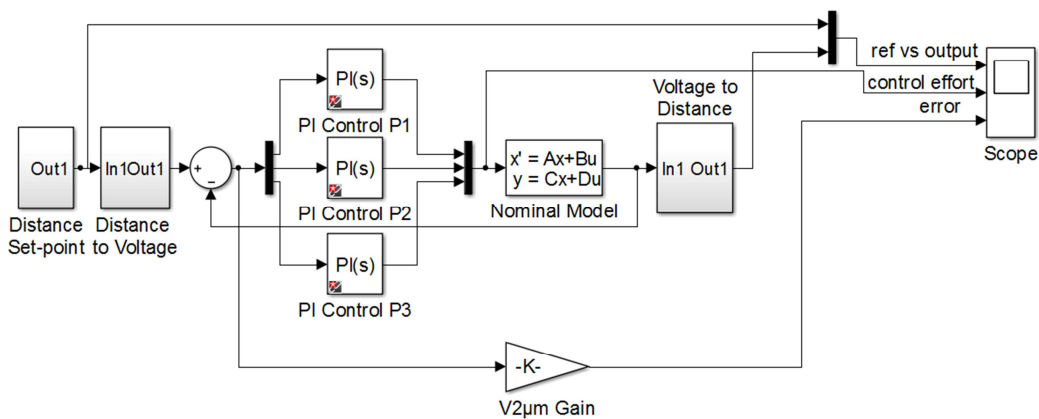
$$k_i = -1.4458e3$$

The control system with voltage input and output, of Fig.58b was chosen for the simulations and validation with the Fabry-Pérot system.

Figure 58 - Simulation block diagram of the Fabry-Pérot model with PI controller



a)



b)

Source: Author

On the set-point subsystem the user can choose between the three different input signals: A ramp, a step or a sinusoidal wave of a chosen frequency.

Since the PI control loop is a control loop for voltage signals, the set-point signal in distance units is converted to a voltage value before entering the control loop with the “Distance to Voltage” block, which has the function defined in eq.(66):

$$V_{input} = 10 - 0.025d_{input} \quad (66)$$

where:

$d_{input}$  is the reference distance value that enters the user.

$V_{input}$  is the corresponding voltage reference value to the specified distance input defined by the user.

This formula takes into account that the APA400MML piezoactuators are pulling actuators, i.e, they contract with positive input voltages and they expand with negative input voltages.

The voltage reference signal is then divided in three paths so the reference signal is the same for the three channels of the Fabry-Pérot.

The PI blocks calculate the control signal according to the error value and the security subsystem has a saturation block to guarantee that the control signal is always between the NI-DAQ’s analog output limits of -10 to 10V.

The model of the Fabry-Pérot responds to the control input signal and delivers the corresponding output of the MC900 modules, in volts.

Consequently the “Voltage to distance” block translates the output voltage value in terms of a distance value using the relation of eq.(67).

$$d_{output} = \frac{10 - V_{output}}{0.025} \quad (67)$$

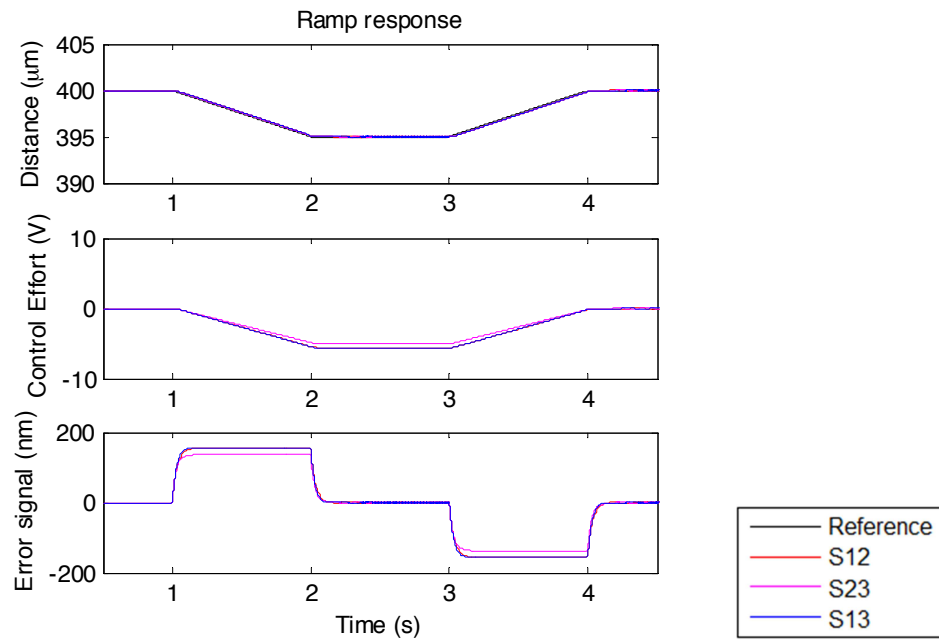
where:

$V_{output}$  is the corresponding voltage value to the distance output of the system and is the value of the feedback signal of the control loop;

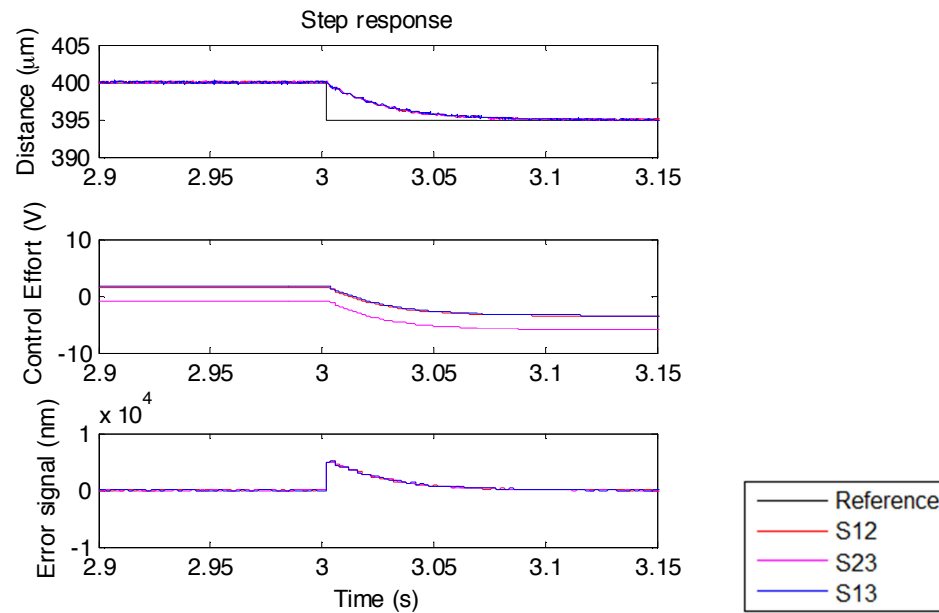
$d_{output}$  is the output of the system in distance units, that is to be compared to the reference.

Figure 59 shows the simulated responses of the parametric model of the Fabry-Pérot system to three different input signals: Ramp, step and sinusoidal, when controlled with the presented PI compensator.

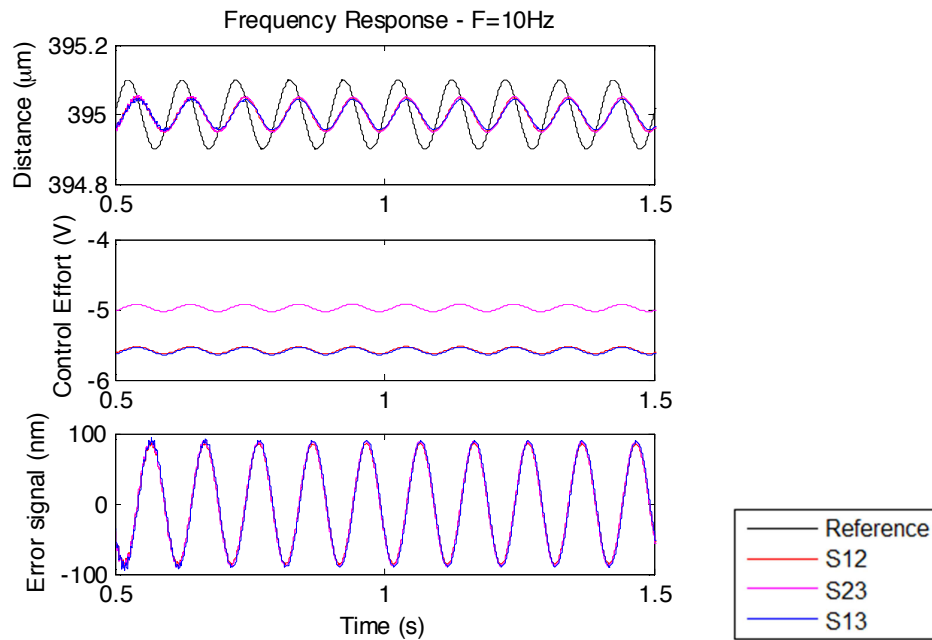
Figure 59 - Response of the Fabry-Pérot system model using a PI controller to different set-point signals.  
 a) Ramp response, b) step response, c) frequency response to a sinusoidal signal of 10 Hz.



a)



b)



c)

Source: Author

It can be seen on the responses that the system follows the reference signals without overshoot and with null steady state error. The bandwidth of this controller, which is the frequency where the amplitude of the frequency response is 70% of the expected value, is found to be 10 Hz. The settling time is of 100 ms.

Table 15 summarizes the characteristics of the response of the system when controlled with the PI compensator.

Table 15 Summary of the response of the FP system model when controlled with a PI compensator

Parameter	Simulation Values
Steady-state average error	0 nm
Steady-state standard deviation	2.1352e-7 nm
Delay time (50% of final value)	30 ms
Overshoot	0 nm
Settling time	100 ms
Bandwidth controller	10 Hz

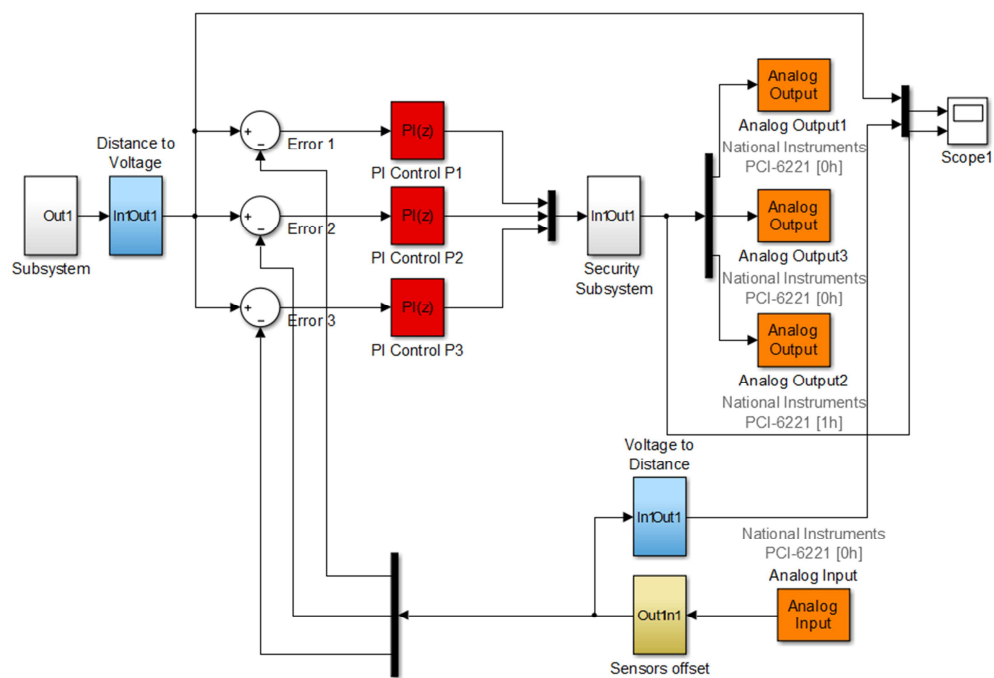
The second plot on each figure shows that the control effort on the three experiments is within the limits of the controller and the driver. The responses have practically null steady-state standard deviation, the noise value is considered as a numerical error of the calculation,

indicating that the control system does not add noise to the continuous-time system model response.

### 9.2.4 Experimental Validation of the Proportional-Integral Compensator

Figure 60 shows the block diagram of the real-time experimental set-up for the Fabry-Pérot prototype Proportional-Integral compensator.

Figure 60 - Real time PI controller for the Fabry-Pérot prototype



Source: Author

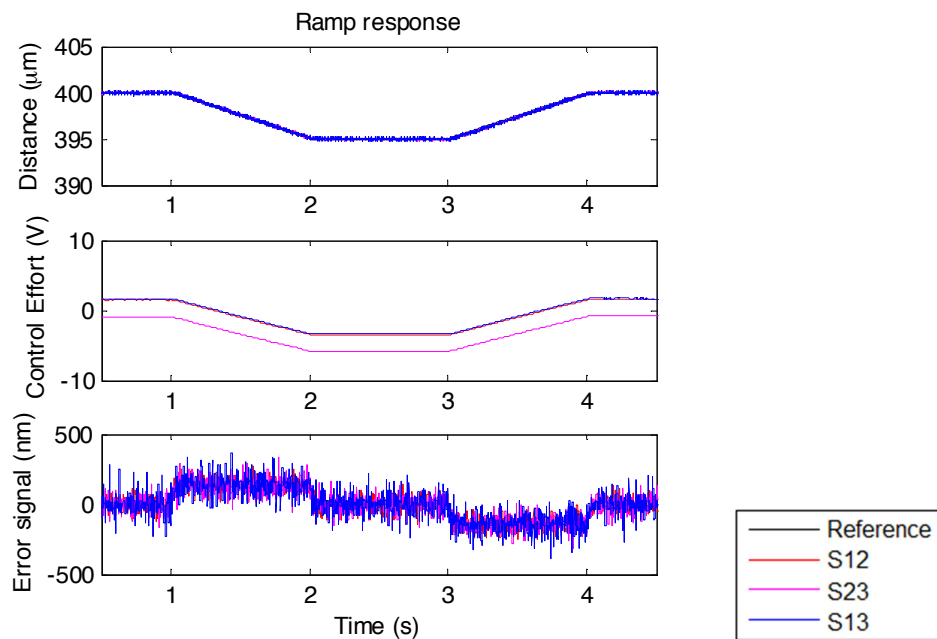
The difference between this block diagram and the one on Fig.(58) are the discrete versions of the PI controller (in red) and the analog inputs and outputs of the system that communicate between the simulation and the real Fabry-Pérot system (in orange).

The digital control signal is converted to an analog signal through the Analog Output blocks with a sampling frequency equal to the frequency of the digital redesign, which was of 500 Hz.

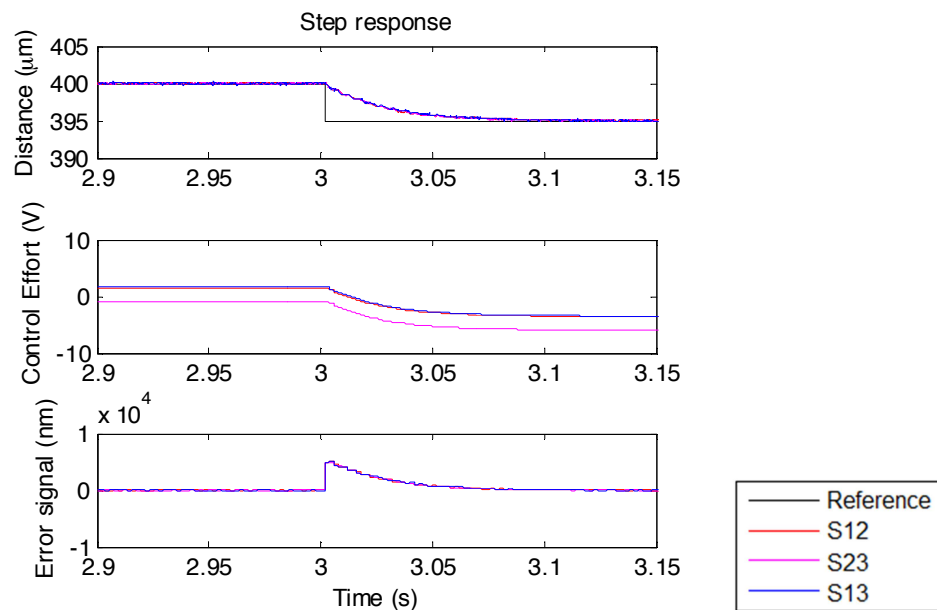
The orange Analog Input block converts the analog voltage of the MC900 output to a digital value at 5000 Hz. The yellow block on the feedback loop corrects the initial offset of the sensors. The calibrated voltage value is the feedback signal of the control loop.

Figure 61 shows the response of the real plant to the Proportional –Integral compensator.

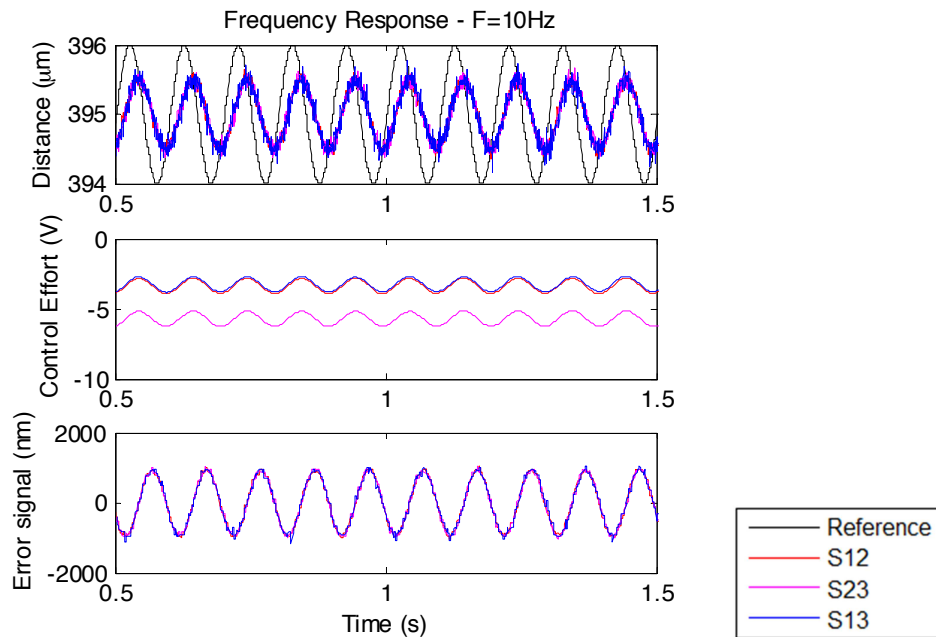
Figure 61 - Response to different set-point signals of the Fabry-Pérot prototype using a PI controller.  
 a) Ramp response, b) step response, c) frequency response to a sinusoidal signal of 10 Hz.



a)



b)



c)

Source: Author

The dynamic response of the system fits well the response of the model, which validates the model and the discrete controller. It can be seen in the figure that the Fabry-Pérot follows the reference signals and has a settling time and bandwidth equal to the simulated system.

The standard deviation observed in the open-loop signal is 35.5 nm, yet the standard deviation observed in the steady-state signal in closed-loop for the ramp and step response is of 37.3 nm. The difference of 2 nm is not present in the simulated responses shown in Table 15. Possible causes for this additional noise in the system include bad performance of the discrete controller due to the digital redesign process, an inadequate control technique or a high modeling error. On the other hand, the simulations do not consider the error introduced by the analog-to-digital converters. Further analysis is required in order to determine the precise cause and solution.

Table 16 summarizes the characteristics of the response of the system when controlled with the PI compensator.

Table 16 Summary of the response of the FP system when controlled with a PI compensator

Parameter	Validation values	Simulation values
Open-loop noise RMS	35.5 nm	0 nm
Steady-state standard deviation	37.3 nm	2.1352e-7 nm
Steady-state average error	0 nm	0 nm
Delay time (50% of final value)	30 ms	30 ms
Overshoot	0 nm	0 nm
Settling time	100 ms	100 ms
Cut-off frequency	10 Hz	10 Hz

#### 9.2.4.1 Spectral Analysis of the Real Response

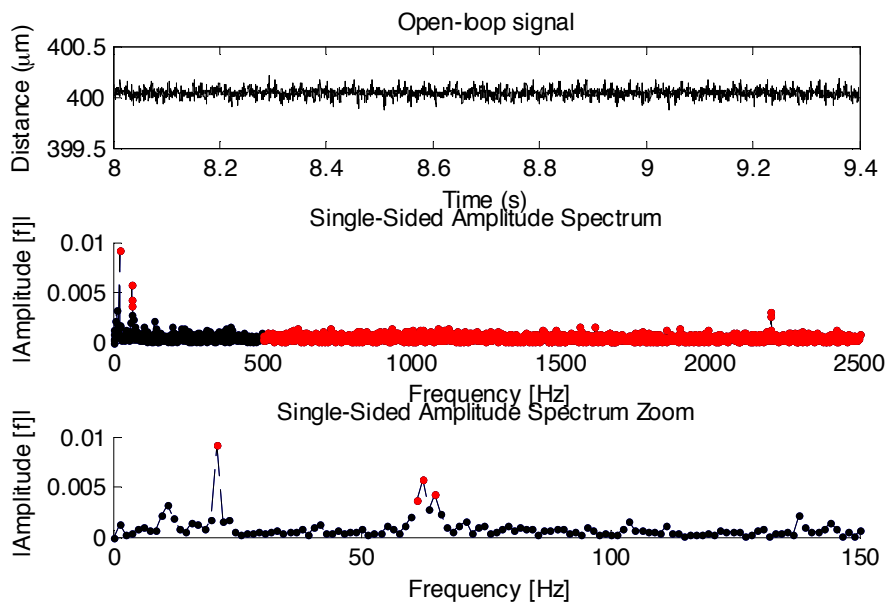
A fast Fourier transform was used to plot the single-sided amplitude spectrum for a spectral analysis of the acquired signals for the open-loop and closed-loop systems.

The objective with the spectral analysis is to compare the frequency decomposition in open-loop to the closed-loop and evaluate if the control system adds frequency components that could affect the resolution of the system in the range of interest.

Figure 62 shows the spectrum of the output of the system in open-loop. The first subplot is a portion of the temporal signal to be analyzed. The second one shows the complete single-sided amplitude spectrum. Since the sampling frequency of the ADC was set to 5000 Hz, the spectrum shows the frequency components up to 2500 Hz, but the frequency components beyond 500 Hz, in red, were filtered to analyze only the dynamics of the control loop and not the high-frequency components of the data acquisition system. Finally, the third plot presents a zoom from 0 to 150 Hz of the previous plot to show in detail the dynamics of the zone of interest.

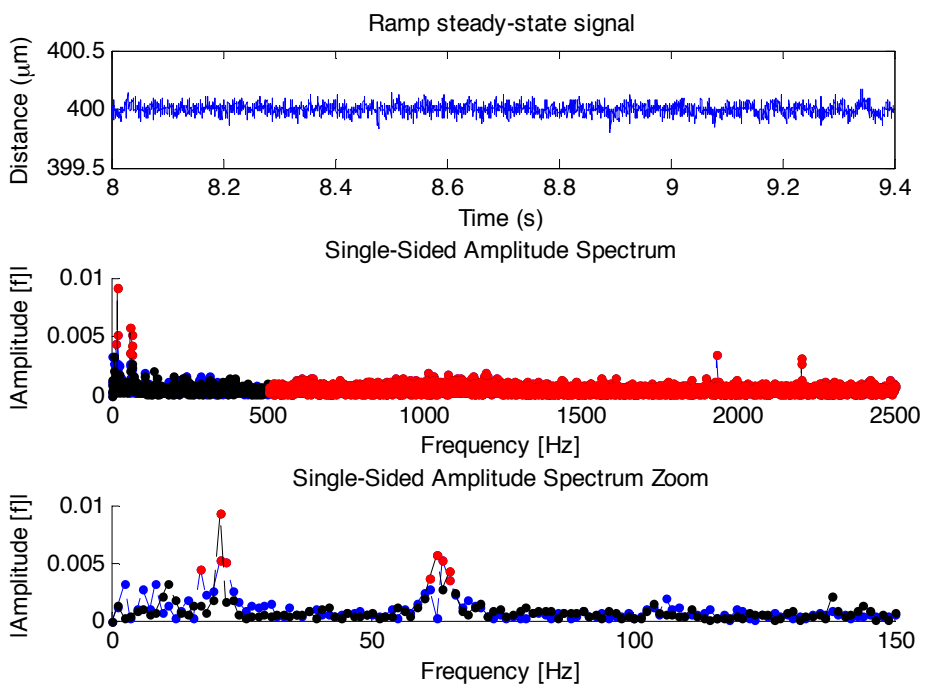
Figure 63 shows the same plots for the ramp and step response of the Fabry-Pérot system. The open-loop spectrum is also plotted in black in these figures, for visual comparison.

Figure 62 - Spectral analysis of the open-loop MC900 acquired signal

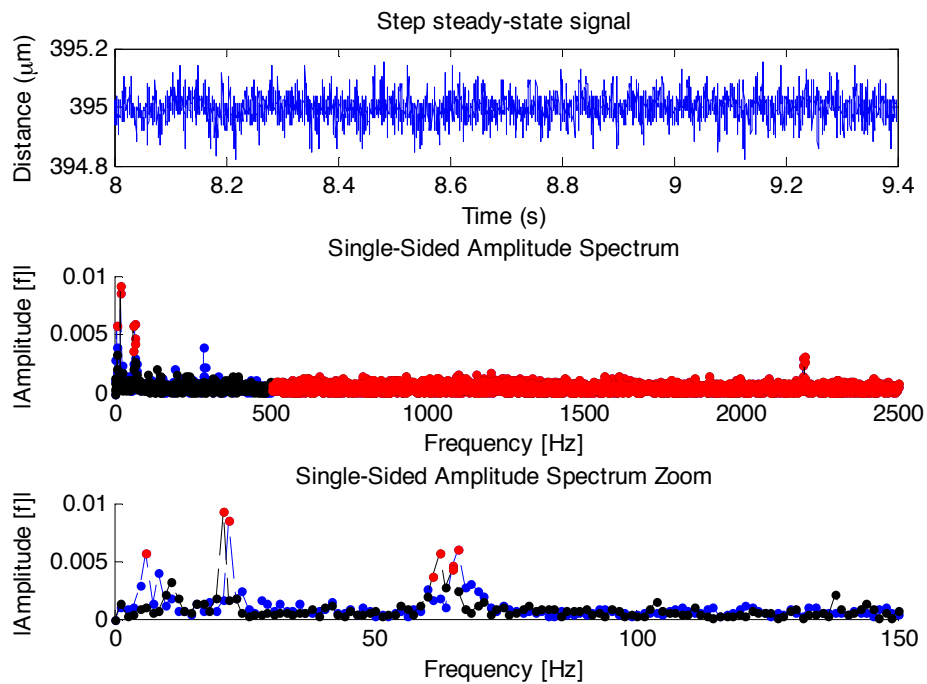


Source: Author

Figure 63 - Spectral analysis of the ramp (a) and step (b) closed-loop response, in blue, for the PI controller. The open-loop spectrum is also plotted in black for visual comparison. The red points are not considered on the statistical analysis.



a)



b)

Source: Author

Using the Parseval Theorem, which states that the sum of the square of a function is equal to the sum of the square of its transform, it is possible to calculate the standard deviation of a range of frequencies using their power spectral density.

Analyzing only the band of frequencies up to 500 Hz, the noise for the open-loop signal is of 9.9 nm and the closed-loop signal is of 12.11 nm. These values are lower than the noise calculated using the time-domain signal (35.5 nm for open-loop and 37.3 for closed-loop), because the higher frequencies are not in the calculation, but once again the closed-loop signal has higher noise than the open-loop signal.

On the other hand, comparing the spectrum of the open-loop signal with the closed-loop signal for both, the step and the ramp responses up to 150 Hz, it can be concluded that the PI control system does not add significant dynamics to the system.

### 9.3 MIMO ROBUST COMPENSATOR

The Linear Quadratic-Gaussian method with Loop-Transfer Recovery LQG/LTR control design methodology was the chosen technique to design a MIMO robust feedback control.

The principal reasons why this technique was selected among others is because given the characteristics of the Fabry-Pérot system model, and the ability of calculating the multiplicative modeling error of the system, the LQG/LTR technique offers a compensator with few parameters of design and systematic development, that makes the control system robust against dynamics of the system that are not considered in the system model, and permits to focus in the frequency domain while guaranteeing good performance in the time domain.

As pre-requisites of the system, the model of the plant, which is defined in section 6.3.1 by equations (39) and (40) and whose state-space matrices  $[\mathbf{A}, \mathbf{B}, \mathbf{C}]$  are defined in equations (41) (42) and (43) respectively, should be linear and time-invariant (LTI). The pair matrices  $[\mathbf{A}, \mathbf{B}]$  must be stabilizable, that is, all unstable modes of the system have to be controllable. The pair  $[\mathbf{A}, \mathbf{C}]$  must be detectable, that is, all unstable modes in the space state representation have to be observable.

As mentioned before, the size of the modeling errors have to be known and must be addressed using the multiplicative error, defined in eq.(47). The error  $EM(s)$  is assumed to be the maximum possible error in the worst possible direction as a function of frequency.

The design plant model  $G(s)$  is in the standard negative identity MIMO feedback loop configuration. The impact of the disturbances is reflected in the system output, and the measurement noise is introduced in the feedback signal.

#### 9.3.1 Prerequisites of the Parametric Model of the System

##### 9.3.1.1 Linearity

The parametric dynamic model of the complete system, presented in section 6.3.1 is a time invariant linear LTI system, with three input, three output and six state variables.

The real Fabry-Pérot system, however, is a non-linear system due to the non linearities of the piezoactuators. These non-linearities will be greatly compensated by the driver by charge, currently under development by Marchiori et. al. (2013).

For the design of the robust controller the system is assumed to be linear.

#### 9.3.1.2 Observability

In control theory, if a system is observable the internal states of the system can be inferred by knowledge of its external outputs.

MATLAB allows to easily create the observability matrix taking the system matrices  $[A, C]$  and using the *obsv(A,C)* command. The observability matrix of the Fabry-Pérot system model has full rank, which means the system is observable.

#### 9.3.1.3 Controllability

The concept of controllability refers to the ability of a controller to arbitrarily alter the functionality and behavior of the system plant by changing the system input.

As with the observability property, MATLAB allows to easily create the controllability matrix with the *contr(A,B)* command. Then in order to determine if the system is controllable or not one can determine if the controllability matrix has full rank, which is the case of the Fabry-Pérot system model.

#### 9.3.1.4 Stability

One method to analyze the stability of a multivariable system is to guarantee that the poles of the transfer functions in the MIMO transfer function matrix has a negative real part.

In open-loop configuration, the Fabry-Pérot system parametric model eigenvalues are all located in the open left-half plane, therefore the system is stable. The designed robust controller will guarantee that the system will be stable in closed-loop.

#### 9.3.1.5 Transmission Zeros

Lastly, the system in open-loop has to have all its transmission zeros as minimum phase zeros to guarantee both, the good performance of the control system and also the recovery process.

A review on the transmission zeros of the system model, using the  $tzero(sys)$  function in MATLAB, helps corroborate all the zeros of the system are located in the left half plane, i.e. they are indeed minimum phase zeros.

### 9.3.2 Theory of the Robust Compensator

After corroborating the fulfillment of the system prerequisites, the objective of the design process is to specify the dynamic compensator,  $K(s)$ , that guarantees nominal stability on the system, stability-robustness to modeling errors and good performance.

The LQG/LTR method involves two basic steps. The first one is to generate a MIMO target feedback loop (TFL) that meets the posed performance specifications without violating the stability-robustness constraints. The second one is a recovery procedure, where the compensator  $K(s)$  is defined from some adjustable parameters, so that the performance of the feedback system approximates the performance of the target feedback loop established in step one.

The methodology starts with the definition of the Design Plant Model (DPM), that includes not only the nominal model of the dynamics of the physical system that is going to be controlled, but also reflects the scaling of the variables and augmentation of the dynamics to meet special command-following and disturbance-rejection performance specifications when necessary (Athans, 1986).

The performance specifications for following the reference signal are defined by the parameters  $\alpha_r$ , and  $\omega_r$  which define the “Follow reference signal barrier”. The first is the relation between the signal amplitude and the acceptable error, and  $\omega_r$  is the frequency up to which the controller must be able to respond. The “Noise rejection barrier” is defined according to the relative values of  $\alpha_n$ , and the frequency  $\omega_n$ .

To guarantee null steady state error in the step response, the dynamics of the model of the Fabry-Pérot system were augmented including one integrator on each input channel and the DPM is defined as in eq.(66).

$$\text{DPM}(s) = \begin{bmatrix} G_{11} & G_{12} & G_{13} \\ G_{21} & G_{22} & G_{23} \\ G_{31} & G_{32} & G_{33} \end{bmatrix} \begin{bmatrix} \frac{1}{s} & 0 & 0 \\ 0 & \frac{1}{s} & 0 \\ 0 & 0 & \frac{1}{s} \end{bmatrix} \quad (66)$$

With an integrator on each input channel, the DPM of the system has then 9 states variables: 6 from the original Fabry-Pérot model and 3 from the additional integrators.

The robust compensator is as defined in eq.(67):

$$\mathbf{K}(s) = \mathbf{G}(s\mathbf{I} - \mathbf{A} + \mathbf{B}\mathbf{G} + \mathbf{H}\mathbf{C})^{-1}\mathbf{H} \quad (67)$$

where:

$\mathbf{K}(s)$  is the matrix of the robust controller;  
 $\mathbf{G}$  is the control gain matrix of the LQG/LTR method;  
 $\mathbf{A}$ ,  $\mathbf{B}$  and  $\mathbf{C}$  are the matrices of the parametric model of the Fabry-Pérot; defined in equations (41) (42) and (43) respectively of section 6.3.1;  
 And  $\mathbf{H}$  is the filter matrix as defined in eq.(68).

$$\mathbf{H} = \frac{1}{\mu_{LQG/LTR}} \Sigma \mathbf{C}' \quad (68)$$

where:

$\mu_{LQG/LTR}$  is a free design parameter defined by the control engineer;  
 And  $\Sigma$  is found solving the Ricatti equation of eq.(69).

$$0 = -\mathbf{A}\Sigma - \Sigma\mathbf{A}' - \mathbf{L}\mathbf{L} + \frac{1}{\mu_{LQG/LTR}} \Sigma \mathbf{C}' \mathbf{C} \Sigma \quad (69)$$

where:

$\mathbf{L}$  is the singular values matching matrix, also defined by the control engineer.

For an augmented plant, the design matrix  $\mathbf{L}$  is chosen so that the singular values of the reference target loop match in both, high and low frequencies, as defined in eq.(70) (Cruz, 1996).

$$\mathbf{L} = \begin{bmatrix} L_L \\ L_H \end{bmatrix} = \begin{bmatrix} -(\mathbf{C}\mathbf{A}^{-1}\mathbf{B})^{-1} \\ -\mathbf{A}^{-1}\mathbf{B}L_L \end{bmatrix} \quad (70)$$

By choosing the value of  $\mu_{LQG/LTR}$  and the  $\mathbf{L}$  matrix the control engineer is using Kalman Filter methods to design the target feedback loop to be recovered on the next steps.

The values of  $\mu$  and  $\mathbf{L}$  are chosen so the singular values of eq.(71) obey the performance and stability barriers defined by the control problem specifications.

$$\sigma_i\left[\frac{1}{\sqrt{\mu}}\mathbf{C}(j\omega - \mathbf{A})^{-1}\mathbf{L}\right] \quad (71)$$

After finding  $\mathbf{H}$ , it is saved and used on the definition of the Target Feedback Loop by the matrix  $G_{KF}(j\omega)$  in eq. (72).

$$G_{KF}(j\omega) = \mathbf{C}(j\omega - \mathbf{A})^{-1}\mathbf{H} \quad (72)$$

The only other remaining design parameter in  $\mathbf{K}(s)$  is the control gain matrix  $\mathbf{G}$ , of eq.(73):

$$\mathbf{G} = \frac{1}{\rho}\mathbf{B}'K_{LQG/LTR} \quad (73)$$

where:

$\rho$  is another design parameter, also defined by the control engineer until satisfactory performance of the controller is reached;  
 $K_{LQG/LTR}$  is found solving the Ricatti equation of eq.(74).

$$0 = -K_{LQG/LTR}\mathbf{A} - \mathbf{A}'K_{LQG/LTR} - \mathbf{C}'\mathbf{C} + \frac{1}{\rho}K_{LQG/LTR}\mathbf{B}\mathbf{B}'K_{LQG/LTR} \quad (74)$$

The resultant MIMO compensator will then have 12 states (6 states from the original system model + 3 integrators of the DPM + 3 integrators included in the controller) and is of the form of eq.(75).

$$\mathbf{K}(s) = \mathbf{K}(s)\frac{1}{s}\mathbf{I}_3 = \mathbf{G}(s\mathbf{I} - \mathbf{A} + \mathbf{B}\mathbf{G} + \mathbf{H}\mathbf{C})^{-1}\mathbf{H}\frac{1}{s}\mathbf{I}_3 \quad (75)$$

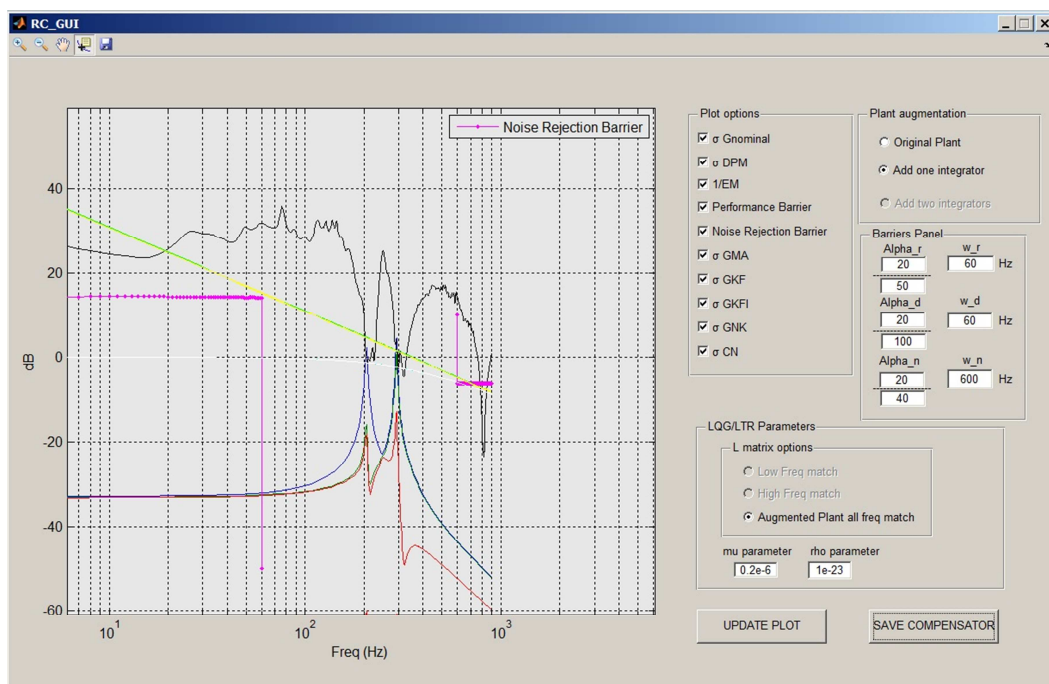
where:

$\mathbf{I}_3$  is an identity matrix.

Because the followed methodology for the design of the LQG/LTR robust controller (Cruz, 1996) is a graphical procedure, a graphical user interface was developed in MATLAB for better visualization of the impact of the parameters values in the controller design.

Figure 64 shows a picture of the developed graphical user interface, which is named *RC\_GUI*, after Robust Controller Graphical User Interface.

Figure 64 - LQG/LTR controller Graphical User Interface



Source: Author

This GUI permits the control designer to select the plots that are interesting for the project:

- Singular values of the nominal model of the system,  $G(s)$ , defined in eq.(45).
- Singular values of the Design Plant Model,  $DPM(s)$ , as defined in eq.(66).
- Inverse of the modeling error,  $EM(s)$ , as defined in eq.(47).
- Performance barrier, according to the relative values of  $\alpha_r$ , and  $\omega_r$ , which are defined in the Barriers Panel of the RC\_GUI.
- Noise rejection barrier, according to the relative values of  $\alpha_n$ , and  $\omega_n$ , which are defined in the Barriers Panel of the RC\_GUI.

- Singular values of the Target Feedback Loop design as defined in eq.(71).
- Singular values of the  $G_{KF}$  as defined in eq.(72).
- Singular values of the compensated open-loop system.
- Singular values of the compensated closed-loop system.

### 9.3.3 Design of the Robust Compensator

A robust controller for the Fabry-Pérot interferometer, called *Robust controller A*, was designed with the following specifications:

- Follow a step reference signal with null steady state error
- Reject disturbances up to 60 Hz.

The  $\omega_r$ , frequency value of 60 Hz was chosen taking into account the performance barriers and the limitation imposed by large modeling error around 200 Hz.  $\alpha_r$  was defined as 0.3, for a 3 nm accepted error value for a 10 nm step signal. The frequency for rejection of the measurement noise was defined as a decade greater than the “follow the reference barrier” frequency, which makes  $\omega_n$  equal to 600 Hz.  $\alpha_n$  was defined as 0.3 as well. These values have to be redefined once the characterization of the distance measurement system can be performed in the laboratory.

In order to guarantee satisfactory performance in the specified frequency, the LQG/LTR technique designs a controller with a higher bandwidth.

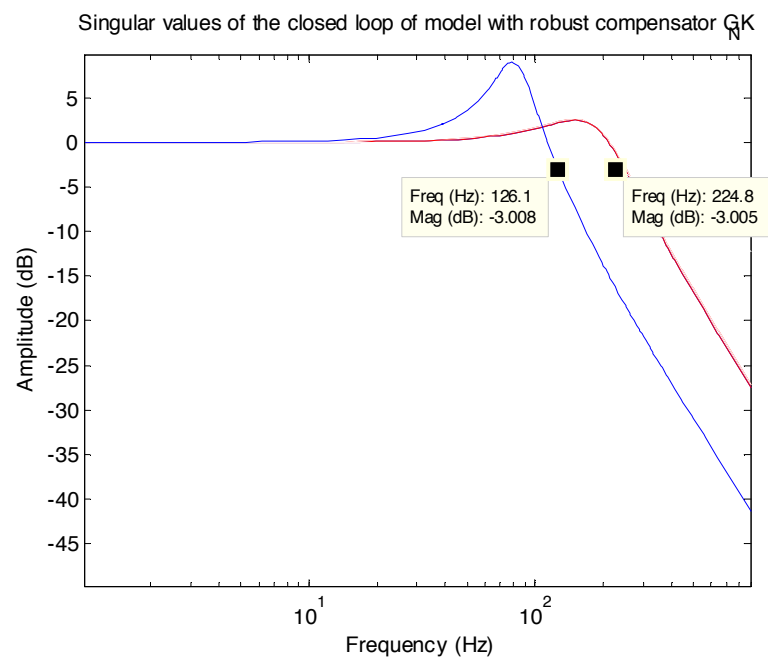
For instance, the bandwidth of the *controller A*, designed to follow the reference up to 60 Hz was found to be around 300 Hz. This high frequency imposes a high sampling frequency for the digital redesign of the controller, presented in section 8.3.1, which at the same time translates into a high sampling frequency for the DAC of the data acquisition system.

Tests for different frequencies for the digital redesign and DAC sampling frequencies for this controller were performed in the laboratory with unsuccessful results. The resulting discrete controllers were unstable or the digital system crashed before any tests could be done.

With this limitations a second controller, called *robust compensator B* was designed adding a filter to the dynamics to the previous *robust compensator A* so it could have lower bandwidth and validation tests could be performed in the laboratory.

Figure 65 shows the closed-loop singular value of both controllers A, in solid line, and B, in dashed line. It can be seen in the figure the difference on the bandwidths of both systems. The implemented filter decreased 100 Hz of the frequency response of the original system.

Figure 65 - Singular values of the closed-loop of the robust controller A in red, and B in blue



Source: Author

The additional dynamics are represented by a filter of the form of eq.(76), and it was implemented after the robust *controller A* in the signal flow.

$$Filter(s) = \frac{1}{0.005s + 1} \quad (76)$$

The robust controller presented on eq.(75) has now the form of eq.(77)

$$K_f(s) = K(s) Filter(s) \quad (77)$$

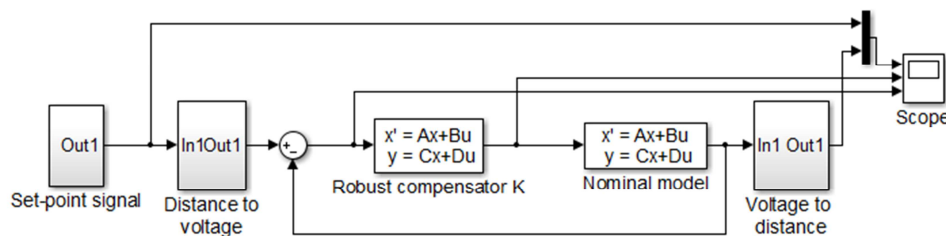
It is important to analyze and corroborate the nominal stability of the closed loop with the dynamics of the filter before implementing the digital version on the real system.

The *robust compensator B* was successfully digitalized and the sampling frequencies of the DAC and the ADC converters of the data acquisition boards were within the operational limits. For this reason this controller was the one used for validation on the real Fabry-Pérot prototype of section 9.3.5.

### 9.3.4 Simulation Results of the Robust Compensator

Figure 66 shows the block diagram of the MIMO robust controller simulation. Contrary to the PI controller, the robust compensator considers the coupling between the different inputs and outputs of the system, and calculates the control effort taking into account the three error signals.

Figure 66 - Block diagram of the MIMO robust controller simulation



Source: Author

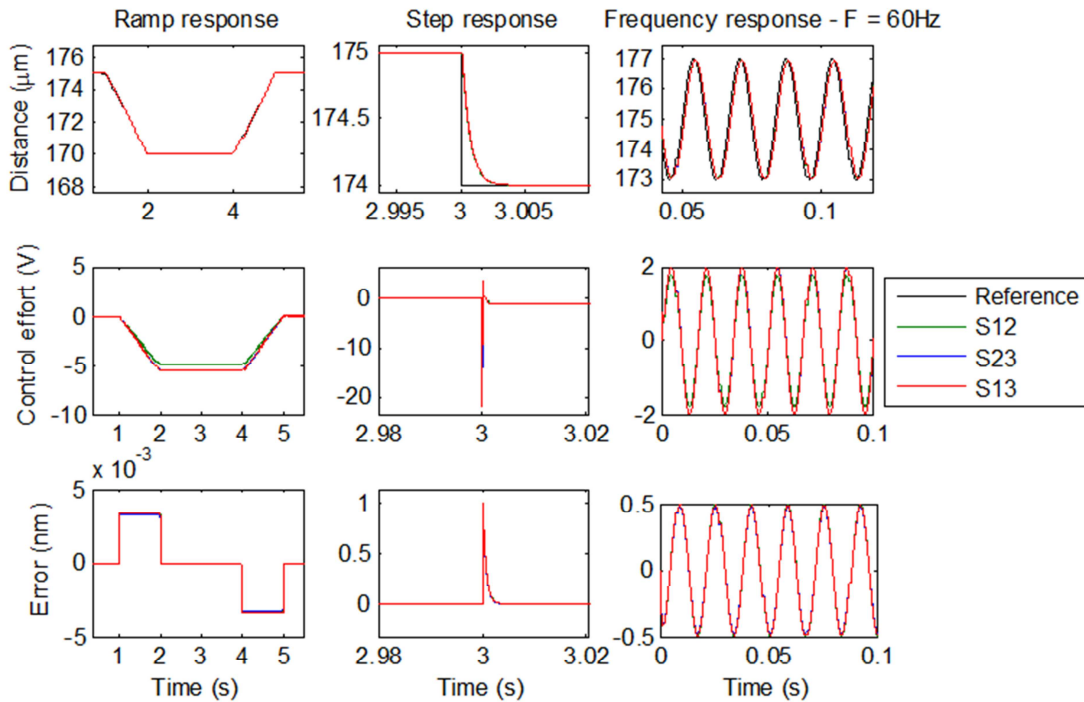
Figure 67 shows the simulated response of the Fabry-Pérot model when controlled by the *robust controller A*, presented in the previous section.

It can be seen on the responses that the system follows the reference signals without overshoot and with null steady state error. The settling time for a step input is of 3 ms and the system follows with minimum error a 60 Hz signal which shows the system bandwidth is well beyond this frequency, as expected.

Both in the simulated ramp and step responses have null steady state standard deviation, meaning the continuous-time system dynamics does not insert noise to the system model. However the digital control system might not present the same optimal characteristics.

The control effort on the three experiments is within the limits of the system. However it can be seen that the control effort on the step signal has a drastic change of -20 V which is not adequate for the safety of the piezoactuators. That is why a ramp signal is recommended to safely operate the system.

Figure 67 - Response of the Fabry-Pérot system model using the robust controller A.



Source: Author

Table 17 summarizes the characteristics of the response of the system when controlled with the robust *compensator A*.

Table 17 Summary of the response characteristics of the FP system model when controlled with a robust compensator A

Parameter	Simulation values
Steady-state standard deviation	0 nm
Steady-state error	0 nm
Delay time (50% of final value)	0.5 ms
Overshoot	0 nm
Settling time	3 ms
Bandwidth	300 Hz

On the other hand, Figure 68 shows the simulated response of the Fabry-Pérot model when controlled by the *robust controller B*, presented in eq.(77) of section 9.3.3.

One main difference of this controller is that the extra dynamics make the step response have an overshoot and higher accommodation time of 27 ms.

The bandwidth of the system is lower than the previous robust controller. On 60 Hz the magnitude of the frequency response decays to 70% of the expected value as it can be seen in Figure 68.c.

The system follows the reference signals with null steady-state error, and both in the ramp and step responses the system have practically null steady-state standard deviation. The noise value, which is practically null can be interpreted as numerical error of the computation.

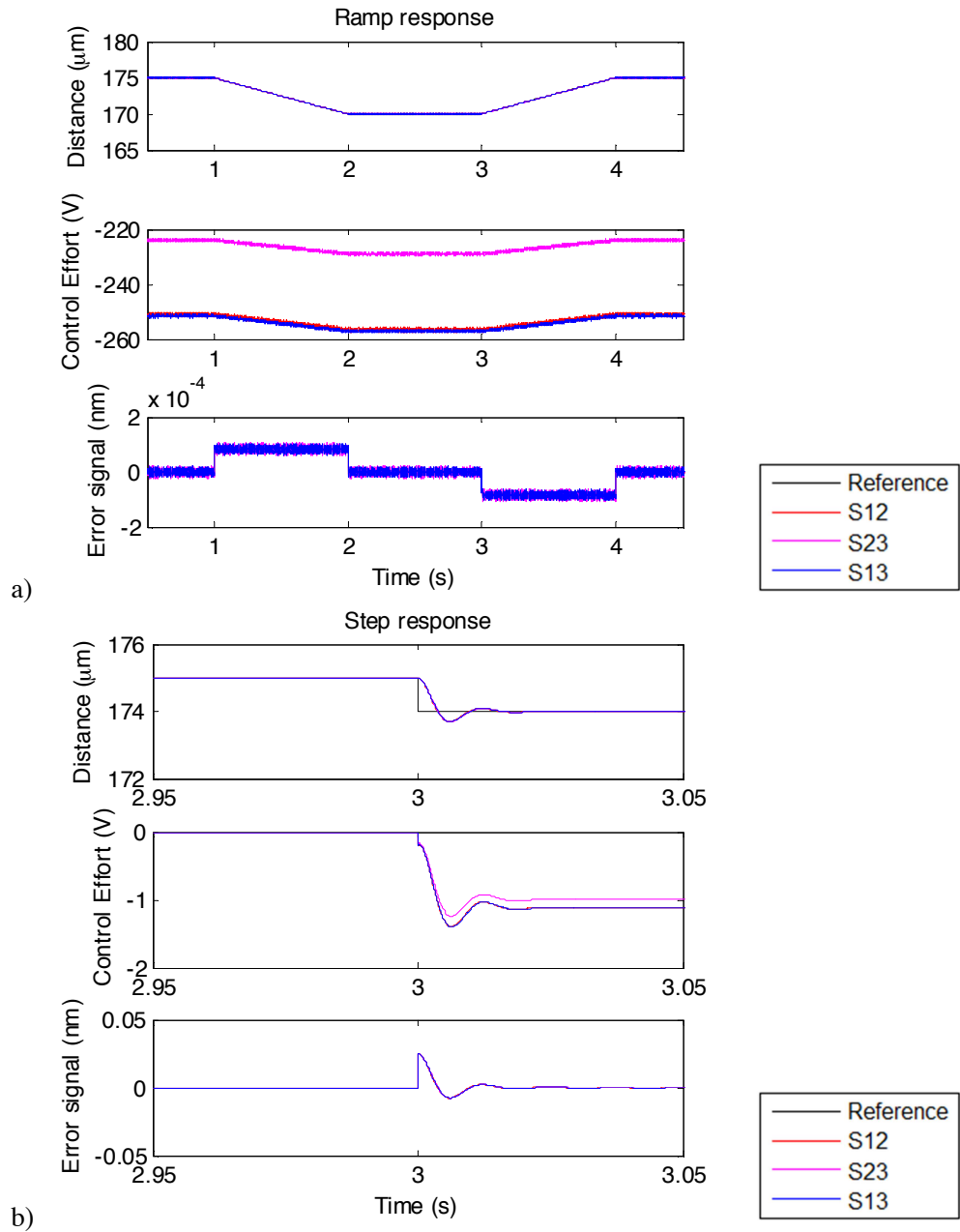
The control effort on the three experiments is within the limits of the drivers, even for the step response, which makes it safe to validate this response on the real system.

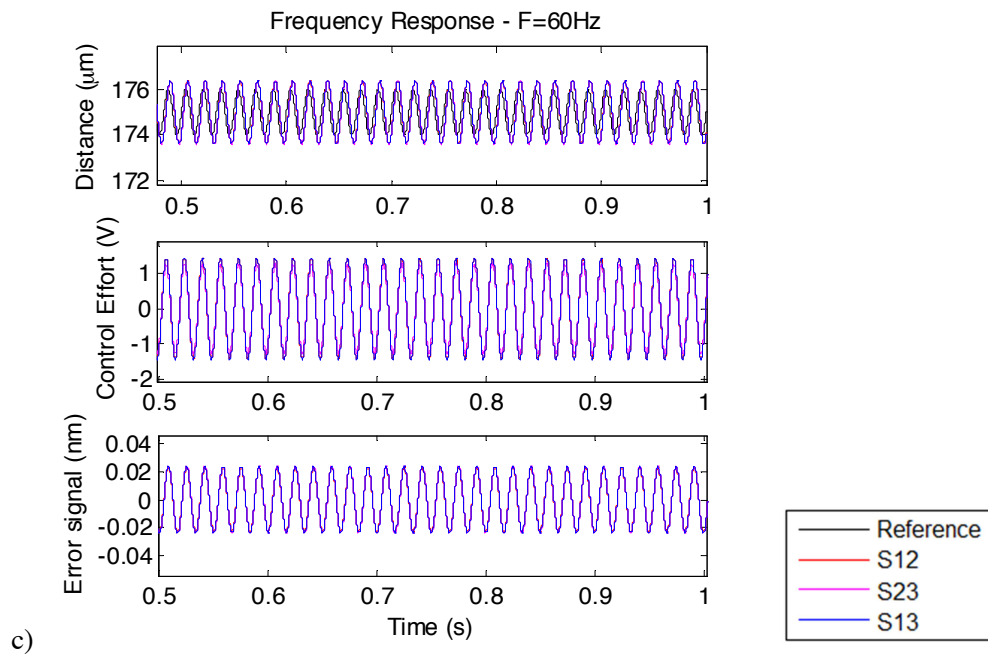
Table 18 summarizes the characteristics of the response of the system when controlled with the robust compensator B.

Table 18 Summary of the response characteristics of the FP system model when controlled with the robust compensator B.

<b>Parameter</b>	<b>Simulation values</b>
Steady-state standard deviation	2.7178e-07 nm
Steady-state average error	0 nm
Overshoot	0.3 $\mu$ m
Settling time	27 ms
Bandwidth	60 Hz

Figure 68 - Response of the Fabry-Pérot system model using the robust controller B.



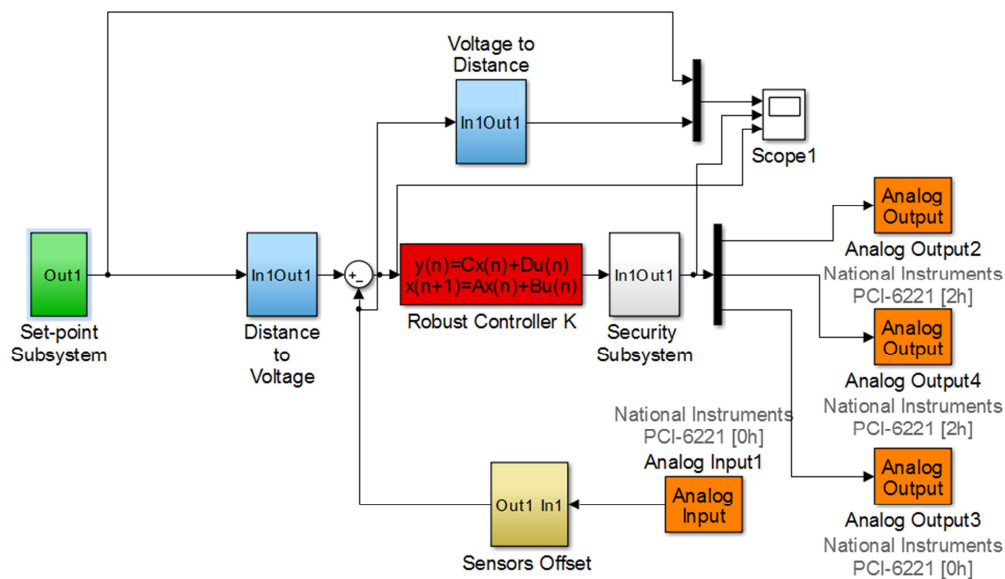


Source: Author

### 9.3.5 Experimental Validation of the Robust Compensator

Figure 69 shows the block diagram of the real-time experimental set-up for the control system of the Fabry-Pérot prototype with the *robust compensator B*.

Figure 69 - Real time robust controller for the Fabry-Pérot prototype



Source: Author

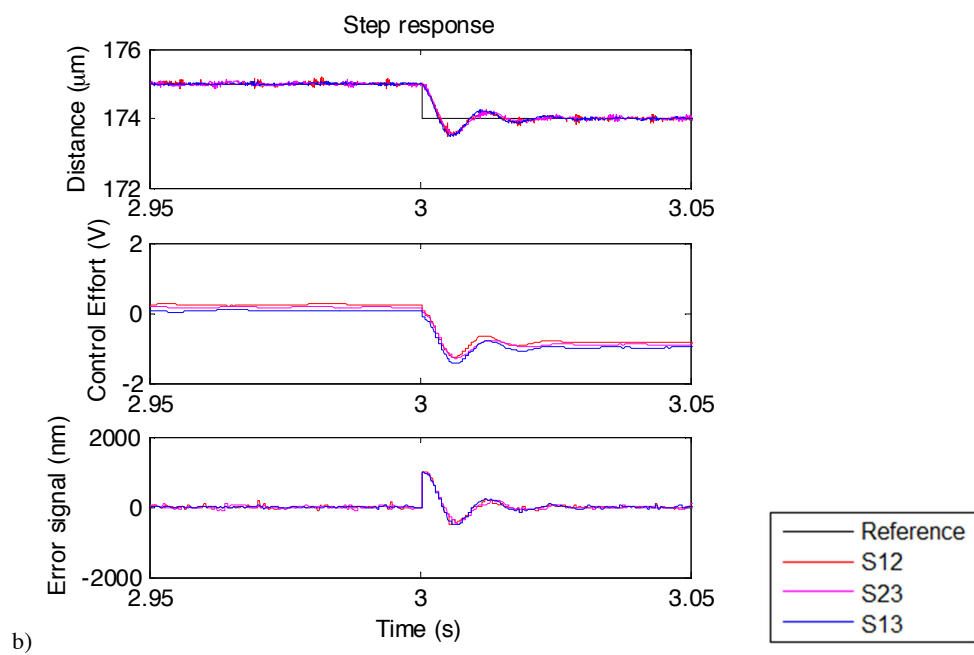
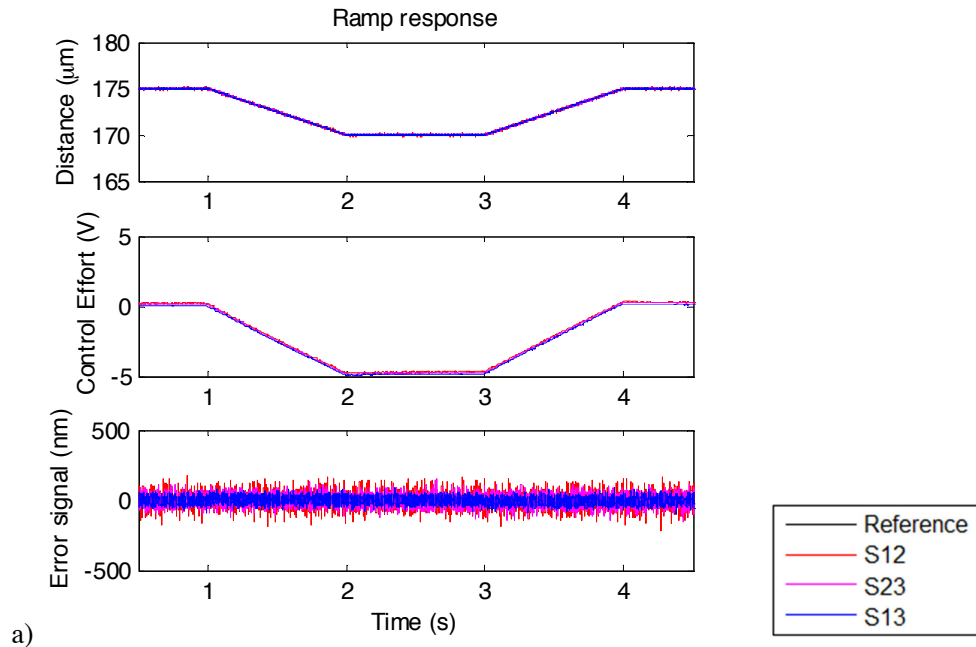
The green set-point subsystem, blue units conversion subsystems, orange analog-to-digital converters and the yellow system to calibrate the sensor initial position, have the same function as in the PI controller simulation of Figure 57.

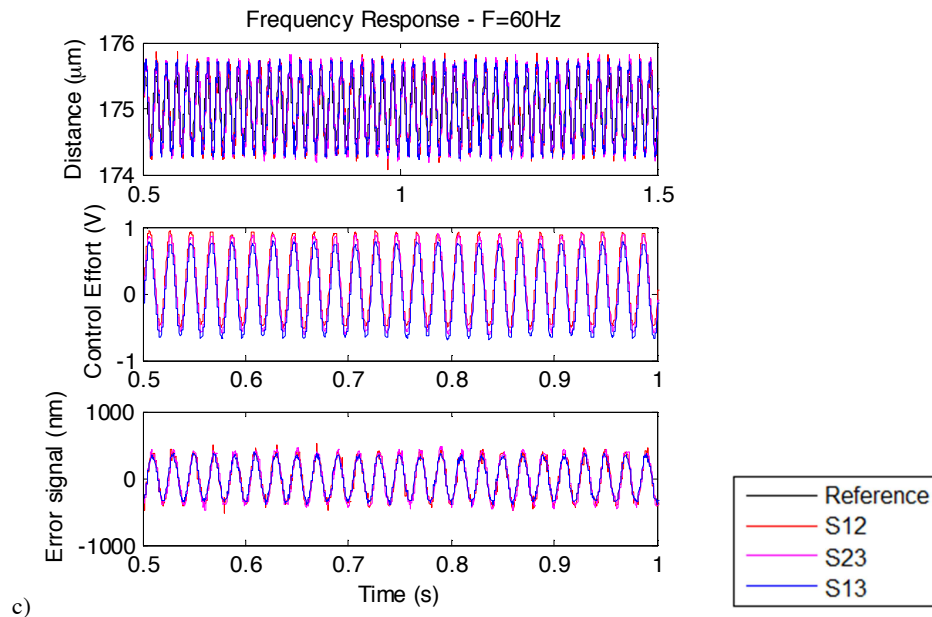
The robust controller, in red, calculates the control signal for the three channels according to the error value and, after passing through a saturation block for protecting the NI-DAQ, it is converted to an analog signal through the orange Analog Output blocks with a sampling frequency equal to the frequency of the digital redesign which was of 2000 Hz.

The orange Analog Input block converts the analog voltage of the MC900 output to a digital value at 10000 Hz. The yellow block on the feedback loop corrects the initial offset of the sensors. The calibrated voltage value is the feedback signal of the control loop.

Figure 70 shows the response of the real plant of the Fabry-Pérot prototype when controlled by the *robust compensator B*.

Figure 70 - Response to different set-point signals of the real Fabry-Pérot system using a robust controller.





Source: Author

As can be seen in the figure, the response of the real system fits well the response of the model of the system with equal settling time and bandwidth, which validates the model and the discrete controller.

The standard deviation observed in the open-loop system is 35.8 nm, yet the standard deviation observed in the steady-state signal in closed-loop for the ramp and step response is of 38.5 nm. As with the PI controller, the difference of almost 3 nm is not present in the simulated responses summarized on Table 18. Possible causes for this additional noise in the system include bad performance of the discrete controller due to the digital redesign process, an inadequate control technique or a high modeling error. Also, the 3 nm that are not present on the simulations may be missing due to the lack of consideration of the dynamics introduced by the analog-to-digital and digital-to-analog converters.

Table 19 summarizes the characteristics of the response of the system when controlled with the robust compensator.

Table 19 Summary of the response characteristics of the FP system when controlled with robust compensator B

Parameter	Validation values	Simulation values
Open-loop noise RMS	35.8 nm	0 nm
Steady-state standard deviation	38.5 nm	2.7178e-07 nm
Steady-state average error	0 nm	0 nm
Overshoot	0.5 $\mu$ m	0.5 $\mu$ m
Step delay time (50% of ss)	2 ms	2 ms
Step settling time	27 ms	27 ms
Cut-off frequency	60 Hz	60 Hz

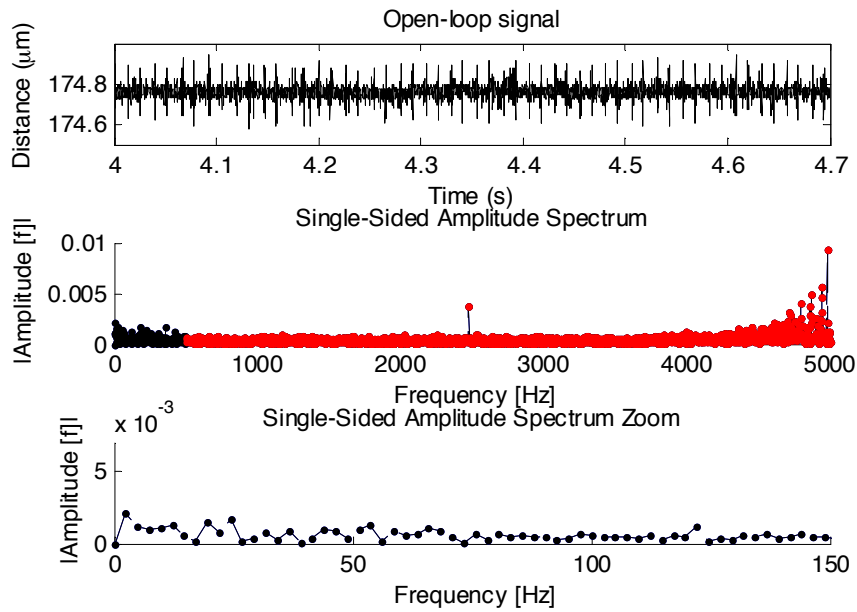
### 9.3.5.1 Spectral Analysis of the Real Response

To analyze the spectrum of the acquired signals, a fast Fourier transformation was done to plot the single-sided amplitude spectrum. Since the sampling frequency of the ADC in the robust control system was set to be 10000 Hz, the spectrum shows the frequency components up to 5000 Hz.

Figure 71 shows the spectrum of the output of the system in open-loop. The first subplot is a portion of the temporal signal to be analyzed. The second one shows the complete single-sided amplitude spectrum. Since the sampling frequency of the ADC was set to 10000 Hz, the spectrum shows the frequency components up to 5000 Hz, but the frequency components beyond 500 Hz, in red, are filtered to analyze only the dynamics of the control loop and not the high-frequency components of the data acquisition system. Finally, the third plot presents a zoom from 0 to 150 Hz of the previous plot to show in detail the dynamics of the zone of interest.

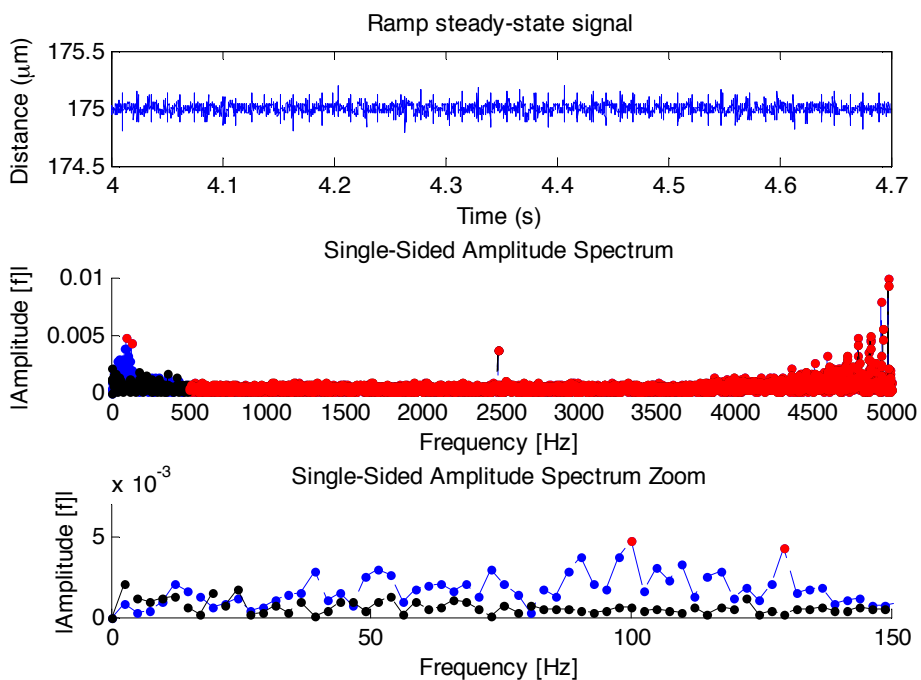
This spectrum shows high-energy frequencies starting in 4500 Hz and a dominant frequency in 2500 Hz. As presented in section 4.7.1, the source of these frequency components is the data acquisition board used in the laboratory, and not the measurement system.

Figure 71 - Spectrum of the acquired signal in open-loop.

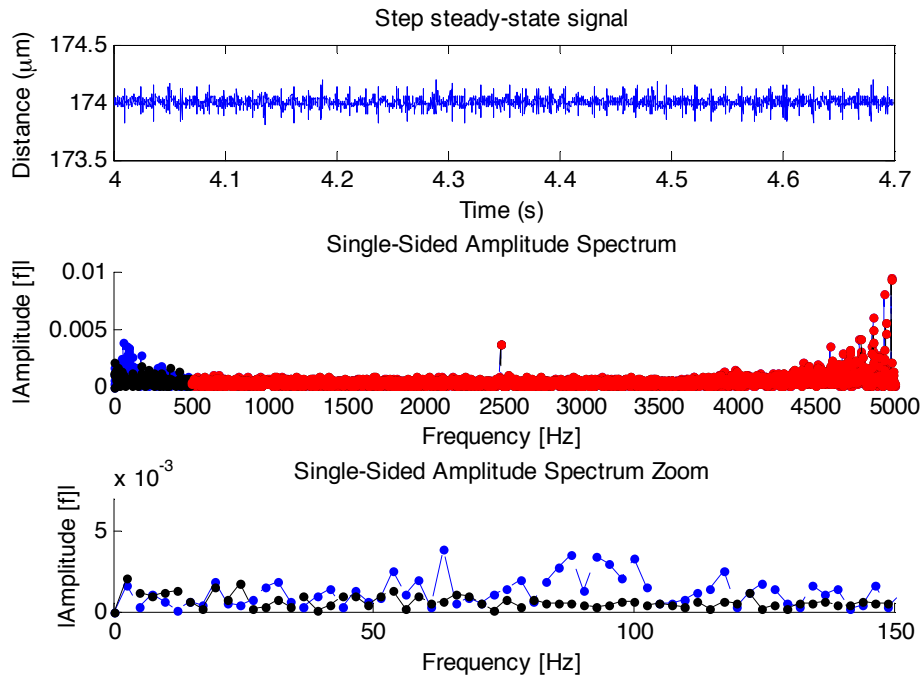


Source: Author

Figure 72 - Spectral analysis of the ramp (a) and step (b) closed-loop response, in blue, for the robust controller. The open-loop spectrum is also plotted in black for visual comparison. The red points are not considered on the statistical analysis.



a)



Source: Author

Figure 72 shows the same plots for the ramp and step response of the Fabry-Pérot system. The open-loop spectrum of Figure 71 is also plotted in black for visual comparison.

Comparing the spectrum of the open-loop signal with the closed-loop signal for both, the step and the ramp responses up to 150 Hz, it can be concluded that the robust control system has higher energy than the open-loop system between 50 and 100 Hz. The performance of the control loop can improve significantly in terms of the noise if these frequencies are treated to be as close as possible to the open-loop dynamics.

Using the Parseval Theorem, and analyzing the band of frequencies up to 500 Hz, the noise for the open-loop signal is of 6.5 nm and the closed-loop signal is of 11.2 nm. As with the PI control system, this noise error is lower than the noise calculated using the time-domain signal (35.8 in open-loop and 38.5 in closed-loop), because it filters the high-frequency noise.

The difference between the PI and the robust controller can also be appreciated. The high energy between 50 and 100 Hz in the case of the robust controller is clearly one of the reasons why the robust controller is noisier than the PI controller. However other noise sources and the nature of the high frequency noise for both open and closed loops is still uncertain and to study it is proposed as future work.

## 10 DISCUSSION AND CONCLUSIONS

A suitability analysis for the instrument is required in the early stages of the controller design. As it was shown, the suitability analysis performed in our case showed that a new control board and actuator drivers were necessary in order to meet the performance requirements. This analysis also showed that the three 200 um MC900 modules required recalibration.

The distance measurement system noise was studied thoughtfully and characterized to define the maximum resolution of the distance measurement system. The main result of this study was the identification of a noise source in the data acquisition components used in the laboratory. The subsystem composed by two computers, two NI-DAQ 6221 acquisition boards, cables and PCI slots introduces measurement noise with a mean as high as 350 nm and as low as 22.9 nm. The conclusion was that the magnitude of the measurement error depends on the hardware. Considering that the data acquisition boards will be replaced for a dedicated control board with high-precision analog-to-digital converters and low noise electronics in the final stage of the instrument implementation, the effort to minimize the noise from the NI-DAQ 6221 was not considered in this work. Based on the results of this study, the instrument performance was specified to have a measurement noise as low as the noise of the acquired MC900 signal in open-loop.

As a consequence there is the need for characterizing the measurement system with the final digital acquisition system, in order to decide whether the FOGALE system is able to provide the resolution specified by the scientific needs or not. Another measurement system, manufactured by LION Precision, was presented as a possible solution in the case it is decided in the future that the FOGALE system is not adequate.

The characterization of the actuator subsystem led to the conclusion that having a frequency response of 50 Hz the drivers by voltage were the electronic components that limited the most the performance of the entire system. Another solution based on a driver by charge was proposed by other team members. This proposed driver by charge not only has a higher bandwidth but gives a compensation of 98% of the hysteresis behavior of the piezoelectric actuators, linearizing the system and simplifying the control problem.

The study and understanding of the functioning principles and characteristics of the piezoelectric actuators was the base to the physical linear model of the piezoelectric actuators.

A sixth-order model for the complete system was developed considering the three second-order models of the actuators and it was validated comparing the model against every data point of the frequency response of every input and output combination measured with a Dynamic Signal Analyzer. The resulting modeling error shows that the model has high error in the surroundings of the two main resonance frequencies of the system. This is in part due to the low-resolution of the digital signal analyzer with which the real data was acquired and in part due to higher dynamics on the system not taken into account in the model.

A second modeling technique was used, developing a graphical user interface to identify the system using a gray-box approach. Even though the identified model has better fit to both the step and the frequency response, which translates in significant lower modeling error in the whole studied spectrum (up to 1 kHz), both models present the same cross-over frequency of the modeling error at around 200 Hz, which imposes a limitation in the frequency response of the control system design following the LQG/LTR technique.

The models designed for the piezoelectric actuators and the complete Fabry-Pérot instrument represent satisfactorily the system real behavior up to the first resonant frequency. Given that both models have the same limitations for the design of the controllers, the parametric physical model was the chosen approach given that it provides a deeper understanding of the dynamics of the system.

For the validation tests on the instrument's prototype, the digital system resolution and frequencies of operation were defined in section 8. The number of bits for the digital converters was specified following a 10-order criterion to be of 20.4 bits for the high-resolution FP and of 19.4 bits for the low-resolution FP, in order to achieve the desired measurement resolution of 3 nm for the scientific applications. Besides the electronic noise introduced by the actual acquisition boards NI-DAQ 6221, the system theoretically cannot provide a resolution better than 12 nm given that its analog to digital converters has 16 bits operating at a 20 V measurement range.

The FOGALE distance measurement system operates at a fixed frequency of 10000 Hz. This configuration allows to measure high frequency perturbations but at the same time introduces high-frequency measurement noise. The lower the bandwidth, the lower the electronic noise and better resolution; but at the same time, measuring the distance at a lower frequency limits

the velocity of response of the control system to which the sensors are given feedback, making it unable to respond and compensate high frequency perturbations.

A careful compromise between resolution and bandwidth had to be defined. Since perturbations higher than 200 Hz are not ruled out in the environment of the telescope, as presented on the vibrational study of section 8.2, it was decided to specify the control frequency as the cut-off frequency of the complete system, which is around 450 Hz. The definition of the sampling frequency for the analog-to-digital converters was done using a 10x criteria to avoid aliasing effect. Therefore, the ADC of the final system should sample at a 4500 Hz rate.

The future design of the control board must take into consideration the frequencies specifications presented in this work to guarantee the performance requirements for scientific applications. In the end, the selection of the components is a compromise between the bandwidth of the control system and the cost, availability and resolution of the required components.

Since the proportional-integral compensator was not the main focus of the project and was solely designed as a benchmark for the robust controller, the PI control system was simplified and considered as three SISO decoupled systems, ignoring the coupling of the piezoactuators with the mirror mass. The proportional and integral constants were found using a genetic algorithm. This approach was a methodological solution to improve the popular trial and error approach. Even though the genetic algorithm is not exact and delivers a new pair of PI parameters every time the algorithm is used, the step response performance of each one of the proposed parameters satisfied the specified requirements of no overshoot and null steady state error. In the end, the faster PI controller proposed, with an accommodation time of 100 ms was chosen for validation in the Fabry-Pérot prototype.

The simulated responses to the step, ramp and sine wave inputs of the control system with the parametric model of the Fabry-Pérot, had equal performance results as the responses of the control system with the prototype in the laboratory, except for the measurement noise of 37.5 nm. The similar dynamic behavior validates both the model of the instrument and the nanopositioning controller. The measurement noise, however, is 2 nm higher to the noise of the MC900 output signal acquired with the NI-DAQ 6221 in open-loop. Possible causes for this additional noise in the real system include bad performance of the discrete controller due

to the digital redesign process, an inadequate control technique or a high modeling error. Also, the simulation did not include the digital converters which can introduce error as well. Further analysis is required in order to determine the precise cause and solution.

In conclusion, the proportional-integral controller tuned with the genetic algorithm achieves the performance specifications with limited low bandwidth. The single-sided spectrum of the three responses of the system shows that the control system does not introduce high-frequency noise to the response.

A robust controller was designed following the LQG/LTR technique defining the same performance specifications and an operating frequency higher than 60 Hz. The data acquisition system used in the laboratory imposes yet another restriction on the sampling frequencies. The system's maximum sampling frequency for the ADC and DAC in real-time simulations is around 10000 Hz. Which is a limitation for the redesign frequency of the digital controller.

Additional dynamics were added to the robust controller in the form of a filter in order to validate the compensator in the laboratory, considering the mentioned computational limitations. The initial robust controller had a bandwidth of 300 Hz, which had to be reduced to 60 Hz inserting a filter in the compensator path. With the filter's additional dynamics, an overshoot is present in the step response. The overshoot is an undesired characteristic because it constrains the operation at the extremes. However, it is expected that on a dedicated board, the initially proposed robust controller, with higher cut-off frequency can be implemented without any problem in the digital redesign. The overshoot is also not a big concern considering that the suggested reference signal for operation of the instrument is a ramp signal to avoid high stress in the piezoactuators given by drastic changes in the input voltage.

The final robust controller used for validation presents faster response than the PI controller, with an accommodation time of 10 ms and 60 Hz of bandwidth. The steady-state average error is null and the noise error in open-loop is 3 nm lower than the closed-loop noise.

Different to the PI control system responses, the single sided spectrum of the three responses of the robust control system shows that the compensator introduces high-energy components in the 50-150 Hz frequency range. These components can be the reason why the standard deviation of the robust controller is higher than the PI controller.

The Parseval theorem permits calculate the standard deviation for a determined region of the spectrum. Results show the same behavior of lower noise in open-loop than in closed-loop.

Both the robust controller designed following the LQG/LTR technique and the proportional-integral controller tuned with a genetic algorithm, achieve the performance requirement of following the reference with null steady-state error. Comparing both controllers, the robust controller is by far the best suited for the Fabry-Pérot instrument in terms of performance and stability because of its higher bandwidth and robustness to modeling errors. However, the main advantage of the Proportional-Integral controller is the low computational cost for its implementation.

It was shown in this project that the actual resources available in the laboratory, specifically the data acquisition system with its low resolution ADC, high measurement noise and limited sampling frequency for real time simulations, limits the design and validation of the control system. However, by understanding each of the limitations and designing a feasible control system under the given restrictions, it was possible to validate the proposed techniques and procedures.

The main products of the work done during this research project are summarized in the following items:

- Summary of the physical and electric characteristics of the instrumentation of the Fabry-Pérot interferometer.
- Study of the FOGALE measurement system and data acquisition boards noise.
- Study and compilation of the characteristics of the piezoelectric actuator subsystem.
- 2th order model for the APA400MML piezoelectric actuator.
- 6th order model for the BTFI Fabry-Pérot interferometer.
- Genetic algorithm for tuning the Proportional Integral parameters.
- Proportional Integral controller.
- Graphical user interface to design a controller using the LQG/LTR technique.
- Robust controller following the LQG/LTR technique.
- Real time simulations with the model of the Fabry-Pérot.
- Real time validations of the control system with the Fabry-Pérot prototype.

In this way the main objectives proposed to this work were satisfactorily achieved.

The information compiled in this document and the addressed main products of this work represent the fundamental bases to a successful implementation of the BTFI Fabry-Pérot interferometer in the SOAR telescope.

## 11 FUTURE WORK

The developed work of this dissertation is part of the study and definition phase of the instrument and is the base for several future works before the Fabry-Pérot interferometer starts its commissioning phase at the SOAR telescope.

As mentioned in section 3.1, the final mirrors of the Fabry-Pérot interferometer are currently in manufacturing stage, and all the modeling and characterization of the system was made with a temporary mirror borrowed from a former Fabry-Pérot. If the final mirrors present major differences in terms of the weight and mass distribution on the disk, the model of the Fabry-Pérot system would change significantly and a whole new model and control system must be made. Also a temperature dependence of the system dynamics must be modeled and the control system must be updated to this model.

If future vibrational studies on the environment of the telescope confirm that the bandwidth of the control system needs to be higher, the modeling error should be improved around the resonant frequencies of the system and a new robust compensator must be designed.

A control board hosting the microprocessor and analog to digital converters must be designed taking into account the minimum resolution and sampling frequencies of every component specified on chapter 8. The control system must be compiled and implemented in the microprocessor, eliminating the need of using a computer to control the system. The computer will only host the graphical user interface where the scientists enter the operation data, which has to be specified and developed as well.

Once the control system is compiled in the electronic control board, a long operation stability test must be performed to see if it is robust to environment disturbances as mechanic vibrations, and temperature and humidity changes.

The distance measurement system noise characterization must be made with the final analog-to-digital conversion system, to corroborate that the system can achieve the scientific requirement on resolution. And the three MC900 modules of 200  $\mu\text{m}$  of measurement range have to be recalibrated in order to measure the 250  $\mu\text{m}$  of stroke of the low resolution Fabry-Pérot.

Since the FOGALE distance measurement system operates at a fixed frequency of 10000 Hz and the analog-to-digital converter sample frequency will be set to 4500 Hz an antialiasing filter can also be implemented in the distance measurement system.

Calibration procedures of the start-up system and during the instrument operation phase must be defined and developed in order to compensate the offset of the distance measurement system and the non-parallelism of the Fabry-Pérot mirrors.

And lastly a security start-up system and initial automated calibration system for the parallelism of the Fabry-Pérot mirrors must be specified and planned.

The implementation, integration of the Fabry-Pérot to the BTFI instrument and the commissioning phase in the SOAR telescope represent the further stages of the project and its activities are yet to be defined.

## REFERENCES

ADRIAENS, H.J.M.T.S.; DE KONING, W.L.; BANNING, R. Modeling piezoelectric actuators. *Mechatronics*, **IEEE/ASME Transactions on**, 5(4): 331-341, 2000. DOI: 10.1109/3516.891044

AGILENT TECHNOLOGIES, **Understanding reading accuracy and resolution in a 61/2-digit DMM**, 2006

ÅSTRÖM, K.J.; WITTENMARK, B. **Computer controlled systems: theory and design**. New Jersey: Prentice-Hall, 1984.

ATHANS, M. A tutorial on the LQG/LTR method. American Control Conference. **IEEE** (pp. 1289-1296). 1986.

BLAND-HAWTHORN, J.; ALLINGTON-SMITH, J. 3D spectrophotometric imaging opens a new window into the cosmos. **Laser Focus World**, 46(12): 60-64, 2010. Available at: <<http://www.laserfocusworld.com/articles/print/volume-46/issue-12/features/astronomical-imaging-3d-spectrophotometric-imaging-opens-a-new-window-into-the-cosmos.html>> Access: 20 March 2014.

CAVALCANTI, L.E.M. **Sistema de controle para o filtro óptico sintonizável Fabry-Perot do instrumento BTFI**, 95p. Dissertação (Mestrado). Universidade de São Paulo. Escola Politécnica. Departamento de Sistemas Eletrônicos, São Paulo, 2011.

CASTRUCCI, P.L.; BITTAR, A. E SALES, R. M. **Controle Automático**. Editora GEN/LTC, Rio de Janeiro, RJ, 2011. ISBN: 978-85-216-1786-0

CEDRAT TECHNOLOGIES, **Products Catalog Version 4.1**, 2013.

COMSTOCK, R.H. **Charge control of piezoelectric actuators to reduce hysteresis effects**. United States Patent nº US 4,263,527. 1981. Available at : <<http://www.freepatentsonline.com/4263527.pdf> > Access: 20 March 2014.

CRUZ, J.J. **Controle robusto multivariável: o método LQG/LTR**. São Paulo: Editora da Universidade de São Paulo, 1996.

DORATO, P., LEVIS, A. (1971). Optimal linear regulators: the discrete-time case. *Automatic Control*, **IEEE Transactions on**, 16(6), 613-620.

GARCIA, C. **Modelagem e Simulação de Processos Industriais e de Sistemas Eletromecânicos**. São Paulo: Editora da Universidade de São Paulo, São Paulo, 1997.

FOGALE NANOTECH, **Technical Manual Capacitive Measurement system MC900**, 2008.

LION PRECISION, **Capacitive Sensor: Elite Series CPL190 & CPL290**, 2011. Available at <<http://www.lionprecision.com/capacitive-sensors/cpl190.html>>. Access: 20 March 2014.

LION PRECISION, **Error Sources: Probe/Target Angle**, 2004. Available at: <<http://www.lionprecision.com/tech-library/technotes/tech-pdfs/cap-0010-probe-tilt.pdf>>. Access: 20 March 2014.

MACIEL, W.J. **Astronomía e Astrofísica**. São Paulo: Instituto de Astronomia e Geofísica – Universidade de São Paulo, ISBN 85-85047-05-4. 1991.

MARCHIORI V.A; FIALHO F. O.; OUATTARA I. Design and realization of na electronic charge control circuit to attenuate the hysteresis of the high resolution Fabry-Pérot interferometer's amplified piezoelectric actuators. In: 22nd International Congress of Mechanical Engineering, **COBEM**, São Paulo, 2013.

NATIONAL INSTRUMENTS CORPORATION, **DAQ M Series User Manual. NI 622x, NI 625x, and NI 628x Devices**, 2008.

NATIONAL INSTRUMENTS CORPORATIONS, **Using a Digitizer for Time-Domain Measurements**, 2006.

NATIONAL INSTRUMENTS CORPORATION, **Resolution**. 2006. Available at: <<http://www.ni.com/white-paper/4806/en/>>. Access: 20 March 2014.

OGATA, K. **Discrete-Time Control Systems**. New Jersey: Prentice-Hall, 1987.

OGATA, K. **Engenharia de Controle Moderno**. 2.ed. São Paulo: Prentice-Hall do Brasil, 1993.

DE OLIVEIRA, C. M., TAYLOR, K., QUINT, B., ANDRADE, D., FERRARI, F., LAPORTE, R., ... & CARIGNAN, C. The Brazilian Tunable Filter Imager for the SOAR Telescope. **Publications of the Astronomical Society of the Pacific**, 125(926), 396-408. 2013.

PEREZ, R., AGNUS, J., BREGUET, J.M., CHAILLET, N., BLEULER, H., CLAVEL R.. Characterization and control of a 1 DOF monolitique piezoactuator (MPA). In: **Proceedings of SPIE** Microrobotics and Microassembly III, v. 4568, Newton – USA, p. 151-162. 2001.

PHYSIK INSTRUMENTE 1, Tutorial: **Capacitive Position Sensors: –Measuring Displacement with Sub-Nanometer Precision**, [http://www.capacitance-sensors.com/capacitive\\_sensor\\_tutorial.htm](http://www.capacitance-sensors.com/capacitive_sensor_tutorial.htm)

PHYSIK INSTRUMENTE 2, **Capacitive Position Sensors / Controllers for Nanometrology**. Available at: <http://www.capacitance-sensors.com/>. Access: 20 March 2014.

PIEZOMECHANIK GmbH, **First Steps towards Piezoaction**. 2010. Available at: <http://www.piezomechanik.com>. Access: 20 March 2014.

**APPENDIX A - Published Papers**



## HIGH RESOLUTION FABRY-PÉROT INTERFEROMETER – DYNAMIC SYSTEM MODELING AND NANOPositionING CONTROL SYSTEM DESIGN USING LQG/LTR TECHNIQUE

**Ana María Molina Arcila**

**Fábio de Oliveira Fialho**

Laboratório de Automação e Controle – Departamento de Telecomunicações e Controle da Escola Politécnica da Universidade de São Paulo – Avenida Professor Luciano Gualberto. Trv. 3, n° 158, São Paulo, Brasil

ammolina@usp.br

fabio.fialho@usp.br

**Fernando Orsatti**

Laboratório de Automação e Controle – Departamento de Telecomunicações e Controle da Escola Politécnica da Universidade de São Paulo – Avenida Professor Luciano Gualberto. Trv. 3, n° 158, São Paulo, Brasil

fernando.orsatti@oepe.com.br

**Victor Atilio Marchiori**

Laboratório de Automação e Controle – Departamento de Telecomunicações e Controle da Escola Politécnica da Universidade de São Paulo – Avenida Professor Luciano Gualberto. Trv. 3, n° 158, São Paulo, Brasil

victoratilio@usp.br

**Issa Ouattara**

Laboratoire d'Astrophysique de Marseille – 38, rue Frédéric Joliot-Curie, Marseille, France

issa.ouattara@oamp.fr

**Leonardo Pinheiro da Silva**

Laboratório de Automação e Controle – Departamento de Telecomunicações e Controle da Escola Politécnica da Universidade de São Paulo – Avenida Professor Luciano Gualberto. Trv. 3, n° 158, São Paulo, Brasil

leonardo.pinheiro@oepe.com.br

**Jair Pereira de Souza**

Laboratório de Microeletrônica – Departamento de Engenharia de Sistemas Eletrônicos da Escola Politécnica da Universidade de São Paulo – Avenida Professor Luciano Gualberto. Trv. 3, n° 158, São Paulo, Brasil

jpsouza@lme.usp.br

**Claudia Lucia Mendes de Oliveira**

Instituto de Astronomia, Geofísica e Ciências Atmosféricas da Universidade de São Paulo – Rua do Matão, n° 1226, São Paulo, Brasil

oliveira@astro.iag.usp.br

**Abstract.** *In this paper, we present the design of the mirror nanopositioning controller of the state-of-the-art Fabry-Pérot interferometer to be installed in the Brazilian Tunable Filter Imager (BTFI) on the Southern Astrophysical Research (SOAR) telescope in Chile. The three-input-three-output multivariable (MIMO) Fabry-Pérot system is composed of three high-range Amplified Piezoelectric Actuators (APA) of 230  $\mu\text{m}$  stroke and three 400  $\mu\text{m}$ -range capacitive measurement systems. Its positioning control system is specified to achieve a maximum steady-state noise of 3nm rms. A sixth-order non-minimum phase complete system model was built on top of a second-order piezoelectric actuator model with hysteresis effect compensation. The multivariable robust controller was designed following the Linear Quadratic Gaussian/Loop Transfer Recovery (LQG/LTR) method. The built controller was validated in the real system and its performance was compared against a proportional-integral (PI) controller as benchmark. Simulation results show that the control algorithm is valid.*

**Keywords:** *Dynamic Modeling, Multivariable Systems, Robust Controller, Fabry-Pérot Interferometer, Nanopositioning Systems.*

Ana María Molina Arcila, Fábio de Oliveira Fialho, Fernando Orsatti  
High Resolution Fabry-Pérot Interferometer – Dynamic System Modeling And Nanopositioning Control System Design

## 1. INTRODUCTION

The Brazilian Tunable Filter Imager (BTFI) is a highly versatile, new technology, tunable optical imager to be used both in seeing-limited mode and at higher spatial fidelity using the SAM Ground-Layer Adaptive Optics facility (SOAR Adaptive Module) which is being deployed at the SOAR telescope. The BTFI employs Fabry-Perót interferometers in order to achieve high spectral resolutions up to  $R \sim 30,000$  (Oliveira et al, 2013).

A scanning process is required to provide 2D-images within a given spectral band using a Fabry-Perót interferometer. Such process is implemented by changing the distance between its two highly reflective parallel mirrors. Current Fabry-Perót interferometers are designed to work in a fixed spectral resolution and allow for an initial adjustment of the distance between the mirrors in a range of  $10 \mu\text{m}$  with a scan range of  $2 \mu\text{m}$ . The proposed Fabry-Perót interferometer is designed to work in a larger range of spectral resolutions ( $R \sim 1000$  to  $R \sim 30000$ ), which requires a range for the distance between the plates from zero to at least  $200 \mu\text{m}$ . To meet such specific requirement, high-excursion piezoelectric actuators (APA400MML, manufactured by CEDRAT Technologies Co) and high-sensitivity capacitive sensors compose the feedback nanopositioning system. Such feedback control system is needed to set and control the desired distance between the plates and is the aim of this work to develop different approaches to the design of a successful controller for the BTFI Fabry-Perót system.

For the purpose of designing the control system, a parametric second-order model of the piezoactuator was created for the specific stack actuator APA400MML. The parametric sixth-order model of the Fabry-Perót interferometer was created on top of the piezoactuator model. The result is a linear, time invariant model of the system.

With the parametric model of the Fabry-Perót system, the linear quadratic Gaussian with loop transfer recovery LQG/LTR robust MIMO (multiple input multiple output) controller design technique, presented in Athans (1986), was applied. This technique was chosen because it ends with a robust controller, able to reject disturbances and reject noise measurement with stability guaranteed in its entire range of operation. Another approach implemented for the controller was using the classic Proportional-Integral SISO (single input single output) design.

The paper is organized in the following way: Section 2 describes the instrumentation and physical configuration of the device, followed by a description of the parametric second-order model of the piezoactuators and the sixth-order model of the Fabry-Perót interferometer (Section 3). The control problem is introduced in Section 4, and the control design is presented in Section 5. The simulated and experimental results are presented in Section 6 and 7. Finally, the results are discussed in Section 8.

## 2. FABRY-PERÓT INSTRUMENT

The Fabry-Perót interferometer is composed of two parallel highly reflecting circular glass plates (commonly referred as the mirrors, or etalon). One plate is mounted firmly in a cylindrical mechanical system that comprises the body of the Fabry-Perót interferometer, and the second one is mounted on the same cylinder through three piezoelectric actuators (or piezoactuators), used for fine-positioning the mirrors. The piezoactuators APA400MML are solid-state long-stroke actuators based on the expansion of the active material and on a mechanism to amplify the displacement (CEDRAT 2013), allowing a maximum displacement of  $250 \mu\text{m}$  at  $150 \text{V}$ . Three capacitive sensors measure the distance between the two plates of the interferometer for feedback, with sub-nanometer resolution. Such capacitive sensors are MCC10HS ones, which have metal-resin technology and triaxial technology manufactured by FOGALE Nanotech Company.

Each of the three MCC10HS is fixed to the Fabry-Perót mount and the measurement target of each piezoactuator is fixed to the upper mirror of the etalon. In this way the sensors always measure the distance between the upper mirror and the fixed position of the sensor. The offset between the sensor fixed position and the bottom mirror is corrected a priori.

The outputs of the capacitive sensors are connected directly to MC900 modules. Such modules convert the capacitance of the sensors measure into a voltage value that is proportional to the measured distance. The modules output varies from 0 to 10 volts and the sensitivity can be calibrated based on the desired measurement range. The bandwidth of the MC900 modules is set and fixed in  $10 \text{kHz}$ .

A picture of the Fabry-Perót etalon and the complete instrumentation of the system is shown in Fig. 1.

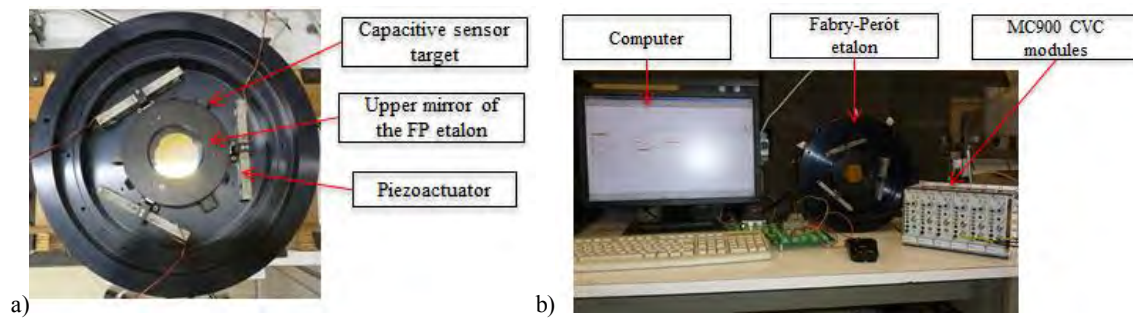


Figure 1. (a) Fabry-Perot upper mirror and piezoactuators. There is one measurement target between two piezoactuators, separated 60 degrees each. (b) Fabry-Perot control system instrumentation.

### 3. FABRY-PERÓT MODEL

#### 3.1 Piezoactuator second-order model

The overall mechanical behavior of the piezoactuator practically equals that of a single mass-spring-damper system (Adriaens et al., 2000). The differential equation used in the model of the piezoactuator system, is the well-known general differential equation for linear time invariant second-order systems written as:

$$m\ddot{y} + c\dot{y} + ky = cu + ku \quad (1)$$

Where  $y$  and  $u$  represent the actuator displacement and input voltage, respectively. The effective mass  $m$ , in Eq. (2) is a function of the natural frequency  $Wn$ , and the stiffness of the piezoactuator  $k$ , which is specified in the piezoactuator datasheet (CEDRAT TECHNOLOGIES, 2013).

$$m = \frac{k}{Wn^2} \quad (2)$$

The damping coefficient  $c$ , is calculated as in Eq. (3):

$$c = 2m\zeta Wn \quad (3)$$

where  $\zeta$  is the damping coefficient, calculated as a function of the gain  $P$ , of the natural frequency  $Wn$ , as shown in Eq.(4). Both  $P$  and  $Wn$  are inferred from the piezoactuator frequency response.

$$\zeta = \sqrt{\frac{1}{4(P^2 - 1)}} \quad (4)$$

These equations are applied to the three piezoactuators of the system; therefore  $m_1$ ,  $c_1$ , and  $k_1$  refer to these variables in piezoactuator 1;  $m_2$ ,  $c_2$  and  $k_2$  to the variables in piezoactuator 2; and  $m_3$ ,  $c_3$  and  $k_3$  for piezoactuator 3. A small time delay  $\tau$  was introduced to the model to give a good fit to the phase curve of the real system frequency response in Fig. 3.

After Laplace transformation of Eq. (1) the transfer function of the piezoactuator can be written as:

$$\frac{Y(s)}{U(s)} = \frac{cs + k}{ms^2 + cs + k} e^{-\tau s} \quad (5)$$

#### 3.2 Identification of the piezoactuator second-order model

To build a model for the piezoactuators, the frequency response of the system was taken using a Dynamic Signal Analyzer (DSA HP35665A), where a sinusoidal input signal of 1 V of amplitude over the frequency range of interest (1 Hz to 3 kHz) was applied to the piezoactuator. The resulting low displacement of the piezoactuator ( $\pm 1 \mu\text{m}$ ), in the  $z$  direction as shown in Fig. 2, was measured by the capacitive sensors and fed back to the DSA.

Ana María Molina Arcila, Fábio de Oliveira Fialho, Fernando Orsatti  
High Resolution Fabry-Pérot Interferometer – Dynamic System Modeling And Nanopositioning Control System Design

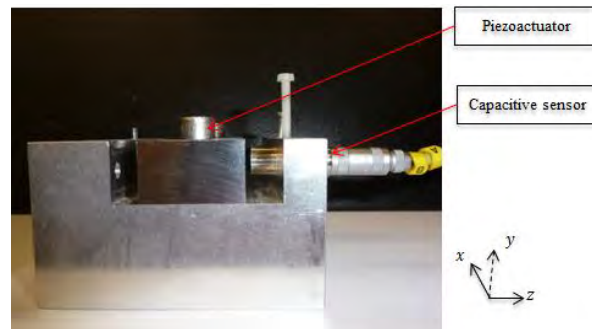


Figure 2 Test bench setup for the acquisition of the piezoactuator dynamic response.

The frequency response of the piezoactuator is plotted as a Bode plot shown in Fig. 3. The parameters  $P$  and  $Wn$  of the piezoactuators model were taken from this Bode plot, were  $P$  has a value of -5 dB and  $Wn$  has a value of 655 Hz.

The Bode plot of the transfer function of Eq. (5) is also shown in Fig. 3 (dashed red line). The system only shows one peak, while experimental results (solid black line) indicate that there are more peaks and valleys in between every two peaks. As stated by Adriaens et al. (2000), there can be infinite peaks and valleys because the mass of the piezoactuator is not concentrated in some points, as in linear mass-spring-damper systems of arbitrary order, but distributed over the element. Considering this, the model presented here is a good approximation up to the first natural frequency and such limitation imposes a constraint to the design of the control law (Sec. 5). In practice, as stated by Bashas et al. (2007), the working frequency of the piezoactuator barely exceeds its first natural frequency. Therefore, the distributed parameters nature of the piezoactuator could be safely neglected and the model could be reduced to a lumped parameter representation, especially when integrated with flexural mechanical compartments.

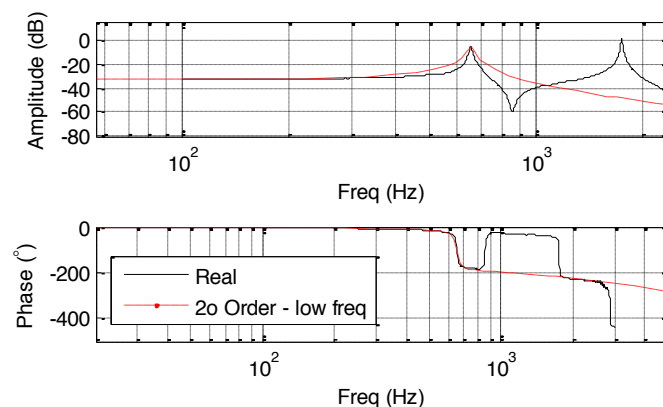


Figure 3 APA400MML piezoactuator frequency response. The solid black line represents the experimental frequency response taken with a Dynamic Signal Analyzer. The dashed red line is the Bode plot of the second order model.

### 3.3 Fabry-Perót sixth-order model

A sixth-order parametric model for the Fabry-Perót system, which is composed of three piezoactuators coupled with the mirror mass, was built on top of the previously presented model for the piezoactuator. The input of the MIMO system are the three piezoactuators voltage inputs,  $u_1$ ,  $u_2$  and  $u_3$ , and the outputs are the measurement of the capacitive sensors,  $s_{12}$ ,  $s_{23}$ ,  $s_{13}$ , all of them in Volts.

The model takes into account the geometrical position of the sensors. The measurement targets of the sensors are placed 60 degrees from each of the piezoactuators, as shown in Fig. 4b. The graphical representation of the system is shown in Fig. 4a.

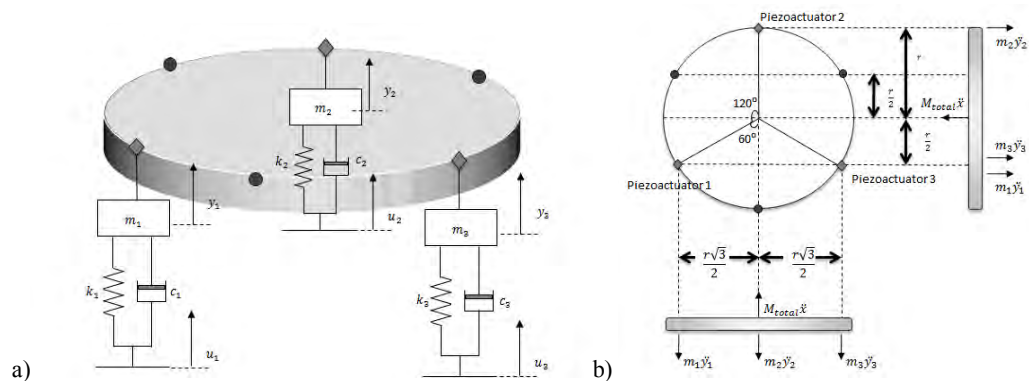


Figure 4. a) Schematic of the Fabry-Perot instrument. The disk represents the upper mirror, the mass-spring-damper systems represent the piezoactuators, and the dots on the disk represent the capacitive sensors measurement targets. b) Fabry-Perot system geometrical representation and force diagram.

The total mass of the system is the sum of the masses of the mirror plate and the effective masses of the piezoactuators second order model, as stated in Eq. (6).

$$M_{total} = m_{mirror} + m_1 + m_2 + m_3 \quad (6)$$

Taking  $x$  as the total displacement of the mirror plate, the force-balance equation, applying the expression of Eq. (1) for every piezoactuator results in:

$$M_{total}\ddot{x} = -k_1y_1 - k_2y_2 - k_3y_3 - c_1\dot{y}_1 - c_2\dot{y}_2 - c_3\dot{y}_3 + k_1u_1 + k_2u_2 + k_3u_3 + c_1\dot{u}_1 + c_2\dot{u}_2 + c_3\dot{u}_3 \quad (7)$$

The moment of force for the plate in the  $y$  axis is:

$$I_y\ddot{\theta}_y = -[k_1(y_1 - u_1) + c_1(\dot{y}_1 - \dot{u}_1)]\frac{r\sqrt{3}}{2} + [k_3(y_3 - u_3) + c_3(\dot{y}_3 - \dot{u}_3)]\frac{r\sqrt{3}}{2} \quad (8)$$

Similarly, the moment of force for the plate in the  $z$  axis is:

$$I_z\ddot{\theta}_z = -[k_1(y_1 - u_1) + c_1(\dot{y}_1 - \dot{u}_1)]\frac{r}{2} + [k_2(y_2 - u_2) + c_2(\dot{y}_2 - \dot{u}_2)]r - [k_3(y_3 - u_3) + c_3(\dot{y}_3 - \dot{u}_3)]\frac{r}{2} \quad (9)$$

The distance output in the location of the capacitive sensors measurement targets:

$$s_{12} = x + \theta_y \frac{r\sqrt{3}}{2} - \theta_z \frac{r}{2} \quad (10)$$

$$s_{23} = x - \theta_y \frac{r\sqrt{3}}{2} - \theta_z \frac{r}{2} \quad (11)$$

$$s_{13} = x + \theta_z r \quad (12)$$

Finally, the space state representation is given by Eq. (13) and Eq. (14), with the matrix **A**, **B**, **C**, **D** defined as in Appendix 1a. The result is a linear and time-invariant (LTI) model with 3 controls, 3 outputs and 6 state variables.

$$\dot{x} = \mathbf{A}x + \mathbf{B}u \quad (13)$$

$$y = \mathbf{C}x + \mathbf{D}u \quad (14)$$

This space state representation can be transformed to a transfer function representation for each input/output relation.

The transfer functions for the Fabry-Perot system are showed in Appendix 1b.

### 3.4 Identification of the Fabry-Perót model

As in the modeling of the piezoactuators, presented in section 3.1, the frequency response of the system was taken for every input and output combination using the same dynamic signal analyzer, in the range of frequency of interest (1 Hz – 1 kHz). The Bode plots for each input and output combination are shown in Fig. 5.

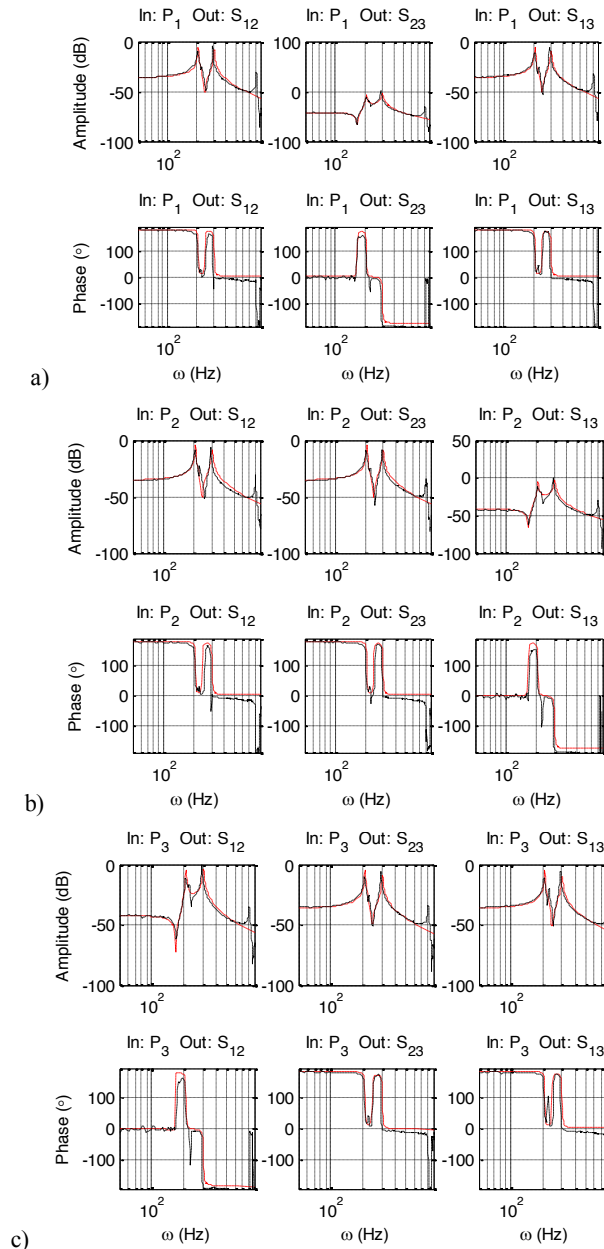


Figure 5 Bode plot of the Fabry-Perót system when exciting only one input. a) Input signal only in  $u_1$ , b) Input signal only in  $u_2$ , c) Input signal only in  $u_3$ . Solid black line is the Bode plot of the parametric model. Dashed red line is the real response of the system.

The presented model has limitations because some important effects, like hysteresis, creep, temperature and humidity, were not taken into account in order to simplify the modeling of the system allowing the use of linear control techniques like the LQG/LTR controller design. Nevertheless, an ongoing work (Atilio et al, 2013) that drives the piezoactuators by charge instead of voltage to eliminate the hysteresis and creep effects will make the linear dynamical model proposed here very close to the real system.

### 3.5 The Fabry-Perót modelling error

With the frequency response presented in Fig. 5 it was possible to calculate the modeling error  $EM$ , using the following multiplicative error formula on the acquired data points:

$$EM(s) = [G_R(s) - G_N(s)]G_N(s)^{-1} \quad (15)$$

Where  $G_R$  is the transfer function of the real plant and  $G_N$  is the nominal model of the system.

This representation for the error was adopted because it describes the error, reflected in the plant output, in the modeling of the plant transfer function as well as the error in the loop transfer function (Da Cruz, 1996).

Next, the frequency response of the inverse of the modeling error of Eq. (16) was taken, as presented in Fig. 6. This helped in the analysis of how well the model represents the system as a function of the frequency and is also needed for the LQG/LTR design method, which will be presented in the next section.

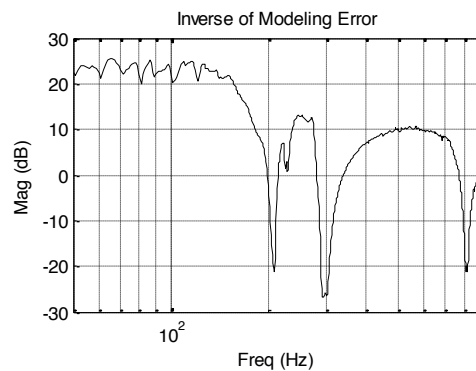


Figure 6 Fabry-Perót system multiplicative modeling error

Fig. 6 shows high-frequency modeling errors which impose a limit to the control system bandwidth, limiting the performance of the feedback system (Athans, 1986). For the current model of the system, the crossover frequency is on 200 Hz, which is taken into account in the robust control design in section 5.2.

## 4. FABRY-PERÓT CONTROL PROBLEM

### 4.1 Main operation mode

The main operation mode of the Fabry-Perót instrument is the scanning one, which consists in varying the distance between the mirrors of the interferometer, between one distance position to another, and going the way back, in  $n$  steps. This is repeated for a number  $m$  of times creating a sequence of ladders.

### 4.2 Performance specifications

The performance specifications for the feedback control system in scanning mode are the following:

1. Follow the reference (small steps) signal with null steady state average error, and steady state maximum standard deviation of 3nm rms.
2. Reject disturbances up to 100 Hz.

Finally, step response overshoots must be minimized in order to maximize the instrument operation range.

## 5. CONTROL SYSTEM DESIGN

### 5.1 Proportional-Integral Compensator

As a benchmark, and due to its simplicity of implementation and satisfactory performance on following step references with zero steady-state error, a simple Proportional Integral (PI) controller of the form of Eq. (16) has been implemented.

Ana María Molina Arcila, Fábio de Oliveira Fialho, Fernando Orsatti  
High Resolution Fabry-Pérot Interferometer – Dynamic System Modeling And Nanopositioning Control System Design

$$K_{PI} = kp + ki \frac{1}{s} \quad (16)$$

Where  $kp$  is the proportional constant,  $ki$  is the integral constant and  $s$  is the Laplace complex angular frequency.

The PI compensator for the FP is assumed to be an ensemble of three SISO (single input single output) uncoupled control loops stated by  $G_{11}$ ,  $G_{22}$ ,  $G_{33}$  transfer functions as in Appendix 1.b.

Coupling transfer functions of the system defined by  $G_{12}$ ,  $G_{23}$ ,  $G_{13}$  are neglected, meaning that we only consider the mass of glass over the actuators, not the coupling force provoked by the circular mirror over the three piezoactuators.

The same compensator,  $K_{PI}$ , was used for the three SISO systems.

Experimental tuning has been chosen as the methodology for the PI parameters tuning.

## 5.2 Linear quadratic Gaussian with loop transfer recovery compensator.

The system is assumed to be linear in order to be able to design a robust controller.

The main characteristics of the LQG/LTR robust controller are that it has nominal stability and stability-robustness to modeling errors while achieving good performance (Athans, 1986).

The goal is to design a MIMO LQG/LTR compensator,  $K(s)$ , for this model to meet the performance specifications presented in Section 4.2. For this purpose, three integrators, one for each input channel of the plant, were added to the Design Plant Model (DPM) in order to achieve null steady-state error to a step input. Also, and considering that a typical step size for the scanning mode is of 10 nm, the controller was set to have a noise-signal ratio smaller than 30%, in order to achieve a steady state maximum standard deviation of 3 nm. And, lastly, the bandwidth of the closed loop system was set beyond 100 Hz in order to reject disturbances up to this frequency.

The model of the Fabry-Perót instrument, presented in section 3.3, includes 6 state variables. The resultant MIMO compensator will then have 12 states (6 states from the original system model + 3 integrators of the DPM + 3 integrators included in the controller) and will be given by:

$$K(s) = G(sI - A + BG + HC)^{-1}H \quad (17)$$

Where  $A$ ,  $B$  and  $C$  are the matrices of the space state representation of the system model, as defined in the Appendix 1a,  $G$  is the gain matrix of the controller and  $H$  is the Kalman Filter observer gain matrix, both defined as in Appendix 2.

## 6. SIMULATION RESULTS

### 6.1 Proportional-Integral compensator simulation results

Figure 7 shows the block diagram of the PI control loop simulation:

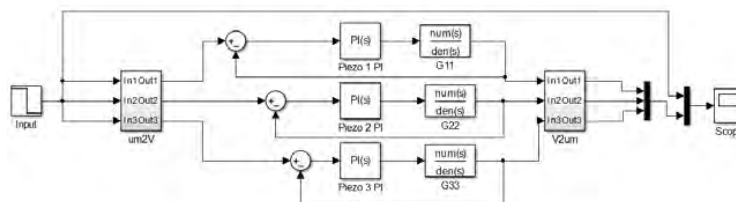


Figure 7 Unity feedback configuration for the PI controller of the Fabry-Perót system.

And the simulation results for a step input signal of 5  $\mu\text{m}$  is shown in Fig. 8.

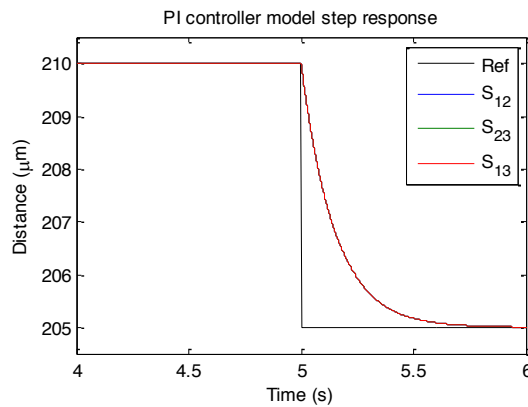


Figure 8 Fabry-Perót model step response with PI controller simulation

As it can be seen in the figure, the outputs of the system do not present overshoot in the dynamic response and follow the reference with null steady state error, achieving the performance requirements.

**6.2 LQG/LTR compensator simulation results**

The robust controller simulation block diagram is as shown in Fig. 9.

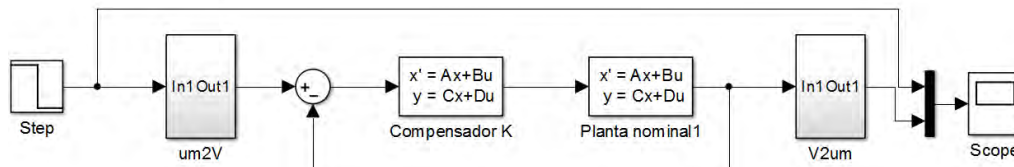


Figure 9 Robust controller simulation block diagram

The simulation results for a step input signal of 5µm is shown in Fig. 10.

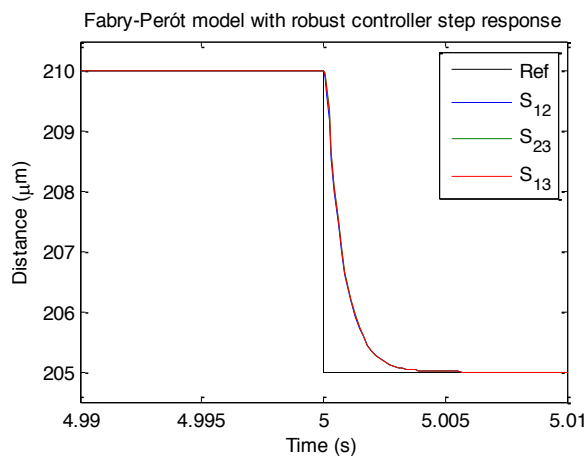


Figure 10 Fabry-Perót system step response with robust controller

The outputs of the system do not present overshoot in the dynamic response and follow the reference with null steady state error, achieving the performance requirements.

Ana María Molina Arcila, Fábio de Oliveira Fialho, Fernando Orsatti  
High Resolution Fabry-Pérot Interferometer – Dynamic System Modeling And Nanopositioning Control System Design

## 7. EXPERIMENTAL VALIDATION OF COMPENSATORS

For the experimental validation of the compensators in the real system, the simulations presented in Fig. 7 and 9 are run in real time using a sample frequency of 4500 Hz. The digital to analog interface between the computer and the piezoactuators, and the analog to digital conversion between the MC900 output and the computer, is done by two data acquisition boards, NI 6221.

### 7.1 Proportional-Integral compensator experimental results

The experimental results for a step input signal of  $5\mu\text{m}$  is shown in Fig. 11.

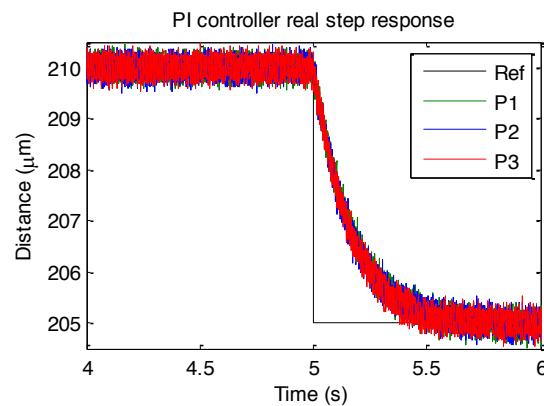


Figure 11 Fabry-Perót system step response with PI controller

As it can be seen in the figure, the outputs of the system do not present overshoot in the dynamic response and follow the reference with null steady state error. However, the output signals of the system, acquired by the data acquisition boards, present a steady-state standard deviation of 140 nm. The source of this noise was studied, reaching the conclusion that the noise is introduced by the computer and the data acquisition boards, which will not be part of the system once the control algorithm is implemented in an isolated controller board in the future. For this reason, the noise specification used for the validation is the relative specification of noise-signal ratio of 0.3.

For these experimental results, the signal has a steady state standard deviation of  $0.140\mu\text{m}$  for a  $5\mu\text{m}$  mean step signal, resulting in a noise-signal ratio of 0.03.

### 7.2 LQG/LTR compensator experimental results

The experimental validation of the LQG/LTR robust controllers with hysteresis compensation is part of our current work. For the final version of this paper we are planning to show the results of this validation.

## 8. CONCLUSIONS

This paper has proposed a linear time-invariant second-order model for the amplified piezoactuator APA400MML and a sixth-order LTI model for the Fabry-Perót system of the BTFI instrument. These models were used to design a PI and a robust LQG/LTR nanopositioning controllers for the Fabry-Perót system.

The simulation and implementation results of the controllers have verified the effectiveness of the proposed control schemes, demonstrating that they can achieve a fast and smooth reference following response, rejecting disturbances up to 100 Hz and having a satisfactory noise-signal ratio.

## 9. ACKNOWLEDGEMENTS

We would like to thank the Laboratório de Microeletrônica do Departamento de Sistemas Eletrônicos of the Universidade de São Paulo for their support and for sharing their space and resources with us. The first author would also like to thank the Fundação de Amparo a Pesquisa do Estado de São Paulo, FAPESP, process number 2011/11877-5 for financial support.

10. REFERENCES

Adriaens, H. J. M. T. S., Willem L. De Koning, and Reinder Banning. "Modeling piezoelectric actuators." *Mechatronics*, IEEE/ASME Transactions on 5.4 (2000): 331-341.

Athans, Michael. "A tutorial on the LQG/LTR method." American Control Conference, 1986. IEEE, 1986.

CEDRAT TECHNOLOGIES, 2010. "Technical Datasheet APA400MML". 1 May 2010  
http://www.cedrat\_technologies.com/fileadmin/user\_upload/cedrat\_groupe/Mechatronic\_products/Piezo\_actuators\_electronics/APAs/APA400MML\_GB\_v3.3.pdf

CEDRAT TECHNOLOGIES, 2013. "CEDRAT TECHNOLOGIES Piezo Products Catalog Version 4.1"

de Oliveira, Cláudia Mendes, et al. "The Brazilian Tunable Filter Imager for the SOAR Telescope." *Publications of the Astronomical Society of the Pacific* 125.926 (2013): 396-408.

Doyle, J.C. "Analysis of Feedback Systems with Structured Uncertainties", *IEE proceedings*, vol. 129, Parte D, n 6, pp. 242-250, nov. 1982.

J. J. Da Cruz, "Controle Robusto Multivariável", Edusp, São Paulo, SP, 1996.

11. RESPONSIBILITY NOTICE

The authors are the only responsible for the printed material included in this paper.

APPENDIX 1.

a. Fabry-Perót space state sixth order model matrix definition:

$$A = \begin{bmatrix} 0 & 1 & 0 & 0 & 0 & 0 \\ -\frac{ka+kb+kc}{M} & -\frac{ca+cb+cc}{M} & -\frac{ka-kc}{M}r\frac{\sqrt{3}}{2} & -\frac{ca-cc}{M}r\frac{\sqrt{3}}{2} & -\frac{\frac{ka}{2}-kb+\frac{kc}{2}}{r} & -\frac{\frac{ca}{2}-cb+\frac{cc}{2}}{r} \\ 0 & 0 & 0 & 1 & 0 & 0 \\ -\frac{ka-kc}{I_y}r\frac{\sqrt{3}}{2} & -\frac{ca-cc}{I_y}r\frac{\sqrt{3}}{2} & -\frac{ka+kc}{I_y}r^2\frac{3}{4} & -\frac{ca+cc}{I_y}r^2\frac{3}{4} & -\frac{ka-kc}{I_y}r^2\frac{\sqrt{3}}{4} & -\frac{ca-cc}{I_y}r^2\frac{\sqrt{3}}{4} \\ 0 & 0 & 0 & 0 & 0 & 1 \\ -\left(\frac{ka}{2}-kb+\frac{kc}{2}\right) & -\left(\frac{ca}{2}-cb+\frac{cc}{2}\right) & -\frac{ka-kc}{I_z}r^2\frac{\sqrt{3}}{4} & -\frac{ca-cc}{I_z}r^2\frac{\sqrt{3}}{4} & -\frac{\frac{ka}{4}+kb+\frac{kc}{4}}{I_z}r^2 & -\frac{\frac{ca}{4}+cb+\frac{cc}{4}}{I_z}r^2 \end{bmatrix}$$

$$B = \begin{bmatrix} \frac{ca}{M} & \frac{cb}{M} & \frac{cc}{M} \\ -\frac{ca+cb+ccc}{M} & -\frac{ca-cc}{M}r\frac{\sqrt{3}}{2} & -\frac{ca-cc}{M}r\frac{\sqrt{3}}{2} & -\frac{ca-cc}{M}r\frac{\sqrt{3}}{2} & -\frac{ca-cc}{M}r\frac{\sqrt{3}}{2} & -\frac{ca-cc}{M}r\frac{\sqrt{3}}{2} \\ \frac{ca+cb+ccc}{M} & \frac{ca-cc}{M}r\frac{\sqrt{3}}{2} & \frac{ca-cc}{M}r\frac{\sqrt{3}}{2} & \frac{ca-cc}{M}r\frac{\sqrt{3}}{2} & \frac{ca-cc}{M}r\frac{\sqrt{3}}{2} & \frac{ca-cc}{M}r\frac{\sqrt{3}}{2} \\ \frac{ca+cb+ccc}{M} & \frac{ca-cc}{M}r\frac{\sqrt{3}}{2} & \frac{ca-cc}{M}r\frac{\sqrt{3}}{2} & \frac{ca-cc}{M}r\frac{\sqrt{3}}{2} & \frac{ca-cc}{M}r\frac{\sqrt{3}}{2} & \frac{ca-cc}{M}r\frac{\sqrt{3}}{2} \\ \frac{ca+cb+ccc}{M} & \frac{ca-cc}{M}r\frac{\sqrt{3}}{2} & \frac{ca-cc}{M}r\frac{\sqrt{3}}{2} & \frac{ca-cc}{M}r\frac{\sqrt{3}}{2} & \frac{ca-cc}{M}r\frac{\sqrt{3}}{2} & \frac{ca-cc}{M}r\frac{\sqrt{3}}{2} \\ \frac{ca+cb+ccc}{M} & \frac{ca-cc}{M}r\frac{\sqrt{3}}{2} & \frac{ca-cc}{M}r\frac{\sqrt{3}}{2} & \frac{ca-cc}{M}r\frac{\sqrt{3}}{2} & \frac{ca-cc}{M}r\frac{\sqrt{3}}{2} & \frac{ca-cc}{M}r\frac{\sqrt{3}}{2} \end{bmatrix}$$

$$C = \begin{bmatrix} 1 & 0 & r\frac{\sqrt{3}}{2} & 0 & -\frac{r}{2} & 0 \\ 1 & 0 & -r\frac{\sqrt{3}}{2} & 0 & -\frac{r}{2} & 0 \\ -1 & 0 & 0 & 0 & r & 0 \end{bmatrix}$$

b. Fabry-Perót system model transfer function representation:

$$G_{11} = \frac{-0.7765s^5 - 3.378 \times 10^4 s^4 - 7.549 \times 10^6 s^3 - 1.661 \times 10^{11} s^2 - 1.345 \times 10^{13} s - 2.004 \times 10^{17}}{s^6 + 163.4s^5 + 7.311 \times 10^6 s^4 + 7.79 \times 10^8 s^3 + 1.742 \times 10^{13} s^2 + 9.014 \times 10^{14} s + 1.342 \times 10^{19}}$$

$$G_{12} = \frac{0.6612s^5 + 2.875 \times 10^4 s^4 + 5.228 \times 10^6 s^3 + 1.161 \times 10^{11} s^2 + 6.726 \times 10^{12} s + 1.002 \times 10^{17}}{s^6 + 163.4s^5 + 7.311 \times 10^6 s^4 + 7.79 \times 10^8 s^3 + 1.742 \times 10^{13} s^2 + 9.014 \times 10^{14} s + 1.342 \times 10^{19}}$$

$$G_{13} = \frac{-0.7764s^5 - 3.378 \times 10^4 s^4 - 7.409 \times 10^6 s^3 - 1.661 \times 10^{11} s^2 - 1.345 \times 10^{13} s - 2.004 \times 10^{17}}{s^6 + 163.4s^5 + 7.311 \times 10^6 s^4 + 7.79 \times 10^8 s^3 + 1.742 \times 10^{13} s^2 + 9.014 \times 10^{14} s + 1.342 \times 10^{19}}$$

Ana María Molina Arcila, Fábio de Oliveira Fialho, Fernando Orsatti  
High Resolution Fabry-Pérot Interferometer – Dynamic System Modeling And Nanopositioning Control System Design

$$G_{21} = \frac{-0.8499s^5 - 3.378 \times 10^4 s^4 - 7.705 \times 10^6 s^3 - 1.661 \times 10^{11} s^2 - 1.345 \times 10^{13} s - 2.004 \times 10^{17}}{s^6 + 163.4s^5 + 7.311 \times 10^6 s^4 + 7.79 \times 10^8 s^3 + 1.742 \times 10^{13} s^2 + 9.014 \times 10^{14} s + 1.342 \times 10^{19}}$$

$$G_{22} = \frac{-0.8499s^5 - 3.378 \times 10^4 s^4 - 7.613 \times 10^6 s^3 - 1.661 \times 10^{11} s^2 - 1.345 \times 10^{13} s - 2.004 \times 10^{17}}{s^6 + 163.4s^5 + 7.311 \times 10^6 s^4 + 7.79 \times 10^8 s^3 + 1.742 \times 10^{13} s^2 + 9.014 \times 10^{14} s + 1.342 \times 10^{19}}$$

$$G_{23} = \frac{0.7237s^5 + 2.875 \times 10^4 s^4 + 5.354 \times 10^6 s^3 + 1.161 \times 10^{11} s^2 + 6.726 \times 10^{12} s + 1.002 \times 10^{17}}{s^6 + 163.4s^5 + 7.311 \times 10^6 s^4 + 7.79 \times 10^8 s^3 + 1.742 \times 10^{13} s^2 + 9.014 \times 10^{14} s + 1.342 \times 10^{19}}$$

$$G_{31} = \frac{-0.6361s^5 + 2.859 \times 10^4 s^4 - 3.377 \times 10^5 s^3 + 1.157 \times 10^{11} s^2 + 1.046 \times 10^{12} s - 1.00 \times 10^{17}}{s^6 + 163.4s^5 + 7.311 \times 10^6 s^4 + 7.79 \times 10^8 s^3 + 1.742 \times 10^{13} s^2 + 9.014 \times 10^{14} s + 1.342 \times 10^{19}}$$

$$G_{32} = \frac{0.5416s^5 - 3.362 \times 10^4 s^4 - 1.833 \times 10^6 s^3 - 1.657 \times 10^{11} s^2 - 7.772 \times 10^{12} s - 2.002 \times 10^{17}}{s^6 + 163.4s^5 + 7.311 \times 10^6 s^4 + 7.79 \times 10^8 s^3 + 1.742 \times 10^{13} s^2 + 9.014 \times 10^{14} s + 1.342 \times 10^{19}}$$

$$G_{33} = \frac{-0.636s^5 - 3.376 \times 10^4 s^4 - 7.109 \times 10^6 s^3 - 1.661 \times 10^{11} s^2 - 1.345 \times 10^{13} s - 2.004 \times 10^{17}}{s^6 + 163.4s^5 + 7.311 \times 10^6 s^4 + 7.79 \times 10^8 s^3 + 1.742 \times 10^{13} s^2 + 9.014 \times 10^{14} s + 1.342 \times 10^{19}}$$

## APPENDIX 2.

The LQG/LTR design methodology starts designing a plant, called the target loop that meets the performance requirements using Kalman Filter techniques, choosing a proper  $\mu$  constant and L matrix.

$$G_{TL} = \frac{1}{\sqrt{\mu}} C(j\omega I - A)^{-1} L$$

Using the algebraic Ricatti equation (ARE) and the chosen value for  $\mu$ , find the Kalman Filter observer gain matrix H.

$$0 = -A\Sigma - \Sigma A' - LL' + \frac{1}{\mu} \Sigma C' C \Sigma$$

$$H = \frac{1}{\mu} \Sigma C'$$

After the Kalman Filter gain matrix is obtained the recovery process is made. As stated in Doyle (1982), if the system is a square system the **A** and **B** matrices of the system are controllable, the **A** and **C** matrices are observable and the transmission zeros of the system have all negative values, a controller gain matrix can be calculated as:

$$G = \frac{1}{\rho} B' K_p$$

Where  $\rho > 0$  and  $K_p$  is obtained solving the following ARE:

$$0 = -K_p A - A' K_p - C' C + \frac{1}{\rho} K_p B B' K_p$$

With the compensator gain matrix, G, the compensator K for the target loop is defined as:

$$K(s) = G(sI - A + BG + HC)^{-1} H$$

This compensator is made for the design plant model that had augmented dynamics (three integrators in the input signal). Given that we want to design a compensator for the model of the system we need to include the integrators on the compensator as in:

$$K(s) = K(s) * \frac{I_3}{s} = G(sI - A + BG + HC)^{-1} H * \frac{I_3}{s}$$



## DESIGN AND REALIZATION OF AN ELECTRONIC CHARGE CONTROL CIRCUIT TO ATTENUATE THE HYSTERESIS OF THE HIGH RESOLUTION FABRY-PÉROT INTERFEROMETER'S AMPLIFIED PIEZOELECTRIC ACTUATORS

**Victor Atilio Marchiori**

**Fábio de Oliveira Fialho**

Laboratório de Automação e Controle – Departamento de Engenharia de Sistemas Eletrônicos da Escola Politécnica da Universidade de São Paulo – Avenida Professor Luciano Gualberto. Trv. 3, nº 158, São Paulo, Brazil

[victoratilio@usp.br](mailto:victoratilio@usp.br)

[fabio.fialho@usp.br](mailto:fabio.fialho@usp.br)

**Issa Ouattara**

Laboratoire d'Astrophysique de Marseille

38, rue Frédéric Joliot-Curie, Marseille, France

[issa.ouattara@oamp.fr](mailto:issa.ouattara@oamp.fr)

**Ana Maria Molina Arcila**

Laboratório de Automação e Controle – Departamento de Engenharia de Sistemas Eletrônicos da Escola Politécnica da Universidade de São Paulo – Avenida Professor Luciano Gualberto. Trv. 3, nº 158, São Paulo, Brazil

[ammolina@usp.br](mailto:ammolina@usp.br)

**Fernando Moya Orsatti**

Laboratório de Automação e Controle – Departamento de Engenharia de Sistemas Eletrônicos da Escola Politécnica da Universidade de São Paulo – Avenida Professor Luciano Gualberto. Trv. 3, nº 158, São Paulo, Brazil

[fernando.orsatti@oepe.com.br](mailto:fernando.orsatti@oepe.com.br)

**Jair Pereira de Souza**

Laboratório de Microeletrônica – Departamento de Engenharia de Sistemas Eletrônicos da Escola Politécnica da Universidade de São Paulo – Avenida Professor Luciano Gualberto. Trv. 3, nº 158, São Paulo, Brazil

[jpsouza@lme.usp.br](mailto:jpsouza@lme.usp.br)

**Claudia Lúcia Mendes de Oliveira**

Instituto de Astronomia, Geofísica e Ciências Atmosféricas da Universidade de São Paulo

Rua do Matão, nº 1226, São Paulo, Brazil

[oliveira@astro.iag.usp.br](mailto:oliveira@astro.iag.usp.br)

**Abstract.** *This paper presents the design and the realization of a technique to attenuate the hysteresis nonlinear phenomenon of high displacement Amplified Piezoelectric Actuators (APA) mounted in a state-of-the-art Fabry-Pérot interferometer. This interferometer is to be installed in the 3D-spectrometer Brazilian Tunable Filter Imager (BTFI) on the Southern Astrophysical Research (SOAR) telescope in Chile. The hysteresis attenuation technique presented in this paper aims to assist the Fabry-Pérot's nan positioning control system to attain its main scientific specification. In such system, each APA has a maximum stroke of 270µm within a 170V range, and they are used to position a high reflective mirror plate. The Fabry-Pérot's nan positioning control system is specified to limit the APA's positioning steady-state noise to 3nm rms, but the hysteresis limits the positioning accuracy. In order to attenuate hysteresis, an electronic charge control circuit built with a high power operational amplifier has been designed and applied for each APA. The experiments results show that the hysteresis effect has almost been eliminated, and consequently the positioning steady-state noise has significantly been reduced.*

**Keywords:** *Piezoelectric Actuator, Hysteresis, Charge Control, Nan positioning Systems, Fabry-Pérot Interferometer*

V. A. Marchiori;F. O. Fialho;I. Ouattara  
Design And Realization Of Electronic Charge Control System For Attenuating Hysteresis

## 1. INTRODUCTION

The Brazilian Tunable Filter Imager (BTFI) is a highly versatile, new technology, tunable optical imager to be used both in seeing-limited mode and at higher spatial fidelity using the SAM Ground-Layer Adaptive Optics facility (SOAR Adaptive Module) which is being deployed at the Southern Astrophysical Research (SOAR) telescope. The BTFI employs Fabry-Pérot interferometers in order to achieve high spectral resolutions up to  $R \sim 30,000$  (de Oliveira), as well as the use of an innovating technique of combining holographic nets to build a tunable filter. BTFI will be useful for the study of a variety of topics, from solar system bodies, stars, interstellar medium, galaxies, to cosmology.

The BTFI's Fabry-Pérot interferometer (Fig. 1a), or etalon, is an instrument that permits optical filtration by interference processes (Fig. 1d), given by multiple reflection and refraction of light between two parallel highly reflective surfaces (Fig. 1b). The refracted rays interfere on each other, forming a pattern which takes the appearance of a set of concentric rings (Fig. 1e). By tuning the distance between the parallel plates one tune the wavelength of light. In Fabry-Pérot interferometer, the distance between the parallel surfaces is controlled by Amplified Piezoelectric Actuators – APA – CEDRAT TECHNOLOGIES (Fig. 1c), which are fixed on the inner side of the etalon.

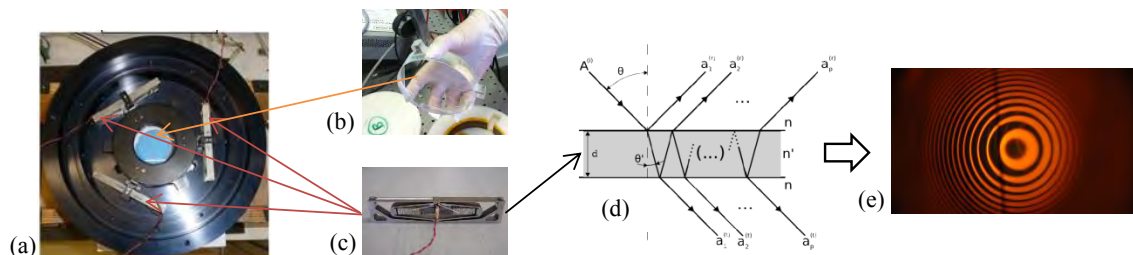


Figure 1. (a) Fabry-Pérot interferometer. (b) Mirror plate. (c) APA. (d) Interference process. (e) Visual pattern of concentric rings in Fabry-Pérot interferometer.

APA is a solid-state long-stroke actuator. It is based on the expansion of the active material and on a mechanism to amplify the displacement, which is also proportional to the applied voltage. The advantages of APA (Cedrat Technologies) are its relatively large displacements combined with its high forces and compact size along the active axis. Since APA is robust, it can also be used in dynamic applications, including in resonant devices. On the other hand, APA has a very typical type of nonlinearity encountered in piezoelectric transducers – the hysteresis – which limits the positioning accuracy.

Such non linearity, which appears when the piezoelectric transducers are submitted to conventional voltage control, is enormously undesirable for the Fabry-Pérot's nanopositioning system, since its main scientific specification imposes that the standard deviation of the positioning error must be limited to  $3nm$  rms. Thus, in order to attenuate the hysteresis effect of each APA in Fabry-Pérot, an analog charge control circuit built with a high power operational amplifier has been designed and applied for each APA. This paper aims to present the design and the implementation of such a solution, and to show its benefits by comparing the performance of the Fabry-Pérot's nanopositioning system with and without hysteresis attenuation.

Other techniques to attenuate the hysteresis have been widely published in other papers (Bazghaleh M., Beck J., Huang L., Rodriguez-Fortun J.M., Vautier B.J.G.). However, they are mostly limited to evaluate the results only in terms of the hysteresis magnitude reduction, without analyzing its improvements on a positioning accuracy point of view. With a more comprehensive approach, this paper focuses the analysis of the hysteresis attenuation in terms of the positioning accuracy of a real and challenging positioning application, giving an interesting contribution on this subject.

This paper is organized as follows: Section 2 describes the main characteristics of the Fabry-Pérot nanopositioning system's parts, Section 3 presents the method used to characterize the APA's hysteresis magnitude, Section 4 presents the charge control technique used to attenuate the APA's hysteresis and Section 5 presents the results obtained with the experiments performed with the APAs for both the classic voltage control (no hysteresis attenuation) and the designed charge control solutions. Finally, the experiment results are discussed in Section 6.

22nd International Congress of Mechanical Engineering (COBEM 2013)  
 November 3-7, 2013, Ribeirão Preto, SP, Brazil

**2. FABRY-PÉROT’S NANOPositionING SYSTEM**

The actuating system of the Fabry-Pérot’s nanopositioning system is composed by three APA400MML model (CEDRAT Technologies) Amplified Piezoelectric Actuators (APA).

The APA400MML (Fig. 2a) has a maximum stroke of  $270\mu m$  ( $-50\mu m$  to  $210\mu m$ ) and it is proportional to the applied voltage within a 170V range ( $-20V$  to  $+150V$ ). The APA400MML has two different excitation conditions: the quasistatic and the dynamic ones. The quasistatic excitation condition corresponds to operations in frequencies up to one-third of the first resonance frequency of the APA, which is about 600Hz. The dynamic excitation condition corresponds to operations in frequencies over the quasistatic bandwidth, in which the displacement becomes up to ten times more sensitive to the applied voltage than in quasistatic condition. Under an electronic point of view, each APA has an equivalent capacitance value of about  $10\mu F$ , which is valid in the quasistatic excitation condition.

The measuring system of the Fabry-Pérot’s nanopositioning system is composed by three capacitive sensors and one converter module. Each capacitive sensor (Fig. 2b) have a measurement range of 1mm and a resolution of  $0,4\text{ nm RMS } \sqrt{Hz}$ . The converter module (Fig. 2c), which converts the signal coming from the capacitive sensors to a voltage signal, has a bandwidth of 10kHz and a maximum noise measure that is shorter than 0,005% RMS of the measure extent.

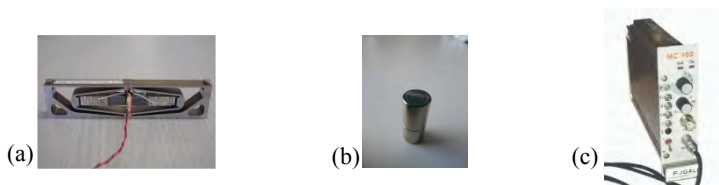


Figure 2. (a) Amplified Piezoelectric Actuator – APA. (b) Capacitive sensor. (c) Converter module.

**3. HYSTERESIS CURVE CHARACTERIZATION**

In general terms, the hysteresis on a dynamic system is a nonlinear phenomenon which presents a lag in response. In piezoelectric materials, this lag occurs between its displacement and the applied voltage. In other words, the displacement may assume different values for the same applied voltage. Like any other piezoelectric device, the Fabry-Pérot’s APAs have this nonlinear characteristic, which limits the accuracy in positioning applications.

A graphical representation of the APA’s displacement hysteresis is presented in Fig. 3. The hysteresis curve is partitioned into an ascending and into a descending branch, since the displacement trajectory depends on the sense of variation of the input voltage.

The calculation of the hysteresis magnitude (Agnus, J., 2003) is shown in Eq. (1):

$$H = \frac{(\delta_1 - \delta_2)}{(\delta_{max} - \delta_{min})} \times 100 \tag{1}$$

$H$  is the percentage hysteresis magnitude,  $(\delta_1 - \delta_2)$  is the maximum displacement difference between the ascending and the descending branches of the hysteresis curve for a same input voltage value, and  $(\delta_{max} - \delta_{min})$  is the difference between the displacement values at the maximum and the minimum applied voltages.

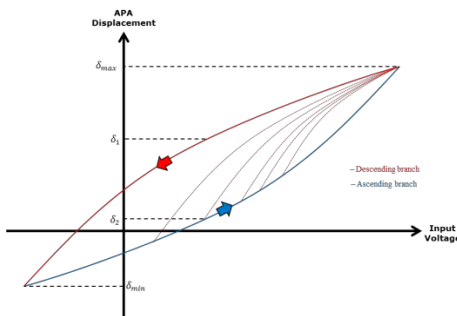


Figure 3. Hysteresis behavior of APA

V. A. Marchiori;F. O. Fialho;I. Ouattara  
 Design And Realization Of Electronic Charge Control System For Attenuating Hysteresis

The dashed ascending branches in Fig. 3 illustrate the variation on the hysteresis curve as the minimum input voltage level is increased. It is possible to note that the terms  $(\delta_1 - \delta_2)$  and  $(\delta_{max} - \delta_{min})$  depend on the maximum and minimum values of the input voltage being applied, so the hysteresis magnitude will therefore depend on the maximum and minimum values of the input voltage.

**4. THE ANALOG CHARGE CONTROL SOLUTION**

The charge control technique used in this paper lies on the principle that the displacement of a piezoelectric material is linearly proportional to the applied charge on it (Perez, R.). The electronic scheme shown in Fig. 4 presents one possible implementation of an analog charge control circuit.

In the scheme shown in Fig. 4, an APA with an inherent capacitance  $C_{pzt}$  is connected to the output and to the negative input of an operational amplifier (OA). This APA is also connected to a reference capacitor  $C_{ref}$  linked to the circuit ground. The input voltage signal is connected to the positive input of the operational amplifier.

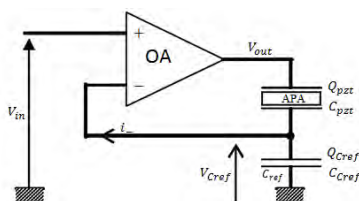


Figure 4. Charge Control solution (Comstock R.H.)

Let  $V_-$  be the voltage at the negative input of the operational amplifier and  $V_{in}$  be the input voltage signal. In that configuration, the current  $i_-$  across the negative input of the operational amplifier is on the order of micro amperes, which implies that the voltage  $V_{Cref}$  across the reference capacitor is practically equal to the voltage  $V_+$  at the positive input of the operational amplifier. In other words,  $V_{Cref}$  is such that:

$$V_{Cref} = V_- = V_+ = V_{in} \tag{2}$$

Moreover, it also implies that the charge  $Q_{pzt}$  across the APA is practically equal to charge  $Q_{Cref}$  across the reference capacitor, which is given by the expression in Eq. (4):

$$Q_{pzt} = Q_{Cref} \tag{3}$$

$$Q_{Cref} = C_{Cref} \times V_{Cref} = C_{Cref} \times V_{in} \tag{4}$$

$C_{Cref}$  is the capacitance value of the reference capacitor  $C_{ref}$ . Combining Eq. (3) and Eq. (4), the charge  $Q_{pzt}$  across the APA is given by the expression in Eq. (5):

$$Q_{pzt} = Q_{Cref} = C_{Cref} \times V_{in} \tag{5}$$

Therefore, the charge  $Q_{pzt}$  across the APA is proportional to the input voltage signal  $V_{in}$ . Since the APA's displacement is linearly proportional to applied charge  $Q_{pzt}$ , it implies that the APA's displacement will be linearly proportional to the input voltage signal  $V_{in}$ .

It is possible to show that the circuit gain, which is the relation between  $V_{out}$  and  $V_{in}$ , is approximately given by the expression in Eq. (6) (Agnus, J., 2003).

$$\frac{V_{out}}{V_{in}} = \frac{C_{Cref} + C_{pzt}}{C_{pzt}} \tag{6}$$

22nd International Congress of Mechanical Engineering (COBEM 2013)  
November 3-7, 2013, Ribeirão Preto, SP, Brazil

## 5. EXPERIMENTAL PROCEDURES

In order to obtain the APA's hysteresis curves and hysteresis magnitudes for both voltage and charge control configurations, according to the characterization method described in Section 3, the experiments shown in Fig. 5 have been set up.

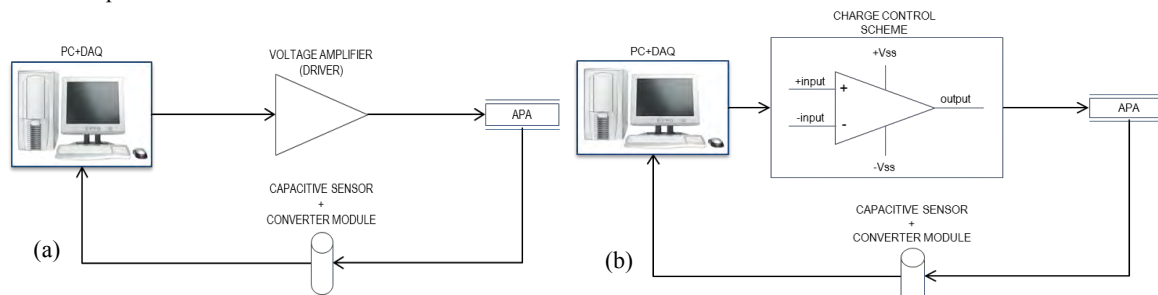


Figure 5. (a) Experiment scheme for determining the APA's hysteresis magnitude under voltage control. (b) Experiment scheme for determining the APA's hysteresis magnitude under charge control.

In these experiments, the PC runs simulation software which supports real-time communication with the data acquisition board (DAQ) connected to it. The DAQ provides a DC voltage signal varying from  $-10\text{V}$  to  $+10\text{V}$ , which supplies a voltage amplifier – driver (Fig. 5a) for voltage control configuration or an operational amplifier (Fig. 5b) for charge control configuration according to the scheme shown in Fig. 4. The driver has a fixed voltage gain which permits the APA to be supplied within its full voltage range ( $-20\text{V}$  to  $+150\text{V}$ ). For the charge control configuration, a high power operational amplifier was applied, which is also capable to deliver the full voltage range of the APA. The gain of the charge control circuit can be tuned by varying the value of  $C_{Cref}$ , as shown by Eq. (6).

The capacitive sensor and the capacitance to voltage converter described in Section 2 are used to measure the APA's displacement, which value is acquired by the PC software through an analog input of the DAQ.

### 5.1 Obtaining the hysteresis curves

In order to obtain the hysteresis curves of each piezo (APA) under voltage control configuration (Fig. 5a), a ramp voltage signal varying from  $-1\text{V}$  to  $+7.5\text{V}$  was generated in the PC software. A single cycle of this signal was transmitted directly to the driver input. Since the driver's voltage gain is 20, each piezo was supplied with a voltage signal varying from  $-20\text{V}$  to  $+150\text{V}$ . It allowed the piezos to achieve its full stroke of  $270\mu\text{m}$ .

In order to obtain the hysteresis curves of each piezo under charge control configuration (Fig. 5b), a ramp voltage signal varying from  $-1\text{V}$  to  $+7.5\text{V}$  was generated in the PC software. A single cycle of this signal was transmitted directly to the circuit input. In this experiment, the charge control circuit's voltage gain was set at approximately 20, therefore supplying each piezo with a voltage signal varying from about  $-20\text{V}$  to about  $+150\text{V}$ . It allowed the piezos to achieve its full stroke of  $270\mu\text{m}$ .

Figure 6 and Fig. 7 show the hysteresis curves obtained for the three piezos (Piezo A, B and C) under voltage and charge control, respectively.

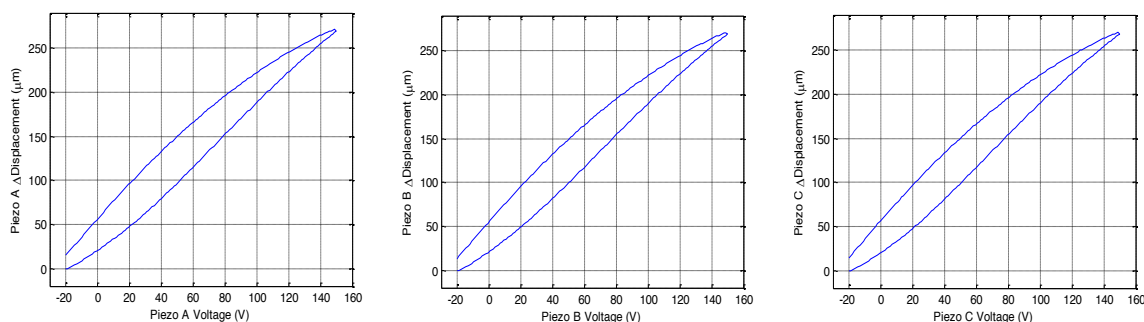


Figure 6. Hysteresis curves obtained for the piezos A (left), B (middle) and C (right) under voltage control.

V. A. Marchiori;F. O. Fialho;I. Ouattara  
 Design And Realization Of Electronic Charge Control System For Attenuating Hysteresis

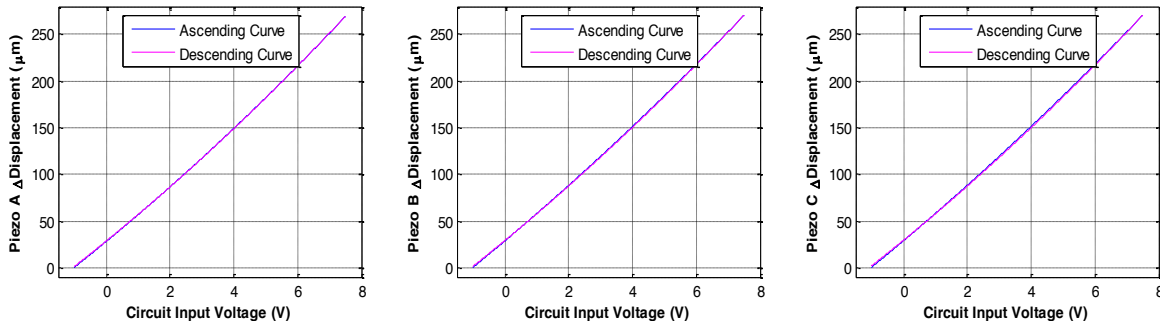


Figure 7. Hysteresis curves obtained for the piezos A (left), B (middle) and C (right) under charge control

Table 1 presents a resume of the results shown from Fig. 6 and Fig. 7 in terms of the hysteresis magnitude of the piezos.

Table 1. Comparative of the experimental results obtained for the hysteresis magnitude, according to Eq. (1), with the voltage control scheme (Fig. 5a) and the charge control scheme (Fig. 5b)

Piezo	Parameter	Voltage Control configuration	Charge Control configuration	Attenuation
A	Hysteresis Magnitude	19,9 %	0,35 %	98,2 %
B	Hysteresis Magnitude	18,7 %	0,47 %	97,5 %
C	Hysteresis Magnitude	19,5 %	0,63 %	96,8%

5.2 Evaluation of hysteresis attenuation in Closed Loop

In section 5.2, it was shown the benefits of using the analog charge control solution for attenuating the hysteresis magnitude. Nevertheless, in terms of nanopositioning, which is the subject of interest of this paper, the hysteresis magnitude does not give the real measure of the advantages that can be obtained by using such a solution.

Thus, additional experiments were performed in order to evaluate more directly the gains it brought for the Fabry-Pérot’s nanopositioning system. To do such evaluation, the voltage control scheme of Fig. 5a and the charge control scheme of Fig. 5b were both set up in a closed-loop configuration, which was built with a digital PI compensator implemented within the simulation software running in the PC environment.

In such configuration (Fig. 8), the measured APA displacement signal  $y(t)$  is compared to a reference (set-point) signal  $r(t)$  in microns, whose error  $e(t)$  is processed by the PI compensator ( $K$ ) which generates a voltage control signal  $u(t)$  (control effort) limited within a -10V to +10V range. The control signal is transmitted to the system ( $G$ ) through the analog output of the DAQ. In voltage control configuration,  $G$  is the APA itself, while in charge control configuration  $G$  is the charge control circuit and the APA.

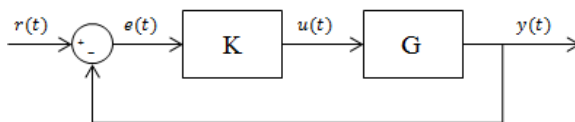


Figure 8. Closed-Loop configuration

For both voltage and charge control configurations, the PI compensator was manually tuned in order to provide the shorter response time possible without destabilizing the closed-loop system.

Figure 9 and Fig. 10 show the results obtained with the voltage control scheme (Fig. 5a) and the charge control scheme (Fig. 5b) submitted both to a closed-loop configuration. In Fig. 9, the control effort  $u(t)$  is evaluated under voltage and charge control configurations for the three piezos, while in Fig. 10 the measured displacement signal  $y(t)$  is evaluated under voltage and charge control configurations for the three piezos.

22nd International Congress of Mechanical Engineering (COBEM 2013)  
 November 3-7, 2013, Ribeirão Preto, SP, Brazil

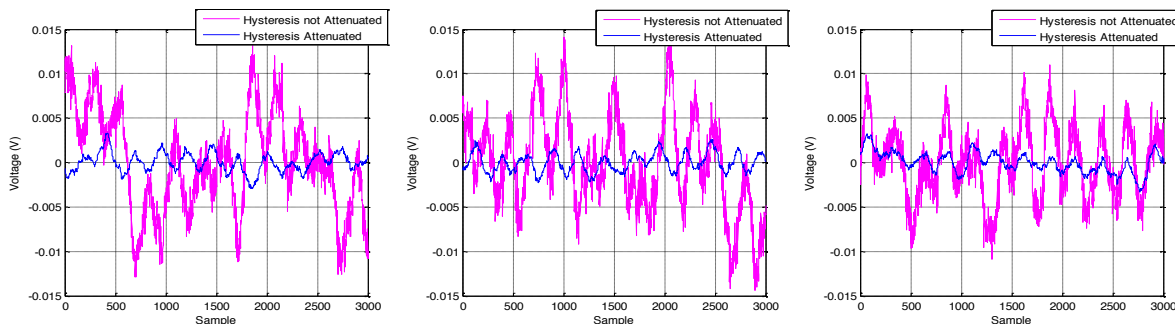


Figure 9. Control effort signals of the piezos A (left), B (middle) and C (right) obtained under voltage control (Hysteresis not Attenuated) and charge control (Hysteresis Attenuated) configurations in closed loop.

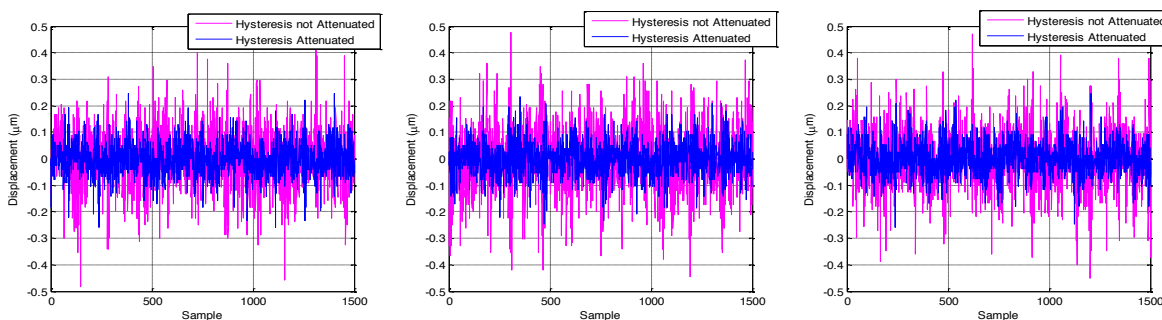


Figure 10. Displacement signals of the piezos A (left), B (middle) and C (right) obtained under voltage control (Hysteresis not Attenuated) and charge control (Hysteresis Attenuated) configurations in closed loop.

Table 2 presents a resume of the results shown from Fig. 9 and Fig. 10 in terms of the standard deviation of the control effort and the positioning error for each of the piezos.

Table 2. Comparative of the experimental results obtained for the control effort and the positioning error with the voltage control scheme (Fig. 5a) and the charge control scheme (Fig. 5b) submitted to a closed-loop configuration

Piezo	Parameter	Voltage Control configuration	Charge Control configuration	Attenuation
A	Control Effort's Standard Deviation	5,6 mV	1,1 mV	80,4%
	Positioning Error's Standard Deviation	108 nm	61 nm	43,5%
B	Control Effort's Standard Deviation	5,4 mV	2 mV	72,2%
	Positioning Error's Standard Deviation	122 nm	61 nm	50,0%
C	Control Effort's Standard Deviation	3,9 mV	1,2 mV	69,2%
	Positioning Error's Standard Deviation	133 nm	59 nm	55,6%

6. CONCLUSION

This paper describes the design and the realization of an analog charge control solution to attenuate the hysteresis nonlinear phenomenon of the Fabry-Pérot interferometer's Amplified Piezoelectric Actuators (APA). With the use of such system, the hysteresis magnitude is almost eliminated (up to 98,2% reduction) compared to the classic voltage control solution. Moreover, in order to verify the direct benefits of attenuating the hysteresis in positioning applications, the behavior of the charge control system is also evaluated in closed-loop. In such experiment, the standard deviations of the control effort and positioning error have significantly been reduced (up to 80,3% and up to 55,6% reduction respectively) compared to the voltage control solution.

7. ACKNOWLEDGEMENTS

V. A. Marchiori;F. O. Fialho;I. Ouattara  
Design And Realization Of Electronic Charge Control System For Attenuating Hysteresis

## 8. REFERENCES

- Agnus, J., 2003. "Contribution à la micromanipulation. Etude, Réalisation, Caractérisation et Commande d'une Micropince Piézoélectrique". Thesis, Laboratoire d'Automatique de Besançon, Besançon.  
<[http://tel.archives-ouvertes.fr/docs/00/36/68/08/PDF/Joel\\_Agnus.pdf](http://tel.archives-ouvertes.fr/docs/00/36/68/08/PDF/Joel_Agnus.pdf)>.
- Bazghaleh M., Grainger S., Cazzolato B., Lu T. "An innovative digital charge amplifier to reduce hysteresis in piezoelectric actuators". School of Mechanical Engineering, The University of Adelaide, SA 5005, Australia.  
<<http://www.araa.asn.au/acra/acra2010/papers/pap111s1-file1.pdf>>.
- Beck. J., Noras M., Kieres J., E. Speich J. "Hysteresis characterization using charge feedback control for a LIPCA device," in *Smart Structures and Materials*, 2006, p. 61701M–61701M.
- de Oliveira, Cláudia Mendes, et al. "The Brazilian Tunable Filter Imager for the SOAR Telescope." *Publications of the Astronomical Society of the Pacific* 125.926 (2013): 396-408.
- Cedrat Technologies. *Products Catalogue* Version 4.1.  
<[http://www.cedrat-technologies.com/download/CEDRAT\\_TEC\\_Catalogue.pdf](http://www.cedrat-technologies.com/download/CEDRAT_TEC_Catalogue.pdf)>
- Comstock R.H., 1981. "Charge control of piezoelectric actuators to reduce hysteresis effects". *United States Patent* n° US 4,263,527 <<http://www.freepatentsonline.com/4263527.pdf>>
- Huang L., Ma Y.T., Feng Z. H., Kong F.R., 2010. "Switched capacitor charge pump reduces hysteresis of piezoelectric actuators over a large frequency range," *Review of Scientific Instruments*, vol. 81, no. 9, pp. 094701–094701, 2010.
- Perez, R., Agnus, J., Breguet, J.M., Chaillet, N., Bleuler, H., Clavel R., 2001. "Characterization and control of a 1DOF monolithique piezoactuator (MPA)". *Proceedings of SPIE Microrobotics and Microassembly III*, Vol. 4568, Newton – USA, pp. 151-162.
- Rodriguez-Fortun J.M., Orus J., Alfonso J., Buil F., 2011. "Hysteresis in Piezoelectric Actuators: Modeling and Compensation". Grupo de Investigación Aplicada (GIA-MDPI), Instituto Tecnológico de Aragón, Zaragoza, Spain. Instituto de Investigación en Ingeniería de Aragón (I3A), Universidad de Zaragoza, Spain.  
<<http://www.nt.ntnu.no/users/skoge/prost/proceedings/ifac11-proceedings/data/html/papers/1063.pdf>>
- Vautier B.J.G., Moheimani S.O.R., 2005. "Charge driven piezoelectric actuators for structural vibration control: issues and implementation". School of Electrical Engineering and Computer Science. University of Newcastle, Callaghan 2308, NSW, Australia <<http://routh.newcastle.edu.au/lab/pdf/J05d.pdf>>.

## 9. RESPONSIBILITY NOTICE

The authors are the only responsible for the printed material included in this paper.

# The Brazilian Tunable Filter Imager for the SOAR telescope

Cláudia Mendes de Oliveira<sup>1</sup>, Keith Taylor<sup>1</sup>, Bruno Quint<sup>1</sup>, Denis Andrade<sup>2</sup>, Fabrício Ferrari<sup>3</sup>, Rene Laporte<sup>4</sup>, Giseli de A. Ramos<sup>5</sup>, Christian Dani Guzman<sup>6</sup>, Luiz Cavalcanti<sup>2</sup>, Alvaro de Calasans<sup>7</sup>, Javier Ramirez Fernandez<sup>2</sup>, Edna Carolina Gutierrez Castañeda<sup>1</sup>, Damien Jones<sup>8</sup>, Fernando Luis Fontes<sup>9</sup>, Ana Maria Molina<sup>1</sup>, Fábio Fialho<sup>2</sup>, Henri Plana<sup>10</sup>, Francisco J. Jablonski<sup>4</sup>, Luiz Reitano<sup>4</sup>, Olivier Daigle<sup>11</sup>, Sergio Scarano Jr.<sup>12</sup>, Philippe Amram<sup>13</sup>, Philippe Balard<sup>13</sup>, Jean-Luc Gach<sup>13</sup>, Claude Carignan<sup>14</sup>

<sup>1</sup>Departamento de Astronomia, Instituto de Astronomia, Geofísica e Ciências Atmosféricas da Universidade de São Paulo, Rua do Matão 1226, Cidade Universitária, 05508-090, São Paulo, Brazil

<sup>2</sup>Escola Politécnica da Universidade de São Paulo, Av. Prof. Luciano Gualberto, travessa 3, no. 380, Cidade Universitária, 05508-010, São Paulo, Brazil

<sup>3</sup>Instituto de Matemática, Estatística e Física, FURG, Av. Itália, Km 8, 96201-900, Rio Grande, RS, Brazil

<sup>4</sup>Instituto Nacional de Pesquisas Espaciais/MCT, Av. dos Astronautas, 1758, 12227-010, São José dos Campos, SP, Brazil

<sup>5</sup>Instituto de Matemática e Estatística da Universidade de São Paulo, Rua do Matão 1210, Cidade Universitária, 05508-090, São Paulo, Brazil

<sup>6</sup>Departamento de Engenharia Eletrica, Pontificia Universidad Católica de Chile, Vicuña Mackenna 4860, Casilla 306, 22 Santiago, Chile

<sup>7</sup>Instituto de Física, Universidade de São Paulo, CP 66318, 05314-970, São Paulo, Brazil

<sup>8</sup>Prime Optics, 17 Crescent Road, Eumundi, Qld 4562, Australia

<sup>9</sup>Universidade Paulista - Unip, Rod. Presidente Dutra, km 157,5, Pista Sul, CEP 12240-420 São José dos Campos, São Paulo, Brazil.

<sup>10</sup>Laboratorio de Astrofísica Teórica e Observacional, Universidade Estadual de Santa Cruz, Rodovia Ilhéus-Itabuna km 16 45650-000 Ilhéus BA, Brazil

<sup>11</sup>Nüvü Caméras, Montréal, Qc, Canada

<sup>12</sup>Southern Astrophysical Research Telescope (SOAR), Casilla 603, La Serena, Chile

<sup>13</sup>Laboratoire d'Astrophysique de Marseille, Université de Provence, CNRS, 38, rue Frédéric Joliot-Curie 13388, Marseille cedex 13, France

<sup>14</sup>Laboratoire d'Astrophysique Expérimentale, Observatoire du Mont Mégantic, and Département de Physique, Université de Montréal, CP 6128, Succursale Centre-Ville, Montréal, PQ H3C 3J7, Canada

## ABSTRACT

This paper presents a description of a new Tunable Filter Instrument for the SOAR telescope. The Brazilian Tunable Filter Imager (BTFI) is a highly versatile, new technology, tunable optical imager to be used both in seeing-limited mode and at higher spatial fidelity using the SAM Ground-Layer Adaptive Optics facility (SOAR Adaptive Module) which is being deployed at the SOAR telescope. Such an instrument opens important new science capabilities for the SOAR astronomical community, from studies of the centers of nearby galaxies and the interstellar medium to statistical cosmological investigations.

The BTFI concept takes advantage of three new technologies. The imaging Bragg Tunable Filter (iTBF) concept utilizes Volume Phase Holographic Gratings in a double-pass configuration, as a tunable filter, while a new Fabry-Perot (FP) concept involves the use of commercially available technologies which allow a single FP etalon to act over a very large range of interference orders and hence spectral resolutions. Both these filter technologies will be used in the same instrument. The combination allows for highly versatile capabilities. Spectral resolutions spanning the range between 25 and 30,000 can be achieved in the same instrument through the use of iTBF at low resolution and scanning FPs beyond  $R \sim 2,000$  with some overlap in the mid-range. The third component of the new technologies deployed in BTFI is the use of EMCCDs which allow for rapid and cyclically wavelength scanning thus mitigating the damaging effect of atmospheric variability through the acquisition of the data cube.

An additional important feature of the instrument is that it has two optical channels which allow for the simultaneous recording of the narrow-band, filtered image with the remaining (complementary) broad-band light. This then avoids the otherwise inevitable uncertainties inherent in tunable filter imaging using a single detector which is subject to temporal variability of the atmospheric conditions.

The system was designed to supply tunable filter imaging with a field-of-view of 3 arcminutes on a side, sampled at  $0.12''$  for direct Nasmyth seeing-limited area spectroscopy and for SAM's visitor instrument port for GLAO-fed area spectroscopy. The instrument has seen first light, mounted on the SOAR telescope, as a visitor instrument. It is now in commissioning phase.

## 1. Introduction

The BTFI concept arose as a response to the need within the Brazilian community for a 3D-spectroscopy instrument able to make use of SAM's full field of view (SAM is the SOAR's ground-layer adaptive optics instrument, Tokovinin et al. 2008). SAM's potential for giving enhanced spatial resolution over a relatively large ( $\sim 3 \times 3$  arcmin<sup>2</sup>) field of view was always envisaged to be a powerful tool that would allow the SOAR community to conduct high impact scientific programs. In order to fully realize the science potential that such an investment allows, it was necessary to utilize not just the superb image quality but also the field-of-view advantage of SAM for not only imaging but also spectroscopy. SOAR already possesses an optical imager (SOI, the SOAR Optical Imager) at the bent Cassegrain focus. Furthermore, SAM has planned the construction of a dedicated GLAO-enhanced optical imager (SAMI, the SOAR Adaptive Module Imager). On the other hand, the BTFI project represents the development of a wide-field tunable filter imager as an effective means for performing area spectroscopy over a wide range of spectral resolving powers on both the SOAR Nasmyth focus and on SAM, so as to fully exploit their science potential.

Of special interest to the Brazilian community is the study of the centers of nearby active galaxies, the study of kinematics and metallicities of cluster and group galaxies at redshifts 0.1-0.3 (for which a number of systems can be observed in one shot) and of stellar mass loss phenomena in the surrounding interstellar medium. For these studies, a larger field of view than the one delivered by SIFS (the SOAR Integral Field Spectrograph, with a field of view of  $3 \times 5$  arcsec, also to be used with SAM, Lepine et al. 2003), was desirable. Moreover, there is currently no Fabry-Perot, Tunable Filter instrument on any telescope working with adaptive optics. It is therefore clearly recognized within the Brazilian community that BTFI offers new capabilities that are worth exploring.

The BTFI project started in February 2007 and it successfully passed its CoDR and PDR in September 2008 and June 2009 respectively. The system was designed to supply tunable filter imaging with a field-of-view of  $\sim 3'$  sampled at  $\sim 0.12''$  (with an f/7 camera) for direct Nasmyth seeing-limited area spectroscopy and for SAM's Visitor Instrument port for GLAO-fed area spectroscopy.

Like many other instruments of its type, BTFI employs Fabry-Perots (FPs) in order to achieve high spectral resolutions up to  $R \sim 30,000$ . In the less explored, low spectral resolution domain, exploited more recently by the Anglo-Australian Telescope's TAURUS Tunable Filter (TTF), the BTFI will utilize a new double-pass Volume Phase Holographic (VPH) grating technology (the imaging Bragg Tunable Filter) to achieve ultra-low to intermediate ( $25 < R < 4000$ ) spectral resolving powers in a highly efficient, cost-effective and compact configuration.

The instrument is being developed by the Instituto de Astronomia, Geofísica e Ciências Atmosféricas (IAG) at the Universidade de São Paulo, Brazil, in collaboration with several other Brazilian Institutions, such as Escola Politécnica (POLI) from the same

university, Instituto Nacional de Pesquisas Espaciais (INPE), Laboratório Nacional de Astrofísica (LNA) and Universidade Federal do Rio Grande, Universidade Estadual De Santa Cruz and international collaborations with the Laboratoire d'Astrophysique de Marseille (LAM), the University of Montreal and Universidad Católica in Chile.

The paper is organized as follows: in Section 2 a description of previous instruments of similar type is presented while in section 3 we outline the instrument concept and its new technologies. In Section 4 we briefly describe the science cases. In Section 5 we detail the BTFI instrument itself and we present the first observations obtained in January 2012.

## 2. Fabry-Perot and Tunable Filter interferometers

In order to clarify the concept of spectroscopy, following Fellgett (1958), two classes should be defined: the spectrographs and the spectrometers. A spectrograph allows a spatial measurement of the position of maximum intensity of a line or of a fringe on the detector while a spectrometer allows its temporal measurement. In other words, a spectrograph is associated to a unique image obtained during a unique reading of the image sensor while a spectrometer is associated to a scanning sequence obtained during several readings of the detector. Both spectroscopies are equally efficient if, at any time, the whole surface of the sensor is optimally used. Spectrographs usually use gratings to disperse the light while spectrometers require interferometers. Examples of spectrometers are Fabry-Perots (FPs) or Tunable Filters (TFs; or low spectral resolution Fabry Perots are sometimes called tunable filters) and Fourier transform imager systems (FTSs). Their "ecologic" niches are different; spectrographs are used when the science drivers request large spectral ranges and small FoVs while spectrometers are preferred when larger FoVs and smaller spectral ranges are preferred.

Providing a 2D-image within a given spectral band using a Fabry-Perot instrument requires scanning the interferometer. Following the Fabry-Perot interference formula,  $2ne \cos(i) = p\lambda$  (where  $n$  is the refractive index,  $e$  the distance between the two parallel plates,  $i$  the angle of incidence of the light,  $\lambda$  the wavelength and  $p$  the interference order), the scan can be achieved by changing  $i$  (selection of the angle on the sky),  $n$  (the index of the layer between the plates, usually through varying the gas pressure between the plates of the interferometer) or  $e$ , by moving the distance between the two plates. Modern interferometers have generally chosen to scan by acting on  $e$  but this was not the case for the first Fabry Perot imagers. It is beyond the scope of this section to provide a historical review of the Imaging Fabry-Perot systems. However we should nevertheless mention the pioneer work of Courtes (1960) in Marseille who scanned the field of view by varying the angle  $i$ , a technique used later by other groups (e.g. de Vaucouleurs & Pence, 1980). Scanning Fabry-Perots through changing  $n$  (pressure) were developed at Maryland by Tully (1974); Roesler et al (1982) for the instrument PEPSIOS, Smith (1981) for the instrument SPIFI and at Rutgers by Williams, Caldwell & Schommer (1984). Scanning by changing the gap was pioneered by Taylor & Atherton (1980) in the instrument

TAURUS followed by Boulesteix et al (1984) with the instrument CIGALE and SPIFI and Rutgers groups.

In the following section we will quickly tabulate some of the more recent Fabry-Perot spectrometers available for astronomy, all of them scanning the gap  $e$ . All of the Fabry-Perot interferometers on large telescopes fit within the collimated section of a focal reducer, following the pioneer concepts suggested by Courtès (1960). All of them are also seeing limited with a spatial sampling that depends on the detector pixel scale. Their spectral resolutions only depend on the interference order,  $p$ , of the interferometers (for a given reflective factor  $R$  of the plates at a given wavelength), furthermore the spectral resolutions given in Table 1 are those usually used with the instruments, generally with different Fabry-Perot etalons.

**TAURUS & TTF** - Taurus is an imaging Fabry-Perot interferometer which was used at the AAT between 1981 and 1983 (Taylor & Atherton, 1980; Atherton et al. 1982). Taurus was the first scanning imaging Fabry-Perot in use for astronomy. The Taurus-II Tunable Filter (TTF) was a more powerful version of the original Taurus; it was in regular use from 1996 to 2003 on the Anglo Australian Telescope (AAT). During this period, a duplicate was also used on the William Herschel Telescope (WHT) from 1996 to 2000. An important feature of the TTF was the use of charge shuffling synchronized to band switching in order to greatly suppress systematic errors associated with conventional imaging (Bland-Hawthorn & Jones, 1998a; Bland-Hawthorn & Jones, 1998b). Taurus-II is no longer offered or supported at the AAT or WHT.

**Table 1: Instrumental Parameters of the Fabry-Perot interferometers.**

Name <sup>1</sup>	Status <sup>2</sup>	Telescope <sup>3</sup>	Wv Range[nm] <sup>4</sup>	R <sub>s</sub> <sup>5</sup>	FoV[ ' ] <sup>6</sup>	S[ " ] <sup>7</sup>
TAURUS	Out. Op.	AAT(3.89m) & WHT (4.2m)	370 – 950	100 - 60000	9.87	0.37
HIFI	Out Op.	CFHT(3.58m) & UH(2.2m)	400-750	4000-16000	10	0.43-0.69
CIGALE	Out Op.	ESO (3.60m)	656.3 – 678.2	15000	5.0	0.45
PALILA	Out Op.	CFHT(3.58m)	656.3 – 678.2	15000	5.8	0.34
MOS-FP	Out Op.	CFHT(3.58m)	365 – 1000	5000 – 15000	10	0.8
GriF	Out Op.	CFHT(3.58m)	H & K Band	2000	0.6	0.12
GHASP	In Op.	OHP(1.92m)	656.3 – 678.2	15000	5.8	0.68
GHaFaS	In Op.	WHT(4.2m)	656.3 – 678.2	5000 – 15000	4.0	0.45
FaNTOmM	In Op.	Mégantic(1.6m)	656 – 678	5000 – 15000	19.4	1.61
PUMA	In Op.	San Pedro(2.1m)	365 – 865	10650	10	0.67
SCORPIO	In Op.	SAO(6m)	500 – 900	3000-10000	6.1	0.40
MMTF	In Op.	Magellan(6.5m)	500 – 920	200-1840	27 / 10	0.60
RSS/FP	In Op.	SALT(11m)	430 – 860	300 – 9000	8	0.25
OSIRIS	Future	GRANTECAN (10.4m)	365 – 1050	300 – 5000	7.8	0.13
TFI	Future	JWST(6.5m)	1500 – 5000	75 – 120	2.2	0.60

<sup>1</sup> Name. <sup>2</sup> Present status. Out Op.: Out of Operation and In Op. In Op.: In Operation. <sup>3</sup> Telescope(s) and primary mirror size. <sup>4</sup> Wavelength range. <sup>5</sup> Spectral resolution. <sup>6</sup> Field of view. <sup>7</sup> Spatial sampling (pixel size).

**HIFI** – (Hawaii Imaging Fabry-Perot Interferometer) was a low resolution Fabry-Perot Imager that differed from the TAURUS systems in its use of large free spectral-range etalons ( $\sim 100\text{\AA}$ ) with high finesse ( $\sim 60$ ) (Bland & Tully 1989) with a CCD at its image plane. HIFI was used both on the University of Hawaii 2.2m and CFHT 3.6 telescopes. It provided seeing limited observations.

**CIGALE** - CIGALE (for CInematics of GALaxiEs) is an imaging Fabry-Perot interferometer built by the Observatoire de Marseille (Boulesteix et al. 1984). It was used on several telescopes: CFHT, the 2.6m Byurakian Telescope, the 6m Zelenchuk Telescope and the 3.6m ESO telescope. It is composed of a focal reducer, a scanning Fabry-Perot and an Image Photon Counting System (IPCS). The IPCS, with a time sampling of 1/50 second and zero readout noise, makes it possible to scan the interferometer rapidly (typically 5 seconds per channel), avoiding sky transparency, air-mass and seeing variation problems during the exposures.

**PALILA** - The focal reducer PALILA was built by the Observatoire de Marseille for the CFHT and was in use at CFHT from 1990 to 1994 until it was donated to the Observatoire du mont Mégantic. It differs from CIGALE in that the detector was a CCD camera instead of an IPCS (Boulesteix & Grundseth, 1987)

**MOS-FP** - MOS/SIS was a dual Multi-Object and Subarcsecond Imaging Spectrograph for CFHT which contained a Fabry-Perot facility (MOS-FP). MOS-FP replaced PALILA in 1994. The MOS/SIS spectrograph was jointly designed and built by teams from the Dominion Astrophysical Observatory in Victoria, the Observatoire de Paris-Meudon, the Observatoire de Marseille and CFHT. MOS-FP saw its first light in July 1992 and it has not been used any longer since 2006. (Le Fèvre et al, 1994)

**GriF** - The three-dimensional spectroscope GriF offered Fabry-Perot capabilities in the near-infrared behind PUEO, the CFHT adaptive optics bonnette, and provided images at the diffraction limit of the telescope in the K band (Clénet et al., 2001). GriF is no longer offered at CFHT.

**GHaSP** - (for Gassendi H $\alpha$  survey of SPirals) is a CIGALE-like instrument attached to the Cassegrain focus of the 1.93m telescope at the Observatoire de Haute-Provence equipped with a scanning Fabry-Perot and a photon counting detector. The instrument has been in continuous operation since 1998. (Garrido et al 2002)

**GHαFaS** - (for Galaxy H $\alpha$  Fabry-Perot System for WHT) is a Fabry-Perot system available at the William Herschel Telescope. It was mounted, for the first time, at the Nasmyth focus of the 4.2m WHT in La Palma in July 2007. With a spectral resolution of the order  $R \sim 15,000$  and a seeing limited spatial resolution, GH $\alpha$ FaS provides a new view of the H $\alpha$ -emitting gas over a 4 arcminutes circular field in the nearby universe (Carignan et al. 2008)

**FaNTOmM** - (for Fabry-Perot de Nouvelle Technologie pour l'Observatoire du mont Mégantic) is the combination of a focal reducer (PANORAMIX: the 1.6m mont Mégantic OmM telescope focal reducer), a scanning Fabry Perot and an IPCS. FaNTOmM is a third generation instrument using a photon counting camera (IPCS) based on an GaAs photo cathode that can achieve quantum efficiency of up to 28%, comparable to a thick CCD, but with zero readout noise (Hernandez et al. 2003).

**PUMA** - (The UNAM Scanning Fabry-Perot Interferometer) is an integral field spectrometer having as the dispersive element a scanning Fabry-Perot interferometer working at optical wavelengths optimized in the red (Rosado et al. 1995). The instrument is attached to the 2.1m telescope of the Observatorio Astronomico Nacional at San Pedro Martir, B.C., Mexico.

**SCORPIO** - (Spectral Camera with Optical Reducer for Photometrical and Interferometrical Observations) is a multi-mode focal reducer containing a Fabry-Perot facility (Afanasiev & Moiseev 2005). 2D spectroscopic observations using an imaging Fabry-Perot at the 6m telescope was initiated in the early 80s using the CIGALE system. In 1997 a CCD was attached to the old focal reducer instead of a photon counter. A new multi-mode focal reducer SCORPIO was developed by the Special Astrophysical Observatory, Russian Academy of Sciences, and was first on sky in 2000.

**MMTF** - The Maryland Magellan Tunable Filter on the Magellan-Baade Telescope is a narrowband filter which is tunable in both central wavelength and transmission band-pass. It has a large field of view (27' full diameter of which  $\sim 10'$  is monochromatic) which means that if the target covers a range in velocity larger than the 10' of the central spot (depending on the wavelength), multiple exposures are needed to capture all line emission. The MMTF operates on similar principles to the Taurus Tunable Filter (Veilleux, S., et al. 2010).

**RSS** - (Robert Stobie Spectrograph) is designed and built for SALT (Southern African Large Telescope) and has the capability to obtain true wide-field imaging spectroscopy through its Fabry-Perot (FP) modes (Rangwala et al. 2008). It has been progressively put in operation since 2010.

**OSIRIS** - (Optical System for Imaging and low-intermediate Resolution) is an imager and spectrograph for the optical wavelength range, located at the Nasmyth-B

focus of GTC (Cepa et al. 1998). It provides narrow-band tunable filter imaging and charge-shuffling capabilities. The blue Tunable Filter mode of OSIRIS has been delivered and is undergoing technical verification tests on the telescope. The on-sky commissioning will be done during 2012.

**TFI** - (Tunable Filter Imager) is an uncertain science instrument for JWST. It is a sensitive camera that shares the optical bench of the Fine Guidance Sensor. The TFI can also perform imaging with a choice of four coronagraphs as well as a non-redundant mask (Ingraham et al. 2010).

### **3. Instrument concept – the new technologies used in BTFI**

The concept of a classical FP-based imaging interferometer for both kinematic work (high interference order) and tunable filter work (low interference order) is depicted in Figure 1. This will later be contrasted with the iBTF technology, however for now it illustrates the basic concept of 3D data cubes for both techniques. The BTFI instrument incorporates both technologies (FP + iBTF) in order to give it great versatility for a wide range of new science.

#### **3.1. The Fabry-Perot operating modes of BTFI**

BTFI uses two FP etalons that can be used individually or in tandem. The FP is typically mounted in the collimated beam for high order of interference, high spectral resolution work or in the divergent beam, near the input focus, for low order of interference low resolution work or in tandem where the low order FP can be used as a tunable order blocker for the high resolution etalon. Each of these modes will be described in detail below.

##### **3.1.1. The classical Fabry-Perot mode**

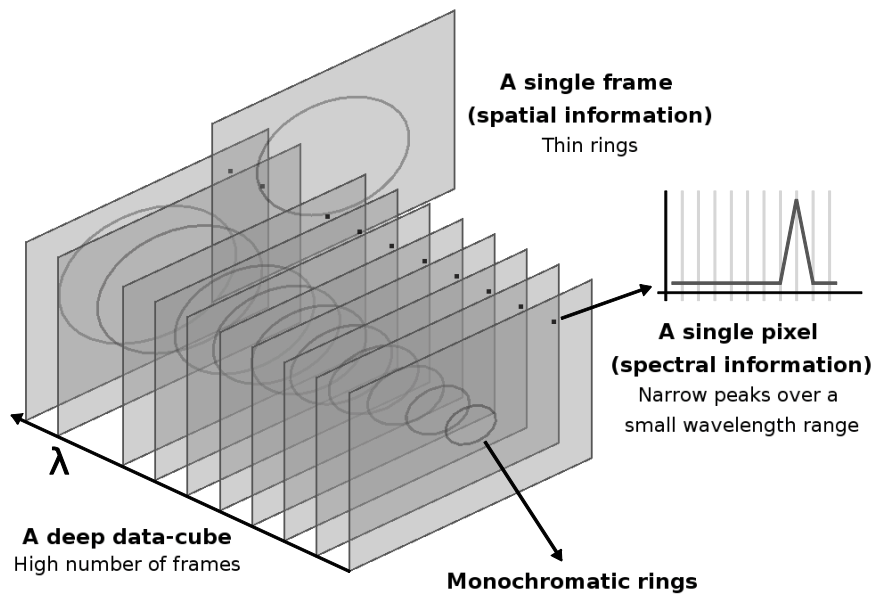
The raw data produced by a scanning FP can be represented by a series of images of the studied object, obtained at different wavelengths (or radial velocities) emanating from the source. The different wavelengths are obtained by changing the spacing between the plates of the FP etalon. The observed wavelength range is isolated using an interference filter. Once calibrated, one has a spectrum for each pixel in the field. Such FP systems have been used primarily for two types of application:

- i) To obtain precise line profiles ( $R > 25,000$ ) in order to derive the physical parameters of emission-line regions.
- ii) To obtain the complete 2-D kinematics of an emission-line source.

While in the nearby universe, the  $H\alpha$  line is mainly used, it can be replaced by the [O II],  $H\beta$  or [O III] lines for higher redshift galaxies. Broadly, the science requires the scanning FP mode of the BTFI to possess the following characteristics:

- Wavelength range: 400 – 1,000nm
- Resolution: up to 30,000
- Pixel size of 15 microns (~0.12" on the sky)
- Field of view: 3 arcmin on a side

### High-Resolution Fabry-Perot Data Structure



## Low-Resolution Fabry-Perot Data Structure

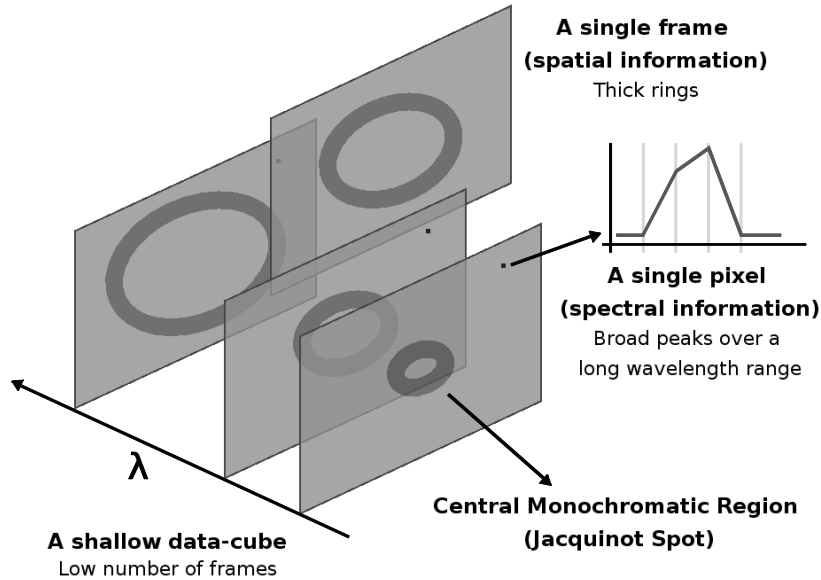


**Figure 1: Illustration of how a Fabry-Perot 3D Spectrograph works. The top figure shows a high interference order FP that yields a stack of high resolution images within a narrow spectral range. The bottom figure represents a low interference order FP and the resulting stack of low resolution images with a larger spectral range.**

For BTFI, in the classical FP mode, we use an FP etalon mounted in the collimated space. This FP etalon was manufactured by SESO (*Société Européenne de Systèmes Optiques* - <http://www.seso.com/>) to allow a far greater range of spectral resolutions than available using the more traditional designs. Older style Fabry-Perots can only cover a few free spectral ranges due to the limited scan range of their piezo-electric transducers. The technology developed for the new SESO etalon by the Cedrat company (<http://www.cedrat.com>), allows us to enlarge the scan range of the piezo-electric transducer from just above zero up to  $\sim 250\mu\text{m}$ , allowing us to cover hundreds of orders. With BTFI we would target a resolution range for the classical FP mode between  $R\sim 6,000$  and  $R\sim 30,000$ .

### 3.1.2. The FP Tunable Filter mode

The first FP Tunable Filter in regular use on a 4m telescope was the Taurus Tunable Filter (TTF), commissioned fully on the AAT in 1995-97 (Bland-Hawthorn and Jones 1998b). The TTF employed a pair of low resolution FP etalons covering 370-650nm (blue range) and 650-960nm (red range) which were deployed separately. The FP etalons for the TTF were manufactured by Queensgate Instruments Ltd. and were conventional etalons other than having a small nominal gap (low order interference). Unlike conventional Queensgate etalons which had been used in the previous generation of FP interferometers, the TTF also incorporated long-range piezo-electric stacks (which

expand the otherwise available plate separation range) and high performance coatings covering almost half the optical wavelength range. Since FPs have a periodic transmission profile, the instrument requires a limited number of order blocking filters. At low resolution ( $R \sim 300$ ), conventional broad-band UVRIz filters suffice. At the higher resolution end of the range ( $R = 1,000$ ), eight intermediate-band filters were used. Thus the TTF system was used to obtain single quasi-monochromatic images centered at a given wavelength while also providing a limited series of narrowband images, stepped in wavelength.

The flexibility of the TTF was well-suited for narrow-band astronomical imaging in emission lines such as [O II] 3727, [O III] 5007,  $H\alpha$ , [N II] 6583, [S II] 6717/6731 and [S III] 9069. Furthermore, it had the capability of obtaining images of spectral lines at arbitrary redshifts. In that sense, it also allowed for a scanning mode, but with a broader band as compared with that typically used for kinematic studies. There are several technical problems driving the development of FP Tunable Filters for narrow-band imaging within standard fixed interference filters. These problems will be highlighted ahead together with suggestions for mitigating them.

In BTFI, for the FP tunable filter, low resolution mode, we use an alternate etalon, also manufactured by SESO, deployed in the diverging beam just above the  $f/16.5$  input focus. As explained above, SESO etalons have the capability of spanning FP gaps of  $\sim 250\mu\text{m}$ , which would, in principle allow a spectral resolution range between  $500 < R < 30,000$ . However, the higher end of this range is curtailed by the divergent beam, allowing resolutions of  $500 < R < 2000$ , for this instrumental mode.

In summary, the new interferometer can be used as a Tunable Filter (low order of interference: low resolution) and as a classical Fabry-Perot (high order of interference: high resolution) and may shift from one mode to the other very quickly. There will, inevitably be a spectral resolution “gap” between the low and high resolution FP domains which can be partially filled by the iBTF mode under certain constraints (as described in section 3.2), and by our ability to stretch the gap range of the SESO etalons themselves. This is currently under investigation.

### **3.1.3. The use of both etalons in series**

As described above, the BTFI has two etalons, one in the divergent beam near the input focus (for low spectral resolutions) and the other in the collimated beam (for higher spectral resolutions). Since both etalons can be deployed independently into the optical beam, it is possible to use these etalons in tandem with the first operating as an order sorter for the second. In this manner great flexibility is achieved in the ability to select a particular order for the higher resolution etalon, a job which is usually done by the use of a fixed interference filter. By using the low resolution etalon as an order selector, avoidance of the acquisition of multiple costly interference filters (and the necessity to mount these) is achieved. The disadvantage is that order selection is achieved with a single-pass Airy profile rather than a clean near top-hat interference filter profile. Nevertheless such a two-etalon capability is seen as a significant advantage for BTFI.

### 3.2. The iBTF operating mode of BTFI

As will be described in more detail in Section 5.2, the iBTF employs two identical VPH gratings which cancel each other's dispersion. The resultant output represents the blaze function, as defined by its Bragg condition at a specific angle of incidence. By changing the angle of incidence of the grating pair this blaze function can be scanned, thus achieving wavelength tunability over a wide range of wavelengths and spectral resolutions, as defined by the grating and the range of accessible angles.

This technique gives the ability to achieve an imaging tunable filter by simply changing the angle of the grating pair; the iBTF optical configuration can employ either transmission or reflection gratings thus increasing the range of resolutions obtainable. Resolutions are then limited to those achievable with current volume phase holographic grating materials.

Gratings made from dichromated gelatin (DCG) allow for very thin grating structures with high refractive index modulations giving resolutions in the range  $5 < R < 500$ , while thick, low refractive index modulation gratings can be made from doped-glass which can reach resolutions towards  $R \sim 4000$ .

### 3.3. The Detector

When observing in wavelength scanning mode with a classical CCD, as is the case for all currently available tunable filters and Fabry-Perot systems, it can take several hours to complete a single scan and as such the observations are susceptible to changes in seeing PSF and transparency between individual frames. The result is that the profile of the scanned line will be biased, unless the scan is rapid enough so that it can then be repeated several times to achieve the desired total exposure time. The changes in seeing and transparency will be averaged when adding all the individual frames corresponding to the same scanning step of the FP (or iBTF). The problem with classical CCDs is that their readout noise will be added on each individual frame and the resulting profile will be relatively noisy. Because of the read-out noise, it is impossible to scan rapidly through the channels (one has to wait for enough counts to be collected in the frame before reading it), with the result that only observations taken in highly photometric conditions are fully reliable since the changes in seeing and transparency cannot be averaged out.

In order to be able to scan rapidly through the channels, one has to work in photon counting (or electron amplification) mode with essentially zero read-out noise. By far the best solution available today is the L3CCD ([www.e2v.com](http://www.e2v.com)). The advantage of L3 technology (an Electron Multiplying Charge Coupled Device or EMCCD) is that it operates at essentially zero read-noise as compared to a classical CCD with typically  $\sim 3$  electrons of rms read-out noise. EMCCDs can be operated in an amplification mode

where gain-noise imposes an effective penalty of  $\sim 2$  in quantum efficiency or in photon counting mode where gain-noise can be eliminated at the cost of a serious reduction in dynamic range. For classical, long exposure, imaging or spectroscopy these disadvantages generally out-weigh the EMCCD's advantages in background-noise limited observations. However, when short exposures are demanded or when detector noise is a limiting factor, then EMCCDs can come into their own.

It will be noted that the domain of short exposure and low background noise is precisely that of the tunable filter. Not only is the background noise suppressed to a greater or lesser extent by the narrow-band imaging but the requirement to mitigate against atmospheric variability implies the use of rapid scanning whereby very short exposures are taken to build up a data-cube through continuous cycling through wavelength space. A detailed analysis showed that for BTFI, under a broad range of operating conditions, the EMCCD in amplification mode (even given the reduction of a factor of 2 in QE) gives higher signal-to-noise performance than a classical CCD when used for rapid scanning tunable filter work. Counter-intuitively, this is not the case for photon counting, despite the fact that the early use of imaging FPs used the Image Photon Counting System (IPCS). While photon counting does not suffer from gain noise inherent in the EMCCD amplification mode operation, the fact is that photon counting has such a limited dynamic range that it is only useful under the most extreme of low light level operation.

#### **4. Science cases**

There are a great number of galactic and extra-galactic studies which can benefit from the unique tunable filter imaging properties of the BTFI. This will be the first such instrument to work with a ground layer adaptive optics module, with a relatively large field of view ( $3 \times 3$  arcmin<sup>2</sup>). The most competitive science projects will then be those which require good spatial resolution, in particular the study of the centers of active galaxies, for investigation of the processes which drive the gas inwards and the study of stellar mass loss processes to the interstellar medium.

In July 2008 there was a survey within the Brazilian community to investigate interest in the use of such an instrument. In the extra-galactic arena the planned BTFI studies included, amongst others:

- The centers of normal and active galaxies;
- Nearby galaxies in clusters and groups;
- Mass distribution of galaxies and their building blocks;
- 2D kinematics of fine structure for galaxy modeling;
- Noncircular motions in the disks of galaxies;
- Barred galaxies;
- Kinematics of galaxies at intermediate redshift;
- Galaxy interactions and merging;
- Blue compact dwarfs, HII galaxies and tidal dwarf galaxies.

While for Galactic work and study of the interstellar medium the following topics of interest included:

- Galactic HII regions;
- Studies of Herbig-Haro objects and associated jets;
- Kinematics of Proplyds;
- Mass loss in stellar systems;
- Structure, metallicities and kinematics of planetary nebulae.

BTFI will be highly complementary to the SOAR Integral Field Spectrograph, which will also work with SAM.

## 5. BTFI Instrument Description

### 5.1. Instrument Concept

In its simplest mode the BTFI instrument is a focal reducer with a single  $f/16.5$  collimator and dual cameras allowing the simultaneous acquisition of the filtered ( $F_\lambda$ ) and complementary ( $T-F_\lambda$ ) images across the observed field-of-view ( $T$  represents the spectrum of pre-filtered light incident on the tunable filter having a tunable band-pass  $F_\lambda$ ). The simultaneous acquisition of filtered and complementary images permits a robust correction for transparency and PSF variations which otherwise plague the reconstruction of photometrically accurate 3D data-cubes.

As far as we are aware, all other FP-based imaging interferometers have done without such a facility, however accuracy of the photometric reconstruction of such data-cubes has been a severe limitation on the scientific utility of the resulting data. While high resolution kinematic data can, with care, be routinely obtained, an accurate, low resolution, tunable filter data cube requires not only superb photometric conditions over the time-frame of the spectral scan but also a stability of the image PSF to preserve spatial resolution through the data-cube. Immunity to such atmospheric instabilities can be mitigated to some degree with photon counting detectors (eg: the original TAURUS system using the Image Photon Counting System, the FaNTOMM fast scanning system or proposed systems using E2V's L3 technology). However, at low resolution, where background noise dominates, standard CCDs may still be required for ultimate sensitivity. Furthermore, the time spectrum of PSF variability as delivered by SAM's GLAO system, while it may have been modeled under the range of atmospheric conditions prevalent at SOAR, will not be confirmed until the SAM system has been fully commissioned. Hence for a system based on long time-scale sequential wavelength scanning, caution argues for inclusion of a complementary channel.

As defined above, the second, complementary, channel ( $T-F_\lambda$ ) approximates to a continuum image of the observed field and hence offers a very deep, high signal-to-noise, image which can be used to monitor the atmosphere. However, this is not the only use of the second channel; the broad-band ( $T-F_\lambda$ ) light can be further filtered with a FP to allow for simultaneous wavelength scanning at a secondary spectral resolution. Provided the second channel is at significantly lower resolution than the first, it can be used both as an atmospheric monitor channel and as a second science channel offering simultaneous wavelength scans at two resolutions and/or wavelengths. The two cameras of the BTFI thus represent a highly versatile instrument concept. The primary channel can be used for high resolution (FP) scans or low to intermediate resolution (iBTF) scans. In both cases the secondary channel can be used for atmospheric monitoring. Alternatively the accuracy of atmospheric monitoring can be traded with scientific utility by using the second channel for the simultaneous acquisition of data-cubes at different resolutions and/or wavelengths. The actual usage of the BTFI will be highly dependent on the science objectives of the user. The two channel concept gives the BTFI a photometric robustness for data cube acquisition while allowing a scientific versatility that is unique amongst FPs and tunable filter imagers.

## 5.2. The iBTF concept

One of the most interesting features of volume phase holographic gratings is the possibility of adjusting the efficiency curve, or “blaze” function, by varying the angle of incidence (Barden et. al. 2000a). Indeed, while their dispersive properties are identical to that of classical gratings, their diffracted energy distribution is governed by Bragg’s law, as for X-rays in a crystalline structure (i.e. radiation that departs significantly from the Bragg condition passes through the grating undiffracted). This tunability can be advantageously used in spectrographs, but it also allows a new type of imaging tunable filter. Using a second grating, it is possible to recombine, or “undisperse”, the light coming from the first grating. An image can be reconstructed as long as the gratings are parallel and have the same line fringe frequency (Blais-Ouellette et al. 2004). The iBTF concept is illustrated in Figure 2. Only light whose wavelength satisfies the Bragg condition is diffracted. It is then possible to adjust the grating angle, effectively tuning the filter’s central wavelength.

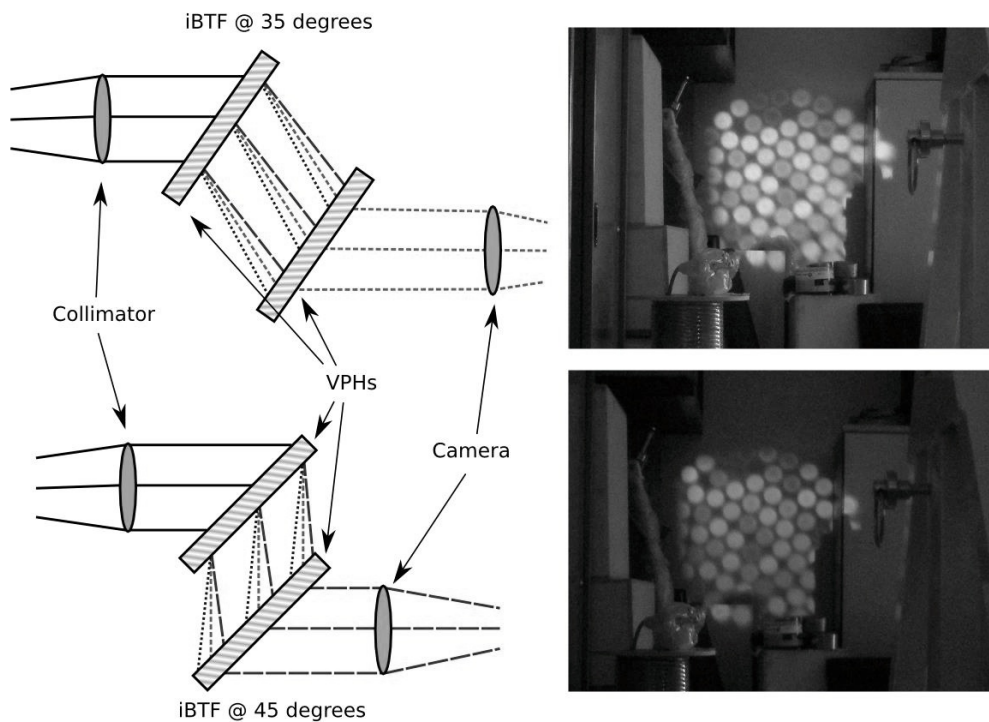


**Figure 2: This figure is a simplified representation of the dual VPH tunable filter concept. A first grating disperses collimated light that satisfies the Bragg condition. A second grating recombines the beam which is then re-imaged onto a detector. Top right: grating angle is 30°, passband is centered on 500 nm for a 2300 lines/mm VPH. Bottom right: grating angle is 45°, passband is centered on 618 nm for the same VPHs. Top and bottom left: pictures taken in the lab with the two corresponding configurations, using a common tungsten light and an optical fiber bundle as source, with a 2300 lines/mm transmission grating.**

The advantages of an iBTF tunable filter concept over a standard Fabry-Perot (or Imaging Fourier Transform Spectrograph) based instrument are as follows:

- The iBTF is compact, robust and built from custom-specified VPH gratings;
- The VPH grating is less expensive than a FP;
- Wavelength tuning is achieved through a simple rotation mechanism rather than complex and highly delicate capacitance micrometry;
- There are fewer internal alignment issues as contrasted with the highly critical and unstable plate alignment of FPs;
- Ultra-low ( $R > 25$ ) together with intermediate ( $R \sim 2,000$ ) spectral resolving powers can be routinely achieved;
- The surface of constant wavelength approximates to a 1<sup>st</sup> order slope in the direction parallel to the dispersion axis as opposed to the complex nested paraboloids of the FP.

The only disadvantage is that it cannot achieve very high ( $R > 4,000$ ) spectral resolving powers if limited to standard materials and a convenient, compact format.

### 5.3. The BTFI instrument

An optical layout of the BTFI instrument is shown in Figure 3. The incident light from the  $f/16.5$  telescope enters the instrument and is focused at the input image plane ( $I_m$ ). The diverging beam propagates through the Field Lenses (FL) which is optionally followed by the first Fabry-Perot ( $FP_{lm}$ ) according to the operational mode of the instrument. Afterwards, the light beam is reflected by two fold mirrors ( $FM_1$  and  $FM_2$ ) that are needed to accommodate space constraints.

The light then passes through the collimator group (CG) and, in the collimated space, it hits the first iBTF support ( $GS_1$ ) that can hold a grating, a mirror or be empty. In the case where a grating lies in  $GS_1$ , the 0<sup>th</sup> diffraction order goes straight to where the second Fabry-Perot ( $FP_{pp}$ ) may be. Then, it goes to the  $C_1$  camera and reaches the detector  $D_1$ .

The 1<sup>st</sup> diffraction order that leaves the grating at  $GS_1$  goes to the second grating support  $GS_2$  where the dispersion is canceled by the second twin grating. The resultant “undispersed” light is finally imaged by the  $C_2$  camera at the  $D_2$  detector.

The chosen 50mm pupil is compatible with readily available VPH gratings and the folds are necessary to allow the instrument to fit within the space envelope of SAM’s visitor instrument port. An EMCCD detector having a format of 1600 x 1600 pixels is matched to the required pixel-scale (0.12”/pixel) and field of view (3 by 3 arcmin).

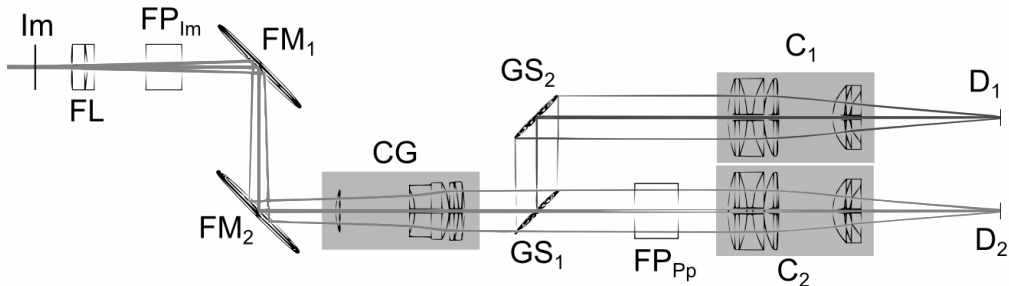


Figure 3: Simplified representation of the BTFI optical path.

## 5.4. BTFI performance summary

### 5.4.1. Spectral Resolving Powers

- $5 < R < 100$ : The lowest resolutions can be achieved with transmission VPHGs formed from Dichromated Gelatin (DCG) (Barden et. al. 2000a);
- $100 < R < 200$ : In reflection the DCG gratings can deliver somewhat higher resolutions;
- $200 < R < 3,000$ : Using doped glass (D-G) rather than DCG intermediate resolutions can be achieved for a transmission configuration;
- $1,000 < R < 4,000$ : while in reflection, D-G gratings can deliver the highest iBTF resolutions attainable with current VPHG materials;
- $500 < R < 30,000$ : FPs (including FP-based tunable filters) are, in principle, unlimited at the high resolution end, however the  $R < 500$  régime is very difficult to achieve in practice.

### 5.4.2. Efficiencies

VPH gratings are intrinsically very efficient gratings ( $\sim 90\%$  at peak). Used in double-pass they are still significantly more efficient than normal surface-ruled gratings ( $\sim 60\%$ ) and FPs ( $\sim 70\%$ ). In order to fully understand the relationship between the efficiency of a grating, the incident angle and the wavelength, one has to use a sophisticated theory, as the one described in (Kogelnik 1969). As an example, Figure 4 shows a simulation using this theory where one can see the efficiency curve for a specific grating ( $R \sim 50$ ) in three different angles. One can also see the locus of peak efficiency as a function of wavelength which is known as the super-blaze (Barden et. al. 2000b).

Some doped glass configurations have further losses of efficiency that occur in the material itself. Nevertheless, the BTFI concept allows for a broad range of spectral resolutions at efficiencies competitive with current techniques but at a fraction of the cost and complexity.

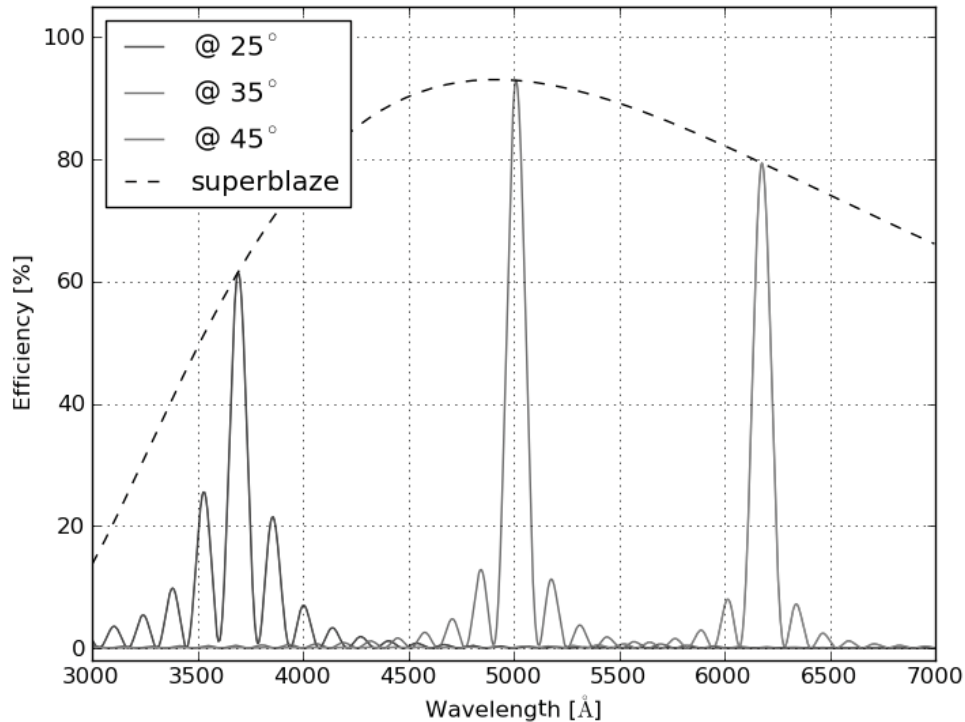


**Figure 4: Simulation using Kogelnik (1969) for a transmission grating with 2300 lines/mm, 42  $\mu\text{m}$  thick and refractive index modulation 0.0065, for three incident angles (solid lines) and the superblaze function (dashed line).**

The full system throughput is a composition of SOAR, collimator and camera, fold mirrors and the EMCCD throughputs. With exception of the EMCCD, the other components have relatively flat responses with values of 0.62 for SOAR, 0.9 for the collimator and camera and 0.82 for the fold mirrors. The EMCDD throughput curve is bell-shaped with a maximum of 0.93 at 550 nm decaying to 0.25 at 350nm and 0.38 at 900nm. The full system throughput curve has the same shape with maximum at 550nm of 0.38 for SOAR+BTFI and 0.3 if SAM is included.

An acceptance test was done with the collimator and camera. The collimator was reversed and fed with a 50mm diameter collimated beam at a wavelength of 633nm. Field angles up to 2.9 degrees were tested. The back focal distance from the field lens was adjusted for best focus. The system is diffraction-limited at the best focus. Image spots were indistinguishable from an Airy disk of diameter  $\sim 0.025\text{mm}$ .

A similar test was done with the camera. In this case, the system was near diffraction-limited at best focus. 80% encircled energies at all field positions were a little larger than the Airy disk whose diameter was  $\sim 0.010\text{mm}$ .

## 5.5. Calibration and Data Reduction

There are special issues involved in the use of a FP which may have a variable gap range of  $< 250\mu\text{m}$  such as is the case for the SESO etalons. In particular, the SESO FP does not have a *nominal* gap from which many etalon parameters can be derived; the gap itself has to be calibrated before any particular gap setting (and hence resolution) can be established. Furthermore, because of the compactness of the BTFI instrument layout and the requirement to operate the instrument remotely, there is no easy way in which the etalons can be inspected by eye when deployed in the instrument. This presents interesting challenges to the problem of aligning, calibrating and operating the instrument. Furthermore, different procedures are required when the FP is operated in diverging and collimated beams; both configurations will be discussed.

In order to establish parallelism, four independent measures of the gap need to be established in the 4 cardinal directions across the surface of the etalon plates.

1. If the etalon is in the diverging beam then the etalon plates themselves are approximately confocal with the detector. In this case 4 spots can be illuminated with fibers, distributed in 4 cardinal points at the input focal plane.
2. If the etalon is in the collimated beam then the pupil has to be segmented so that illumination of 4 cardinal points in the pupil can be isolated. For BTFI, this is achieved using 4 small prisms near the pupil plane.

In either case, a measurement of the gap in the four cardinal positions can be achieved by illumination with two relatively nearby wavelengths ( $\lambda_1$  and  $\lambda_2$  with interference orders  $m_1$  and  $m_2$ ). In this case we will see that:

$$m_1 - m_2 = \lambda_1/\lambda_2 \cdot (z_2 - z_1)/\Delta z_2 - m_1 \cdot (\lambda_1 - \lambda_2)/\lambda_2$$

where  $z_1$  and  $z_2$  are the emission peaks of the two wavelengths  $\lambda_1$  and  $\lambda_2$  as measured in etalon control units (capacitance measures proportional to gap) and  $\Delta z$  is the free-spectral range, as measured in the same units. This equation can be used to determine the gap in each of the four quadrants from which both approximate parallelism and gap calibration can be achieved. Of course, fine parallelism requires the same techniques but only with one wavelength.

**Phase Calibration:** The scanning FP provides spectral line profiles for each pixel in the field. In most cases, these spectra are used simply to obtain kinematic information from the Doppler shift of a given line. The calibration process is here quite simple, since one just needs to scan a reference line, the position of which is then compared with that of the observed line at each pixel (the observed line being selected through any standard interference filter). The detailed process has been described in Amram et al. (1995). With the FP in the divergent beam, the phase map is approximately flat and hence the raw data-cube approximates to that of a series of monochromatic images. With the FP

classically mounted in the collimated beam then the phase map is now parabolic and phase-correction amounts to rectifying the non-monotonic raw data-cube into a monochromatic form.

**Data reduction:** One example of a data reduction package used for FP data is that developed by Jacques Boulesteix, called ADHOC (<http://www.oamp.fr/adhoc/adhocw.htm>). This package is used by several groups observing with scanning FPs (e.g. IAG/USP, Brazil; UNAM, Mexico; Observatoire de Paris Meudon; Université de Montréal and Observatoire du Mont Mégantic, Québec; Byurakan Observatory, Armenia; SAO Zelenchuk, Russia). Illustrations of the data reduction process can be found at the following link: [http://www.oamp.fr/PdG/GHASP/ghasp\\_en.htm](http://www.oamp.fr/PdG/GHASP/ghasp_en.htm).

### 5.6. EMCCD Cameras

As stated above, EMCCD detectors offer images free of read-out noise. Read-out noise is added by the output amplifier at the very last stage of the detector, where the charge in electrons is converted to a measurable voltage. Thanks to an electron multiplication process that occurs before reaching the output amplifier in EMCCDs, each electron (created from incoming photons) generates thousands of electrons. This is a stochastic process producing the  $\sim 2$  reduction in QE mentioned above. The read-out noise added by the output amplifier is still present, but its effect is greatly diminished to negligible values. This is generally stated as sub-electron readout noise (Daigle et al. 2009).

However, any noise added to the photoelectrons before the multiplication process will suffer its multiplicative effect. An example of such a noise source are cosmic rays.

The main noise source in EMCCD that depend on the detector readout electronics is known as Clock Induced Charge (CIC) or ‘spurious charge’ (Tulloch, 2005) and is generated by the transitions of the voltage phases used to transfer the electrons across the device when storing or reading out an image. There are various methods to reduce CIC noise, usually employing wave-shape in the phases (Janesick 2001, so the effect of the transitions is minimized) and running the device in non-inverted mode of operation, or non-MPP, Multi-Phased Pinned (for more details see e2v Technical Note 4, 2004). Unfortunately, dark current is greatly increased in non-MPP mode.

We decided to design and build our EMCCD cameras, as opposed to using commercially available cameras, in order to benefit from a carefully defined set of requirements, such as deep-cooling (lower than -100 C) and arbitrary clocking. We are using readout electronics from the University of Montreal which were specially designed for EMCCDs and are now being commercialized by Nüvü Caméras ([www.nuvucameras.com](http://www.nuvucameras.com), Daigle et al. 2009). The BTFI cameras were built in collaboration with Universidad Catolica in Chile.

### 5.7. Current Status

The iBTF concept has been successfully prototyped through an NSF grant (Award #0352991) confirming the basic functionality and applicability of the double-pass VPHG concept both in transmission and reflection modes. This prototype has now been developed into a commercial product (by the company Photon etc, Montreal) as a laboratory tunable narrow band source and spectrophotometer for instrument and filter calibration. However, there are no other references regarding the use of twin VPHG's as tunable filters, given that BTFI will be the first instrument of this kind in Astronomy. For BTFI we have first developed a schematic optical layout (Figure 3) which satisfied the space constraints of SAM's visitor instrument port and we have developed an opto-mechanical design as shown in Figure 5. In September, 2007, the BTFI project successfully passed through its Concept Design Review and in June, 2008, the Preliminary Design review, the panel members of which were selected from the international astronomical instrument community.

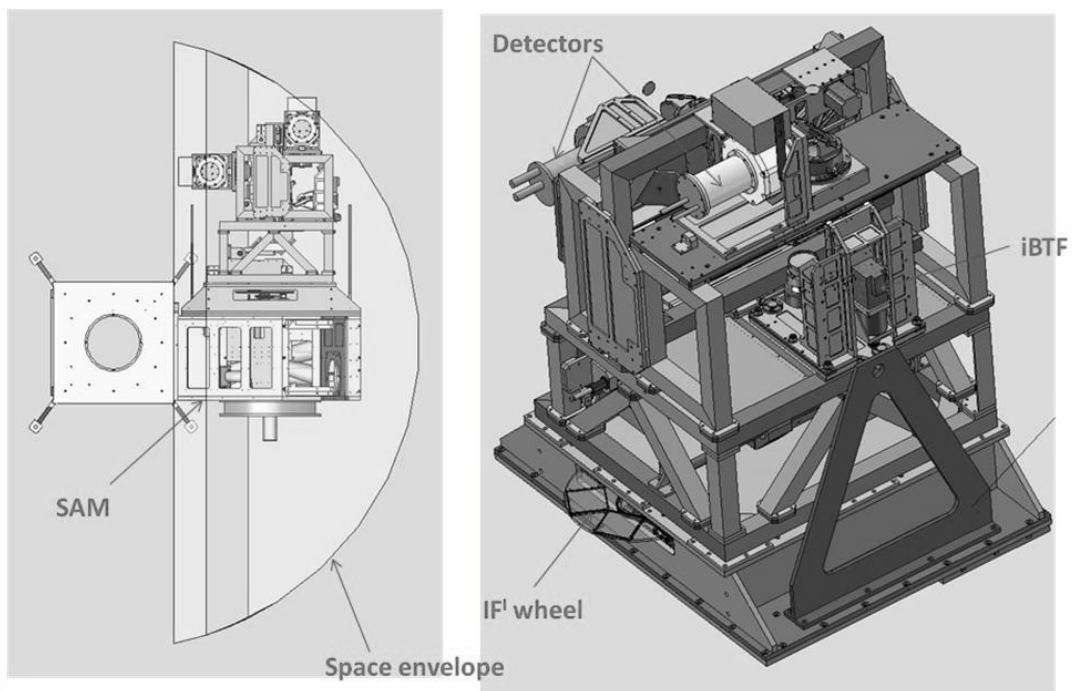


**Figure 5: An overview of the instrument mechanical design. Finite element analysis has validated the structural design.**

The total cost of the instrument is ~ \$1.5 million (USD) and was mostly funded through grants from FAPESP, the Research Funding Agency of the State of São Paulo, supplemented by additional funds from LNA and the Conselho Nacional de Pesquisa

(CNPq). This includes hardware and contract labor, excluding substantial in-house support using IAG and INPE labor.

The project is now in its commissioning phase as a visitor instrument at SOAR. Final stages of electro-mechanical integration took place at USP and INPE in 2010A. It was mounted on the direct port of the SOAR telescope and had its first light in 2010B.

An example data obtained with BTFI is shown in Figure 6. Both images are taken from a data-cube resulting from the observation of the planetary nebulae NGC 2440 using the iBTF with a reflection grating with 2370 lines/mm and scanning from  $38.75^\circ$  to  $41.00^\circ$  in steps of  $0.05^\circ$ .

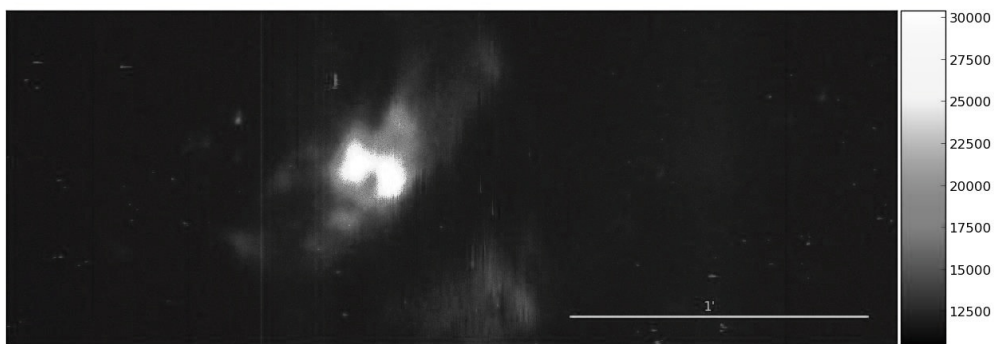


**Figure 6: Data-cube obtained from NGC 2440 collapsed in  $\lambda$ .**

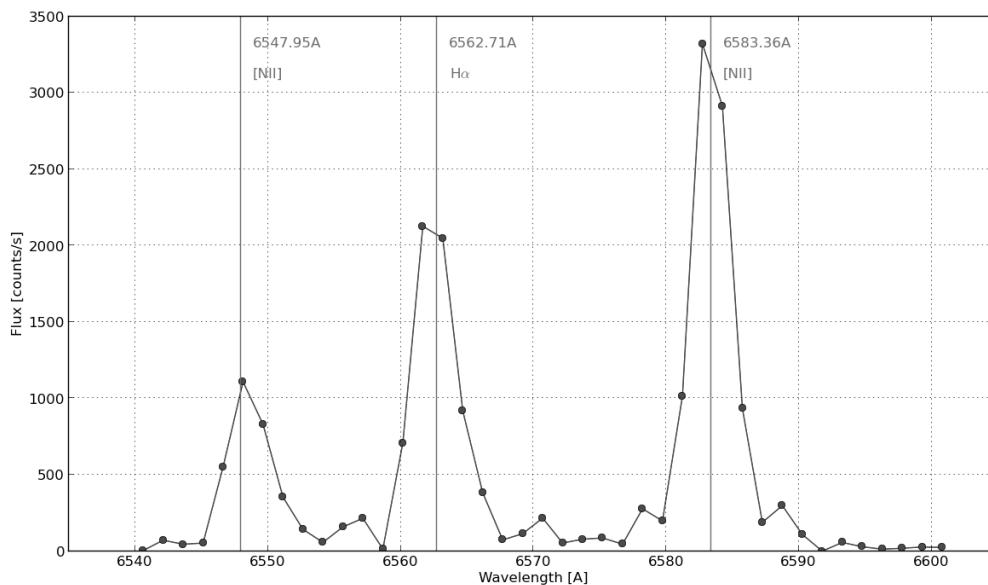


**Figure 7: Spectrum extracted from the central pixel of the upper-left lobe of the NGC 2440.**

## 6. Conclusion

The Brazilian Tunable Filter Imager represents an instrument strategy that optimizes the science potential for optical spectroscopy with the SOAR telescope, with its emphasis on high image quality and its use of Ground Layer Adaptive Optics for image enhancement in the optical over a field of view of  $3 \times 3$  arcmin. It is expected that it will become a regular users' instrument after SAM is fully commissioned.

The authors thank FAPESP (grant 2006/56213-9) and the Instituto Nacional de Ciência e Tecnologia de Astrofísica (grant 2008/08/57807-5), CNPq and LNA/MCTI for funding of the BTFI project. Fellowships granted to four Masters students, one PhD student, and four technicians (technical capacitation fellowships) who worked in the project are acknowledged to FAPESP, CAPES and CNPq. The BTFI team thanks the CTIO technical team for their valuable support and the SOAR director Steve Heathcote, without whom this instrument would have never been completed.

## References

- Afanasiev & Moiseev, 2005, *Astronomy Letters*, 31, 194
- Amram, P., Boulesteix, J., Marcelin, M., Balkowski, C., Cayatte, V., & Sullivan, W. T. III, 1995, *A&AS*, 113, 35.
- Atherton, P.D., Taylor, K., Pike, C.D. et al., 1982, *MNRAS*, 201, 661.
- Barden, S. C., Williams, J. B., Arns, J. A., Colburn, W. S., 2000 *APS Conference Series*, Vol. 195. pp.552
- Barden, S. C., Arns, J. A., Colburn, W. S., Williams, J. B., 2000, *PASP*, Vol 112, pp. 809-820.
- Blais-Ouellette, S., Wishnow, E. H., Shopbell, P. L., van Breugel, W., Taylor, K. & Smith, R. 2004, *SPIE*, 5492, 779
- Bland, J. & Tully, R. B., 1989, *AJ*, 98, 723
- Bland-Hawthorn & Jones, 1998, *PASA*, 15, 44
- Bland-Hawthorn, J. & Jones, D.H. 1998b, *SPIE*, 3355, 855
- Boulesteix, J., Georgelin, Y., Marcelin, M. & Monnet, G. 1984, *SPIE*, 445, 37
- Boulesteix & Grundseth, 1987, *Bulletin CFHT num 17*
- Carignan, C. Hernandez, O. Gach, J. Balard, P. De Denus-Baillargeon, M. Fathi, K. Beckman, J., Koulidiati, J. 2008, *SPIE*, 7014, 188
- Cepa, J. 1998, *ApSS*, 263, 369
- Clénet, Y. et al. 2001: *Semaine de l'Astrophysique Française*, meeting held in Lyon, France, May 28-June 1st, 2001, Eds.: F. Combes, D. Barret, F. Thévenin, *EdP-Sciences*, Conference Series, p.603
- Courtès, G. 1960: *Annales d'Astrophysique*, Vol. 23, p.115.
- Daigle, O., Carignan, C., Gach, J-L., Guillaume, C., Lessard, S., Fortin, C-A. and Blais-Ouellette, S., *PASP* 2009, 121, 866.
- Fellgett, P. 1958, *Present and Future of the Telescope of Moderate Size*. Edited by Frank Bradshaw Wood. Philadelphia: University of Pennsylvania Press, p.51
- Garrido et al 2002*A&A*...387..821G

- Hernandez, O., Gach, J., Carignan, C. & Boulesteix, J. 2003, SPIE, 4841, 1472
- Ingraham, P., Doyon, R., Beaulieu, M., Rowlands, N. & Scott, A. 2010, SPIE 7731, 121
- Janesick, J. R. 2001, Scientific Charge-Coupled Devices (SPIE Press Monograph; PM 83. ISBN 0819436984; Bellingham, WA: SPIE Optical Engineering Press), 651.
- Kogelnik, H., 1969 Coupled wave theory for thick hologram gratings, The Bell System Technical Journal, Vol. 48, no. 9, p. 2909
- Le Fèvre et al, 1994A&A...282..325L
- Lepine, J. R. D., de Oliveira, A. C., Figueredo, M. V., Castilho, B. V., Gneiding, C., Barbuy, B., Jones, D. J., Kanaan, A., Mendes de Oliveira, C., Strauss, C., Rodrigues, F., Andrade, C. R., de Oliveira, L. S., de Oliveira, J. B., 2003, SPIE, 4841, 1086.
- Rangwala, Naseem; Williams, T. B.; Pietraszewski, Chris; Joseph, Charles L. 2008, AJ, 135, 1825
- Roesler, F. L. and Mack, J. E. 1967: J. Physique 28, Supp. C2, 313 - 320.
- Rosado, M.; Langarica, R.; Bernal, A.; Cobos, F.; Garfias, F.; Gutierrez, L.; Tejada, C.; Tinoco, S.; Le Coarer, E. 1995, RMxAC, 3, 263
- Smith, W. H. 1981, in Mod. Observational Tech. for Comets, p. 156.
- Taylor, K.; Atherton, P. D. 1980: Monthly Notices of the Royal Astronomical Society, vol. 191, p. 675-684.
- Tokovinin, A., Tighe, R., Schurter, P., Cantarutti, R., van der Blik, N., Martinez, M., Mondaca, E., Montane, A. 2008, SPIE, 7015, 70154.
- Tulloch, S., Scientific Detectors for Astronomy, 2005, 303.
- Tully, R. Brent 1974: Astrophysical Journal Supplement, vol. 27, p.415
- Veilleux, S.; Weiner, B. J.; Rupke, D. S. N.; McDonald, M.; Birk, C.; Bland-Hawthorn, J.; Dressler, A.; Hare, T.; Osip, D.; Pietraszewski, C.; Vogel, S. N. 2010, AJ, 139, 145-157.
- de Vaucouleurs, G.; Pence, W. D. 1980: Astrophysical Journal, vol. 242, p. 18-29.
- Williams, T. B.; Caldwell, N.; Schommer, R. A. 1984: Astrophysical Journal, vol. 281, p. 579-584.